ČESKÁ ZEMĚDĚLSKÁ UNIVERZITA V PRAZE

Technická fakulta

52. MEZINÁRODNÍ VĚDECKÁ KONFERENCE ČESKÝCH A SLOVENSKÝCH UNIVERZIT A INSTITUCÍ ZAMĚŘENÁ NA VÝZKUMNÉ A VÝUKOVÉ METODY SPOJENÉ SE SPALOVACÍMI MOTORY, ALTERNATIVNÍMI POHONY A DOPRAVOU

Katedra vozidel a pozemní dopravy

PRAHA
22. – 23. září 2021

Sborník přednášek

52. Mezinárodní vědecká konference českých a slovenských univerzit a institucí zaměřená na výzkumné a výukové metody spojené se spalovacími motory, alternativními pohony a dopravou

KOKA 2021

PRAHA
22. – 23. září 2021

Organizační výbor konference:

doc. Ing. Miroslav Růžička, CSc.
doc. Ing. Martin Pechout, Ph.D.
Ing. Martin Kotek, Ph.D.
Ing. Petr Jindra, Ph.D.
Ing. David Marčev, Ph.D.
Ing. Jakub Mařík, Ph.D.
Ing. Veronika Hartová, Ph.D.
Ing. Veronika Štekerová

Publikace neprošla jazykovou úpravou. Za obsah příspěvků odpovídají jejich autoři.

Technická fakulta
Katedra vozidel a pozemní dopravy
2021

ISBN 978-80-213-3132-7

OBSAH

52. INTERNATIONAL SCIENTIFIC CONFERENCE OF THE CZECH AND SLOVAK UNIVERSITY DEPARTMENTS AND INSTITUTIONS FOCUSED ON RESEARCH AND TEACHING METHODS RELATED TO COMBUSTION ENGINES, ALTERNATIVE DRIVES AND TRANSPORT

SEPTEMBER 22 – 23, 2021, PRAGUE
CZECH UNIVERSITY OF LIFE SCIENCE PRAGUE, FACULTY OF ENGINEERING,
DEPARTMENT OF VEHICLES AND GROUND TRANSPORT

MULTI-MODE PHEV WITH A DEDICATED HYBRID TRANSMISSION IN REAL-LIFE DRIVING SCENARIOS

Mikuláš Adámek[1], Rastislav Toman[2], Jan Soukup[3]

Abstract
Our paper studies a plug-in hybrid electric vehicle equipped with Dedicated Hybrid Transmission and optimized specifically for the charge sustaining WLTC performance. Python based quasi-static simulation model of the DHT powertrain is combined with the Pontryagin´s Minimum Principle energy management strategy and was further enhanced to handle different optimization goals (energy consumption, CO_2 emissions, and trip costs), SOC constraints, and additional control inputs. Simulation model was then tested and optimized using the different optimization goals on homologation WLTC driving cycle, and two different real-life scenarios, to assess the potential of SUV type vehicle with two different internal combustion engine concepts.

1. INTRODUCTION

Hybrid Electric Vehicles (HEV) and Plug-in Hybrid Electric Vehicles (PHEV) are widely used powertrain electrification options in modern vehicles aimed at European markets, due to their capability of achieving low CO_2 emissions during the homologation procedure.
The HEV powertrain layouts are various – either the parallel type layouts that are commonly used by the European and American OEMs, or more “HEV-tailored” Dedicated Hybrid Transmissions (DHT), for example Toyota Hybrid Synergy Drive. No matter which powertrain layout is finally chosen, the two other important development challenges remain: energy management strategy, and proper optimization target. However, powertrain layout, energy management strategy, and optimization targets are closely linked.
Regarding the optimization targets, the usual OEM approach is to exploit the current legislation’s goal to minimize tailpipe CO_2 emissions, considering the electric power from the battery as zero emission [1] – this way encouraging larger batteries and use of PHEVs instead of HEVs. The second approach is to look for the actual vehicle CO_2

[1] Mikuláš Adámek, CTU in Prague, Faculty of Mechanical Engineering, Technická 4, 166 07 Prague 6, Mikulas.Adamek@fs.cvut.cz
[2] Rastislav Toman, CTU in Prague, Faculty of Mechanical Engineering, Technická 4, 166 07 Prague 6, Rastislav.Toman@fs.cvut.cz
[3] Jan Soukup, CTU in Prague, Faculty of Mechanical Engineering, Technická 4, 166 07 Prague 6, Jan.Soukup@fs.cvut.cz

footprint, that can vary greatly with geographical location, and possibly with daytime or weather – because of the effective energy mix. The third approach would be the customer's point of view, where the main objective is the cost per driven kilometre rather than homologation or real-life CO_2 emissions. Finally, the fourth approach would be to have a look on the total energy consumption, disregarding its source.
The OEM's homologation approach was already presented by the authors on FISITA 2021 Conference [2], where the focus was to optimize the DHT powertrain for different ICE and vehicle combinations, using the charge-sustaining (CS) WLTC driving cycle. This presented paper progresses on our FISITA paper.

1.1 Goals of the Paper

The main idea is to simulate some real-life driving scenarios with the chosen DHT. Then, the goals follow the abovementioned HEV development challenges, improving our methods already presented in [2]:

- First goal is to enhance our optimal energy management strategy based on Pontryagin´s Minimum Principle (PMP) to account for SOC state limits.
- Second goal is to extend the PMP's control inputs by the series mode charge power, and other Hamiltonian formulations.
- Third goal is to identify the behaviour of chosen DHT powertrain in PHEV configuration in terms of CO_2 emissions, energy consumption, and cost per kilometre for the real-life driving scenarios.

2. MULTI-MODE DEDICATED HYBRID TRANSMISSION

Multi-mode DHT, that is used within our study was first presented by Schaeffler in 2019 [3]. This DHT combines an ICE with two electric motors – generator EM1 and traction motor EM2, friction clutch C0, and three fixed gears (Figure 1). Gear 1 matches the speeds of both electric motors to ICE; gears 2 and 3 then match all motors' speed ranges to the maximum vehicle speed (set to 180 km/h by [3]).

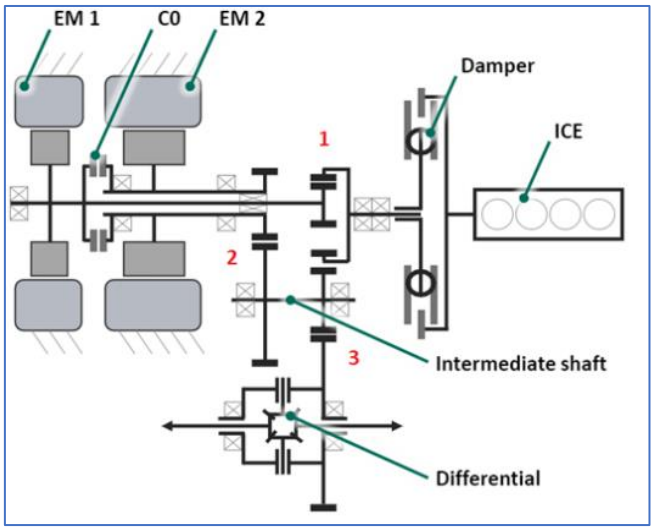

Figure 1: *Multi-mode DHT powertrain layout*

The three basic operation modes of this DHT are following (Table 1):

- *E-Mode* – EM2 only propels the vehicle, bellow the EV_{Lim} vehicle speed limit, when the ICE cannot be used. Therefore, the vehicle always starts at *E-Mode.*
- *P-Mode* – both ICE and EM2 can provide the traction power above the EV_{Lim} vehicle speed limit. The energy management strategy controls the ICE load-point-shifting.
- *S-Mode* – EM2 motor provides the traction power, and ICE charges the battery through the EM1.

	C0	ICE	EM1	EM2
E-Mode	Open	Off	Off	Mot/Gen
P-Mode	Closed	Mot	Off	Mot/Gen
S-Mode	Open	Mot	Gen	Mot/Gen

Table 1: *DHT operation modes*

Schaeffler's study [3] suggests 50 km/h EV_{Lim} vehicle speed limit, and we use the same value.

3. PMP ENERGY MANAGEMENT STRATEGY

The PMP energy management strategy solves the optimal HEV control problem in an offline manner. It uses a quasi-static vehicle model as its basis, requiring an a priori knowledge of the whole vehicle driving cycle, and then calculates the optimal power/torque splits between the powertrain components. PMP obtains the optimal control trajectory of the control inputs vector $\boldsymbol{u}(t)$, by minimizing the Hamiltonian function H (equation 2) for a general formulation of a performance measure J, with a penalty function g, system state variables vector $\boldsymbol{x}(t)$, and their constraints (equation 1). Vector $\boldsymbol{p}$ in equation 1 is then a vector of Lagrange multipliers (co-states), and $\boldsymbol{a}$ a vector of system equality constraints.

$$J(\boldsymbol{u}) = \int_{t_0}^{t_{cycle}} g(\boldsymbol{x}(t), \boldsymbol{u}(t), t)\, dt \tag{1}$$

$$H(\boldsymbol{x}(t), \boldsymbol{u}(t), \boldsymbol{p}(t), t) \triangleq g(\boldsymbol{x}(t), \boldsymbol{u}(t), t) + \boldsymbol{p}^T(t)[\boldsymbol{a}(\boldsymbol{x}(t), \boldsymbol{u}(t), t)] \tag{2}$$

More details on the quasi-static vehicle model, and the Hamiltonian function formulation are present in our paper [2].

3.1 S-Mode Charge Control Input

In our abovementioned study [2] we did use only one control input $\boldsymbol{u}(t)$ – the EM2 torque $T_{EM2}(t)$ – controlling the ICE load-point-shifting in *P-Mode*. However, here we add another control input, the *S-Mode* charge power $P_{S-Mode}(t)$.

Theoretically, the *S-Mode* can be operated in a random ICE/EM1 operating point (respecting the speed and torque limits of both motors), but this would lead to a very large computational matrix, from which the PMP would have to select the one optimal operating point at given time. To reduce this matrix and therefore to speed-up the calculation, we focus on a single operating line (*S-Line*), with the best combined system efficiency (Figure 2, efficiency maps are only illustrational). The *S-Line* then determines

the exact ICE/EM1 operating point based on the chosen control input *S-Mode* charge power P_{S-Mode}.

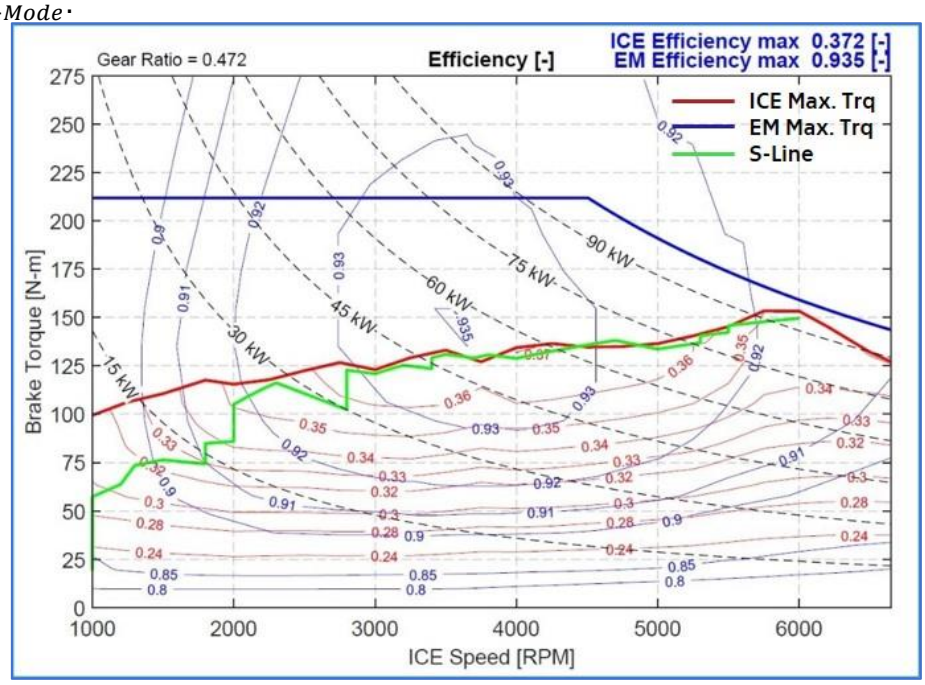

Figure 2: *Combined ICE/EM1 S-Mode operation map with S-Line*

3.2 Hamiltonian Functions

We use two different Hamiltonian formulations – fuel and energy formulation – each for the different simulation scenarios.

3.2.1 Fuel Hamiltonian

Optimality performance measure J from equation 1 for the "fuel" Hamiltonian takes the form of fuel mass $m_f$consumed over the whole driving cycle duration t_{cycle} (equation 3), with the Hamiltonian in equation 4.

$$J(T_{EM2}, P_{EM1}) = \int_{t_0}^{t_{cycle}} \dot{m}_f(T_{EM2}(t), P_{EM1}(t), t)\, dt \tag{3}$$

$$H(\xi(t), T_{EM2}(t), P_{EM1}(t), p(t), t) = \dot{m}_f(T_{EM2}(t), P_{EM1}(t), t) + p(t)\left[\dot{\xi}(\xi(t), T_{EM2}(t), P_{EM1}(t), t)\right] \tag{4}$$

The base Hamiltonian is used for the *S-Mode* behaviour study with the WLTC driving cycle.

3.2.2 Energy Hamiltonian

Then, for the simulations regarding the energy efficiency, we use Hamiltonian written in terms of energy (equation 5), or "energy" Hamiltonian. H_u in equation 5 is Lower Heating value of petrol fuel, and $p(t)$ then represents a non-dimensional penalty coefficient for electric energy.

$$H(\xi(t), T_{EM2}(t), P_{EM1}(t), p(t), t) = H_u \dot{m}_f(T_{EM2}(t), P_{EM1}(t), t) + p(t)\left[\dot{\xi}(\xi(t), T_{EM2}(t), P_{EM1}(t), t)\right] \tag{5}$$

The procedure for energy Hamiltonian iteratively searches for the lowest total energy by changing the final target SOC (initial SOC is always 80 %). Electric energy consumption is determined from the final SOC difference, assuming also the charging efficiency from the grid of 91 %, that correspond to low power "slow" charging [1]. This procedure is also used for CO_2 and cost optimizations.

3.3 SOC Limits Control Method

The optimal control problem definition in equation 2 does not prevent the violation of battery SOC bounds (ξ_{low} or ξ_{high}), for the resulting SOC trajectories. This is usually not a problem when simulating for example the homologation WLTC with larger size batter HEV (especially PHEV), but can happen for RDE or real-life cycles, HEVs with small size batteries, or generally some problems at the boundary.

There are numerous approaches to solve the PMP problem with inequality constraints [4], but here we use the *indirect adjoining method* also used and in length described in [5]. The original problem of finding one optimal equivalence factor p over the entire vehicle driving cycle $[0, t_{cycle}]$ is split into an iterative process of finding optimal p_i values for the sub-intervals with τ_i bordering the intervals (Figure 3). The resulting optimal trajectory of p is then discontinuous.

The procedure first solves the unconstrained problem – if the SOC constraints are not violated, the solution is considered optimal. If the SOC constraint is violated at time τ_i, the time domain splits into two ($[0, \tau_i]$ and $[\tau_i, t_{cycle}]$). The optimal problem is solved for each of these sub-intervals, and SOC limits ξ_{low} or ξ_{high} replace the original unconstrained problem's SOC target/initial condition. Note: The illustrational SOC constrained problem in Figure 3 is for a mild HEV vehicle on a driving cycle, that leads to three SOC limit violations.

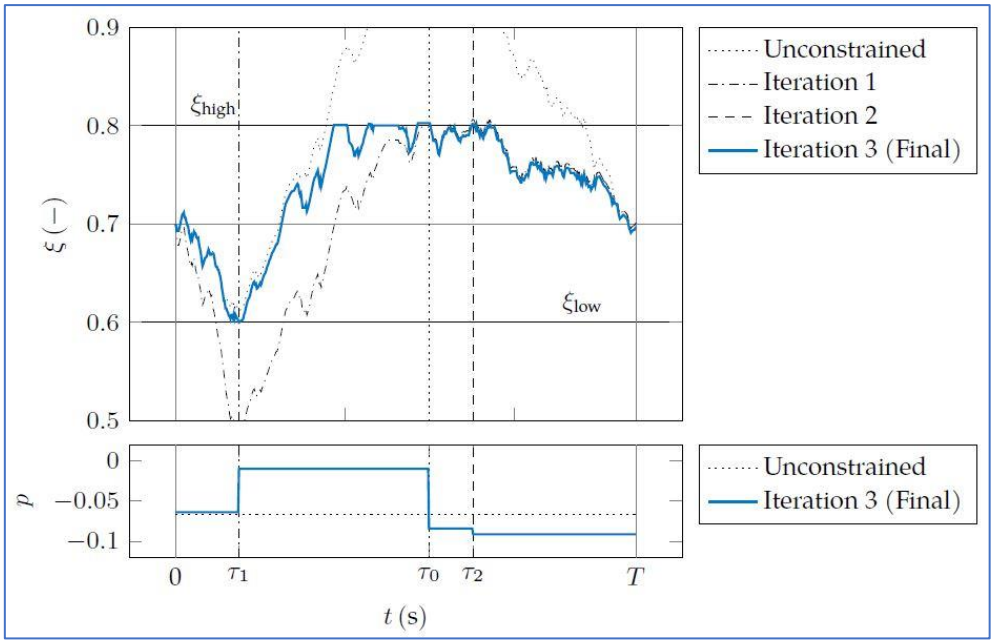

Figure 3: *Equivalence factor iteration for SOC state inequality satisfaction [5]*

4. VEHICLE DATA AND PARAMETERS

Simulated vehicle is a standard larger family SUV with its main characteristic summed up in Table 2. Two electric motors that are part of the DHT are both high efficiency synchronous traction motors with maximum parameters listed in Table 3. Two ICE concepts were simulated: *ICE1* is a classical 1.5 L naturally aspirated engine – presenting the cheap and simple hybridization option; *ICE2* is then a typical modern state of the art downsized turbocharged engine with 1.0 L displacement. Both engines have approximately the same maximum brake power output of 80 kW. Small size turbocharged ICEs are currently prevalent in the industry, therefore also our *ICE2* concept is prioritized in this study, and *ICE1* is then used mostly for comparison.

Base vehicle mass	1935	[kg]
Frontal area	2.60	[m^2]
Drag coefficient	0.35	[-]
Tire rolling resistance factor	0.010	[-]
Tire rolling radius	0.356	[mm]

Table 2: *Main vehicle parameters*

High voltage battery is based on a production 37 Ah lithium-ion prismatic battery cells, down-scaled to 30 Ah capacity, and nominal voltage of 3.7 V. The PHEV battery system is then configured into 104 cells in series, yielding the total energy capacity of 11.0 kWh at 400 V.

	Torque [Nm]	**Power [kW]**	**Speed [RPM]**	**Efficiency [%]**
EM1	100	100	15500	93.5
EM2	335	130	13000	92.9

Table 3: *Maximum parameters of electric motors EM1 and EM2*

Table 4 shows the optimal gear parameters for both ICE concepts from our previous optimization study [2] in CS WLTC driving cycle. Gear 1 optimal parameters are very similar for both ICE concepts, but gears 2 and 3 result in higher operating speeds of all three motors for the *ICE2* concept case.

		Gear 1	**Gear 2**	**Gear 3**
ICE1	z_{in}	39	26	16
	z_{out}	16	77	46
	i	0.410	2.962	2.875
ICE2	z_{in}	43	19	16
	z_{out}	18	98	29
	i	0.419	5.158	1.813

Table 4: *DHT gears for both ICE concepts*

Finally, Figure 4 shows system *S-Line* efficiencies, dependent on *S-Mode* charge power requirement (gear 1 efficiency of 98 % is considered). *ICE2* concept achieves overall better efficiency (around 1.5 %), and in a wider span, compared to *ICE1* concept.

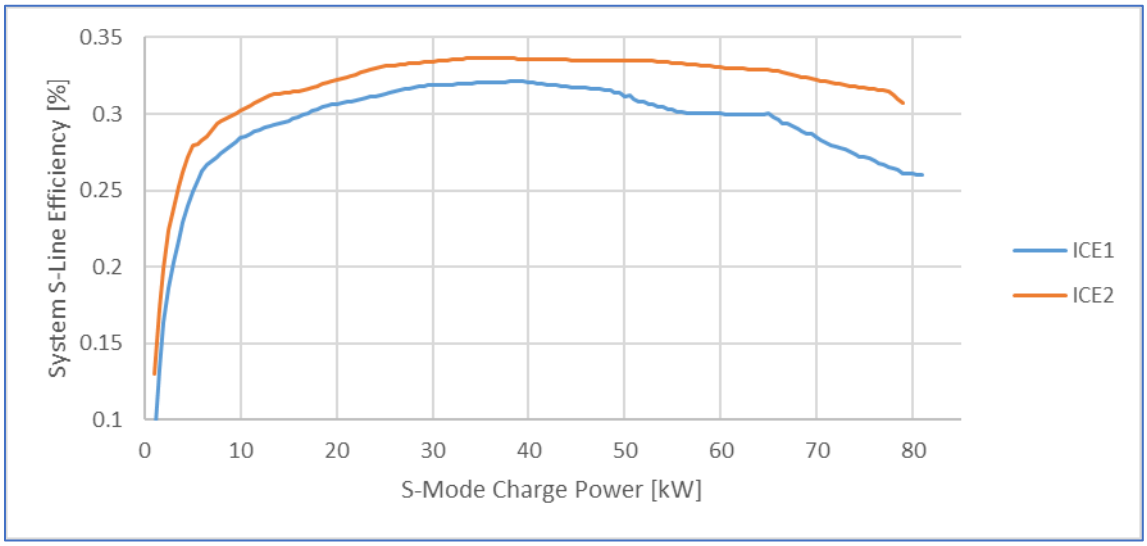

Figure 4: *S-Line system efficiencies for both ICE concepts*

5. SIMULATION RESULTS

The simulation results are split into two main areas: *S-Mode* behaviour testing on the homologation WLTC driving cycle, and energy, cost, and CO_2 minimization results. Therefore, before presenting the results, we also present the two real-life driving cycles.

5.1 Real-Life Driving Cycles

The real-life cycles were measured for master thesis of one of the authors [5]. Figure 5 shows these scenarios' vehicle speed and elevation profiles from the GPS measurement:

- Route 3 – city trip – 6.2 km
- Route 6 – intercity/city trip – 47.1 km

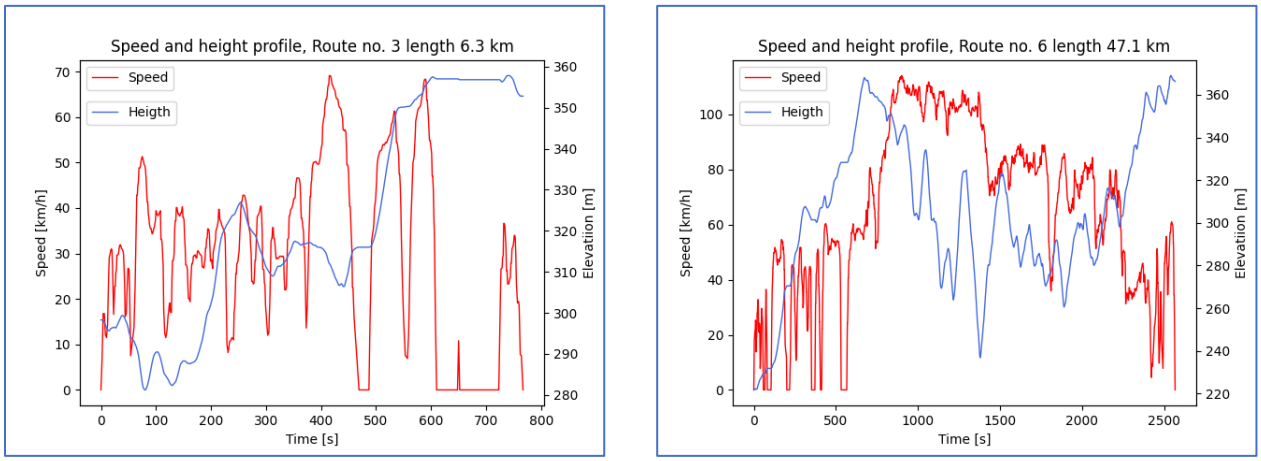

Figure 5: *Real-life driving cycles (left – Route 3; right – Route 6)*

5.2 S-Mode WLTC Sensitivities

The first results are the *S-Mode* behaviour sensitivities. Figure 6 shows the vehicle fuel consumption dependency on energy charged into battery. The fuel consumption naturally grows with charged energy, with slightly higher rate for the *ICE1* compared to *ICE2*.

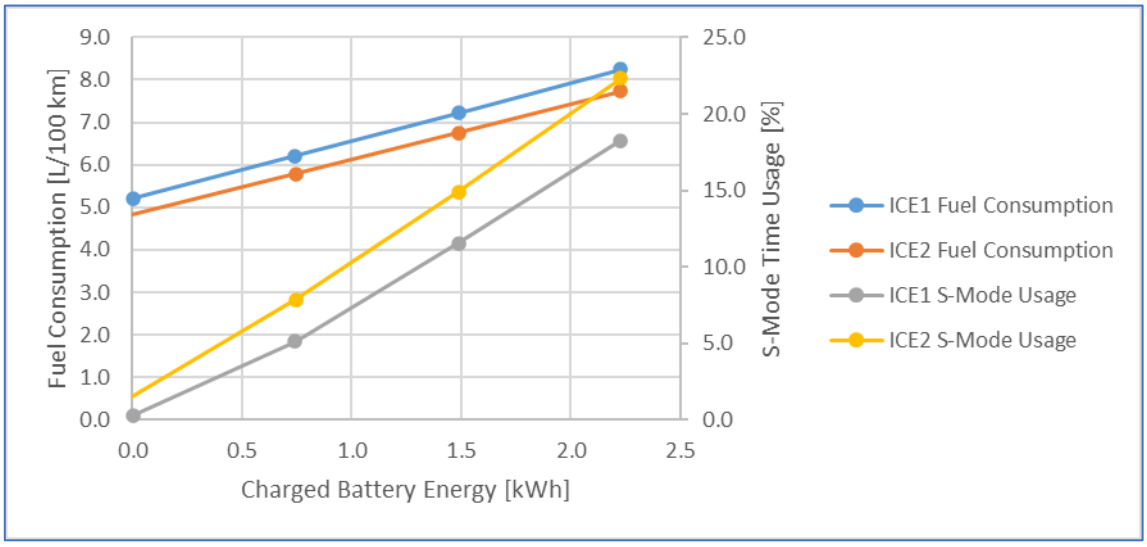

Figure 6: *S-Mode results in WLTC driving cycle*

The *S-Mode* usage (100 % would mean, that *S-Mode* is used whenever possible) rises steadily for higher charge requirements. *ICE2* concept uses the *S-Mode* charging generally more, then *ICE1*.

S-Mode charging for both concepts is almost exclusively run at the optimal ICE/EM1 system efficiency. The *P-Mode* ICE operating points stay very similar for all charging sensitivity cases – the PMP strategy only "adds" the necessary charging events via energy-optimal *S-Mode*.

Finally, an interesting result is that both *ICE1* a *ICE2* are using the *S-Mode* also for the WLTC CS results (although very little, for 3 and 14 seconds respectively). This further

improves the results from [2] for about 0.5 gCO_2/km – after balancing the SOC to the exact CS level.

5.3 Energy Minimization

This optimization scenario uses the energy Hamiltonian, and the results represent the total consumption energy dependent on used battery capacity (Figure 7 – negative values signify battery charging, positive a battery discharge, and zero value is for CS cycle).

The optimization highly prioritizes energy from battery, but with visible minima close to 0.3 kWh/km of energy consumption. *ICE2* concept gives better results according to expectation, and *S-Mode* is eliminated in the optimal simulations.

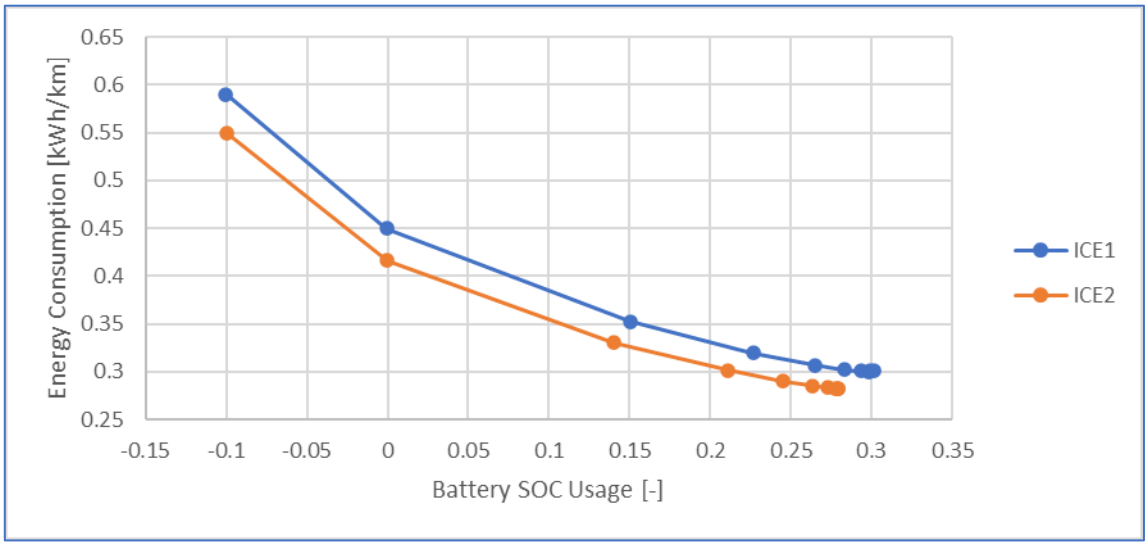

Figure 7: *Energy optimization results*

Figure 8 then shows the EM2, and ICE use in the energy optimized Route 6 scenario (the same behaviour is apparent for the other real-life scenarios, and WLTC). The operating points represent the actual efficiencies of both motors, normalized by their best achievable efficiency, thus indicating how well are the respective power sources used. It is apparent that PMP algorithm uses the ICE as secondary power source, only when it must, at lower than maximum achievable efficiencies, although at high torque demands. This behaviour is more apparent for low demand “city” cycles.

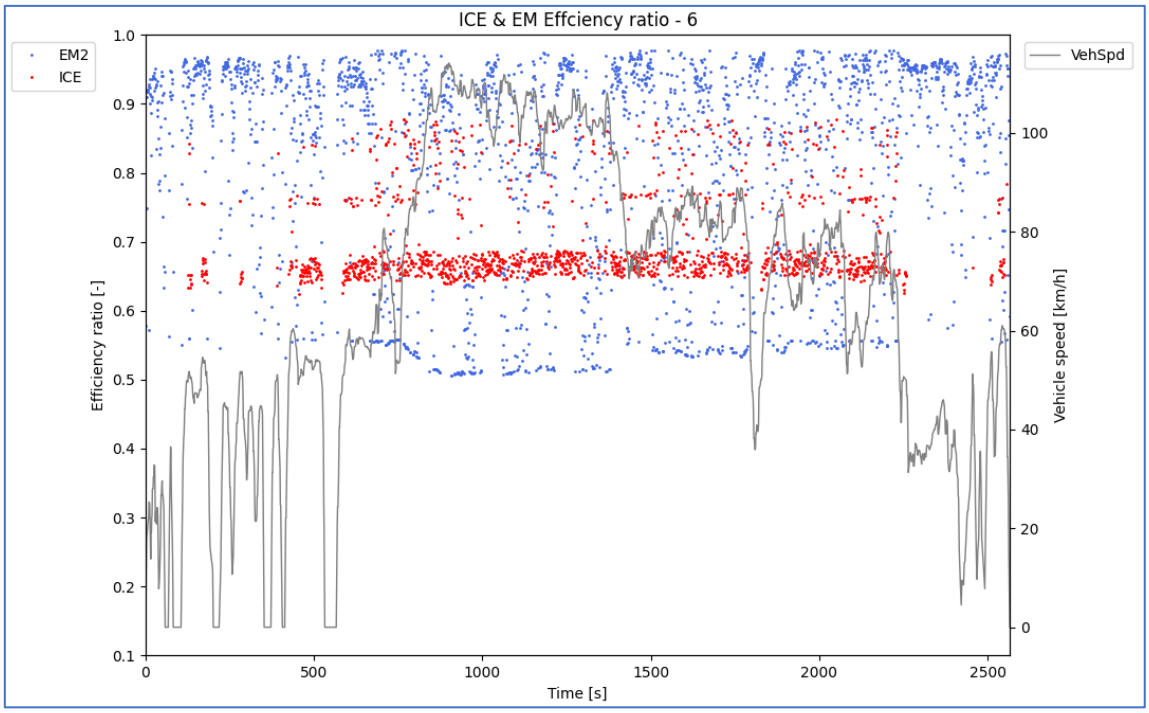

Figure 8: *Efficiency ratios along the energy optimized Route 6 driving cycle for ICE2 concept*

5.4 Cost and CO_2 Minimization Results

The minimization of cost depends on the costs of individual components: fuel and charged electric energy. Similarly, for the CO_2 emissions minimization, the result is heavily dependent on emitted gCO_2/L and gCO_2/kWh.

For both optimization options, we have fixed the fuel cost or emission coefficient and varied the respective values for the electric energy. Fuel price is 1.26 €/L, which is an average current value in Czech Republic. The fuel emission coefficient is 22.8 gCO_2/L, corresponding to E10 gasoline, that was used for the ICE full maps. Electric energy cost was varied in a range from 0.079 to 0.553 €/kWh, with a step of 0.079 €/kWh. The electric energy emission coefficient was then varied from 200 to 800 gCO_2/kWh, with a step of 200 gCO_2/kWh.

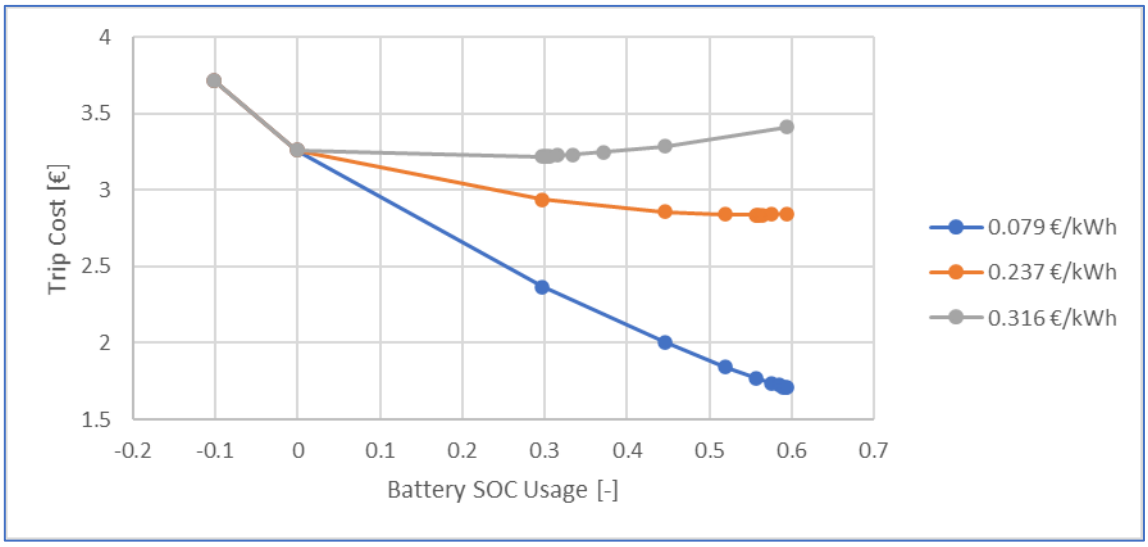

Figure 9: *Trip costs for Route 6 driving cycle optimizations with ICE2*

Figure 9 yields interesting conclusions for *ICE2* trip cost optimization at Route 6:

- For electric energy costs around 0.237 €/kWh, there is a clear optimum and further discharging of the batter does not improve the trip cost.
- For electric energy costs bellow 0.237 €/kWh, the trip costs improve with preferring the electric energy.
- Finally, from electric energy costs upwards of 0.316 €/kWh, the trip costs are best for the CS operation.

Similar behaviour is observed for other driving cycles, and *ICE1* concept.

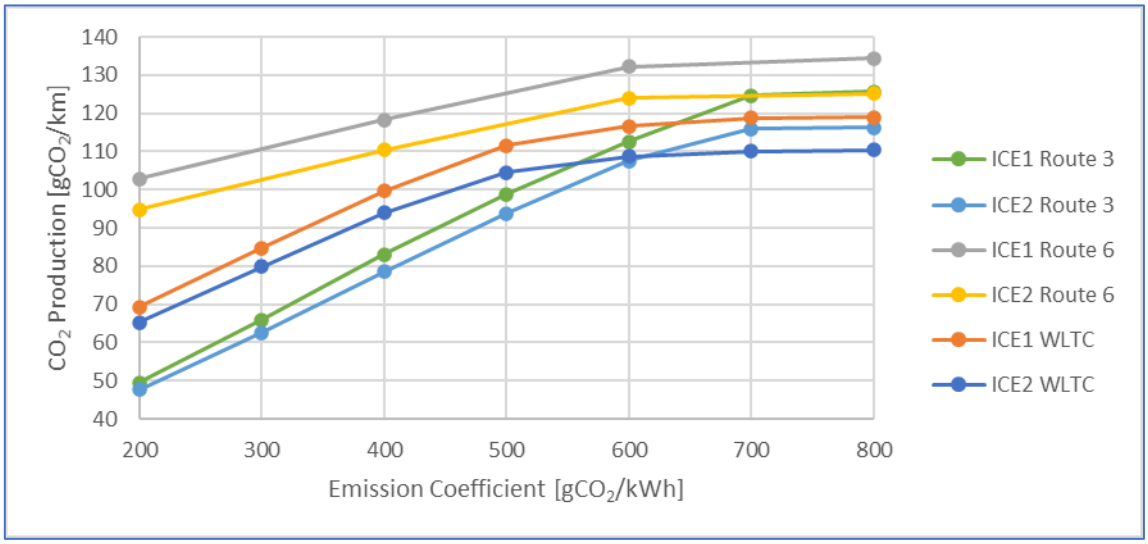

Figure 10: *CO_2 production for both ICE concepts*

CO_2 emission optimizations give similar results (Figure 10). The boundary values for electric energy emission coefficient are around 600 to 700 gCO_2/kWh. Bellow these emission coefficient's values it is advantageous to use the electric energy from the

battery. Values above lead to the CS mode as optimal. The sensitivity on ICE concept, and driving cycle is rather high.
ICE2 concept gives better overall results also for these two optimizations. The same applies for the *S-Mode* use, that is eliminated in all the optimal simulations.

6. CONCLUSION

Our paper presented enhancements to the existing Pontryagin's Minimum Principle (PMP) energy management strategy combined with a quasi-static model of a PHEV equipped with DHT powertrain. These enhancements are the additional control input of *S-Mode* charge power, the SOC limit control method, and finally different Hamiltonian formulations, that allow for different optimization goals: total energy, cost, or CO_2 emissions minimizations.
These new functions were tested on WLTC homologation cycle and two real-life driving cycles for all three abovementioned optimization goals:

- Energy optimizations show, that the PMP control strategy maximizes battery use – although there is some limit for a particular driving cycle.
- Cost optimizations (with constant gasoline price of 1.26 €/L) show, that to gain some profit from electric energy usage, the price must be below 0.316 €/kWh.
- CO_2 emission optimizations show that the use of electric energy from the grid is advantageous only when the emission coefficient is below 600 or 700 gCO_2/kWh, depending on ICE concept and driving cycle (assuming 91 % charge efficiency from the grid).

PMP control strategy prefers battery charging either via *P-Mode* ICE load point shifting, or via *S-Mode* at peak available efficiencies, when the target is battery charge (final SOC higher then initial); however, when the target is battery discharge, the ICE is used only as a secondary power source, with a clear preference of electric drive – *S-Mode* is never used at these cases. This behaviour also relates to the energy management's control parameter EV_{Lim} (set to 50 km/h), that determines the change from *E-Mode* to *P-Mode*. PMP strategy with EV_{Lim} parameter must use the ICE at prescribed moments, and therefore must do compromises.
It is important to stress, that our Hamiltonian function, that is minimized by the PMP, does not use any additional terms to control e.g., the frequent ICE on/off behaviour, maximum ICE torque rise, aftertreatment thermal behaviour, or similar parameters.

REFERENCES

[1] MORKUS J., MACEK J., 2021. Kam kráčíš, elektromobilito?, https://www.fs.cvut.cz/verejnost/pr-media/pribehy-z-ustavu/kam-kracis-elektromobilito/
[2] TOMAN R., ADAMEK M., HERMANOVA J., DENK P., SOUKUP J., 2021, Evaluation Study of a Multi-Mode HEV with a Dedicated Hybrid Transmission, FISITA 2021 Conference, 2021, doi: 10.46720/F2020-ADM-108
[3] LAUINGER CH., REITZ D., BAYOUX L., ADRIAN M., CIESEK M., 2019. Hybrid Transmissions of the Future, Proceedings of 18th International CTI Symposium Automotive Drivetrains

[4] HARTL R. F., SETHI S. P., VICKSON R. G., 1995. A Survey of the Maximum Principles for Optimal Control Problems with State Constraints, SIAM Review, pp. 181-218. http://www.jstor.org/stable/2132823
[5] SOUKUP J., 2021. Two-Level Energy Management Strategy for Hybrid Electric Vehicle using Planned-Trip Information. Praha. Master Thesis. ČVUT v Praze.

ACKNOWLEDGEMENT

This work was realized using support of:

- Technological Agency, Czech Republic, programme National Competence Centres, project # TN01000026 Josef Bozek National Center of Competence for Surface Vehicles.
- The Grant Agency of the Czech Technical University in Prague, grant No. SGS21/155/OHK2/3T/12.

This support is gratefully acknowledged.

52. MEZINÁRODNÍ VĚDECKÁ KONFERENCE ČESKÝCH A SLOVENSKÝCH UNIVERZIT A INSTITUCÍ ZAMĚŘENÁ NA VÝZKUMNÉ A VÝUKOVÉ METODY SPOJENÉ SE SPALOVACÍMI MOTORY, ALTERNATIVNÍMI POHONY A DOPRAVOU

22.-23. ZÁŘÍ 2021, PRAHA
ČESKÁ ZEMĚDĚLSKÁ UNIVERZITA V PRAZE, TECHNICKÁ FAKULTA,
KATEDRA VOZIDEL A POZEMNÍ DOPRAVY

WATER HARVESTER UNIT FOR WATER INJECTION SYSTEM

Jiří Bazala[1], Guillaume Hébert[2], David Svída[3], Martin Beran[4]

Abstract
Reducing fuel consumption and thus CO2 emissions is one of the most urgent tasks of current research in the field of internal combustion engines. Water Injection has proven its benefits to increase power or optimize fuel consumption of passenger cars. This technology enables knock mitigation to either increase the engine power output or raise the compression ratio and efficiency while enabling λ = 1 operation in the complete engine map to meet future emission targets. Current systems have limited container capacity. It is necessary to refill the water tank regularly. This also means that we cannot get the benefits of an engine with a higher compression ratio. For this reason, the self-contained system was investigated. This article is a methodology for finding the right design of a self-contained water injection system, but also a vehicle test that proves the function.

1. INTRODUCTION

The need to further reduce fossil fuel consumption in the context of current and future global CO2 emission limits requires intensive search for new solutions for automotive engines. For reciprocating internal combustion engines, the mass of CO2 emitted into the atmosphere is a function of their fuel consumption. Therefore, research into internal combustion engines is currently focused both on reducing the passive resistances of all mechanisms and on improving the efficiency of their thermodynamic cycles. As for the second option, the most promising solution is to lower the in-cylinder temperature and ensure stoichiometric combustion throughout the engine operating map. The maximum operating conditions of gasoline internal combustion engines are, in general, restricted by the temperature limit of engine components and knocking conditions. Knocking is sharp sound effects caused by premature combustion of part of the com-

[1] Jiří Bazala, Hanon Systems Autopal Services s.r.o., Hluk, Czech Republic; jbazala@hanonsystems.com
[2]Guillaume Hébert, Hanon Systems Autopal Services s.r.o., Hluk, Czech Republic; GHEBERT4@hanonsystems.com
[3] David Svída, ÚDAI, VUT Brno, Brno, Czech Republic, svida@fme.vutbr.cz
[4] Martin Beran, ÚDAI, VUT Brno, Brno, Czech Republic, beran.m@fme.vutbr.cz

pressed air-fuel mixture in the cylinder. This phenomenon is destructive for engine itself and it is mainly caused by high temperature of combustion mixture. Knocking is controlled by engine management by fuel enrichment. With modern turbocharged gasoline engines, the maximum acceptable exhaust gas temperature is limited by the thermal material resistance of the turbine. To protect critical components, fuel enrichment ($\lambda < 1$) has been used under these conditions. The high vaporization enthalpy of the gasoline enables a significant reduction of the exhaust gas temperature without putting additional thermal load on the cooling system [1].
Nowadays, mixture enrichment is undesired along with the expected extension of regulations in future legislation, which may also include restrictions on Fuel Consumption/CO2 emissions. The new emission regulation will require stoichiometric operation ($\lambda = 1$) under all engine operating conditions. Consequently, a different medium with a high vaporization enthalpy is required. Based on the patent of Pierre Hugon in 1865 [2], Water Injection (WI) into the combustion chamber of a gasoline engine can also be used to control the temperature of engine components.

Water Injection can be used either for:

- Engine performance improvement or
- Improved fuel consumption

For improved performance, the injection of water into the cylinder lowers the gas temperature, mitigating knocking and allowing a higher load at $\lambda = 1$. As shown in Figure 1 below, this increases power/torque characteristics.

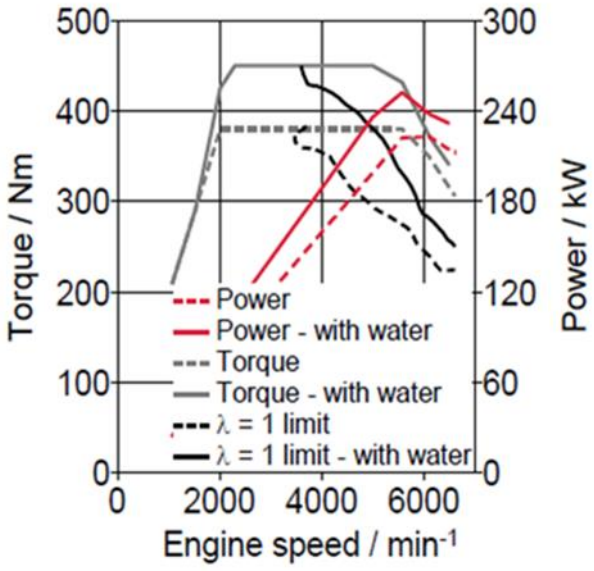

Figure 1: *Performance/Torque improvement using water injection [3]*

As far as fuel consumption (FC) improvement is concerned, using WI on a down-sized, turbocharged gasoline engine allows improved combustion phasing and knock mitigation at an increased Compression Ratio (CR) while avoiding fuel enrichment. This will allow stoichiometric operation throughout the entire engine map. Current engine developments seem to concentrate on the effect of “Performance Improvement”, but it can be expected that the development of engines for the mid 2020’s will shift focus to improving fuel consumption [4,5,6,7,8,9]. What both strategies

have in common is the use of vaporization enthalpy of a liquid. Injecting Water for vaporization offers an improved cooling effect compared to fuel by a factor of more than 5. It must be mentioned that the “Water Injection”—Technology is only one option of FC improvement through mixture dilution. It competes with Exhaust Gas Recirculation (EGR) in some modes for the same purpose (Figure 2). It has been demonstrated that at medium load a 40–50% Water-to-Fuel Ratio (WFR) with Port Water Injection (PWI) has the same effect as an EGR-rate of 10% [10].

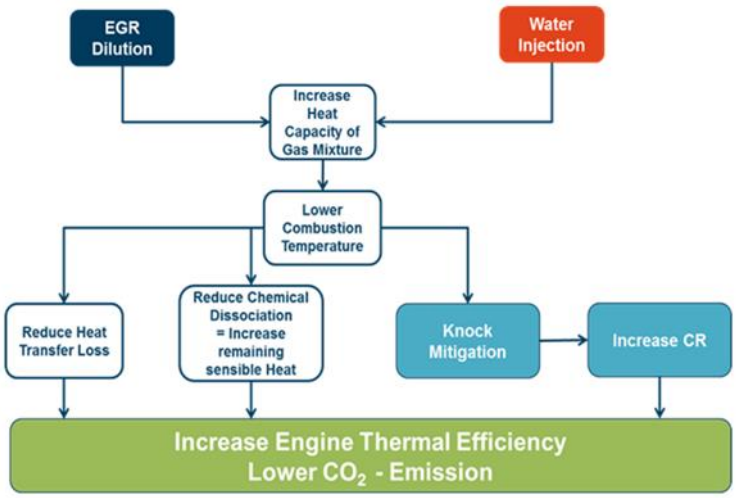

Figure 2: *Summarizes the respective effects of EGR and Water Injection.*

However, WI does have benefits when compared to EGR, especially better controllability as this is not a closed-loop as with EGR, the timing of injection is not linked to other parameters such as turbo charger backpressure, limited inertia (PWI timing not linked to engine operation) and combustion delay (as present with EGR). Additionally, it does not deteriorate combustion stability significantly. The combustion delay linked to EGR dilution and the necessary adaption of the recirculated gas mass flow to the maximum turbocharger characteristics are typically two limiting parameters of the maximum acceptable EGR rate.

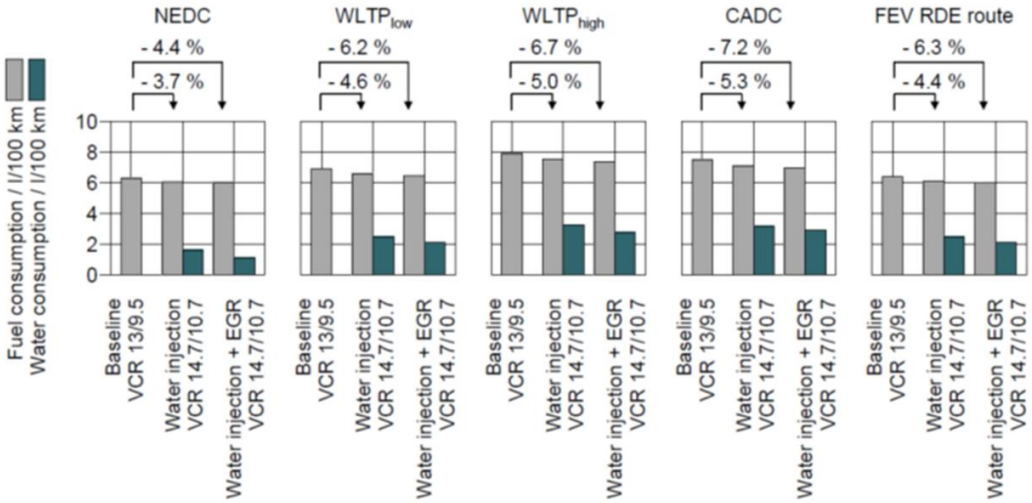

Figure 3: *Fuel consumption benefits of EGR and WI for various drive cycles*

2. MOTIVATION

As Figure 3 shows, WI has significant effect on fuel consumption. It is without doubt that Fuel Consumption is even lower with a higher compression ratio. Unfortunately, current WI systems in series production are not able to use this maximum possible benefit to their advantage. If the water injection liquid were drained from the tank and the combustion mixture were not cooled through water evaporation, fuel consumption would significantly increase, as evaporation of fuel would take place instead of evaporation of water. To ensure the system has a sufficient amount of water injection liquid, a self-contained tank is necessary.

Competing On-board water sources

There are limited sources of liquid that can be contained without human refill. These are:

- Harvesting air humidity from ambient (e.g., by A/C condensate)
- Surface Water (e.g., rain water collected from vehicle body)
- Exhaust Gas Condensate

The first two variants are highly dependent upon weather ambient conditions with sufficiently high humidity levels or driver habits (A/C operation is undesirable). Consequently, an adequate supply of water cannot be ensured. On the contrary, the condensation of water vapour formed during gasoline combustion is a reliable source of water. The temperature and humidity levels have only a minor contribution to the full amount of water being present in the exhaust gas. Almost all water in exhaust comes from a combustion reaction from carbohydrates and oxygen from air, not from humidity in air. This can be seen in Equation (1) where ideal combustion is described.

$$C_8H_{18} + 12{,}5(O_2 + 3{,}76N_2) \rightarrow 8CO_2 + 9H_2O + 47N_2 \quad (1)$$

The formula above can calculate that 1 kg of fuel on the left side of the formula is 1.4 kg of water vapour on the right side which can be harvested as liquid for WI.

3. WAHASY Efficiency

The fact that water vapour (WC) is present in exhaust is already known. In order to harvest water from exhaust, it is necessary to condensate water vapour to water liquid. The exhaust pressure at tailpipe is around 1 bar and it is common knowledge that water molar concentration is 14%. Therefore, the partial water vapour pressure can be deter-mined according to Dalton's law which is 0.14 bar. The water vapour partial pressure specifies dew point, below which the water vapour condensates as shown in Figure 4, based on the data in [11]. At a pressure of 0.14 bar, the saturation temperature is 53 °C (see Figure 4).

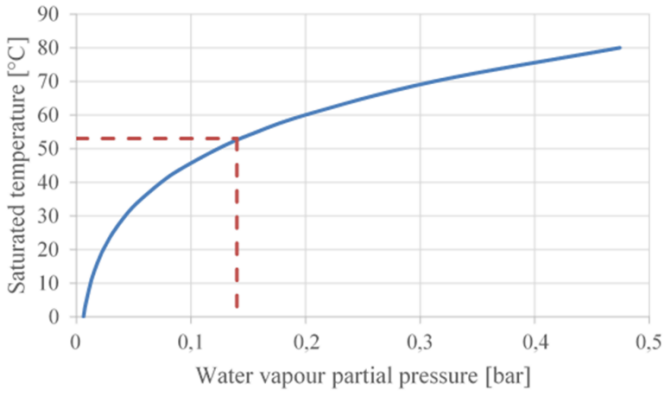

Figure 4: *Water saturation pressure.*

In order to achieve a "closed-loop"-operation (e.g., on-board generation of water using exhaust gas) a system called WAHASY (WAter HArvesting SYstem) has been developed. Its primary target is to provide enough water in liquid state to match the required amount as needed for intended engine operation. This amount is given by Equation (2), where WFR stands for "Water to Fuel Ratio" (e.g., the volume of liquid water injected) compared to the volume of fuel and the WAHASY efficiency is the total efficiency of the system (e.g., the amount of water which can effectively be used for the water injection). In an ideally dimensioned system, this efficiency also matches the amount of water being condensed divided by the total amount of water present in the exhaust gas.

$$\frac{WFR}{WC} = \Phi_{WAHASY} = \frac{M_{condensed_{water}}}{M_{water_{in_{exhaust_{gas}}}}} \tag{2}$$

Initial investigation in the past showed a wide array of water consumption figures when applying Water Injection, depending on test procedures and/or driving habits (see Figure 5).

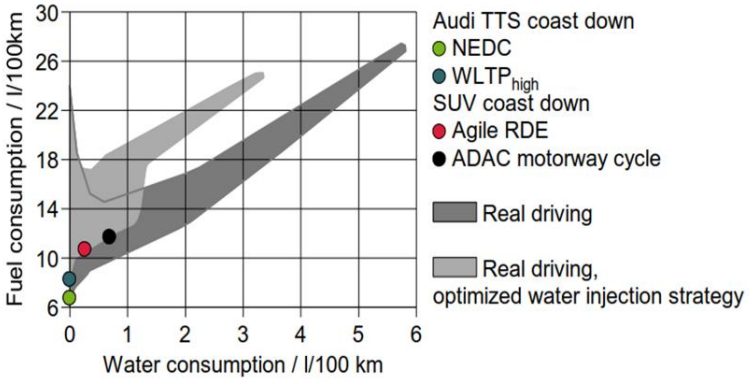

Figure 5: *Water Consumption for Various Test Conditions [12]*

Figure 5 shows that the required Water-to-fuel ratio (WFR) even if it is able to raise up to 20% is mostly under 10% in the tested drive cycles. This leads to a required WAHASY-efficiency of around 8% (up to 15% is considered for the most extreme "Real

Drive" (RDE) profile). The efficiency of the WAHASY system is comprised of water condensation efficiency and the separation efficiency of small droplets from the exhaust stream.

4. RESULTS

4.1. GT-Suite 1D model

To determine the right WAHASY size, a GT-Suite model was developed and verified by engine testing. GT Suite is the industry-leading simulation tool with capabilities and libraries aimed at a wide variety of applications in automotive technology. Criteria of the decision matrix were:

- Limit system complexity
- Increase package compactness
- Maximize thermal performance
- Minimize heat dissipated through the LT coolant loop
- Minimize costs

A two-stage cooling design was selected as the best design (initial HT HEX followed by a second LT HEX) to condensate water vapour. A third device ("Harvester") is intended to separate the condensate droplets from the exhaust gas flow. The GT-Suite 1D Tool was chosen to model behaviour measured on a real vehicle (see Figure 6). See the maximum available water content in exhaust gases below.

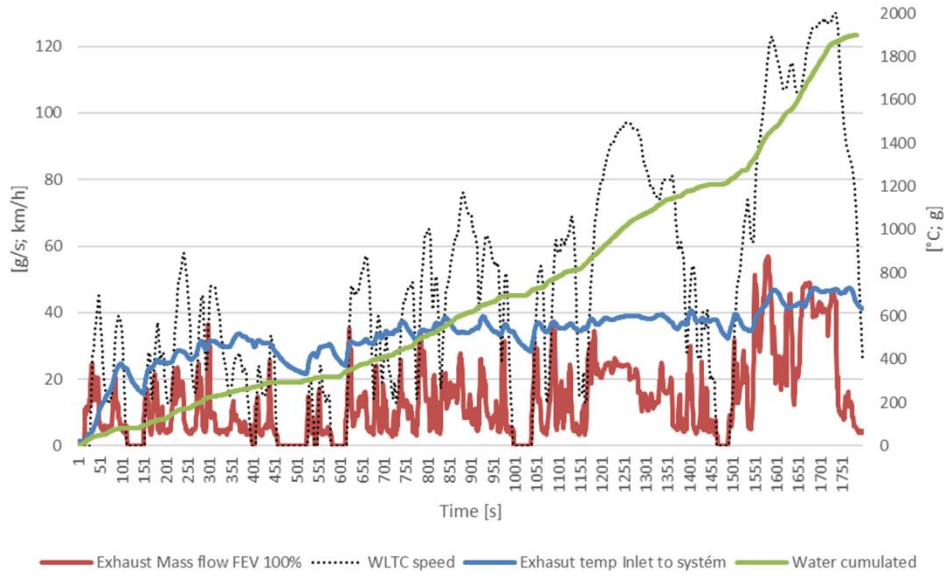

Figure 6: *Data from the vehicle test*

The data above will serve as inputs to the GT model (Figure 7), especially the inlet temperature and mass flow of exhaust. As mentioned above, the system has two coolant loops. High temperature (HT) and low temperature (LT). The high-temperature loop has two parallel coolers with a temperature of 90 °C. The low-temperature cooler is connected to a low-temperature radiator cooled by ambient air. The cooler thermal properties were taken from real calorimeter measurements (Figure 8).

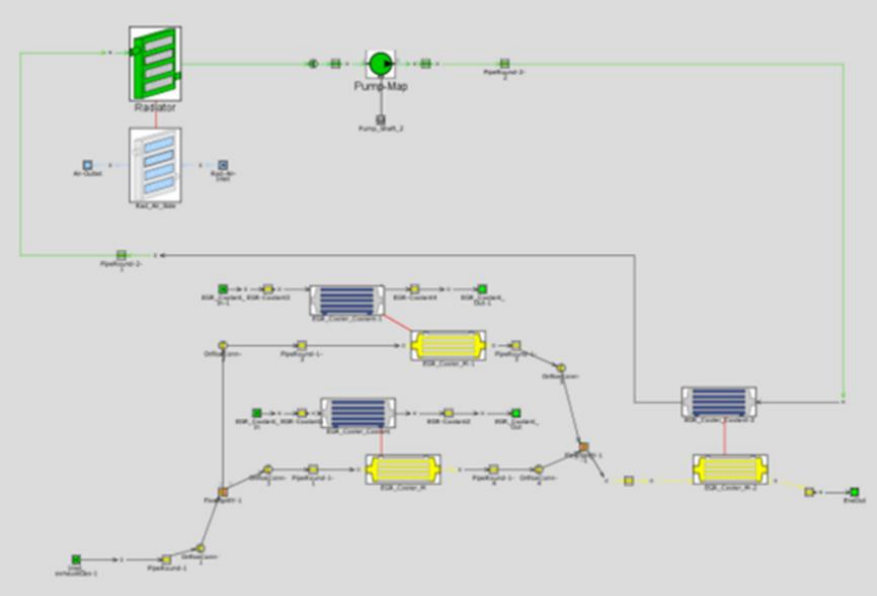

Figure 7: *GT model of HAWASY system*

Main Data Output Advanced

Attribute	Unit	Object Value
Type of Performance Input		heat-rate
Master (Internal) Flow Rate Input		Mass_Flow_Rate
Slave (External) Flow Rate Input		Volume_Flow_...

Att...	Master Mass Flow	Master Inlet Temperature	Master Inlet Pressure	Master Outlet	Slave Volume	Slave Inlet Temperature	Slave Inlet Pressure	Slave Outlet	Heat Transfer
0	g/s	C	mbar	mbar	L/min	C	mbar	mbar	kW
1	11.1	450.0	1500.0	1497.8	20.0	95.0	1500.0	1440.4	3.8
2	22.2	450.0	1500.0	1491.5	8.33	95.0	1500.0	1490.3	7.0
3	19.4	480.0	1500.0	1493.3	10.0	95.0	1500.0	1485.6	6.8
4	22.2	480.0	1500.0	1491.3	10.0	95.0	1500.0	1485.6	7.7
5	12.5	650.0	1500.0	1496.6	10.0	95.0	1500.0	1485.6	6.7
6	5.6	450.0	1500.0	1499.2	10.0	95.0	1500.0	1485.4	1.9
7	8.3	450.0	1500.0	1498.6	10.0	95.0	1500.0	1485.4	2.9
8	11.1	450.0	1500.0	1497.7	10.0	95.0	1500.0	1485.4	3.8
9	13.9	450.0	1500.0	1496.4	10.0	95.0	1500.0	1485.5	4.6
10	16.7	450.0	1500.0	1495.0	10.0	95.0	1500.0	1485.6	5.5
11	22.2	450.0	1500.0	1491.5	10.0	95.0	1500.0	1485.7	7.0
12	27.8	450.0	1500.0	1487.2	10.0	95.0	1500.0	1485.7	8.6
13	33.3	450.0	1500.0	1482.5	10.0	95.0	1500.0	1485.8	10.0
14									
15									

Figure 7: *Thermal data of heat exchangers used for 1D simulation.*

To check proper function of the GT Suite model, an engine test was established (Figure 9), using the same engine as FEV their vehicle test (Figure 6). For repeatability reasons, stationary points from WLTC driving cycle measurements were selected. For M07 point the engine settings was 2700 rpm and torque 100 Nm which represents 31.4 g/s as exhaust mass flow. Exhaust gas temperature was monitored on the downstream and upstream of each cooler. Measured results data was used for comparison with the GT Suite model (Figure 10).

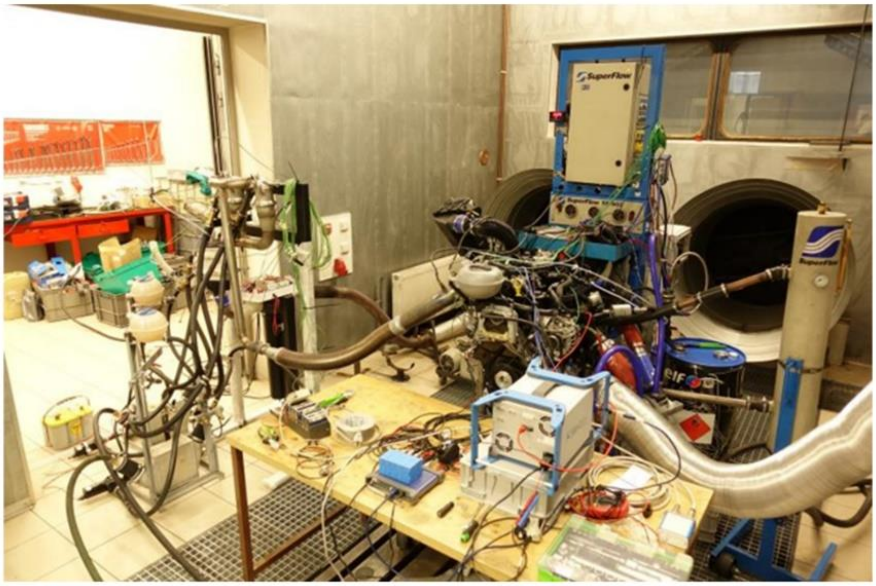

Figure 9: *Engine test stand*

Figure 10 shows the three temperatures EGT1, EGT2 and EGT3 from the test. All of these sensors have a twin value from GT Suite. EGT1 is at the inlet temperature to the HT coolers, EGT2 temperature is inlet temperature to the LT cooler. EGT3 is the main temperature from the output of the LT cooler. It is obvious that this temperature is safely under the Dew point (53 °C) of water vapour in the exhaust calculated above.

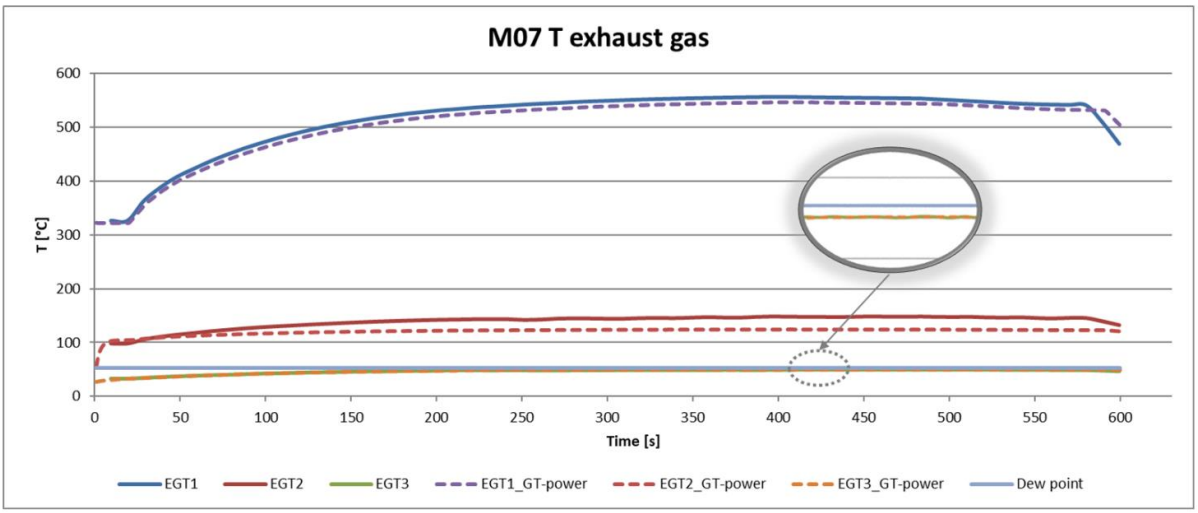

Figure 10: *Comparison of exhaust temperatures between experiment and simulation*

The 1D model was verified by experiment and can be used for WAHASY modelling and finding its suitable parameters. Figure 5 shows that WAHASY with an efficiency of only 15% in worst conditions is necessary. Hypothetically, if applied to the WLTC cycle, only 300 mL of water is necessary to harvest. This would be enough to operate the WAHASY system and also to replenish the tank condensate. This is also the reason why the WAHASY is focused only on low load modes where lower back pressure

losses in exhaust and better efficiency of condensate harvester are expected. Only 693 mL of water is available for the first 1000 s of WLTC cycles. By applying our GT-Suite model, it was found that just two coolers (one HT and one LT) are enough (Design—J). Figure 11 shows that up to the first 1000 s, both variants have similar efficiency. If the exhaust gas has more energy than our 1 + 1 design is able to cool, it will be automatically bypassed by the exhaust valve outside the WAHASY unit.

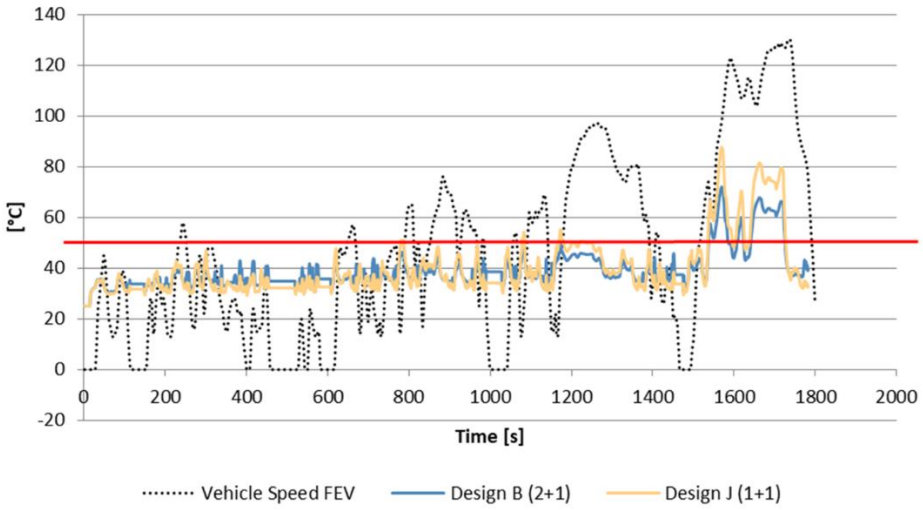

Figure 11: *Comparison of exhaust temperatures between experiment and simulation*

4.2 Harvester separator unit

As explained above, the efficiency of water vapour cooling under the dew point is only the first phase of total efficiency. The second phase concerns collecting the condensate droplets and separating them in the tank. For the unit to be developed, it was necessary to measure the size and distribution of droplets in the exhaust. An experiment was therefore carried out where photos were taken, through which droplet size and distribution could be measured indirectly (Figure 12).

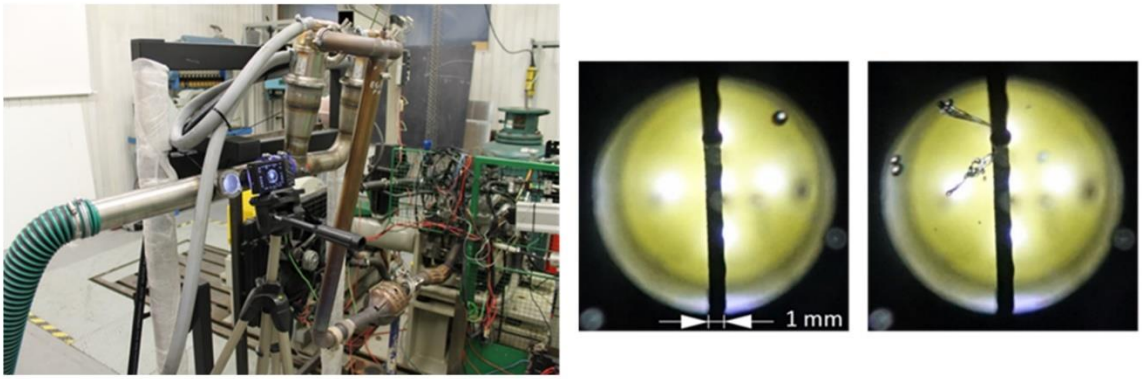

Figure 12: *Condensate droplets size measuring*

The mode of measured diameters was determined as 0.47 mm and the minimal diameter as 0.3 mm. In the CFD simulation, the diameter was set to uniform for all droplets with its value of 0.25 mm to overcome possible inaccuracy of measurements

and simulate worse scenario. The CFD model analyses droplets movement by DPM (Discrete phase model) settings in Fluent (Figure 13). In DPM settings the interaction with continuous phase was enabled and the injection of water droplets was subjected to inlet surface. The diameter of droplets was assumed to be uniform with a value of 0.25 mm and mass flow rate of the droplets was set to 3.8 g/s, mass flow of total (water droplets and exhausts gas) was set to 47.9 g/s. This point comes from 88 s of the WLTC cycle considered aver-age value.

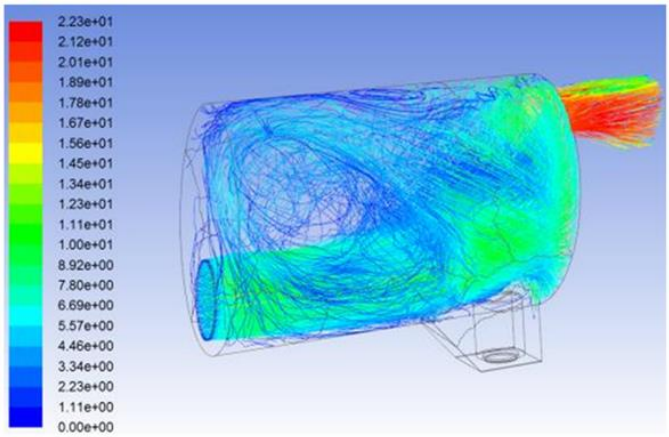

Figure 13: *CFD Simulation of flow in harvester unit*

The calculation of harvester efficiency was determined as follows. If the water droplets touch the inside wall of the harvester, they are then considered “caught”. After calculation, the results of efficiency are at 95%.

Vehicle experiment

After system simulation, a vehicle prototype was built to measure the actual efficiency of the WAHASY system. To simulate similar conditions, 88 s point of the WLTC cycle was simulated by driving at constant speed at 3rd gear and 3500 rpm to have identical inputs as during simulation. The results recorded in the graph (Figure 14) show that the run achieved an efficiency 90%.

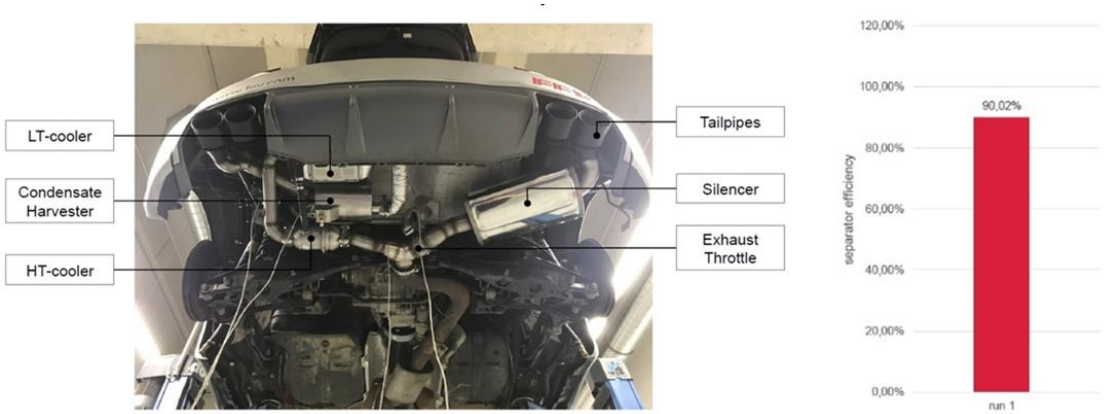

Figure 14: *Vehicle test and vehicle test results*

5. CONCLUSIONS

The scope of the WAHASY project was to demonstrate the possibility of an autonomous, self-contained system, able to condensate and harvest sufficient amounts of water to allow a “maintenance-free” and “user-independent” water injection strategy.
WAHASY, a water condensation & harvesting system, was developed and subsequently proven through engine and vehicle testing. It has been demonstrated that sufficient water can be condensed and harvested. Analytical methods and simulation models have been worked up and a vehicle has been modified with the on-board WAHASY (FEV’s Audi TT-S WI Demonstrator Vehicle).
In the nearest future, additional tests allow extensive research of condensate. The comparison of the required condensation efficiency with the actual efficiency of this “first generation” WAHASY sample revealed the possibility to significantly reduce the size of the system without restricting its potential. Simplifying and downsizing the overall design will sup-port applications with different engine and exhaust system packages and lay-outs Figure 15.

Figure 15: *Investigated downsized design*

Tail pipe emissions have not been investigated during the initial study and will re-quire further attention. As demonstrated in another study, WI has a positive impact of NOx emissions but may create some increase of unburned HC [13]. This is especially a problem during the first 30 to 50 s after cold start, before the three-way catalyst achieves its light-off temperature. Another study [14] has indicated that a partial wash-out of un-burned HC can be achieved through water condensation. As water is not injected during cold start but WAHASY may be used, this could enable an emission advantage when using the unit.
Also, anti-freezing techniques must be investigated to make the system reliable in all weather conditions. Nevertheless, currently existing solutions for other fluids (e.g., as urea injecting) may be re-used if necessary.
Finally, self-contained water harvesting enables the option of wide-spreading on water injection as a future fuel consumption improvement technology without creating difficulties for final customers to accept. The possible positive global impacts of water injection applications on the environment and public health can also be documented by the following facts. Figure 3 shows that a gasoline engine with water injection can save more than 3% of fuel consumption. According to EUROPEAN VEHICLE MARKET STATISTICS, Pocketbook 2020/21 [15], 16.6 million new passenger cars

were registered in the European Union in 2019, of which 60% with gasoline engines. If average emissions of 127 g CO2/km are considered, the application of water injection could save 531,495 ton of CO2 emission per year for new cars.

SOURCES

1. FRANZKE, B.; VOßHALL, T.; ADOMEIT, P.; MÜLLER, A. Water Injection for Meeting Future RDE Requirements for Turbocharged Gasoline Engines. *MTZ Worldw.* **2019**, *80*, 30–39. [Google Scholar] [CrossRef]
2. HUGON, P. Improvement in Gas Engines. U.S. Patent No. 49346, 8 August 1865. [Google Scholar]
3. Water Injection More Power, Less Fuel Consumption. Available online: https://water-injection.fev.com/ (accessed on 18 February 2021).
4. DURST, B.; UNTERWEGER, G.; REULEIN, C.; RUPPERT, S.; LINSE, D.; KERN, W. Increased performance of gasoline engines through various water injection concepts. In Proceedings of the MTZ-Fachtagung Ladungswechsel im Verbrennungsmotor. 8, Stuttgart, Germany, 20–21 October 2015; pp. 113–125. (In German). [Google Scholar]
5. PAUER, T.; FROHNMAIER, M.; WALTHER, J.; SCHENK, P.; HETTINGER, A.; KAMPMANN, S. Optimization of gasoline engines through water injection. In Proceedings of the 37th International Vienna Motor Symposium, Vienna, Austria, 28–29 April 2016; pp. 105–115. (In German). [Google Scholar]
6. DURST, B.; LANDERL, C.; POGGEL, J.; SCHWARZ, C.; KLECZKA, W.; HUßMANN, B. BMW water injection: First experiences and future potential. In Proceedings of the 38th International Vienna Motor Symposium, Vienna, Austria, 28–29 April 2016; pp. 139–141. (In German). [Google Scholar]
7. HOPPE, F.; THEWES, M.; SEIBEL, J.; BALAZS, A.; SCHARF, J. Evaluation of the Potential of Water Injection for Gasoline Engines. *Engines SAE Int. J. Engines* **2017**, *10*, 2500–2512. [Google Scholar] [CrossRef]
8. HERMANN, I.; GLAHN, C.; KLUIN, M.; PAROLL, M.; GUMPRICH, W. Water Injection for Gasoline Engines—Quo Vadis? In Proceedings of the 5th International Conference Knocking in Gasoline Engines, Berlin, Germany, 12–13 December 2017; pp. 117–129. [Google Scholar]
9. AQIAN, L.; ZHAOLEI, Z.; TAO, P. Effect of water injection on the knock, combustion, and emissions of a direct injection gasoline engine. *Fuel* **2020**, *268*. [Google Scholar] [CrossRef]
10. CONWAY, G. Injection of Alternative Fluids for Knock Mitigation. In Proceedings of the International Powertrains, Fuels and Lubricants Meeting, San Antonio, TX, USA, 22–24 January 2019; pp. 121–133. [Google Scholar]
11. The Engineering Toolbox: Water-Saturation Pressure. Available online: https://www.engineeringtoolbox.com/water-vapor-saturation-pressure-d_599.html (accessed on 18 February 2021).
12. THEWES, M. FEV Final Report. In *On-Board Water Generation from Exhaust for Water Injection in Gasoline Engines*; FEV Europe GmbH: Aachen, Germany, 2019. [Google Scholar]

13. HUNGER, M.; BÖCKING, T.; WAITHER, U.; GÜNTHER, M. Potential of Direct Water Injection to Reduce Knocking and Increase the Efficiency of Gasoline Engines. In Proceedings of the 5th International Conference Knocking in Gasoline Engines, Berlin, Germany, 12–13 December 2017; pp. 338–359. [Google Scholar]
14. ROUNDS, F.G.; BENNETT, P.A.; NEBEL, G.J. Some Effects of Engine-Fuel Variables on Exhaust Gas Hydrocarbon Content. *J. Air Pollut. Control. Assoc.* **2012**, *5*, 109–119. [Google Scholar] [CrossRef]
15. European Vehicle Market Statistics. Available online: http://eupocketbook.org/wp-content/uploads/2020/12/ICCT_Pocketbook_2020_Web.pdf (accessed on 4 May 2021).

FUNDING

The authors gratefully acknowledge funding from the Specific research on BUT FSI-S-20-6267.

52. MEZINÁRODNÍ VĚDECKÁ KONFERENCE ČESKÝCH A SLOVENSKÝCH UNIVERZIT A INSTITUCÍ ZAMĚŘENÁ NA VÝZKUMNÉ A VÝUKOVÉ METODY SPOJENÉ SE SPALOVACÍMI MOTORY, ALTERNATIVNÍMI POHONY A DOPRAVOU

22.-23. ZÁŘÍ 2021, PRAHA
ČESKÁ ZEMĚDĚLSKÁ UNIVERZITA V PRAZE, TECHNICKÁ FAKULTA,
KATEDRA VOZIDEL A POZEMNÍ DOPRAVY

AN ANALYSIS OF THE FORCE ACTING ON THE APEX SEAL OF A ROTARY ENGINE

Michael Böhm[1], Josef Štětina[2], David Svída[3]

Abstract
When using rotary motors such as a Wankel engine, gas leakage due to imperfect sealing between the rotor's apex and the combustion chamber often occurs. The most problematic point in designing the sealing is the dynamic and the pressure load on the apex seal. The aim of this article is to describe the forces acting on the apex seal, which are necessary to know for the optimal design of the sealing mechanism. The investigation shows that the effect of the apex seal spring and force generated by this spring is significant for correct sealing of the rotary engine. In the future, we should try to find a way of designing the sealing mechanism based on the results of advanced simulations, which have not yet been created.

1. INTRODUCTION

Nowadays, rotary motors are seeing growing utilization due to their simple design and compact dimensions. They are mainly used in areas where the weight of the drive unit plays a major role. These are mainly water sports, unmanned aircraft and motorsports, mainly racing karts. The disadvantage of these engines is still the imperfect sealing of the combustion chambers, which increases fuel consumption and exhaust emissions. Sealing the combustion chambers remains one of the most difficult tasks for the development of rotary piston engines. With advances in computing and simulations, it is now possible to predict and simulate some of these disadvantages, or to eliminate them partially or even completely based on the results. The greatest progress has been made in the apex seal, where the gas blowing mechanism has been reduced by using three-part apex seals. Further significant progress has been made in the simulation of

[1] Ing. Michael Böhm, Brno University of Technology, Faculty of Mechanical Engineering, Technicka 2896/2, Brno, Czech Republic, Michael.Bohm@vutbr.cz
[2] Prof. Ing. Josef Štětina, Ph.D., Brno University of Technology, Faculty of Mechanical Engineering, Technicka 2896/2, Brno, Czech Republic, Josef.Stetina@vutbr.cz
[3] Ing. David Svída, Ph.D., Brno University of Technology, Faculty of Mechanical Engineering, Technicka 2896/2, Brno, Czech Republic, David.Svida@vutbr.cz

all gas purge mechanisms and it is now possible to identify the most critical site and to concentrate further design modifications on it.
For an optimal design and geometry of the apex seal it is necessary to know the acting forces on this seal. During the rotation of the rotor, the sealing condition must be fulfilled. This condition is verified by a force analysis of forces action on the apex seal. A major influence on the sealing ability of the apex seals are forces in the radial direction. On the contrary, the effect of forces in the transverse direction is insignificant. Determining the cause of gas leakage in a rotary motor is very demanding due to the problem with measuring the pressure in chambers, which keep rotating. It is always better to design optimal sealing assembly to prevent the gas leakage around the top of the rotor and between adjacent chambers than to repair the motor in very short intervals. This article also highlights the use of the basic kinematic and dynamic analysis to solve the problems described above.

2. CONSTRUCTION OF APEX SEAL

Apex seals are in direct contact with hot gases in combustion chambers. They are under very high-temperature-load. The contact between the apex seal and the running face of the housing is theoretically linear (point contact in front view).
But real contact is in a certain number of points or areas due to deformations of the apex seal and the running face, manufacturing inaccuracies and clearances between the seal and the piston grooves (not just simple point/line contact). It is therefore not possible to achieve run-in state of the system as in classic piston engines. Due to these surface imperfections, there are the uneven temperature distribution and pressure force changes. These negative effects can be reduced by keeping oil layers between surfaces, possibly using a split seal that can reduce these imperfections to a small extent. The apex seals are today known in three types and shapes. The one-piece apex seal is the simplest and cheapest sealing. It is possible to create basic analytic equations only for this configuration.
The next two types, two-piece and three-piece seals, are much better in compensating clearances between the seal and the gaps in the rotor and the leakage is smaller. Nevertheless, it is hard to predict the actual position and configuration of the system, and it is almost impossible to create analytic equations for these systems. With advanced simulation programs is possible to simulate leakage and concentrate research on specific leakage mechanisms.

3. FORCE ANALYSIS OF THE APEX SEAL

Forces acting on the top of the seal can be divided into two groups. The first group is the inertia forces generated by two movements: rotation of the shaft and rotation of the rotor. The second group is forces generated by pressure in a combustion chamber acting on the sides of the apex seal. As some forces change their magnitude and direction during operation, the coordinate system associated with the rotor is selected for illustration. This system is firmly connected to the rotor and rotates with it.

3.1 Inertia Forces

There are three different forces acting on the apex seal corresponding to the movements mentioned above. One of the forces is inertia force of the apex seal spring which acts on the bottom of the seal and provides contact and sealing during low-speed conditions.

Inertia force $\mathbf{F_{S1}}$ generated by the rotation of the shaft has a direction of the connector of the eccentric shaft and the top of the rotor and begins in the center of gravity of the apex seal. Its size is calculated by the equation:

$$\mathbf{F_{S1} = m_L a_1 = m_L e \omega^2} \quad , \tag{1}$$

where m_L is the weight of the apex seal, e eccentricity of the shaft and ω rotation speed of the shaft.

This force is divided into tangential and radial components:

$$\mathbf{F_{S1_R} = F_{S1} \cos(\alpha_P)} \quad , \tag{2}$$

$$\mathbf{F_{S1_T} = F_{S1} \sin(\alpha_P)} \quad . \tag{3}$$

The second inertia force F_{S2} generated by the rotation of the rotor has only radial direction:

$$\mathbf{F_{S2} = m_L a_2 = m_L a_{TL} \omega_P^2 = \frac{1}{9} m_L a_{TL} \omega^2} \quad . \tag{4}$$

It is obvious that this equation is very similar to force F_{S1}. The differences are in the distance, where a_{TL} is the distance between the center of the rotor and the center of gravity of the apex seal, and in the rotation speed, because the rotor rotates three times slower $\mathbf{\frac{1}{9} \omega^2 = \omega_P^2}$.

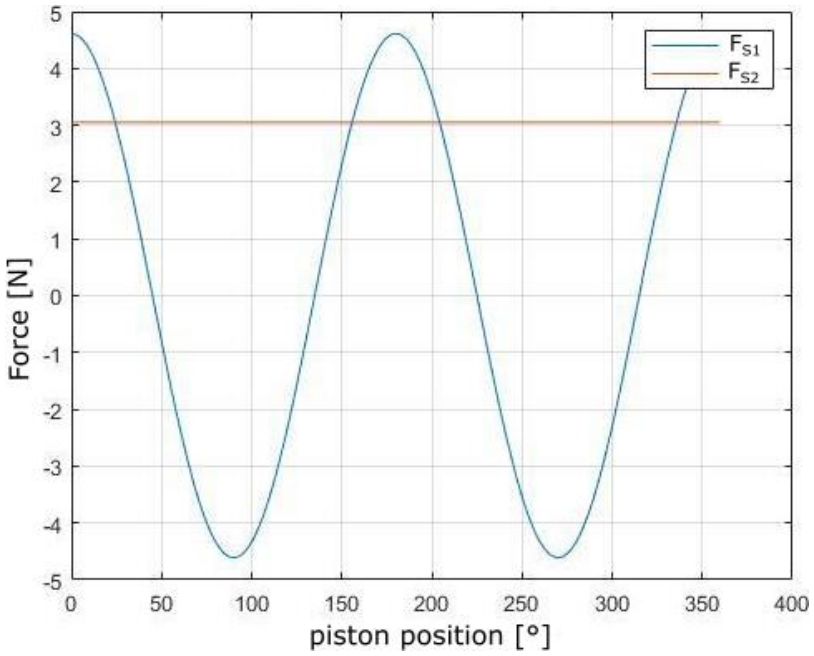

Figure 1: *Inertia forces*

The last acting inertia force $\mathbf{F_{Z2}}$ generated by the mass of the apex seal spring is described very similarly:

$$F_{Z2} = \frac{1}{9} m_Z a_{TZ} \omega^2 \quad , \tag{5}$$

where $\mathbf{a_{TZ}}$ is the distance between the center of the rotor and the center of gravity of the apex seal spring, and $\mathbf{m_Z}$ is the weight of the spring.

3.1.1 Pressure Acting Forces

Apex seals are loaded with a system of forces which are generated on the sides of the seals. This pressure load is not symmetric, because the pressure in adjacent chambers is different. Figure 2 shows an apex seal loaded with forces, when pressure $\mathbf{p_1}$ in the first chamber, which acts on the right side of the apex seal, is bigger than the pressure in the second chamber, which acts on the left side.

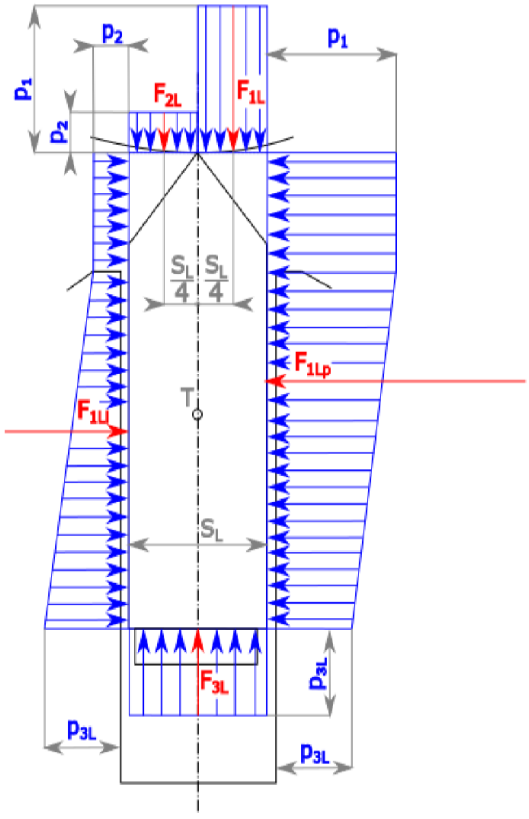

Figure 2: *Pressure acting forces on the apex seal*

The most problematic phenomenon is pressure under the apex seal. This value is used in all analytic equations for calculating the acting forces on the apex seal. After many laboratory experiments it was discovered that the pressure under the apex seal has almost the same peak value and progress as the pressure in adjacent chamber with higher values of the pressure, only there is a short time-lag compared to the pressure in the adjacent chamber with an actual pressure.

Forces acting on the sides of the apex seal are generated by the pressure in adjacent chambers. The chambers are numbered counterclockwise and the first chamber with index 1 is on the right side of the given rotor top (Figure 2). A force generated by

pressure $\mathbf{p_1}$ in the first chamber acting on the right side of the apex seal is described by this equation:

$$\mathbf{F_{1Lp} = l_L \left(p_1 h_L - \frac{1}{2} c (p_1 - p_{3L}) \right)}, \quad (6)$$

where $\mathbf{l_L}$ is the length of the apex seal, h_L height of the seal, **c** height of the gap for apex seal in the rotor, $\mathbf{p_1}$ pressure in the first combustion chamber and $\mathbf{p_{3L}}$ pressure under the apex seal.
A similar equation is used for the description of force acting on the left side of the apex seal:

$$\mathbf{F_{1Ll} = l_L \left(p_2 h_L - \frac{1}{2} c (p_{3L} - p_2) \right)}. \quad (7)$$

The top of the apex seal is loaded with a pair of forces which are equal to the pressure in the adjacent chamber and the surface affected by this pressure. The apex seal is divided into two halves, corresponding to adjacent chambers:

$$\mathbf{F_{1L} = p_1 \left(\frac{1}{2} b_L l_L \right)}, \quad (8)$$

$$\mathbf{F_{2L} = p_2 \left(\frac{1}{2} b_L l_L \right)}, \quad (9)$$

where $\mathbf{b_L}$ is the width of the apex seal.

Forces acting on the bottom of the apex seal are the most problematic variables in the system. Pressure under the apex seal $\mathbf{p_{3L}}$ generates force $\mathbf{F_{3L}}$. The value of this force is always bigger than a sum of the forces acting on the top of the apex seal:

$$\mathbf{F_{3L} = p_{3L} (b_L l_L)}. \quad (10)$$

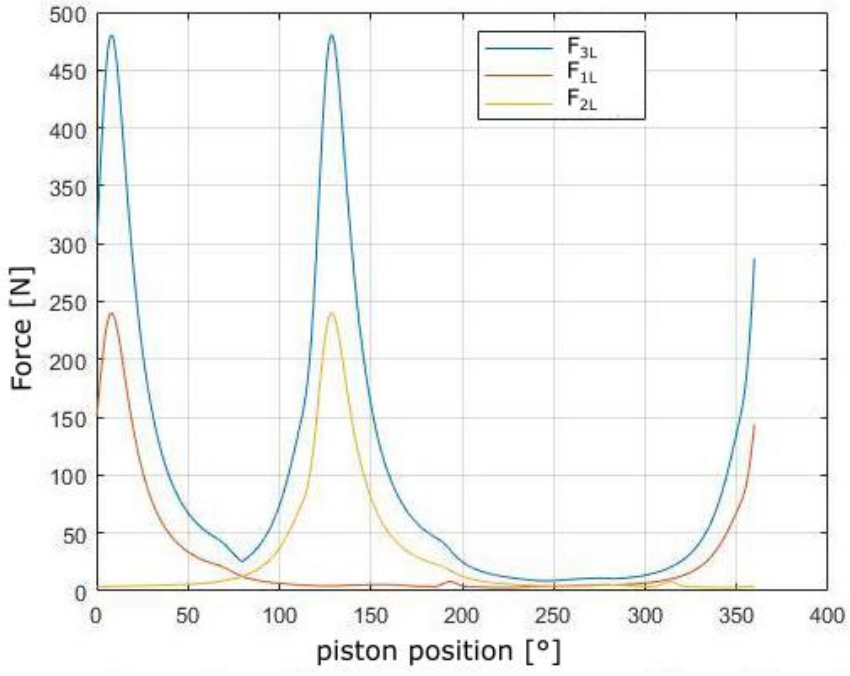

Figure 3: *Pressure acting forces*

The seal must be completed with a compression spring to minimalize the leakage between the apex seal and the surface of the combustion chamber. There is no simple analytic equation for this force; this value is determined based on the vector sum of forces in a radial direction. Sections where the radial force reaches negative values are obtained from the resulting course of the radial force acting on the apex seal. However, this is contrary to the basic condition of rotary engine sealing ability, when it is necessary to observe the following condition:

$$F_N \geq 0 \tag{11}$$

In order to meet this condition, the force set must be supplemented by spring force F_Z. Its size is necessary to be as small as possible, because if the contact force is too high, the frictional forces in the mechanism increase.

4. RESULTS AND DISCUSSION

The sealing assembly was designed for the conditions in which the motor operates most frequently. For this paper engine with operation engine speed of 6000 min-1 and geometry was chosen (Table 1). This section presents a plot the radial force against the crank position.

Rotor geometry	Symbol	Value [mm]	Apex seal geometry	Symbol	Value [mm]
Rotor radius	**R**	55.8	Width	b_L	2.0
Rotor width	**b**	47.0	Length	l_L	47.0
Eccentricity	**e**	9.0	Height	h_L	7.0
			Radius of the top of the seal	r_L	1.4

Table 1: *Geometry of the rotor and the apex seal*

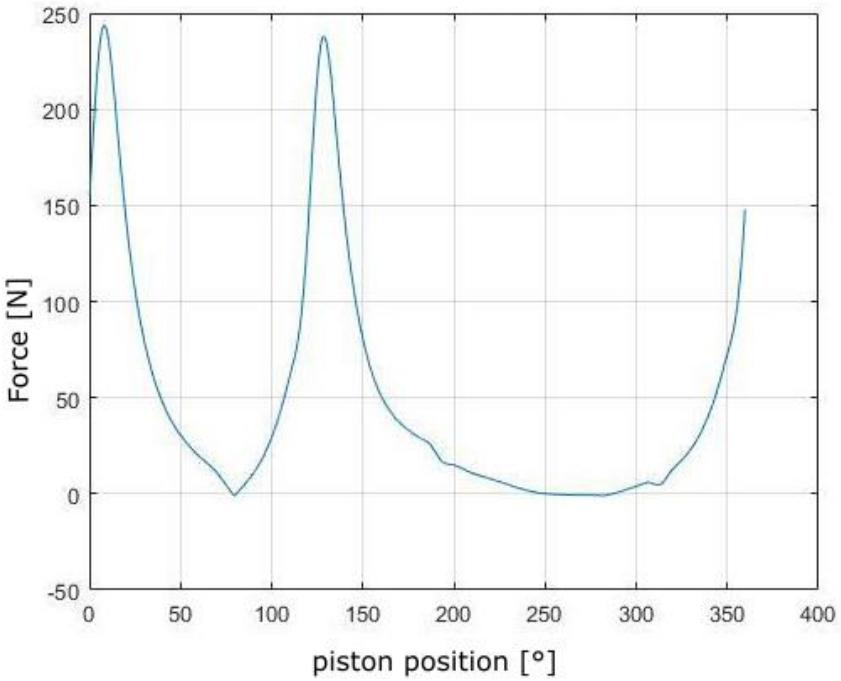

Figure 4: *Resulting radial force*

This plot (see Figure 4) shows the resulting radial force acting on the top of the apex seal. The trend of the force corresponds to the trend of pressure acting in adjacent chambers. During almost the entire rotation of the rotor, the resulting radial force is meeting the sealing condition described in the previous chapter (equation (11)). However, there are two critical points which are more noticeable on closer inspection (Figure 5).

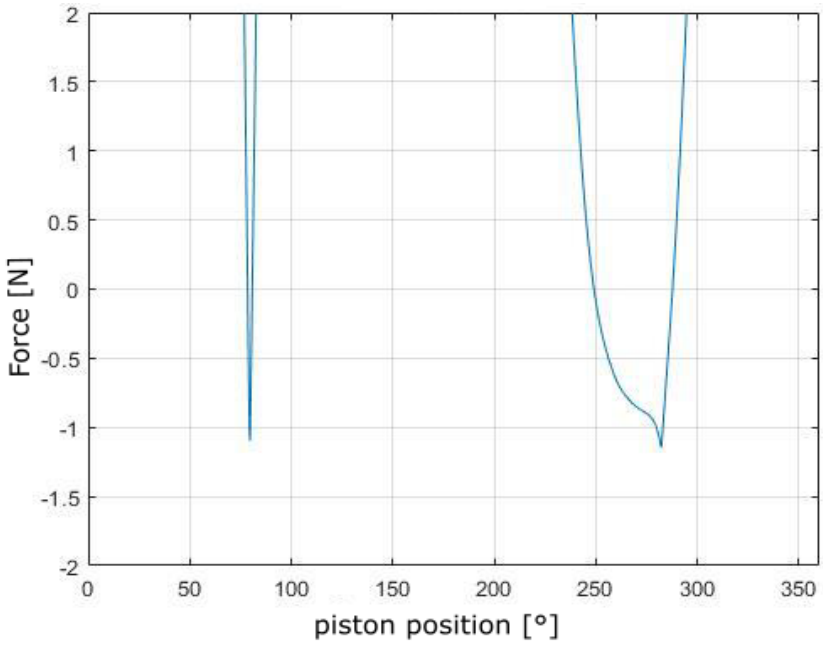

Figure 5: *Critical points*

These negative values of the resulting force must be eliminated by the force generated by the apex seal spring (including its inertia force). For this specific example, the force generated by the apex seal spring is:

$$F_{Z2}+F_Z = 1.15N \ ,$$

where F_{Z2} is the inertia force of the spring and F_Z is the force, generated by the spring in maximum compression.

4. CONCLUSIONS

As described above, connecting the rotary motor and its sealing mechanism brings many pitfalls based on the complicated motion of the rotor. For this reason, it is necessary, as already mentioned, to design the optimal apex seal spring. The aim of this design is to prevent the leakage of the gasses between the adjacent chambers and around the rotor, thereby degrading the lubricants and increase the exhaust gas emissions.

The theoretical model for an investigation of forces acting on the apex seal with analytic equations was created. A one-piece apex seal with an additional apex seal spring is used as a sealing assembly, for which the simple analytic equations were created.

The results show that pressure in adjacent chambers has in the high-speed conditions major impact on sealing ability. However, to meet the sealing condition the apex seal

spring is needed in every point of the working spectrum of the engine. This is caused mainly by the pressure fluctuations phase in adjacent chambers during the whole engine cycle.
Even though we took all known measures into consideration in order to eliminate the gas leakage, the sealing is still imperfect. This is due to the limitations of the basic analysis which can only cover steady-state states. It is necessary to focus on the dynamic simulations which can cover the transient states which are not described in this paper.

REFERENCES

[1] KOVAŘÍK, Ladislav. Motory Wankelovy a jim příbuzné. Praha: SNTL – Nakladatelství technické literatury, 1970. ISBN 04-227-70.
[2] YAMAMOTO, Kenichi. Rotary Engine. Tokyo: Toyo Kogyo CO., 1971.
[3] YAMAMOTO, Kenichi. Rotary Engine. Tokyo: Sankaido CO., 1981. ISBN 978-99- 973-4117-4.
[4] KNOLL, J., C. R. VILMAN, H. J. SCHOCK a R. P. STUMPF. A dynamic analysis of rotary combustion engine seals. NASA, USA, 1984. https://ntrs.nasa.gov/archive/nasa/casi.ntrs.nasa.gov/19840006451.pdf.
[5] SHIMIZU, Ritsuharu, Tomoo TADOKORO, Toru NAKANISHI a Junichi FUNAMOTO. Mazda 4-Rotor Rotary Engine for the Le Mans 24-Hour Endurance Race. SAE International. 1992, 1992-02-01, 1992(920309), DOI: 10.4271/920309. ISSN 0148-7191. https://www.sae.org/content/920309/.
[6] WESTON, Kenneth C. Energy conversion. St. Paul: West Pub. Co., c1992. ISBN 978- 031-4933-898.
[7] TOYO KOGYO COMPANY LIMITED. Apex seal for rotary piston engine. Japan. 3658451. Uděleno 14. 9. 1970.
[8] ZHANG, De-lou, WU, Yu-ting, WANG, Jing-fu, DU, Chun-xu, CHEN, Xia, MA, Rui, MA, Chong-fang. Theoretical Study of Seal Spring in a Wankel Compressor.2016. International Compressor Engineering Conference. Paper 2488. http://docs.lib.purdue.edu/icec/2488.
[9] Australian Journal of Basic and Applied Sciences: Analysis of the Forces Acting on Apex Seal of A Wankel Engine. 2010, 2010(4(9). ISSN 1991-8178.
[10] PICARD, Mathieu, Tian TIAN a Takayuki NISHINO. Predicting Gas Leakage in the Rotary Engine—Part I: Apex and Corner Seals. Journal of Engineering for Gas Turbines and Power. 2016, 138(6). DOI: 10.1115/1.4031873. ISSN 0742-4795. http://gasturbinespower.asmedigitalcollection.asme.org/article.aspx?doi=10.1115/1.4031873.

ACKNOWLEDGMENTS

The authors gratefully acknowledge funding from the Specific research on BUT FSI-S-20-6267.

52. MEZINÁRODNÍ VĚDECKÁ KONFERENCE ČESKÝCH A SLOVENSKÝCH UNIVERZIT A INSTITUCÍ ZAMĚŘENÁ NA VÝZKUMNÉ A VÝUKOVÉ METODY SPOJENÉ SE SPALOVACÍMI MOTORY, ALTERNATIVNÍMI POHONY A DOPRAVOU

22.-23. ZÁŘÍ 2021, PRAHA
ČESKÁ ZEMĚDĚLSKÁ UNIVERZITA V PRAZE, TECHNICKÁ FAKULTA,
KATEDRA VOZIDEL A POZEMNÍ DOPRAVY

EXTENSION OF THE RANGE OF A VEHICLE EQUIPPED WITH A DUAL-FUEL HYDROGEN DIESEL ENGINE BY REPLACING HYDROGEN WITH NATURAL GAS

Ivan Bortel[1], Jiří Vávra[2], Michal Takáts[3]

Abstract
The passenger car equipped with a dual-fuel hydrogen diesel engine shows the way how to fulfil the future requirement of regulations for CO_2 tail pipe emissions of the internal combustion engine. One of the disadvantages of hydrogen vehicles is the lack of hydrogen filling stations. The dual-fuel hydrogen diesel engine can operate with diesel fuel only, however the CO_2 tail pipe emissions are not reduced. Further possibility, how to extend the range is a substitution of hydrogen by natural gas, because the natural gas has lower carbon content than diesel oil and natural gas infrastructure is more developed than hydrogen one. This work deals with the substitution of hydrogen with natural gas in the case of a single cylinder research engine, which is partially optimized for diesel-hydrogen operation. The emission and combustion parameters are assessed and compared. The needed data are extrapolated into full-size four-cylinder engine, which is consequently used in the simulation of vehicle drive in GT-Suite. The main results of the simulation are CO_2 tail pipe emissions of passenger cars in NEDC and WLTC cycles for pure diesel, diesel-hydrogen, and diesel-natural gas operation.

1 INTRODUCTION

Contemporary and future European regulations for passenger cars force to a strong reduce of tailpipe emissions of CO_2. It is impossible to accomplish the future regulations with internal combustion engine and conventional fuel while the electric mobility is unilaterally preferred. Moreover, the overall ecological effect of electric mobility is not enough discussed and compared with contemporary drive systems and others alternatives such as fuel cells and hydrogen combustion, synthetic fuel, and advanced biofuels produced from waste. Therefore, the challenge for researchers and engineers have to warn about this situation and look for solutions, which have the least environmental consequences despite the regulations.

[1] Ivan Bortel, ČVUT v Praze, Fakulta strojní, Technická 4, Praha 6, ivan.bortel@fs.cvut.cz
[2] Jiří Vávra, ČVUT v Praze, Fakulta strojní, Technická 4, Praha 6, jiri.vavra@fs.cvut.cz
[3] Michal Takáts, ČVUT v Praze, Fakulta strojní, Technická 4, Praha 6, michal.takats@fs.cvut.cz

One of the approaches is the further development of compression ignition (CI) engine concept including the dual fuel concept with alternative gaseous fuels. Dual fuel (DF) CI hydrogen engine concept shows promising results from the view of the requirements for carbon dioxide reduction (CO_2) [1], which are being tightened up significantly. However, the overall "well-to-wheel" effect depends on the origin of hydrogen [2]. The significant obstacle of hydrogen mobility is the lack of infrastructure. Dual fuel compression ignition (DF CI) engines can operate as a standard diesel engine, however, without any benefit for CO_2 tail pipe emissions. The infrastructure of compressed natural gas (CNG) is much more developed than the hydrogen one. Therefore, the use of natural gas should partially improve CO_2 tail pipe emissions in case of unavailability of hydrogen.
The hydrogen and natural gas (NG) have different requirements on the engine configuration. The hydrogen needs a leaner mixture and lower compression ratio [2] than CI or DF CI natural gas engine to avoid the occurrence of abnormal combustion as a knock or preignition or backfire [3]. In contrast, natural gas is characterized by the high knock resistivity of methane, which is compatible with the compression ratio of CI engines.
The total hydrocarbon (THC) emissions are the weak spot of DF CI natural gas engine. It should be partially improved by enrichment of the mixture of air and natural gas, but with respect to HC and NO_x trade-off. On the contrary, hydrogen keeps the products of uncomplete combustion close to the level of the original diesel engine [2]. In general, both fuels, NG and hydrogen lead to a reduction of overall PM and PN emissions [4], [5] and [6], [7], [8], [9].
This work extends the previous work of the authors [2], where the concept vehicle of DF CI hydrogen engine was presented. The purpose of this work is to investigate the possibility of the substitution of hydrogen with natural gas in the case of the mentioned concept. This approach should improve the CO_2 tail pipe emissions of the concept, while hydrogen is unavailable. The new issue given by the substitution of hydrogen by natural gas is assessed.

2 EXPERIMENTAL SETUP AND CONDITIONS

2.1 Methods

The approach of this study is twofold, experimental and theoretical. At first, the experimental single cylinder engine investigations describe the mapping of natural gas share from the pure diesel operation up to the maximum possible share of natural gas, constrained by practical limits. These were the minimum diesel fuel injection quantity for combustion initiation and combustion efficiency. The occurrence of knock and maximum cylinder pressure are not the main limitation, because the engine is primarily adapted for hydrogen. This mapping was done for engine loads covering the whole load spectrum of the hydrogen dual fuel CI engine presented in [2]. The load spectrum corresponds to the contemporary turbocharged automotive compression ignition engine. The exhaust back pressure was controlled respecting the constant fictitious overall turbocharger (TC) efficiency (OTE) of 50%.
This mapping was performed in three engine speed conditions 1200, 2000, 3200, and 4000 rpm and resulted in performance maps with different fuelling strategies.

Secondly, the simulation part introduces an example of the potential practical implementation of natural gas on the DF CI hydrogen engine used as a power unit for a passenger van. Three different fuelling strategies were selected and compared.

- Diesel fuelling only
- The maximum allowable share of H_2 energy
- The maximum allowable share of NG energy

Full performance maps for these strategies were compiled and drive cycle simulations were performed to assess a drive cycle CO_2 emission. The GT-Suite simulation software was used.

2.2 Test engine and measurement equipment

All measurements presented in this paper were performed in a steady state operation on an AVL 5402 diesel single cylinder research engine in the engine laboratory. The combustion chamber geometry and position of the injector was adopted from the diesel engine. Initial compression ratio (CR) of 16:1 was tested, however, due to preignition at medium and high loads during DF hydrogen operation the CR was reduced to 14:1. The engine specifications are presented in Table 1. The engine is equipped with a Bosch CR 4.1 common rail diesel fuel injection with a centrally mounted injector. The injector had to be equipped with a copper cooling sleeve [10] on the injector tip to reduce tip thermal stress and to avoid injector clogging [2] (Figure 1).
The laboratory is equipped with the 200 bar CNG line. The gas pressure was reduced to approximately 9 bar by the Metatron heated automotive pressure regulator. The VW CNG port fuel injector was installed in one of the three intake manifold ports as shown in Figure 1 and was used for a sequential injection and homogeneous air-fuel mixture formation in the intake port within the whole intake stroke. During all mentioned experiments, all ports were kept open. The diesel fuel injection pressure for this study was set at 700 bar for the engine speed of 1200 and 2000 rpm and increased up to 1400 bar at 3200 and 4000 rpm.

Bore x stroke, compression ratio	85 x 90 mm, 14:1
Number of valves	4
Diesel Injection type	BOSCH Common Rail, CP 4.1, 1800 bar
Diesel Injection Nozzle	DLLA 162 P2160, 8 x 0.12 mm x 162°
Engine control unit	Ricardo rCube2
Cylinder pressure measurement	Cylinder pressure transducer AVL GU22C
Piston bowl design	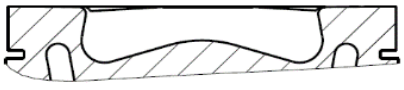

Table 1: *Engine specifications*

The test cell (Figure 2) is equipped with an AVL 515 Boost Unit and an external compressor that allowed independent control of intake air pressure and temperature. The exhaust manifold was equipped with a 60 L tank and a back pressure throttle valve

downstream of it. A Bosch LSU 4.9 lambda sensor was installed downstream of the throttle valve to avoid the sensor response variation with increased pressure level and oscillations. The signal from the lambda sensor was processed via an ETAS ES635 Lambda Module.

Figure 1: *A copper sleeve for a passive cooling of the diesel injector tip (left), a gaseous fuel injector installed in the engine inlet manifold (right).*

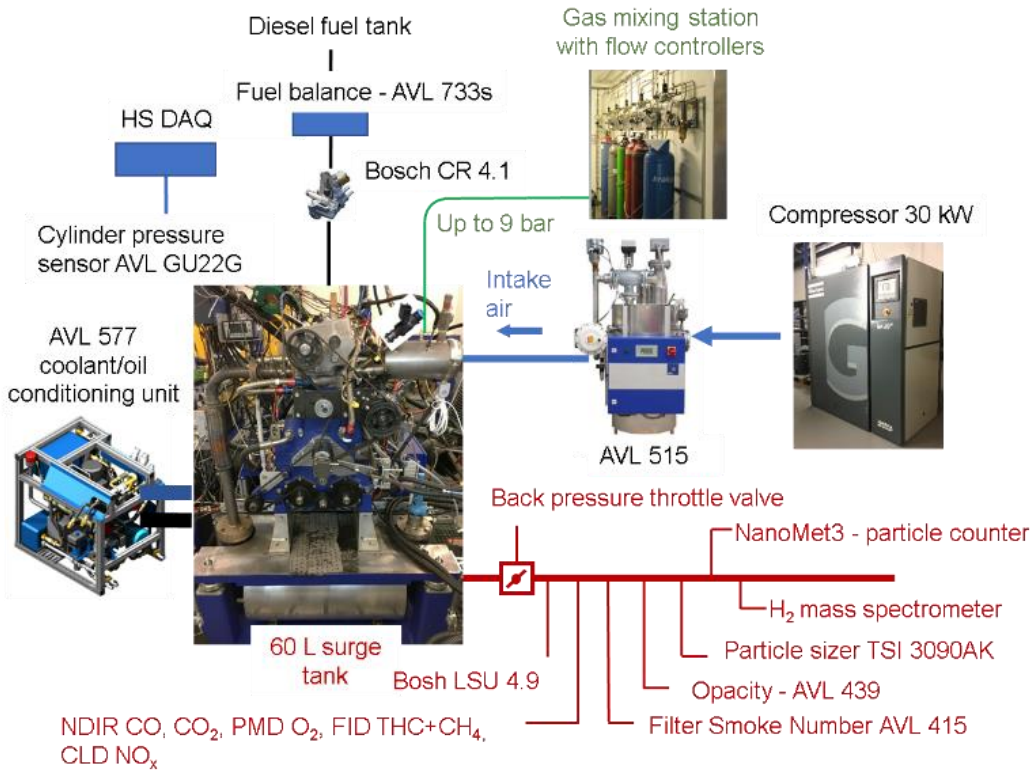

Figure 2: *Overview of the single cylinder test cell.*

The oil and coolant flows are driven externally via an AVL 577 conditioning unit that keeps the constant pressure and temperature. Coolant temperature was set at 80°C and oil temperature at 85°C. Diesel fuel consumption was measured by an AVL 733s A model 2700R11 of Micro Motion Coriolis flow meter was used for measurement of NG mass flow. An uncooled piezoelectric pressure sensor AVL GU22C was installed in the cylinder head and for fast measurements of intake and exhaust gas pressure, the piezoresistive KULITE ETL-189-190M absolute pressure transducers were

installed in the intake/exhaust manifold next to the connection flanges. The AVL INDIMODUL and accessories were used for high-speed data acquisition. A 365C crank angle encoder was installed at the free end of the engine crank shaft. The high-speed quantities were sampled on a crank angle base with the resolution of 0.1° crank angle (CA). Typically, 200 consecutive cycles were recorded, and an average cycle was evaluated and used for detailed thermodynamic analysis. All specific parameters in this paper are related to the indicated power.
A rapid prototyping engine control unit (ECU) Ricardo rCube2 [11] was used for an independent control of injection of both fuels. An in-house developed control algorithm in Matlab/Simulink was used for a complete control of a diesel fuel rail pressure and a precise control of multiple injections per cycle for both diesel and gaseous fuels. The ECU parameterization was performed using an INCA software. The test cell is equipped with an in-house developed control and low-speed data acquisition system based on National Instruments cDAQ and cRIO hardware, and a LabVIEW software. An in-house developed software [12] was used for a detailed heat release analysis of the crank angle indexed in the cylinder pressure record.
All emissions were measured in raw exhaust gas. Bottom part of Figure 2 displays the arrangement of the exhaust manifold and emission sampling. Gaseous emissions were measured by AVL AMA i60 with a heated prefilter. AMA i60 includes measurement of nitrogen oxides NO_x using a chemiluminescence detector (CLD), total hydrocarbons (THC) via a flame ionization detector (FID), and carbon monoxide (CO) and carbon dioxide (CO_2) via non-dispersive infrared (NDIR) measurement technique. Content of oxygen was measured with a paramagnetic detector (PMD). Particle number (PN) was measured by the NanoMet3 particle counter or by AVL 489 particle counter.

3 RESULTS AND DISCUSION

This article is focused on the DF CI natural gas concept and its comparison with DF CI hydrogen concept. Therefore, the hydrogen concept is not expressly discussed in this paper. More details about the hydrogen concept are in [2].

3.1 Experimental results

Initial mapping of NG share was performed at the engine speed of 2000 rpm. The behaviour at others speeds is similar. The assessed quantities are displayed as a function of H_2 or NG energetic share of the total energy delivered to the engine by fuels, see Equation (1).

$$\sigma_{CNG/H2} = \frac{m_{CNG/H2}}{m_{CNGH2} + m_{diesel}} \left[\frac{kg}{kg}\right] \quad (1)$$

The air excess is given by the compromise between combustion efficiency (and unburned hydrocarbons) and NO_x. It corresponds to $\lambda \approx 1.7$ for the indicated mean effective pressure (IMEP) higher than 10 bar. Below this threshold, the lambda fluently growths up to $\lambda \approx 3$ in the case of IMEP = 4 bar. As can be seen from Figure 3, natural gas does not achieve the limits of the engine represented by the maximum cylinder pressure Pcylmax = 150 bar and maximum rate of pressure rise Rmax = 10 bar/°CA. Furthermore, the NG allows higher maximum energy share for IMEP = 16 bar without preignition or backfire. Therefore, the potential of NG remains untapped due to the adaptation of the engine to hydrogen. Combustion phasing given by the point of 50 %

mass fraction burned (CA50) shows that NG allows keeping CA50 at an optimal value for 8–10°CA ATDC except for modes with the highest NG energy share of IMEP until 8 bar (Figure 3), which is given by the poor combustion efficiency (Figure 4). Combustion of hydrogen is slightly retarded from the optimal value due the mentioned limitations and knock occurrence. Comparison of diesel fuel injection timing shows that NG needs earlier injection timing. The brake in the graph of main injection timing is given by reducing the number of injections of diesel fuel from two to one (Figure 3). If only one injection is used, then the timing corresponds to timing of the pilot injection of the two injections strategy. It looks that the second injection supplies turbulence into the combustion process, because the single injection strategy leads to retarded combustion represented by an increase of CA50 (Figure 3) despite the decrease of THC displayed in Figure 4.

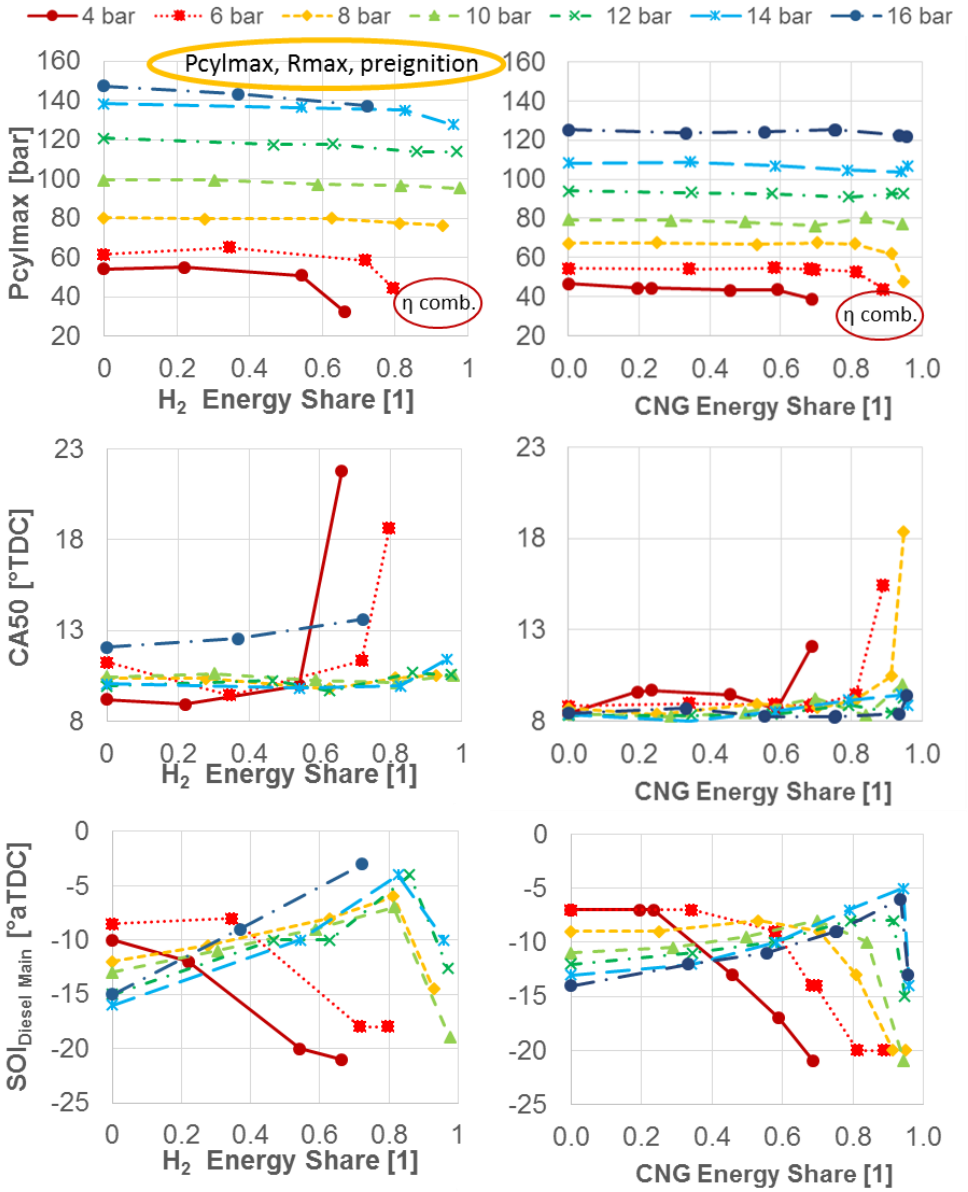

Figure 3: *Maximum cylinder pressure (Pcylmax), combustion phasing (CA50), main injection start timing (SOIDiesel Main)*

Combustion efficiency reaches the highest value at maximum energy shares for both fuel (Figure 4). Exceptions are the modes with IMEP = 4 and 6 bar fuelled by NG, where the increase of combustion efficiency at the highest energy shares is not reached, because the mixture of air and NG remains to lean at these level loads. The right bottom part of Figure 4 shows that the decrease of the combustion efficiency is caused by combustion of NG. It is confirmed by the fact that methane is the dominant component of THC. The less pronounced effect corresponding to the higher combustion efficiency of hydrogen combustion is shown by traces of unburned hydrogen (not displayed). It looks that hydrogen burns better in the crevices of the diesel combustion chamber. The emission of THC from hydrogen operation remains close to pure diesel operation. Emissions of THC are significant different for the hydrogen and NG concept.

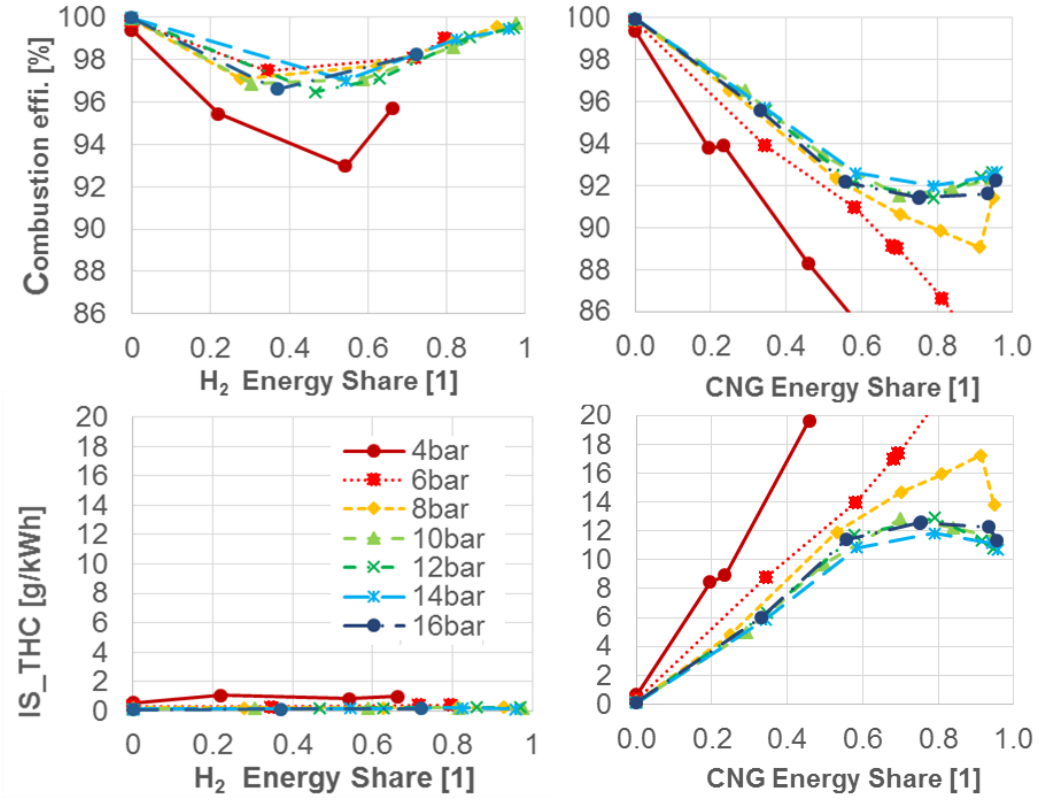

Figure 4: *Combustion efficiency and indicated specific emissions of unburned hydrocarbons*

Transient to combustion of a homogenous mixture leads to the increase of emissions of CO as a typical product of this concept of combustion with hydrocarbon fuels, while natural gas is used (Figure 5). The decrease of CO emissions in the case of hydrogen combustion is by lower amount of carbon in the combustion process due the substitution of hydrocarbon fuel by hydrogen. Usage of NG in the dual fuel concept leads to an increase of NO_x emissions between 20–50 %, while acceptable combustion efficiency is reached. The exception is the load level of 10 bars of IMEP. It is caused by the impossibility to keep the optimal CA50 with a single injection, which leads to slower combustion with lower peaks of combustion pressure.

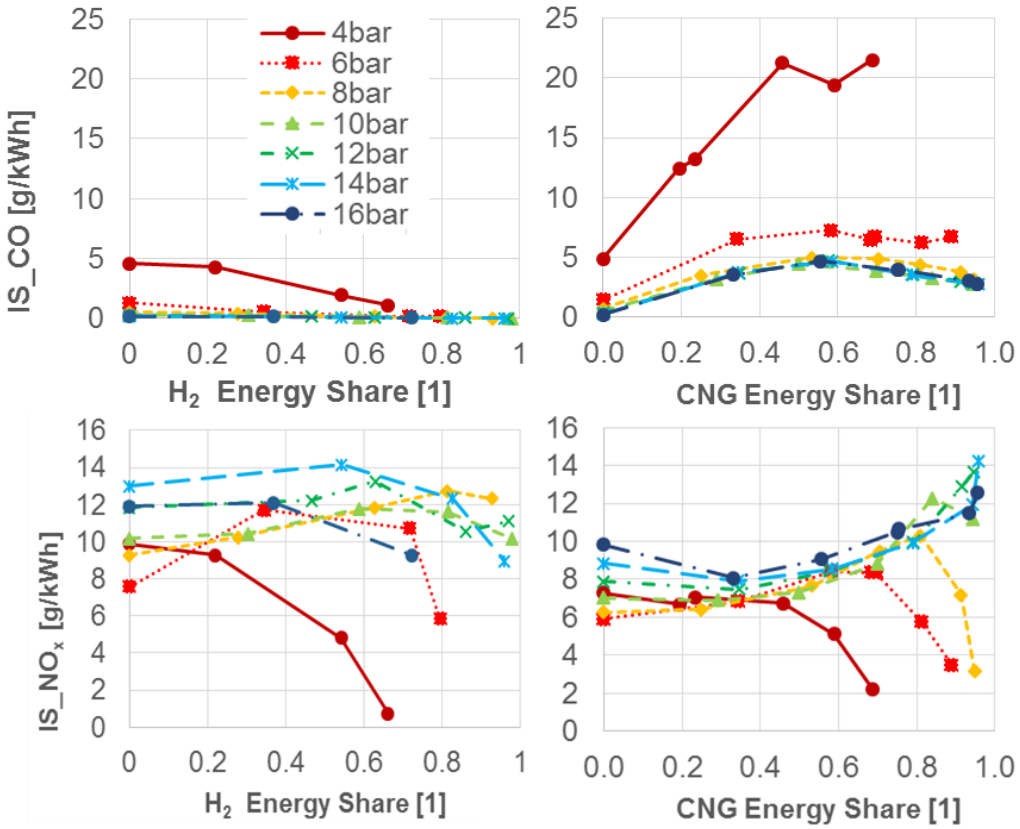

Figure 5: *Indicated specific emissions of CO and NO_x*

Dual fuel operation leads to the reduction of the number of emitted particles (PN) by one to two orders (Figure 6). It should be assumed that the difference between H_2 and NG is affected by the usage of different measurement devices for PN measurement, NanoMet3 for hydrogen concept and AVL 489 for NG concept.
Emissions of CO_2 are displayed in Figure 6. The real engine is equipped with an oxidation catalyst, therefore the emission of CO_2 is recalculated with the assumption of perfect oxidation of THC and CO on the catalyst. This assumption is necessary to fulfil, because the unburned NG has 25 times higher global warming potential than CO_2. Dual fuel NG concept has the potential to decrease the CO_2 between 12–20 %. The significant reduction of DF CI hydrogen concept approximately corresponds to the achieved H_2 energy share. However, the real impact depends on the operating conditions, therefore the next paragraphs deal with the compilation of stationary engine maps of CO_2 and consequently with drive vehicle simulation.

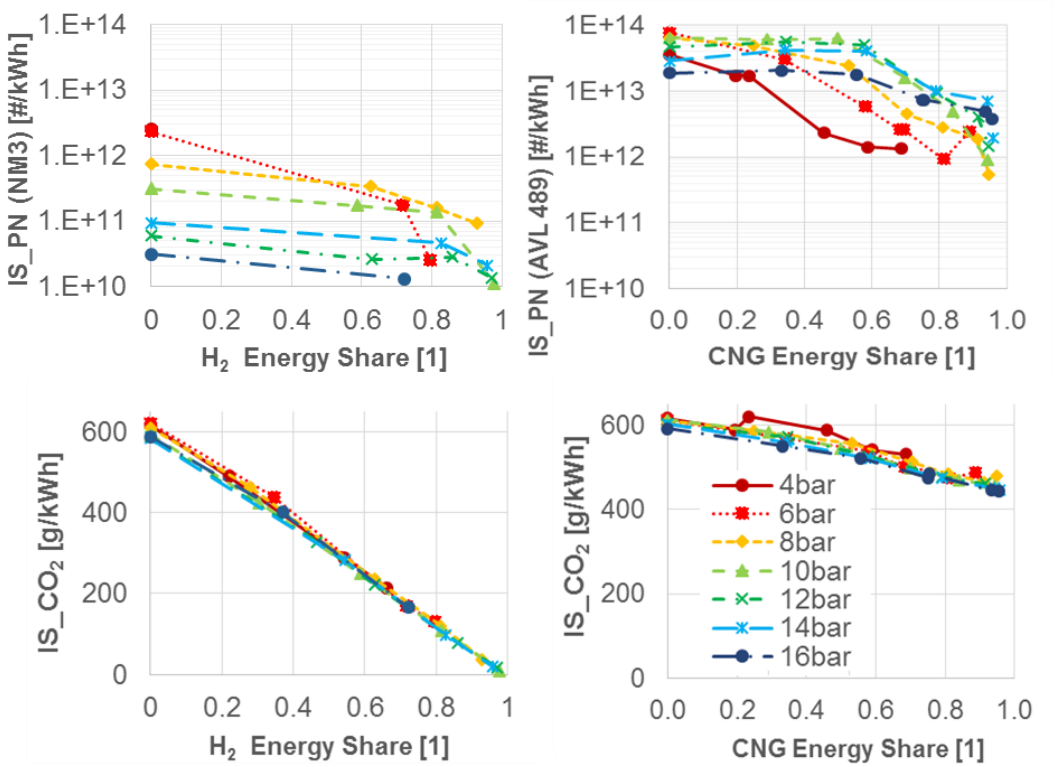

Figure 6: *Indicated specific number of particles (PN) measured by NanoMet3 (hydrogen) and by AVL 489 (natural gas)*

3.2 Dual fuel engine maps and vehicle drive simulation

Measurements, as described in the previous section, were performed as well for engine speed of 1200, 2000, 3200, and 4000 rpm. In the next step, three fuelling strategies were selected from all measured data points. The selection criteria are reduction of CO_2 and minimum combustion efficiency 90 %, otherwise pure diesel operation is selected. At low loads, the hydrogen share was limited by the slow and incomplete combustion. To provide the input data to the simulation of the driving cycle, extrapolations were performed to increase the speed range. In this way, four-cylinder engine maps were designed. Data describing the overall CO_2 emissions are introduced in Figure 9. Measured data were recalculated from indicated to effective parameters, using the realistic estimate of friction losses according to [13]. Map of engine effective power is presented in Figure 7. The maps of H_2/CNG energetic share are displayed in Figure 9.

The model in GT-Suite uses so-called quasi-steady approach to calculate the longitudinal vehicle dynamics according to the prescribed velocity profile and gear ratio. It includes all driving resistances. Fuel consumption and CO_2 emissions are interpolated from the steady state engine maps (Figure 9) for each time step selecting the proper operational point.

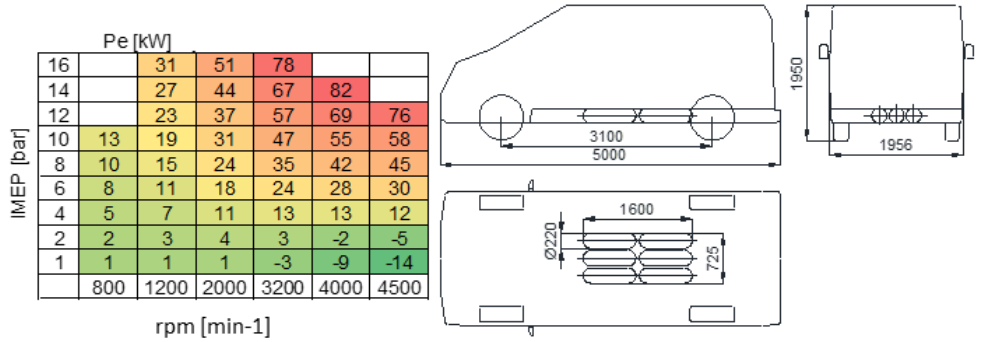

IMEP [bar] \ rpm [min-1]	800	1200	2000	3200	4000	4500
16		31	51	78		
14		27	44	67	82	
12		23	37	57	69	76
10	13	19	31	47	55	58
8	10	15	24	35	42	45
6	8	11	18	24	28	30
4	5	7	11	13	13	12
2	2	3	4	3	-2	-5
1	1	1	1	-3	-9	-14

Figure 7: *Extrapolated 4 cylinder engine power map and the concept of gaseous fuel storage in the van*

Diesel H_2/CNG energetic share

IMEP [bar] \ rpm [min-1]	800	1200	2000	3200	4000	4500
16		0%	0%	0%		
14		0%	0%	0%	0%	
12		0%	0%	0%	0%	0%
10	0%	0%	0%	0%	0%	0%
8	0%	0%	0%	0%	0%	0%
6	0%	0%	0%	0%	0%	0%
4	0%	0%	0%	0%	0%	0%
2	0%	0%	0%	0%	0%	0%
1	0%	0%	0%	0%	0%	0%

H_2 energetic share

IMEP [bar] \ rpm [min-1]	800	1200	2000	3200	4000	4500
16		74%	73%	0%		
14		98%	97%	70%	0%	
12		96%	97%	64%	42%	0%
10	95%	96%	98%	94%	91%	89%
8	97%	97%	94%	82%	74%	69%
6	86%	84%	80%	74%	69%	67%
4	65%	66%	68%	0%	0%	0%
2	0%	0%	0%	0%	0%	0%
1	0%	0%	0%	0%	0%	0%

CNG energetic share

IMEP [bar] \ rpm [min-1]	800	1200	2000	3200	4000	4500
16		90%	96%	93%		
14		95%	96%	92%	90%	
12		89%	95%	89%	90%	90%
10	87%	90%	94%	87%	84%	82%
8	85%	88%	95%	72%	65%	61%
6	82%	74%	58%	51%	29%	0%
4	81%	54%	0%	0%	0%	0%
2	0%	0%	0%	0%	0%	0%
1	0%	0%	0%	0%	0%	0%

Figure 8: *Characteristics of H_2/CNG energy share of diesel, hydrogen, and natural gas concepts*

Diesel mdot CO_2_ACAT100 kg/h

IMEP [bar] \ rpm [min-1]	800	1200	2000	3200	4000	4500
16		20.2	32.6	50.4		
14		17.7	28.6	43.4	57.3	
12		15.2	24.7	38.8	49.3	55.8
10	8.4	13.0	21.0	32.8	41.1	46.3
8	6.7	10.7	16.7	26.6	34.2	39.0
6	5.0	8.3	12.6	19.9	25.7	29.4
4	3.4	5.0	8.5	13.4	16.8	18.9
2	1.7	2.5	4.2	6.7	8.4	9.5
1	0.8	1.3	2.1	3.4	4.2	4.7

H_2 mdot CO_2_ACAT100 kg/h

IMEP [bar] \ rpm [min-1]	800	1200	2000	3200	4000	4500
16		5.3	9.0	50.4		
14		0.3	0.9	13.7	57.3	
12		0.6	0.7	13.6	22.1	55.8
10	0.6	0.5	0.3	2.0	3.1	3.8
8	0.2	0.3	1.0	4.8	7.4	9.0
6	0.8	1.4	2.7	5.6	7.5	8.7
4	1.7	2.1	2.9	13.4	16.8	18.9
2	1.7	2.5	4.2	6.7	8.4	9.5
1	0.8	1.3	2.1	3.4	4.2	4.7

CNG mdot CO_2_ACAT100 kg/h

IMEP [bar] \ rpm [min-1]	800	1200	2000	3200	4000	4500
16		16.7	26.2	39.0		
14		13.2	23.2	34.8	47.2	
12		11.3	19.8	30.7	39.9	45.6
10	5.8	9.5	17.0	26.5	34.2	39.0
8	3.9	7.5	14.7	22.3	28.9	33.0
6	2.3	5.6	12.1	17.6	22.9	29.4
4	2.1	4.3	8.5	13.4	16.8	18.9
2	1.7	2.5	4.2	6.7	8.4	9.5
1	0.8	1.3	2.1	3.4	4.2	4.7

Figure 9: *Characteristics of CO_2 emissions of diesel, hydrogen, and natural gas concepts*

In this section, the initial assessment of the impact of H_2/CNG DF engine use in a real powertrain of the van will be outlined. For this purpose, the vehicle model was compiled in GT-Suite, assuming the vehicle parameters in Table 1. The effect of increased vehicle mass due to gaseous fuel cylinders was taken into account. Weight factor (defined as the weight of hydrogen divided by the total tank system weight) of 5% has been adopted from [14]. Estimated water volume of the tanks is 160 L. For 700 bar fuel pressure, the storage capacity is 6.3 kg of H_2 or 24 kg of CNG.

	Diesel engine	DF H_2/CNG – diesel engine
Vehicle mass [kg]	1930	2110/2128
Frontal area [m2]	3	
Gear number [1]	6	
Air drag coefficient [1]	0.38	
Rolling resistance [1]	0.07	

Table 2: *Simulated vehicle specifications*

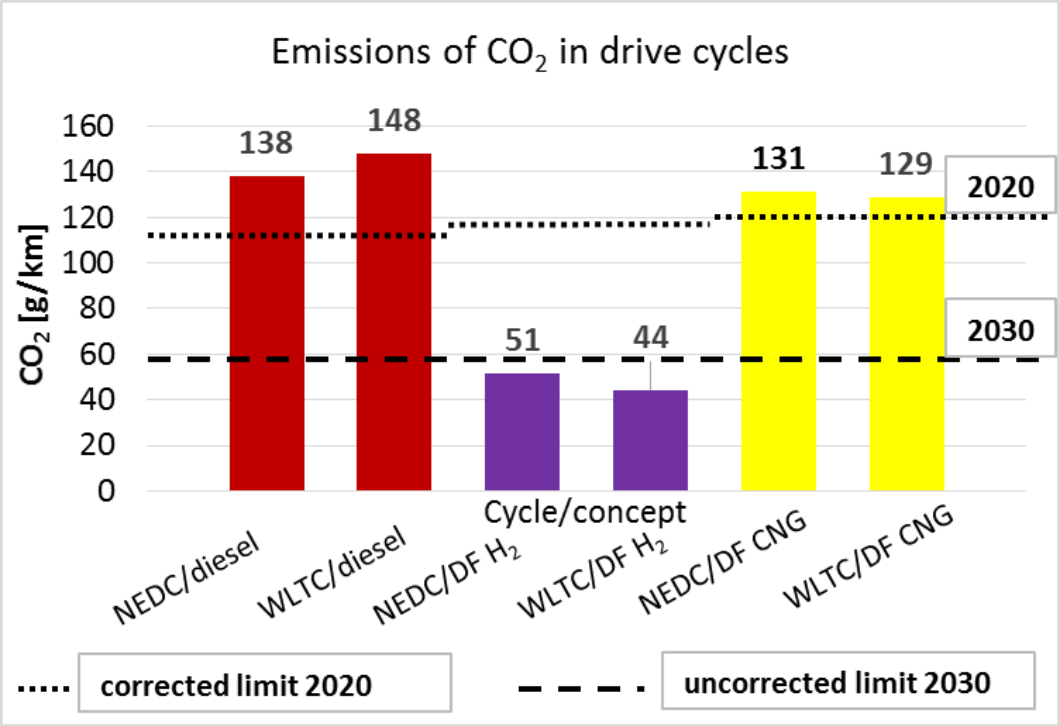

Figure 10: *CO_2 emissions in NEDC and WLTC drive cycles*

Drive cycle/DF concept	**NEDC diesel**	**WLTC diesel**	**NEDC DF H_2**	**WLTC DF H_2**	**NEDC DF CNG**	**WLTC DF CNG**
Energetic share in cycle [%]	0	0	59	69	46	71
Range [km]	**887**	**868**	**531**	**455**	**400***	**771**
Reduction of CO_2 v [%]	-	-	-63	-70	-5	-13
Limit CO_2 2020/2030 [g/km]	113.2/-	-/59.4**	119.1/-	-/59.4**	119.7/-	-/59.4**

Table 3: *Results of vehicle simulations. *Limited by diesel tank, ** Correction factors not available*

The results of the simulation of two driving cycles (NEDC and WLTC) and three fuelling strategies (diesel only, H_2 and CNG maximum allowable energy share) are presented in Table 3 and Figure 10. The simulated reference data of pure diesel concept shows realistic results, which are 138 g/km for NEDC and 148 for WLTC cycle. The results of DF CI hydrogen concept show the potential to accomplish requirements valid after 2030, as presented in [2]. The results of DF CI natural gas concept shows only 5 % reduction of CO_2 in NEDC cycle, because the less loaded engine has to more often operate as a pure diesel engine. Therefore, the more dynamic WLTC cycle leads to lower CO_2 emission than NEDC one and higher reduction of CO_2 represented by 13 % for DF CI natural gas concept. It is evident that DF CI natural gas concept does not meet the contemporary and future requirements. However, it extends the range of the vehicle equipped with H_2 DF engine with lower CO_2 emissions than pure diesel operation. Therefore, the CNG DF concept can help reduce emissions during hydrogen infrastructure development.

4 SUMMARY AND CONCLUSIONS

The substitution of hydrogen by natural gas in DF CI hydrogen engine was discovered experimentally and the emissions of CO_2 were assessed via vehicle drive simulation in drive cycles. The compression ratio of 14:1 was optimized for hydrogen operation.

- The potential of NG is not developed, because the compression ratio and maximum IMEP are given by the limits of hydrogen operation. NG should be used with higher compression ratio and IMEP.
- Dual fuel operation with H_2 allows to use the dual fuel concept at lower loads than NG. On the other hand, NG makes it possible to maintain higher energy share even at maximum load, while H_2 leads to problems with backfire, preignition and knocking in these operating modes.
- NG leads to a significant decrease of combustion efficiency and consequently a significant order of magnitude increase of hydrocarbon and CO emissions. Therefore, NG operation brings new demands on aftertreatment systems.
- The NO_x emission is approximately 20 % higher for IMEP ≥ 10 bar, while NG instead of H_2 is used. NG provides lower NO_x for IMEP < 10 bar, but with poor combustion efficiency.
- The dual fuel operation decreases the PN emission in the order of magnitude approximately. It is impossible to compare the NG and H_2, because different devices are used for each measurement.
- The vehicle simulation shows a decrease of CO_2 emission of 5 % at NEDC and 13 % at WLTC cycle for DF natural gas operation, while H_2 leads to a decrease of 63 % at NEDC and 70 % at WLTC cycle, compared to diesel operation.

The substitution of H_2 by NG provides an insufficient decrease of tail pipe emissions of CO_2 in comparison with future requirements of regulations, while hydrogen allows to meet these requirements. Therefore, the DF CI natural gas concept can help reduce emissions during hydrogen infrastructure development, because leads to lower CO_2 tail pipe emissions of CO_2 than pure diesel operation. However, the separate use of DF CI natural gas engine concept does not lead to sufficient benefits.

REFERENCES

[1] https://treaties.un.org/pages/ViewDetails.aspx?src=TREATY&mtdsg_no=XXVII-7-d&chapter=27&clang=_en
[2] Vavra, J., Bortel, I., and Takats, M., "A Dual Fuel Hydrogen - Diesel Compression Ignition Engine and Its Potential Application in Road Transport," SAE Technical Paper 2019-01-0564, 2019, https://doi.org/10.4271/2019-01-0564.
[3] Tomita, E., Kawahara, N., Piao, Z., Fujita, S. et al., "Hydrogen Combustion and Exhaust Emissions Ignited with Diesel Oil in a Dual Fuel Engine," SAE Technical Paper 2001-01-3503, 2001, https://doi.org/10.4271/2001-01-3503.
[4] T. Tsujimura and Y. Suzuki, “ScienceDirect The utilization of a hydrogen in hydrogen / diesel dual fuel engine,” Int. J. Hydrogen Energy, vol. 42, no. 19, pp. 14019–14029, 2017.
[5] F. Xiao and G. A. Karim, “An Investigation of the Combustion in an IDI Diesel Engine with Low Concentrations of Added Hydrogen,” SAE Paper No. 2011-01-0676, 2011.
[6] N. Saravanan, G. Nagarajan, C. Dhanasekaran, and K. M. Kalaiselvan, “An Experimental Investigation of Hydrogen Fuel Injection in DI Dual Fuel Diesel Engine,” SAE Paper no. 2008-01-1784, 2008.
[7] S. D. Iorio, A. Magno, E. Mancaruso, B. M. Vaglieco, Characterization0 of particle number and mass size distributions from a small compression ignition engine operating in diesel/methane dual fuel mode, Fuel 180 (2016) 613-623.
[8] Hartikka, T., Kuronen, M. and Kiiski, U., Technical Performance of HVO (Hydrotreated Vegetable Oil) in Diesel Engines, SAE Technical Paper 2012-01-1585, 2012, doi:10.4271/2012-01-1585
[9] S. Di Iorio, A. Magno, E. Mancaruso, B. M. Vaglieco, Performance, Gaseous and Particle Emissions of a Small Compression Ignition Engine Operating in Diesel/Methane Dual Fuel Mode, SAE Paper (2016-01-0771). doi:10.4271/2016-01-0771.
[10] Königsson, F., Stalhammar, P., and Angstrom, H., "Controlling the Injector Tip Temperature in a Diesel Dual Fuel Engine," SAE Technical Paper 2012-01-0826, 2012
[11] www.ricardo.com/rCube2
[12] Takáts, M.; Vávra, J., INTEQv2017, http://fs12120.fsid.cvut.cz/softlib/2017/, CTU Prague, 2017
[13] Macek, J., Fuente, D., and Emrich, M., “A Simple Physical Model of ICE Mechanical Losses,” SAE Technical Paper 2011-01-0610, 2011, doi:10.4271/2011-01-0610.
[14] T. Q. Hua, R. K. Ahluwalia, and J-K Peng, M. Kromer, S.and K. Lasher, Technical Assessment of Compressed Hydrogen Storage Tank Systems for Automotive Applications, Argonne National Laboratory, ANL-10/24, 2010

ACKNOWLEDGEMENT

This research has been realized using the support of The Ministry of Education, Youth and Sports program NPU I (LO), project # LO1311 Development of Vehicle Centre of Sustainable Mobility. This support is gratefully acknowledged.

52. MEZINÁRODNÍ VĚDECKÁ KONFERENCE ČESKÝCH A SLOVENSKÝCH UNIVERZIT A INSTITUCÍ ZAMĚŘENÁ NA VÝZKUMNÉ A VÝUKOVÉ METODY SPOJENÉ SE SPALOVACÍMI MOTORY, ALTERNATIVNÍMI POHONY A DOPRAVOU

22.-23. ZÁŘÍ 2021, PRAHA
ČESKÁ ZEMĚDĚLSKÁ UNIVERZITA V PRAZE, TECHNICKÁ FAKULTA,
KATEDRA VOZIDEL A POZEMNÍ DOPRAVY

EXPERIMENTÁLNÍ PŘEVODOVKA

Ing. Marek Bous[1]

Abstrakt
Článek se zabývá možností testování řadicích spojek automobilových převodovek. Dále popisuje nově vzniknuvší stanoviště, v laboratořích Ústavu automobilů, spalovacích motorů a kolejových vozidel, Fakulty strojní ČVUT v Praze na Julisce, pro testování řadících spojek automobilových převodovek a jeho možný přínos v jejich vývoji.

1. ÚVOD

V laboratořích ČVUT na Julisce je vybudováno stanoviště, na kterém je možné testovat převodové skříně z osobních automobilů [1]. Převodová skříň je namontována v celku; pouze se zablokovaným diferenciálem. Na převodovou skříň je napojen setrvačník, který je poháněn elektromotorem. Tím je zajištěn pohon skříně a je možné následně řadit jednotlivé rychlostní stupně. Na tomto stanovišti lze v krátkém čase provést velké množství cyklů, takže je možné ověřit životnost součástek v řadícím mechanismu. Z měření ale nelze detailněji vyhodnotit parametry jednotlivých součástí, především synchronizačních spojek. Zabudování měřících senzorů přímo do skříně se ukázalo jako téměř nemožné. Cílem tedy bylo navrhnout nové stanoviště, či úpravu stávajícího tak, aby bylo možné zkoušet synchronizační spojky samostatně, tedy vyjmuté ze sériové skříně.

2. ZÁKLADNÍ PRINCIP STANOVIŠTĚ

Fungování budoucího zkušebního stanoviště je možné zjednodušeně shrnout do několika vět: „Představme si 2 hmoty, rotující rozdílnými otáčkami. Propojme je kuželovou spojkou. Úkolem kuželové spojky (synchronizační spojka) je jejich otáčky vyrovnat. Obě její kuželové části jsou k sobě tedy stlačovány axiální sílou. Díky tření mezi kužely začne spojka přenášet točivý (třecí) moment. Tento jev přetrvává, dokud nejsou otáčky hmot totožné.
Z rovnice pro třecí moment na kuželové spojce se lze dozvědět, na jakých veličinách vlastně závisí. Krom axiální síly nebo rozměrů spojky je zde součinitel tření, který není

[1] Ing. Marek Bous, České vysoké učení technické v Praze, Fakulta strojní, Ústav automobilů, spalovacích motorů a kolejových vozidel, Technická 4 Praha 6 160 00, Marek.Bous@fs.cvut.cz

snadné přesně určit. Závisí především na použitých materiálech spojky; ale má na něj vliv i opotřebení, teplota, mazání, atd. Jenomže tato tribologická veličina je velice důležitá pro vývoj převodových skříní. Velmi ovlivňuje právě ty její vlastnosti, které řidič pocítí nejvíce – například řadící sílu nebo čas pro zařazení. Nezbývá tedy nic jiného než jí zjistit experimentálně.
Požadavky na synchronizační spojky jsou vysoké, jak z tribologického hlediska, tak z hlediska únosnosti a životnosti. V automobilové převodovce musí synchronizační spojka zvládnout desítky tisíc cyklů, proto je velice obtížné provádět zkoušky řazení a synchronizace v provozu. Proto jsou pro laboratorní zkoušky převodovek a jejich částí vyvíjeny speciální jednoúčelové zkušební stavy, které se snaží co nejvěrněji otestovat vlastnosti konkrétní součástky.

2.1. Zkušební stav μ-Comp [2]

Tento zkušební stav byl původně vyvinut na technické univerzitě v Hannoveru, nyní je vyráběn a prodáván firmou SK Hydroautomation společně s řídícím software Synchro firmy HD Automation. Jde o nejjednodušší a nejrozšířenější zkušební stav, jsou na něm namontovány a zkoušeny pouze samostatné synchronizační spojky.

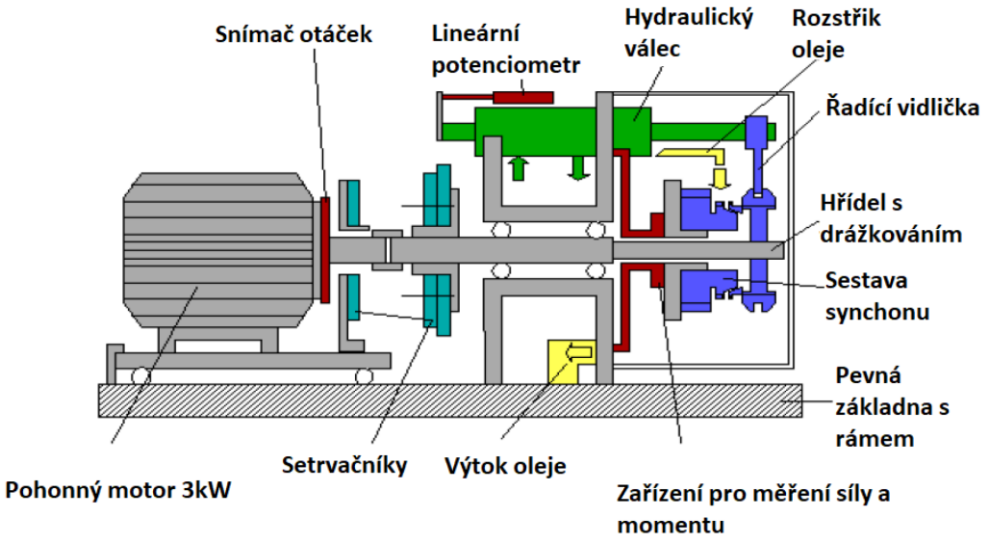

Obrázek 1 *Schéma stroje μ -Comp*

Stroj je poháněn regulovatelným elektrickým motorem, kterým je roztáčena hlavní hřídel. Pro dosažení žádaného momentu setrvačnosti je možné na hřídel namontovat přídavné setrvačníky. Ty nahrazují redukovaný moment setrvačnosti I_{red} komponent v převodovce, které budou synchronizovány. Hřídel prochází rámem a roztáčí náboj synchronizační spojky na otáčky Δn, které odpovídají rozdílu otáček v převodovce před synchronizací (odečtené např. z pilového diagramu). Řadící objímka je posouvána přes řadící vidličku hydraulickým válcem. Ozubené kolo se synchronizačním kroužkem je nasazeno na přírubu, pevně spojenou s rámem, která zároveň slouží jako měřící zařízení. Protože reakce od sil, působící na synchronizační kroužek během řazení se projeví deformací příruby, jsou tyto síly na něm zaznamenávány pomocí tenzometrů. Jmenovitě lze zjistit třecí moment M_S a axiální sílu F_a. Cyklus měření je velice rychlý. Přístroj může zjišťovat například tribologické vlastnosti kuželové spojky (srovnání

různých třecích materiálů, různé mazací podmínky), životnost a opotřebení spojky nebo potřebné řadící síly.
Cyklus měření začíná roztočením hlavní hřídele elektromotorem na požadované otáčky. V okamžiku, když je napájení motoru vypnuto, započne pístnice hydraulického válce lineární pohyb, kterým přitlačí řadící objímku na kuželovou synchronizační spojku. V tento okamžik je dosaženo brždění hlavního hřídele až na nulové otáčky.

2.2. Zkušební stav SSP 180 [2]

Testovací stav byl původně vyvinut pod technickou univerzitou v Mnichově, nyní vyráběn firmou ZF. Rozdíl oproti µ-Comp je ten, že do stavu je uchycen celý blok synchronizačních spojek se sousedícími ozubenými koly, navíc je přidán druhý, hmotnější setrvačník, který nahrazuje setrvačnost jedoucího automobilu
Zatímco ozubené kolo I je pevně zachyceno v rámu, ozubené kolo II se otáčí konstantními otáčkami n_0, odpovídající otáčkám výstupu z převodovky. Jejich stabilitu zajišťuje setrvačný moment většího ze setrvačníků, který je roztočen regulovatelným elektromotorem. Náboj synchronizační spojky je roztáčen stejně jako u předchozího stroje, tedy setrvačníkem nahrazujícím redukovaný setrvačný moment rotujících částí převodovky, které budou synchronizovány, a to na otáčky o Δn rozdílné, odpovídající rozdílu otáček při řazení v převodovce. Pohybem řadící objímky k ozubenému kolu II je náboj synchronu akcelerován/decelerován přes kuželovou třecí spojku až na otáčky n_0, zatímco pohybem ke kolu I dojde k zastavení náboje. Pohyb objímky je opět realizován hydraulickým válcem. U tohoto stroje je možné připojit k ovládání řadící objímky původní řadící mechanismus a poté měřit na něm řadící sílu. Toho je využíváno zejména u řazení ozubeného kola II, protože během tohoto procesu není možné jiné veličiny zaznamenat. Tento způsob je vhodný zejména k testů, životnosti. Řazení na ozubené kolo I probíhá obdobně jako fungování stroje µ-Comp, je tedy možné zaznamenat axiální sílu F_a a třecí moment M_s.

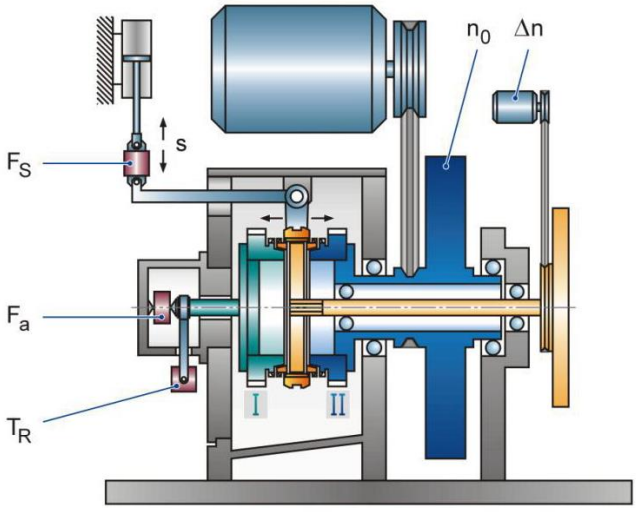

Obrázek 2 *Schéma stroje SSP 180.*
Fs – snímač řadící síly, Fa – snímač axiální síly, TR – snímač třecího momentu, n0 – velký setrvačník, Δn – malý setrvačník, I a II – volně otočná kola se synchronizačním kroužkem.
Zdroj: [21], str. 3.

3. EXPERIMENTÁLNÍ PŘEVODOVKA ČVUT

3.1. Umístění experimentální převodovky

Experimentální převodovka, která vznikla v laboratořích Ústavu automobilů, spalovacích motorů a kolejových vozidel, Fakulty strojní ČVUT v Praze na Julisce využívá setrvačníkový stav řazení zmíněný v úvodu a nahrazuje v něm zkoušenou převodovku s tím, že umožňuje jiný typ zkoušek než je možné provádět s převodovými skříněmi z osobních automobilů. Schéma celé sestavy (setrvačníkový stav – experimentální převodovka – vnější synchronizace) je na obrázku níže.

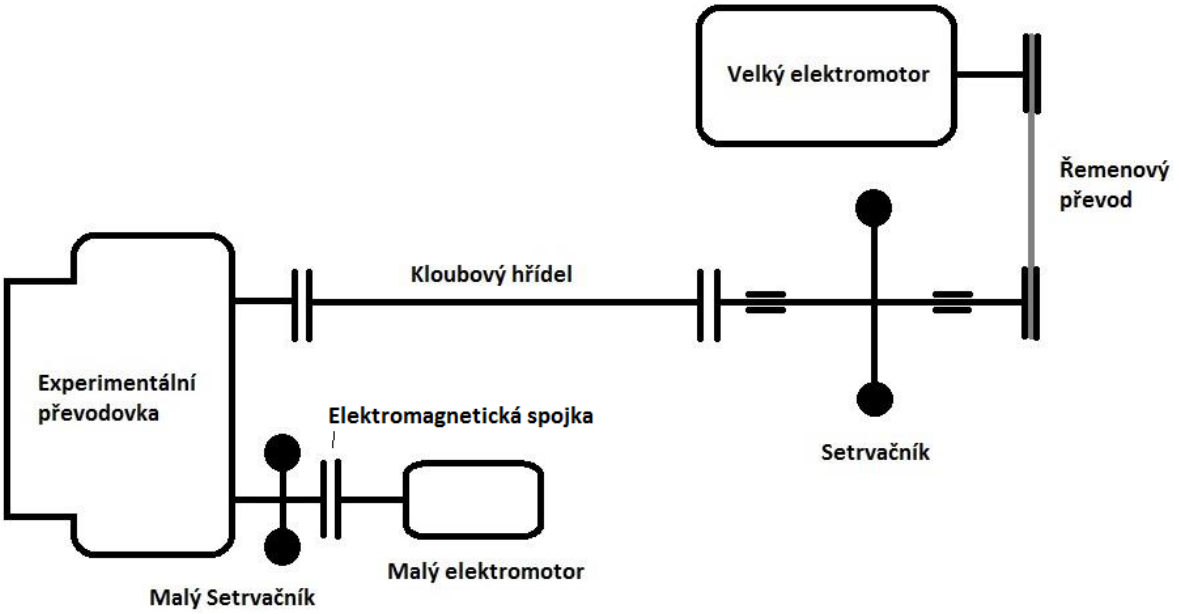

Obrázek 3 *Schéma zkušebního stanoviště s experimentální převodovkou*

3.2. Konstrukce experimentální převodovky [2]

Experimentální převodovka má tří hřídelové uspořádání v jedné kompaktní skříni, je tvořena vodorovně dělenými polovinami obráběnými z ocelových polotovarů. Stálý převod je realizován ozubeným soukolím. Jednotlivé hřídele jsou uloženy ve dvojicích valivých kuličkových ložisek, namontovaných ve stěnách skříně. Ložiska mají dostatečný rozestup, aby zachytávala ohybový moment od letmo uložených konců hřídelů. Tím vznikl uvnitř skříně prostor na umístění ozubeného soukolí stálého převodu.
Převislé konce hřídelí vedou mimo skříň a slouží k montáži zkušebního ozubeného soukolí se synchronizační spojkou. Celý vnější prostor je zakrytován krytem z průhledného plastu (PMMA – plexi sklo).
Vnitřní a vnější prostor jsou odděleny, tudíž každý z prostorů má svůj olejový oběh. Uvnitř skříně je stálá hladina olejové náplně, takže ložiska a těsnící prvky jsou mazány rozstřikem oleje. Olej aplikovaný tryskou k synchronizační spojce steče do spodní části, odkud je olej opět odčerpáván.
Převislé konce hřídelů jsou totožné, tudíž lze namontovat soukolí se synchronizační spojkou na vstupní i výstupní hřídeli. Z tohoto důvodu je i montážní pozice pro snímač

axiální síly na skříni u obou konců. Pneumatický válec s řadící vidličkou je montován na prodloužené stěně mimo vnitřní prostor. Montážní otvory pro válec jsou taktéž nad každým z převislých konců, tudíž je splněn požadavek na umístění synchronizační spojky na libovolné hřídeli. Pneumatický válec bylo vhodné umístit osově co nejblíže hřídelím, aby se snížil ohybový moment na řadící vidličku a pístnici. Proto nebylo možné ponechat jeden montážní otvor na válec v rovině mezi oběma hřídeli (volba hřídele by byla realizována pootočením řadící vidličky na pístnici).

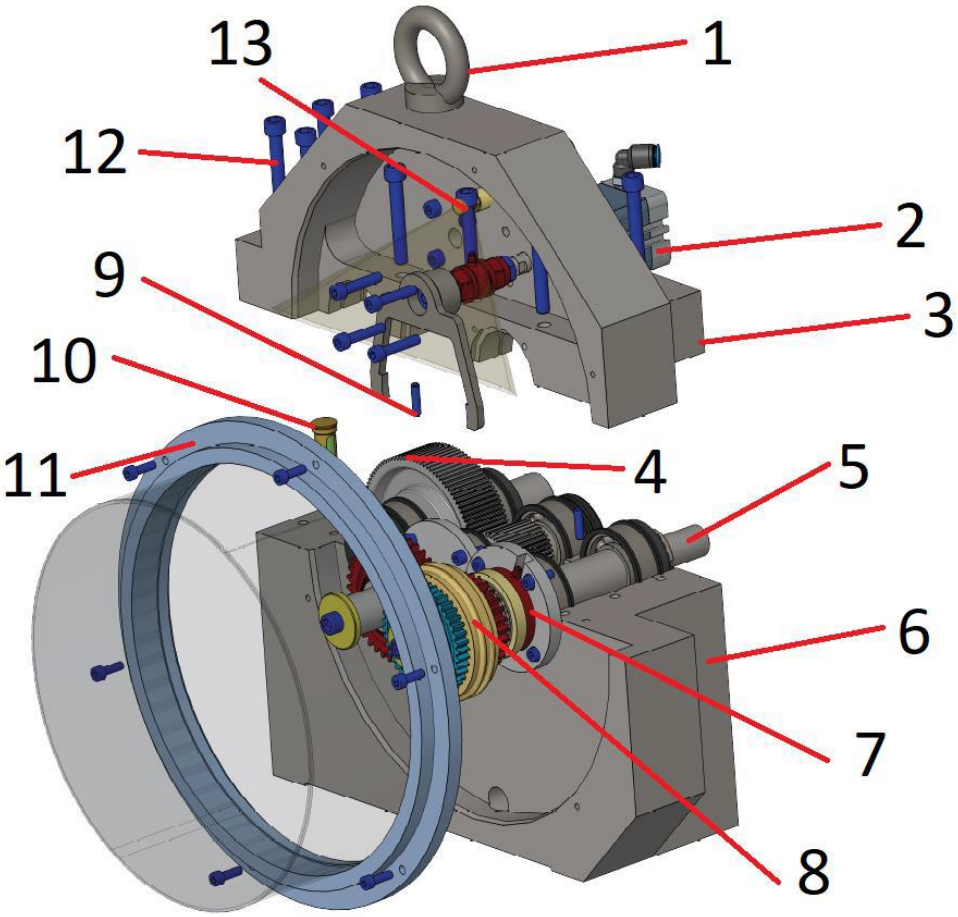

Obrázek 4 *Rozklad finálního návrhu zkušební převodové skříně. [2]*
1 – závěsné oko, 2 – pneumatický válec s řadící vidličkou, 3 – víko skříně, 4 – stálý převod, 5 – hřídele, 6 – vana skříně, 7 – snímač axiální síly, 8 – převislé konce hřídelů se synchronizační spojkou a soukolím, 9 – pozicovací kolík, 10 – olejová měrka, 11 – kryt z plexi skla, 12 – šrouby skříně, 13 – mazací tryska.

3.3. Vnější synchronizace [3]

Na vstupní hřídel experimentální převodovky je pak kromě malého setrvačníku přes elektromagnetickou spojku připojen i synchronní elektromotor kterým je možné přizpůsobit otáčky vstupní hřídele pro dosažení přesného scénáře testu. Tento elektromotor je s hřídelí spojen jen ve fázi „přípravy“ zkoušky a při samotném řazení, je díky elektromagnetické spojce odpojen, aby neovlivňoval chování vstupní hřídele.

4. POROVNÁNÍ ZKUŠEBNÍCH STAVŮ

Návrh experimentální převodovky byl zaměřen na překonání nedostatků zkušebních stavů, které již pro podobný typ zkoušek existují (viz 2.1 a 2.2).
Porovnání jednotlivých zkušebních stavů je v následující tabulce.

Zkušební stav	**μ-Comp**	**SSP 180**	**ČVUT**
výhody	- Letmo uložená synchronizační spojka – snadná výměna. - Rychlý cyklus. - Univerzálnost stroje.	- Rychlý cyklus. - Řazení mezi 2 synchronizačními spojkami. - Simulace setrvačnosti jedoucího vozidla velkým setrvačníkem.	- Letmo uložená synchronizační spojka – snadná výměna. - možnost nastavení téměř libovolné kombinace otáček hřídelů - Simulace setrvačnosti jedoucího vozidla velkým setrvačníkem.
nevýhody	- Aplikace oleje neodpovídá skutečnosti. - Synchronizační kroužek má nulové otáčky. Má to vliv např. na odstředivé síly na olej.	- Složitá výměna zkoušené synchronizační spojky. - Přístroj má 2 módy měření, není možné měřit všechny veličiny současně.	- Problematika měření momentu – vůle v ozubení. - Není samostatné zařízení, potřebuje původní setrvačníkový stav
Měřitelné veličiny	Axiální síla, třecí moment, otáčky, teploty, poloha řadící objímky, průtok oleje.	Třecí moment, axiální síla, řadící síla, otáčky setrvačníků, poloha řadící objímky.	Třecí moment, axiální síla, řadící síla, otáčky setrvačníků, poloha řadící objímky, teplota oleje.
Maximální rozdíl otáček	4500 $1/min$	3000 $1/min$	6000 $1/min$

Tabulka 1 *Porovnání zkušebních stavů*

5. ZÁVĚR

Navržená experimentální převodovka má všechny předpoklady pro to, aby na ní mohly být prováděny zkoušky stejně nebo více kvalitní jako na zkušebních stavech zahraničních univerzit. Hlavním rozdílem je, že převodovka nefunguje jako samostatné zařízení ale využívá setrvačníkového stavu používaného pro zkoušení převodovek osobních automobilů. To ovšem vzhledem k plánovanému použití pro vývojové, prototypové či únosnostní zkoušky v laboratořích na Julisce nijak nesnižuje její užitnou hodnotu. Celý proces je kontrolovatelný a dobře kvantifikovatelný. Montáž a demontáž testovaného dílu je rychlá a jednoduchá. Navíc díky komplexnosti provozních stavů které je možno pomocí experimentální převodovky nasimulovat se zdaleka nemusí omezovat na zkoušky synchronizačních spojek, ale bude možné na ní provádět i

zkoušky prototypových řadicích spojek, kterých už na Ústavu automobilů, spalovacích motorů a kolejových vozidel, Fakulty strojní ČVUT v Praze vznikla celá řada.
V současnosti stále probíhají práce na olejovém okruhu pro mazání zkušeního prostoru a na ovládání řadicí objímky.

POUŽITÉ ZDROJE

[1] PAKOSTA, Jiří a ACHTENOVÁ, Gabriela. Návrh setrvačníkového zkušebního stavu pro zkoušky řazení převodovek. Praha: ČVUT Fakulta strojní, odborný článek, 2015.

[2] HOBLÍK, Jan. Zkušební stanoviště pro testování synchronizačních spojek. Praha: ČVUT Fakulta strojní, diplomová práce, 2019.

[3] HLAVATÝ, Jakub. Integrace vnější synchronizace pro experimentální převodovku. Praha: ČVUT Fakulta strojní, bakalářská práce, 2021.

52. MEZINÁRODNÍ VĚDECKÁ KONFERENCE ČESKÝCH A SLOVENSKÝCH UNIVERZIT A INSTITUCÍ ZAMĚŘENÁ NA VÝZKUMNÉ A VÝUKOVÉ METODY SPOJENÉ SE SPALOVACÍMI MOTORY, ALTERNATIVNÍMI POHONY A DOPRAVOU

22.-23. ZÁŘÍ 2021, PRAHA
ČESKÁ ZEMĚDĚLSKÁ UNIVERZITA V PRAZE, TECHNICKÁ FAKULTA,
KATEDRA VOZIDEL A POZEMNÍ DOPRAVY

PŘESNOST MĚŘENÍ MNOŽSTVÍ VÝFUKOVÝCH PLYNŮ PŘI NESTACIONÁRNÍM CYKLU NRTC

Pavel Brabec[1], Aleš Dittrich[2], Josef Popelka[3], Celestýn Scholz[4]

Abstrakt
Příspěvek se zabývá stanovením množství výfukových plynů spalovacího motoru, porovnáním různých způsobů měření, popř. výpočtu a nakonec určení přesnosti měření u dvou základních způsobů. Údaj o velikosti průtoku výfukových plynů je nutný pro vyhodnocení nestacionárních testů spalovacích motorů podle předpisů EHK, tzn. určení plynných emisí v jednotkách g/kWh.

1. ÚVOD

V laboratořích TUL nejprve probíhaly přípravné práce pro vytvoření měřícího stanoviště. Na elektrickou motorovou brzdu ASD 235 M250 byl nainstalován spalovací dieselový přeplňovaný motor o objemu 2 dm^3. Po instalaci spalovacího motoru na brzdové stanoviště bylo připojeno všechno nutné příslušenství motoru (chlazení motoru a mezichladič stlačeného vzduchu, odvod spalin, přívod paliva, atd.). Byly podrobně prostudovány podklady pro provedení zkoušky NRTC v předpise EHK 96 (popř. WHTC viz předpis EHK 49) a její následné vyhodnocení, co se týče především plynných emisí (dále i měření a vyhodnocení pevných částic). V návaznosti na tyto práce vznikalo mnoho různých programů (aplikací), které například připravují řídicí signály pro zkoušku, upravují naměřená surová data, nebo vyhodnocují celé měření. V předpisech jsou uvedeny různé způsoby pro stanovení průtoku výfukových plynů. První je metoda přímého měření, další možnost je metoda měření vzduchu a paliva - použijí se průtokoměry vzduchu a průtokoměry paliva, které mají předepsanou přesnost. Potom průtok výfukového plynu se vypočítá podle vztahu (1).

[1] Ing. Pavel Brabec, Ph.D., Technická univerzita v Liberci, Studentská 1402/2, 461 17 Liberec 1, pavel.brabec@tul.cz
[2] Ing. Aleš Dittrich, Ph.D., Technická univerzita v Liberci, Studentská 1402/2, 461 17 Liberec 1, ales.dittrich@tul.cz
[3] Ing. Josef Popelka, Ph.D., Technická univerzita v Liberci, Studentská 1402/2, 461 17 Liberec 1, josef.popelka@tul.cz
[4] Prof. Ing. Celestýn Scholz, Ph.D., Technická univerzita v Liberci, Studentská 1402/2, 461 17 Liberec 1, celestun.scholz@tul.cz

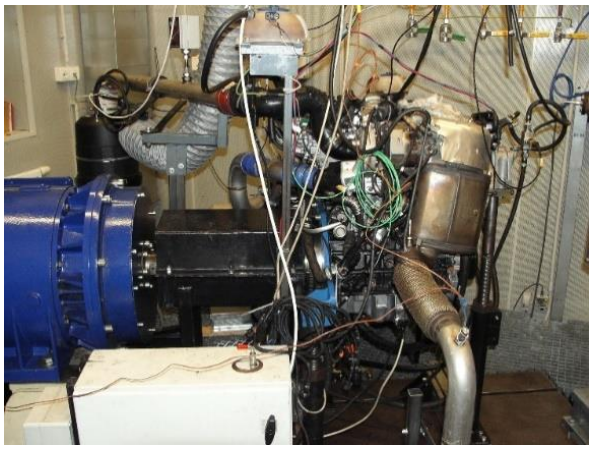
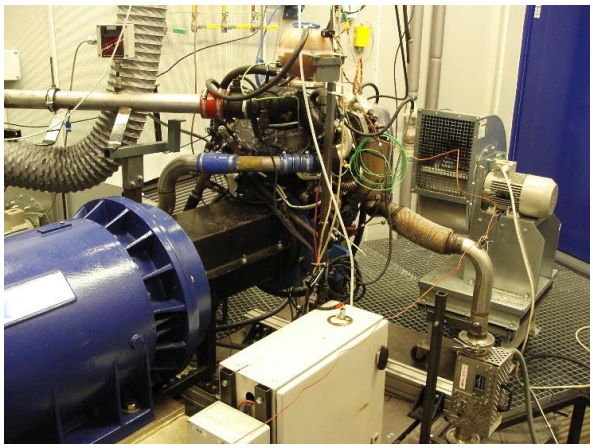

Obrázek 1: *Fotografie měřicího stanoviště*

$$G_{EXHV} = G_{AIRW} + G_{FUEL} \quad (1)$$

kde G_{EXHV} – průtok výfukových plynů, kg/s;
G_{AIRW} – průtok vzduchu, kg/s;
G_{FUEL} – průtok paliva, kg/s.

Další možnost je výpočet hmotnosti zplodin výfuku ze spotřeby paliva a koncentrací výfukového plynu podle metody bilance uhlíku. Poslední metoda pro určení průtoku výfukových plynů je stanovení poměru vzduchu k palivu λ výpočtem (pomocí vztahu (2) - poznámka: výpočet se vztahuje na motorovou naftu, u níž je poměr H/C rovný 1,8) nebo měřením, v našem případě např. pomocí měřidla ETAS, a měření průtoku vzduchu (nebo paliva). Okamžitý hmotnostní průtok výfukového plynu se vypočítá pomocí vztahů (3).

$$\lambda = \frac{\left(100 - \frac{conc_{CO}\cdot 10^{-4}}{2} - conc_{HC}\cdot 10^{-4}\right) + \left(0{,}45 \cdot \frac{1 - \frac{2\cdot conc_{CO}\cdot 10^{-4}}{3{,}5\cdot conc_{CO2}}}{1 + \frac{conc_{CO}\cdot 10^{-4}}{3{,}5\cdot conc_{CO2}}}\right)\cdot\left(conc_{CO2} + conc_{CO}\cdot 10^{-4}\right)}{6{,}9078\cdot\left(conc_{CO2} + conc_{CO}\cdot 10^{-4} + conc_{HC}\cdot 10^{-4}\right)} \quad (2)$$

kde A/F_{st} – stechiometrický poměr vzduch/palivo, kg/kg;
λ – relativní poměr vzduch/palivo;
$conc_{CO2}$ – koncentrace suchého CO2, %;
$conc_{CO}$ – koncentrace suchého CO, ppm;
$conc_{HC}$ – koncentrace HC, ppm.

$$G_{EXHV} = G_{FUEL}\cdot(1 + \lambda\cdot A/F_{st}), \quad G_{EXHV} = G_{AIRW}\cdot\left(1 + \frac{1}{\frac{A}{F_{st}}\lambda}\right), \quad (3)$$

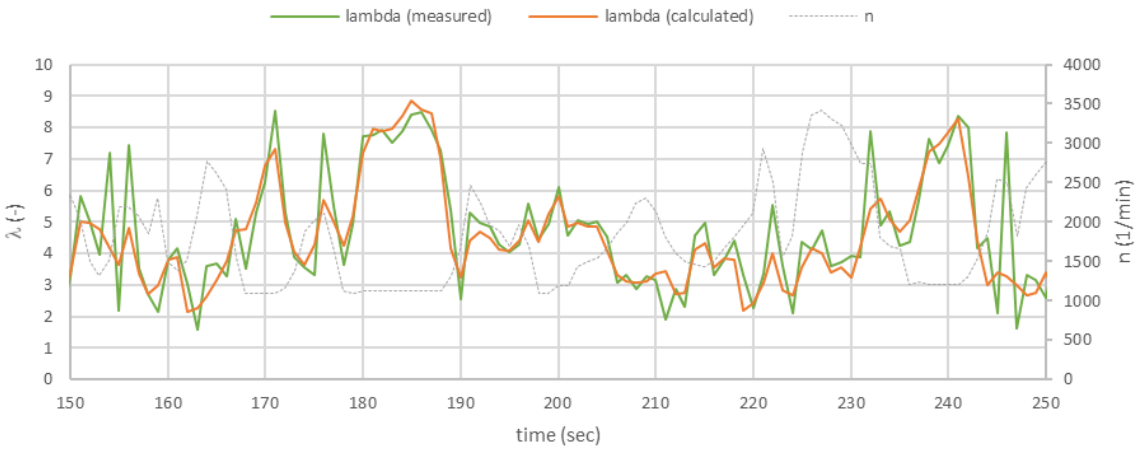

Obrázek 2: *Graf závislosti součinitele přebytku vzduchu - měřeno a vypočteno podle (2) (detail části měření testu NRTC)*

2. POPIS MĚŘENÍ

Pro podrobnější porovnávající analýzu byly vybrány dva způsoby určení průtoku výfukových plynů, a to přímé měření a metoda měření průtoku vzduchu a paliva v testovacím cyklu NRTC podle EHK 96. Byla oslovena firma Horiba, která pro přímé měření nabízí dva použitelné přístroje: EXFM-ONE (employs an ultrasonic method for real-time measurement directly from a vehicle or engine) a PTFM (Pitot tube). Výhodou PTFM je velký rozsah průtoku (0 – 65 m^3/min) z důvodu možnosti použití osmi různým velikostí trubice, další výhodou je možnost použití až do teploty 900°C (pro EXFM-ONE je omezení 0 – 10 m^3/min a 370°C). Nevýhodou PTFM je velká chyba měření pro velmi nízké průtoky.

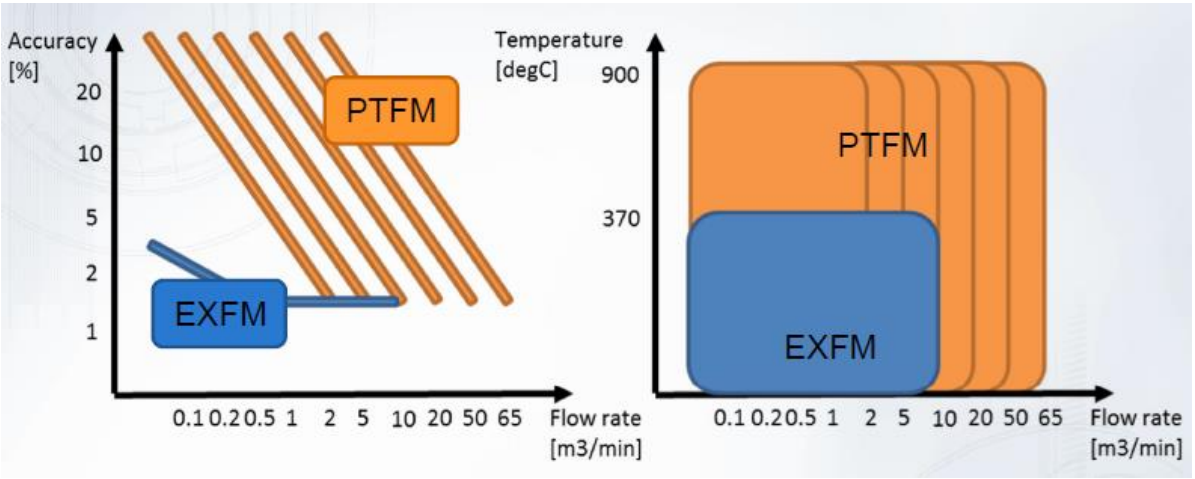

		EXFM	PTFM V2
Accuracy	0.07 – 0.1 m^3/min	± 3 % readings	± 10 % readings
	0.1 – 0.4 m^3/min	± 2 % readings	± 5 % readings
	0.4 – 10 m^3/min	± 1 % readings	± 1.5 % readings
	10 – 65 m^3/min	Out of range	± 1.5 % readings
Flow range		0 – 10 m^3/min	0 – 65 m^3/min over 8 sizes of tube
Gas temperature		370°C (5 min)	900°C
Size		430x580x690 mm	Interface: 360x220x320 mm Tube: 125x210x400 mm
Weight		60 kg	Interface: 8 kg; Tube: 4 kg

Tabulka 1: *Porovnání přístrojů od firmy Horiba*

Pro náš spalovací motor bylo vybráno měřidlo PTFM a byla použita velikost pitotovy trubice C (do 10 000 l/min). Na následujícím obrázku je zobrazeno zjednodušené schéma měření.

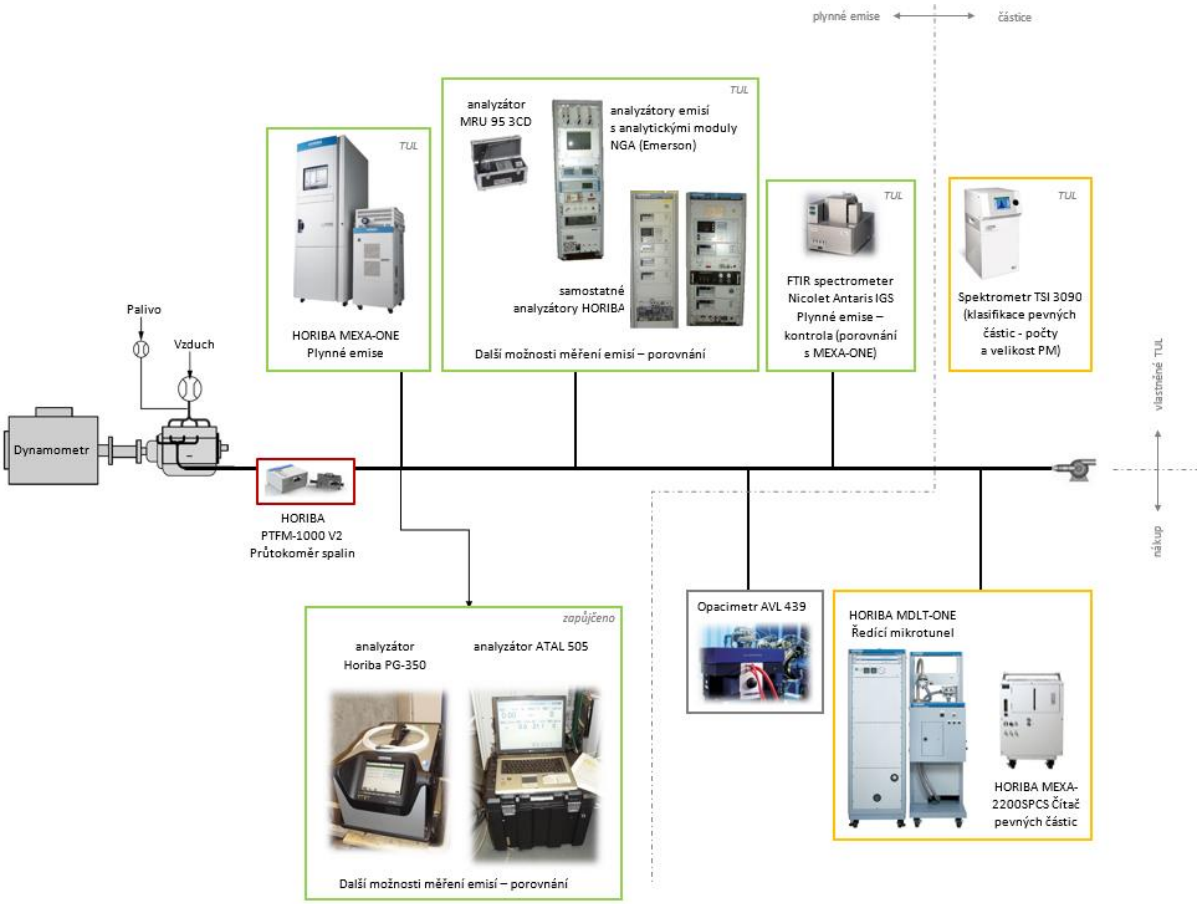

Obrázek 3: *Schéma měřícího stanoviště*

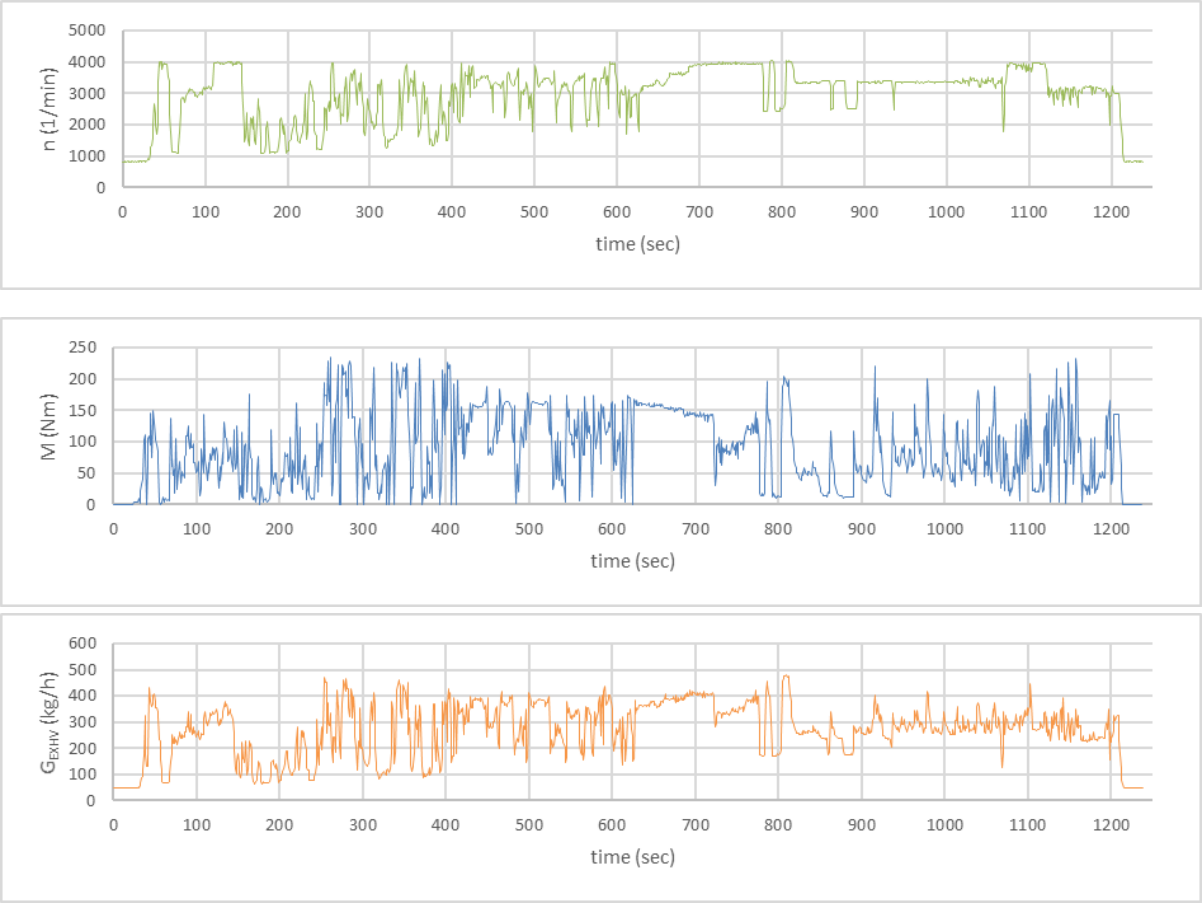

Obrázek 4: *Ukázka měření cyklu NRTC - otáčky motoru, točivý moment a průtok výfukových plynů*

V následující tabulce jsou zobrazeny použité měřicí přístroje a popis jejich parametrů. V grafech pod tabulkou jsou zobrazeny relativní chyby přístrojů, červenými čárami je naznačena oblast měření v cyklu NRTC pro náš spalovací motor (minimální a maximální hodnota změřeného průtoku spalin, vzduchu nebo paliva) a četnosti výskytu naměřených hodnot jednotlivých průtoků.

Výrobce / Model	Fotografie	Rozsah	Přesnost	Opakovatelnost
Spaliny: Horiba / PTFM-1000 Version 2; Příslušenství: Pitot tube C-type (0 – 10 m^3/min)		0 - 10 m3/min	do ± 1% plného rozsahu nebo do ± 1,5% odečtených hodnot (podle toho, co je větší) (při průtoku 20% plného rozsahu)	v rozmezí ± 1,0% odečtených hodnot (při průtoku 20% plného rozsahu)

Vzduch: Sierra Instruments Fast-Flo; Mass Flow Meter / 620S-L04-M1-EN2-V4-DD-0-W1 (Serial No.: 161087)		1 000 kg/h	± 1% z kalibrovaného měřicího rozsahu	± 0,2% z kalibrovaného měřicího rozsahu
Palivo: Micro Motion Elite CMF 010; Coriolios Flow Meter / CMF0 10M302NACZEZZZ (S/N: 476797; P/N: 3005610)		0 - 108 kg/h	±0.10 % z rozsahu	0.05 % z rozsahu

Tabulka 2: *Parametry použitých měřidel*

Průtokoměr spalin: min. 46,2 – max. 487,2 kg/h (0,6386711 - 6,7333672) m^3/min
Průtokoměr vzduchu: min. 42,0 – max. 421,8 kg/h
Průtokoměr paliva: min. 0,000 – max. 17,860 kg/h

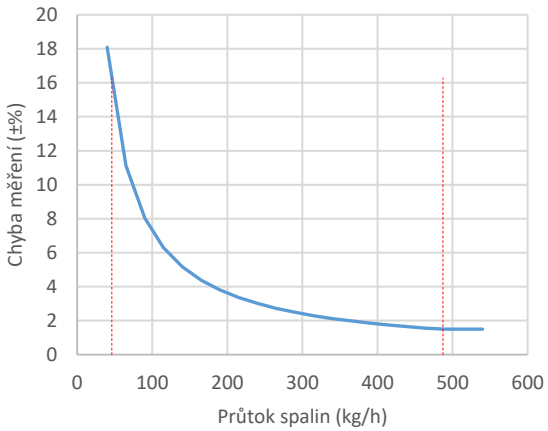

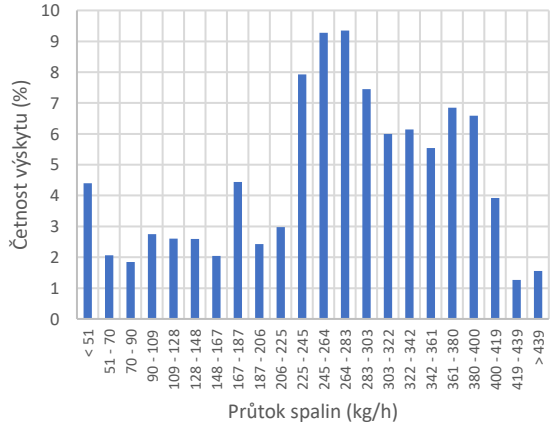

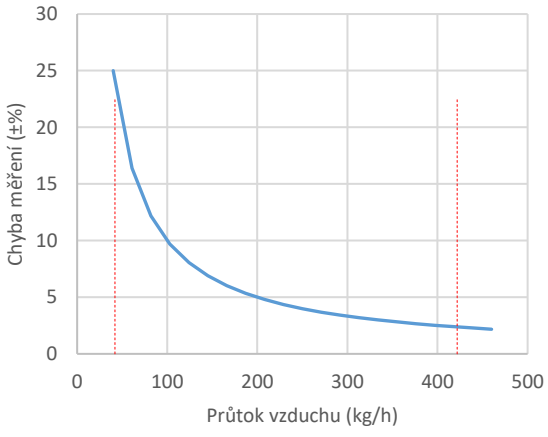

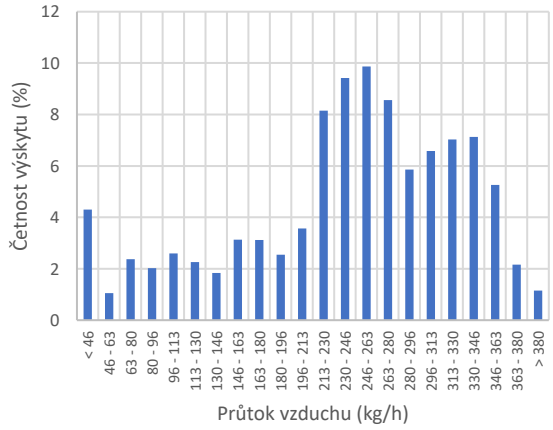

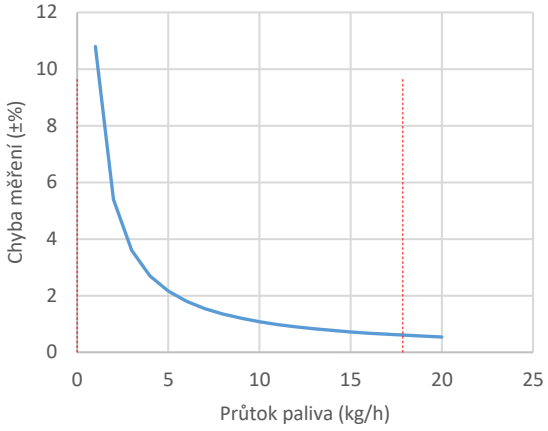

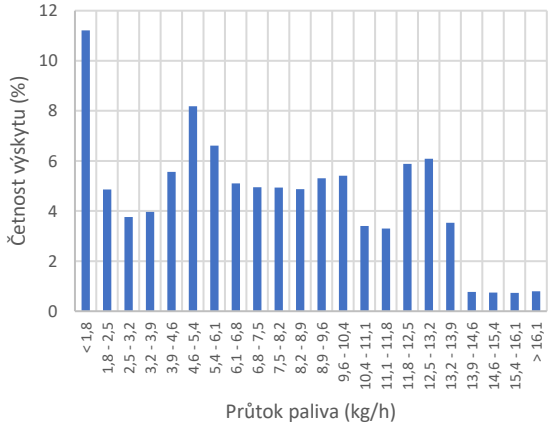

Chyba měření pro průtok spalin pro jednotlivé metody měření byla určena podle následujících vztahů. Pro přímé měření se vycházelo z údaje výrobce měřidla (4), pro nepřímou metou (tj. vzduch + palivo) se použil výpočet pomocí vzorce využívající parciální derivace a přesnosti měření jednotlivých měřidel (5).

přímé měření (PTFM) $$G_{EXHV} \pm \sigma_{GEXHV}, \quad (4)$$

nepřímé měření (vzduch + palivo)

$$G_{EXHV} = G_{AIRW} + G_{FUEL},$$

$$\sigma_{GEXHV} = \sqrt{\left(\frac{\partial G_{EXHV}}{\partial G_{AIRW}} \cdot \sigma_{GAIRW}\right)^2 + \left(\frac{\partial G_{EXHV}}{\partial G_{FUEL}} \cdot \sigma_{GFUEL}\right)^2} = \sqrt{(\sigma_{GAIRW})^2 + (\sigma_{GFUEL})^2} \quad (5)$$

kde G_{EXHV} – průtok výfukových plynů, kg/s;
G_{AIRW} – průtok vzduchu, kg/s;
G_{FUEL} – průtok paliva, kg/s;
σ_{GEXHV} – relativní chyba měření průtoku výfukových plynů, -;
σ_{GAIRW} – relativní chyba měření průtoku vzduchu, -;
σ_{GFUEL} – relativní chyba měření průtoku paliva, -.

3. VÝSLEDKY A ZÁVĚR

Na následujícím grafu jsou zobrazeny četnosti měření podle velikosti relativní chyby. U přímého měření (PTFM) převážná část měření (84,3 %) proběhlo s relativní chybou menší jak 5 %, 93,3 % bylo provedeno s relativní chybou menší jak 10 %. U nepřímého měření vyšly následující hodnoty: 75,1 % s relativní chybou menší jak 5 %, 89,8 % s relativní chybou menší jak 10 %. Přesné hodnoty jsou zobrazeny i v následující tabulce. Z těchto výsledků vychází příznivěji přímé měření průtoku výfukových plynů.

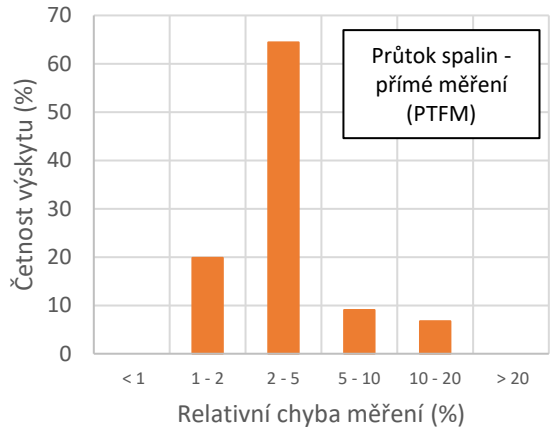

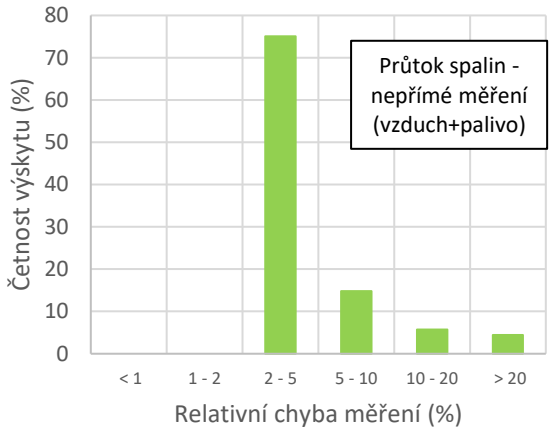

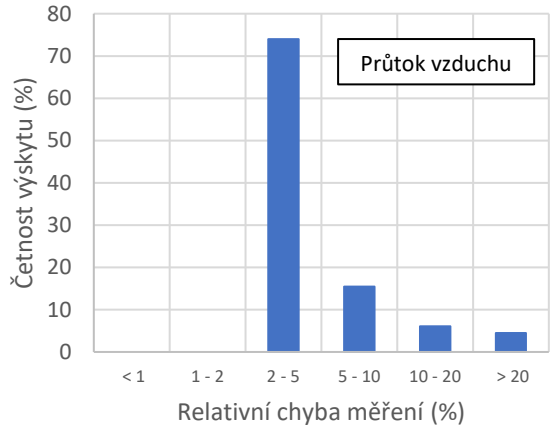

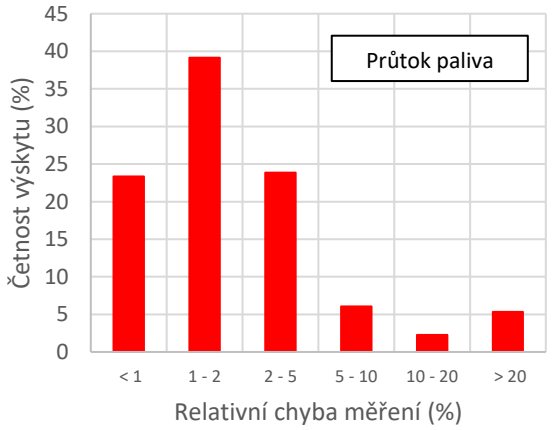

	Přímé měření (PTFM)	Nepřímé měření (vzduch + palivo)	Vzduch	Palivo
Četnost měření s relativní chybou menší jak **1%**:	0	0	0	23.4
Četnost měření s relativní chybou menší jak **2%**:	19.9	0	0	62.5
Četnost měření s relativní chybou menší jak **5%**:	84.3	75.1	74	86.4
Četnost měření s relativní chybou menší jak 1**0%**:	93.3	89.8	89.5	92.4

Tabulka 3: *Četnosti měření podle velikosti relativní chyby pro všechny použité měřidla*

V našem případě příznivěji vyšla metoda přímého měření pomocí přístroje PTFM. Tato metoda není náročná na vyhodnocení, instalace měřicího zařízení je jednoduchá, přístroj umožňuje použití různých paliv, není omezen teplotou výfukových plynů a cenově je dokonce příznivá. Na následujícím grafu je zobrazena relativní chyba měření v závislosti na čase (průběh testu) pro obě varianty (přímé a nepřímé měření).

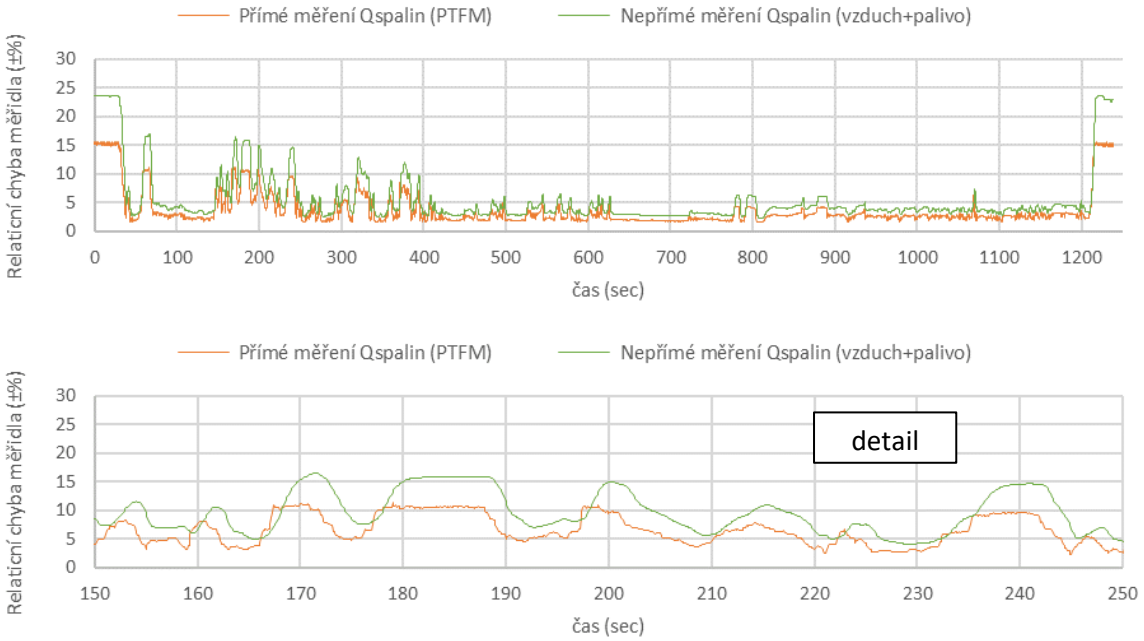

Obrázek 5: *Graf relativní chyby měření v závislosti na čase testu*

Co se týče zhodnocení dalších možných metod měření podle předpisu EHK, tak při určování průtoku spalin pomocí různých metod vycházely odlišné hodnoty (v průměru 6 až 10 %). Nejvyšší hodnoty vycházely u metod, kde se využívalo měření průtoku paliva. U této metody určení průtoku spalin je nevýhoda, že chyba měření u průtoku paliva (popř. i okamžitého poměru přebytku vzduchu) se velmi projeví do chyby určení průtoku spalin (z důvodu absolutních velikostí těchto dvou průtoků). Proto je vhodnější měřit průtok nasávaného vzduchu, kde se velikost chyby měření tohoto parametru, neprojeví tak razantně. Porovnání různých metod určení průtoku spalin je na následujícím obrázku.

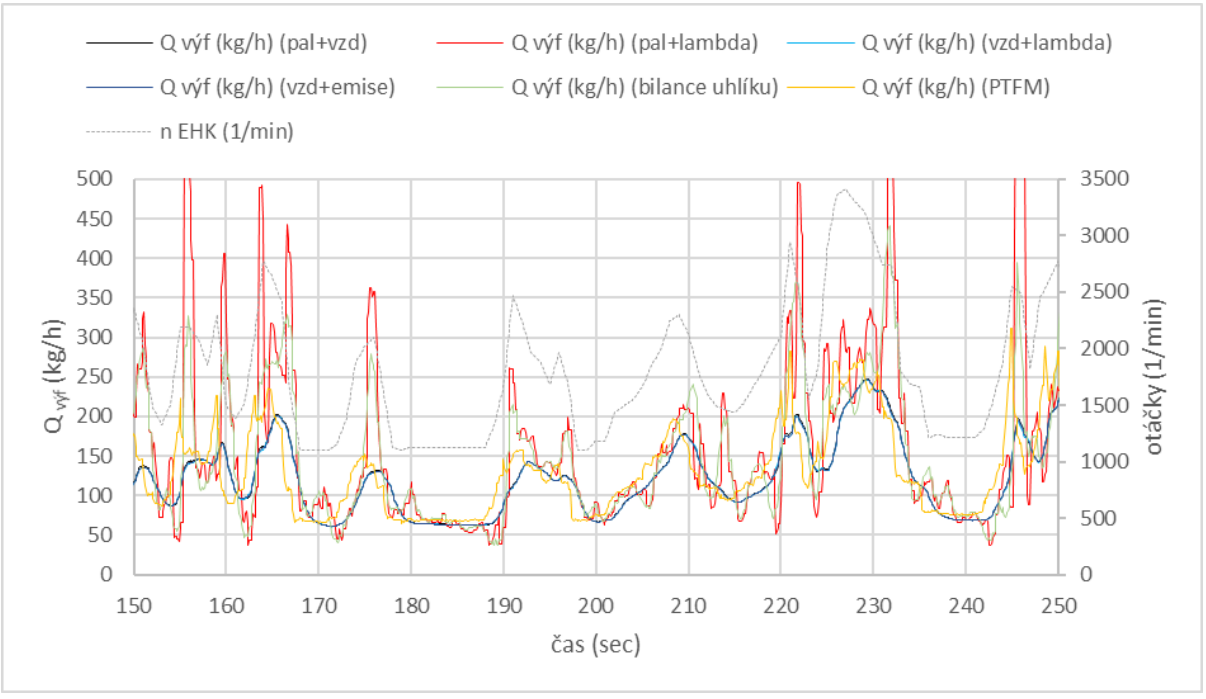

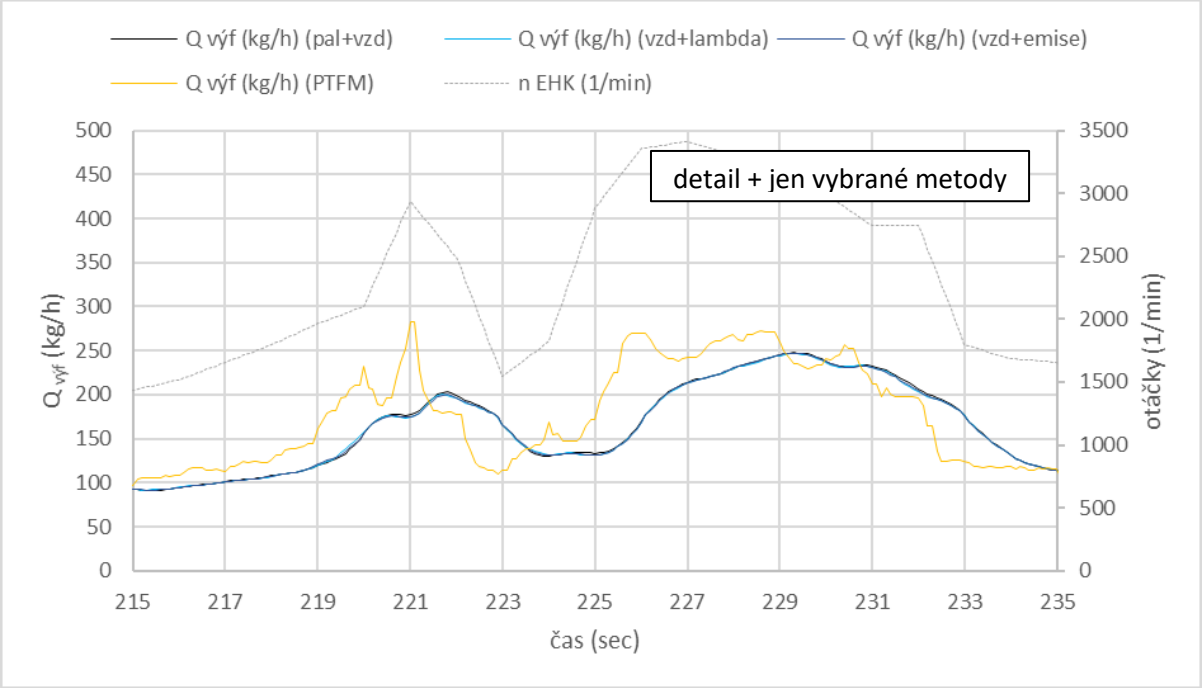

Obrázek 6: *Porovnání různých metod určení průtoku spalin (detail části měření testu NRTC)*

POUŽITÉ ZDROJE

[1] Agreement: Concerning the Adoption of Uniform Technical Prescriptions for Wheeled Vehicles, Equipment and Parts which can be fitted and/or be used on Wheeled Vehicles and the Conditions for Reciprocal Recognition of Approvals Granted on the Basis of these Prescriptions; Addendum 48: Regulation No. 49

[2] Agreement: Concerning the Adoption of Uniform Technical Prescriptions for Wheeled Vehicles, Equipment and Parts which can be Fitted and/or be Used on Wheeled Vehicles and the Conditions for Reciprocal Recognition of Approvals Granted on the Basis of these Prescriptions; Addendum 95: Regulation No. 96

[3] Martyr A. J., Plint M. A. Engine testing - Theory and Practice. Third edition. Burlington, MA 01803, 2007. pp. 242. ISBN-13: 978-0-7506-8439-2.

[4] Giakoumis E. G. Driving and Engine Cycles. Springer International Publishing, 2017. pp. 193, 285. ISBN 978-3-319-49033-5.

PODĚKOVÁNÍ

This publication was written at the Technical University of Liberec, Faculty of Mechanical Engineering with the support of the Institutional Endowment for the Long Term Conceptual Development of Research Institutes, as provided by the Ministry of Education, Youth and Sports of the Czech Republic in the year 2021.

52. MEZINÁRODNÍ VĚDECKÁ KONFERENCE ČESKÝCH A SLOVENSKÝCH UNIVERZIT A INSTITUCÍ ZAMĚŘENÁ NA VÝZKUMNÉ A VÝUKOVÉ METODY SPOJENÉ SE SPALOVACÍMI MOTORY, ALTERNATIVNÍMI POHONY A DOPRAVOU

22.-23. ZÁŘÍ 2021, PRAHA
ČESKÁ ZEMĚDĚLSKÁ UNIVERZITA V PRAZE, TECHNICKÁ FAKULTA,
KATEDRA VOZIDEL A POZEMNÍ DOPRAVY

REDESIGN AND DYNAMICS OF THE VALVE TRAIN OF AN AIRCRAFT ENGINE

Lubomír Drápal[1], Jan Vopařil[2], Kateřina Fridrichová[3], Jozef Dlugoš[4]

Abstract
In aviation, reciprocating internal combustion engines are currently used for propulsion of light aircraft. Their design is often based on older and proven engines. This paper describes part of the modernizing of a spark-ignition inverted in-line four-cylinder air-cooled engine for ultra-light aircraft. The aim of the presented section is to redesign the force transmission from the cam to the push rod of the OverHead Valve system in order to reduce production costs and improve engine performance. For this purpose, state-of-the-art methods of kinematics design and simulation of valve train dynamics are used. The article presents three variants with a flat-faced cam follower differing in the cam lift, in the lever ratio of the rocker arm and the length of the push rod. Based on dynamic simulations, the best variant is then selected with better parameters of the intake and exhaust process with the same lift and timing compared to the initial design, and simultaneously lower demands on production technology.

INTRODUCTION

Reciprocating internal-combustion engines are currently used in aircraft to propel lower weight categories of aircraft for sports, tourist, acrobatic, reconnaissance and other purposes. The advantage of these power units is their economy.

The described activities and results are performed on the MIKRON engine, which is an air-cooled inverted in-line four-cylinder engine with an OHV (OverHead Valve) valve train and two valves per cylinder. Its history dates back to the mid-1930s, when the Czechoslovakian company Walter developed its first evolution under the name

[1] Lubomír Drápal, Institute of Automotive Engineering, Brno University of Technology, Technická 2896/2, 616 69, Brno, Czech Republic, e-mail: drapal@fme.vutbr.cz
[2] Jan Vopařil, Institute of Automotive Engineering, Brno University of Technology, Technická 2896/2, 616 69, Brno, Czech Republic, e-mail: voparil@iae.fme.vutbr.cz
[3] Kateřina Fridrichová, Institute of Automotive Engineering, Brno University of Technology, Technická 2896/2, 616 69, Brno, Czech Republic, e-mail: Katerina.Fridrichova@vutbr.cz
[4] Jozef Dlugoš, Institute of Automotive Engineering, Brno University of Technology, Technická 2896/2, 616 69, Brno, Czech Republic, e-mail: jozef.dlugos@vutbr.cz

MIKRON I. Parma-Technik company has been engaged in the service, production and further development of this engine since the year 1999 [1]. It is the only mass-produced power train of its kind in the world.

Currently, there are a total of three versions of this engine on the market differing in displacement and compression ratio. Table 1 shows some basic parameters and properties of the MIKRON III C variant, which is considered as the base for further redesign of the valve train.

Table 1 Selected technical parameters of the MIKRON III C engine [1]

Cylinder	Aluminium alloy with NIKASIL®
Bore	95 mm
Stroke	96 mm
Displacement	2 722 ccm
Compression ratio	8 : 1
Fuel	Min. RON 95
Engine oil	SAE 15W-40 API SL
Take-off output (5 min)	60 kW @ 2800 rpm
Max. constant output	55 kW @ 2700 rpm
Cruise output	44 kW @ 2500 rpm
Dry engine mass	64–70 kg
Direct of rotation	Left-hand

The MIKRON III engines are used as a propulsion unit for aircraft such as:

- L13-SW Vivat motor glider,
- a replica of the legendary Bücker Bü 131 Jungmann,
- trainer aircraft Trenér Baby,
- Kiebitz B11 biplane,
- FI 156 Storch
- or Praga E-144 Air Baby.

In all cases, the propeller is connected directly to the crankshaft, therefore no reducer is used.

The valve train parts of this engine are described in Figure 1. The base version of the engine is equipped with a custom-made special cam follower with a cylindrical face for contact with cam lobe, whose advantage is very low mass, however the disadvantages are the complicated design, technological demands and relatively high reject rate of production.

The aim is to replace this cam follower with another design. From the previous computations and simulations, considering the complexity of the production process, it emerged as the most suitable variant with the flat-faced cam follower. It is further elaborated into three design variants, which are assessed in terms of valve train dynamics, rocker arm stress, overall valve train installation space and any other necessary design changes.

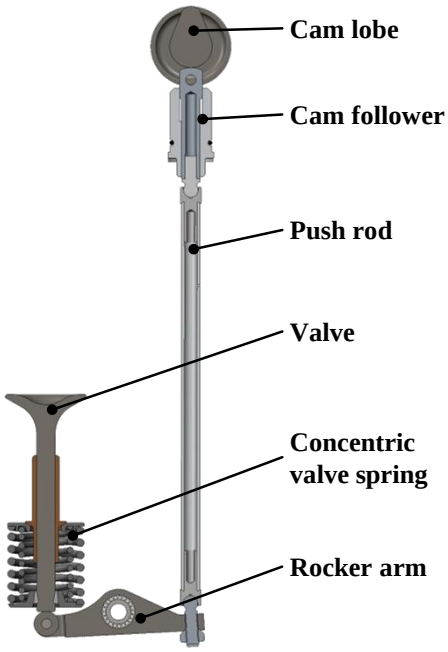

Figure 1 The valve train unit parts of the base MIKRON III engine

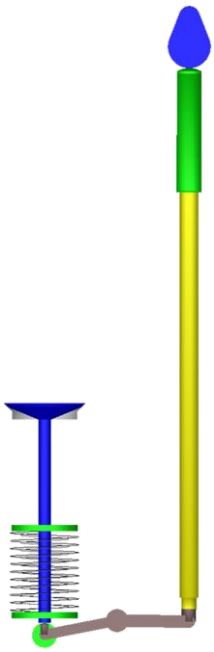

Figure 2 The MBS computational model of dynamics of valve train unit

1 VARIANTS COMPARISON AND KINEMATICS OF THE VALVE TRAIN

The design of the valve train with the flat-faced cam follower is shown in Figure 3. The three derived variants have a maximum valve lift and valve timing as the base; however, they differ with a maximum cam lift of 9.2, 7.8 and 6.6 mm.

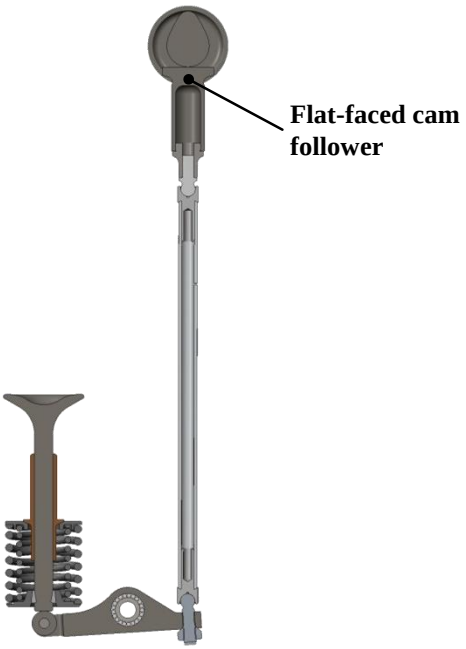

Figure 3 The valve train unit parts with the new flat-faced cam follower and new design of the cam lobe

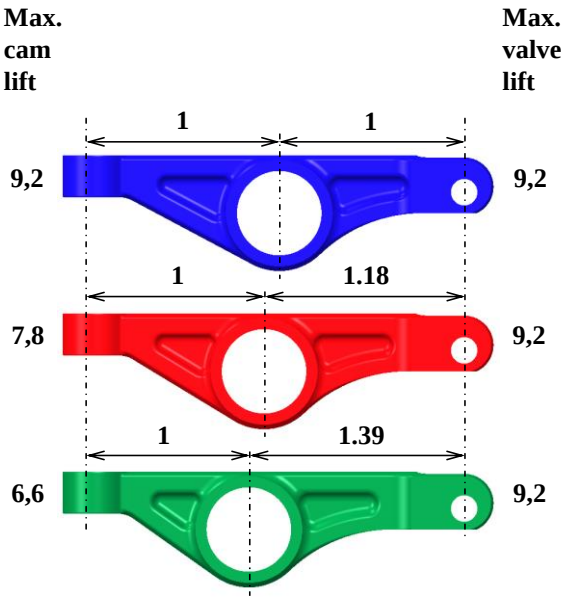

Figure 4 Change of the lever ratio on the rocker arm depending on the maximum cam lift at uniform maximum valve lift

This corresponds to a different lever ratio on the rocker arm with the same maximum valve lift of 1 : 1, 1 : 1.18, 1 : 1.39 (in the same order), see Figure 4.

The valve train kinematics are designed using Bézier splines to increase the valve area integral while keeping the acceleration values of the timing mechanism parts within reasonable limits, more in [2]. The transition opening and closing ramps are also optimized for reduced effort on the valve train components, see [3]. The diagram of the kinematic quantities of the variant with a maximum cam lift of 9.2 mm and flat-faced cam follower is shown in Figure 5. The base version of the engine with the compound cam follower is equipped with a tangential cam lobe.

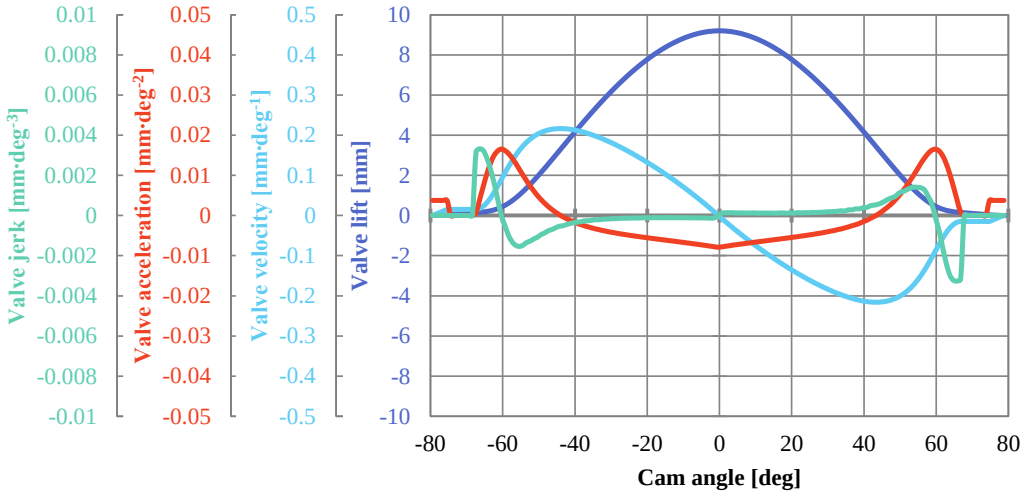

Figure 5 Kinematic quantities of the valve train valve with a flat-faced cam follower and cam with max. lift 9.2 mm

2 VALVE TRAIN DYNAMICS AND SIMULATION RESULTS

Computational model of valve unit dynamics is assembled and solved in MBS environment ADAMS, which is a general code allowing solving of various types of tasks including nonlinearities and so on [4]. The computational model, see Figure 2, considers the delimitation of the valve clearance by heating all parts to operating temperature, the effect of gas pressure in the combustion chamber and the ducts in the cylinder head. The simulation is performed for an exhaust valve that has the same design as the intake valve, however when opened it is more stressed by the gas pressure. The engine speed of 2800 rpm is considered for the simulation.

Figure 6 shows the valve lift curve from the dynamic simulation and Figure 7 shows the results of the valve acceleration course from the same simulation. The valve lift curve shows a practically identical valve lift of all three new design variants and significantly greater valve area integral of their lift curves compared to the base design. The valve area integral of the lift curve is increased by about 8 %.

The force of contact between the rocker arm and the valve is virtually unchanged for all newly designed variants, since the kinematics of the valve itself remain almost

the same. However, differences can be found on the opposite side of the rocker axis of the rocker arm.

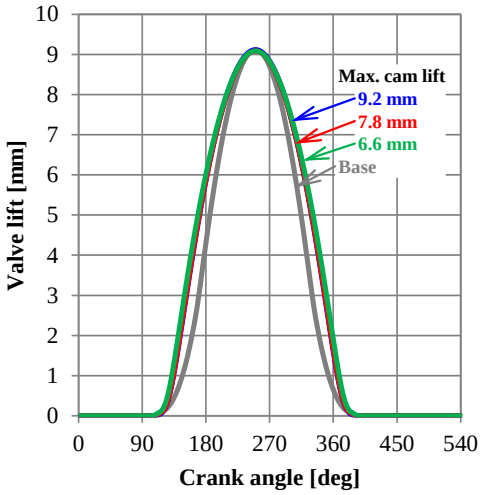

Figure 6 Valve lift curves from dynamic valve train simulation

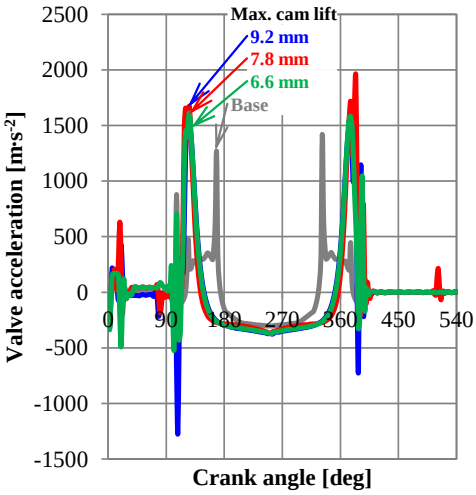

Figure 7 Valve acceleration curves from dynamic valve train simulation

The force in contact of the rocker arm with the push rod is the greater the smaller the maximum cam lift, since the smaller maximum cam lift shortens the arm length between the rocker arm pivot axis and the force application from the push rod. However, the contact of the cam with the cam follower brings interesting results. While the force in this contact, see Figure 8, shows the same tendency as the force in contact between the rocker arm and the push rod, the maximum contact pressure between the cam and the cam follower decreases as the maximum cam lift decreases, see Figure 9. This is a favourable effect in this case.

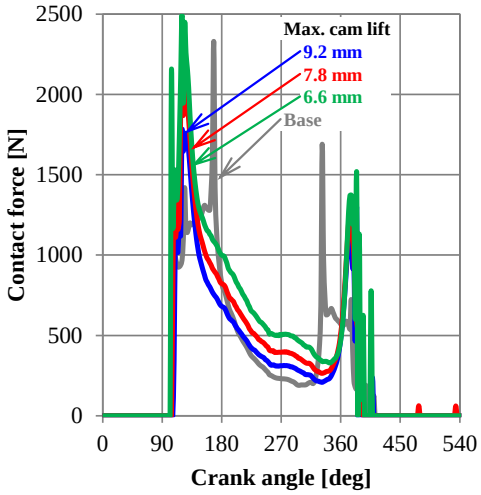

Figure 8 Contact force between the cam lobe and cam follower from dynamic valve manifold simulation

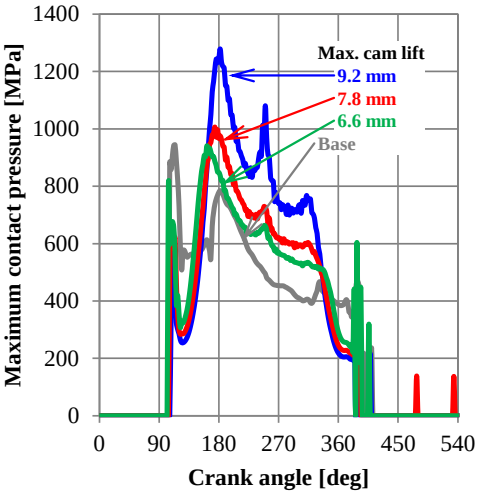

Figure 9 Maximum value of the contact pressure between the cam lobe and cam follower from dynamic valve train simulation

Based on the results of the rocker strength calculation, it is found that the values of the lever ratio change on the rocker indicate an increase in the maximum value of von Misses stress by approximately 42 % for the 6.6 mm variant compared to the 9.2 mm variant. This is not critical, however, because in order to reduce this tension, the rocker arm forging piece can be easily redesigned in the region of the greatest concentration of this stress. The load on the rocker arm for all variants is based on the results of the MBS simulation.

CONCLUSION

Modern simulation tools and virtual prototypes allow you to test a large number of design variants, assess their benefits, and reduce the cost of manufacturing and building real prototypes. This is also used in this project, where the most promising option with a maximum cam lift of 6.6 mm was evaluated. This is because of the three new variants achieves acceptable results in the load of individual parts of the valve train and at the same time is best based on the installation into the initial crankcase. Even existing stock of blanks originally made for the initial tangential cams can be used to produce a camshaft with a new cam profile. The disadvantage is only about 0.02 kg more mass for one valve unit. The new version with the flat-faced cam follower and a cam lobe of 6.6 mm maximum lift is also successfully verified in terms of cylinder induction and exhaust processes on a thermodynamic computational engine model and its documentation is handed over to the prototype production department of Parma-Technik company.

ACKNOWLEDGEMENT

The authors gratefully acknowledge funding from the Specific research on BUT FSI-S-20-6267.

REFERENCES

[1] PARMA-TECHNIK. New engines Mikron III (Nové motory Mikron III) [online]. Parma-Technik, ©2021, [cit.: 2021-06-14]. Available from: https://www.parmatechnik.cz/nove-motory/.
[2] SCHEUER, R., HELLINGER, W. Using Bézier splines for design optimization of cams regarding valve train dynamics. Proceeding of the Institution of Mechanical Engineering, Part K – Journal of Multi-body Dynamics, Vol. 221, Issue 3, 2007, pp. 429–439.
[3] BELOIU, D. M. Modelling and Analysis of Valve Train: Part I – Conventional Systems. SAE International Journal of Engines, Vol. 3, Issue 1, 2010, pP. 850–877.
[4] MSC.SOFTWARE. ADAMS Help. Newport Beach (CA): MSC Software Corporation, ©2019. Version Adams 2019.2.

52. MEZINÁRODNÍ VĚDECKÁ KONFERENCE ČESKÝCH A SLOVENSKÝCH UNIVERZIT A INSTITUCÍ ZAMĚŘENÁ NA VÝZKUMNÉ A VÝUKOVÉ METODY SPOJENÉ SE SPALOVACÍMI MOTORY, ALTERNATIVNÍMI POHONY A DOPRAVOU

22.-23. ZÁŘÍ 2021, PRAHA
ČESKÁ ZEMĚDĚLSKÁ UNIVERZITA V PRAZE, TECHNICKÁ FAKULTA,
KATEDRA VOZIDEL A POZEMNÍ DOPRAVY

CYLINDER DEACTIVATION OF INTERNAL-COMBUSTION ENGINES: HISTORICAL DEVELOPMENT, STATE-OF-THE-ART AND OUTLOOK

Kateřina Fridrichová[1],Lubomír Drápal[2], Jan Vopařil [3], Jozef Dlugoš[4]

Abstract
Due to strict emission limits, the automotive industry needs to look for ways to reduce CO_2 emissions. One of the ways is to increase the efficiency of internal combustion engines by technologies like cylinder deactivation. Cylinder deactivation is a fuel consumption reduction technology. This paper summarises the history of cylinder deactivation and describes various approaches to the implementation of this technology, including its potential and constraints. The synergy of cylinder deactivation with other technologies is also presented and future possibilities are predicted.

1. INTRODUCTION

Cylinder deactivation (CDA) is a fuel consumption reduction technology for internal-combustion engines. The benefit is achieved in part-load operation. By deactivating some of the cylinders, the load on the active cylinders increases and the engine works with higher efficiency and lower BSFC [1]. This effect can be seen in Figure 1, where the engine map shows that, in the same operating conditions under low engine load, the BSFC decreases with the decreasing number of active cylinders [2]. CDA also reduces pollutant emission [3]. This technology is beneficial particularly for throttled spark ignition engines. Using this technology results in improved combustion and lower cylinder-wall heat loss [4]. The pumping losses are notably decreased [5]. Figure 2 shows a pressure-volume diagram using a logarithmic scale. The lower part of the diagram is smaller due to the reduction in pumping losses. There is only expansion and compression of the trapped charge inside the deactivated cylinders [6].

[1] Kateřina Fridrichová, Institute of Automotive Engineering, Brno University of Technology, Technická 2896/2, 616 69, Brno, Czech Republic, e-mail: Katerina.Fridrichova@vutbr.cz
[2] Lubomír Drápal, Institute of Automotive Engineering, Brno University of Technology, Technická 2896/2, 616 69, Brno, Czech Republic, e-mail: drapal@fme.vutbr.cz
[3] Jan Vopařil, Institute of Automotive Engineering, Brno University of Technology, Technická 2896/2, 616 69, Brno, Czech Republic, e-mail: voparil@iae.fme.vutbr.cz
[4] Jozef Dlugoš, Institute of Automotive Engineering, Brno University of Technology, Technická 2896/2, 616 69, Brno, Czech Republic, e-mail: jozef.dlugos@vutbr.cz

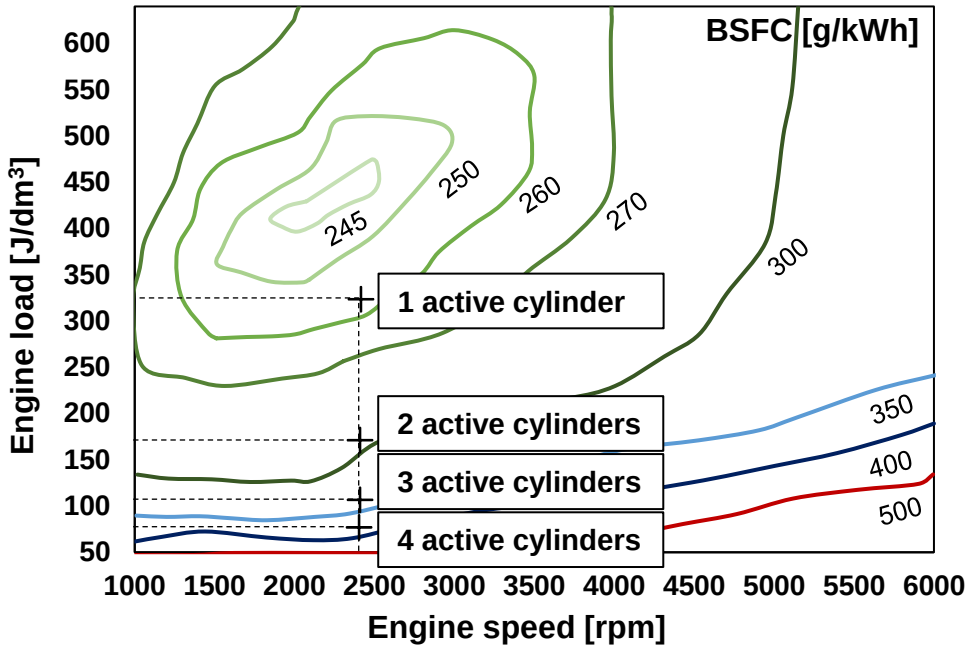

Figure 1: *BSFC improvement displayed on the engine map*

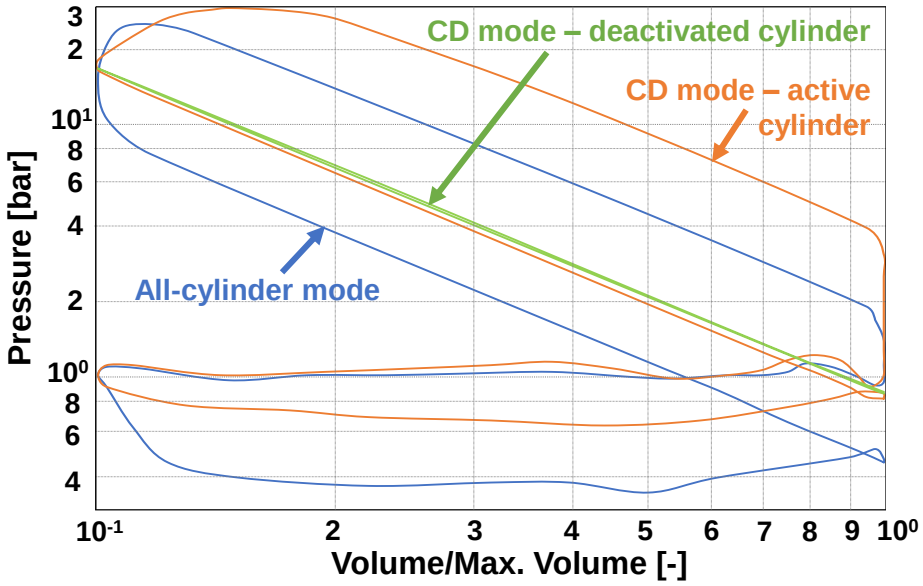

Figure 2: *Pressure-volume diagram of a 1.6 l in-line four-cylinder engine*

Most of the engines deactivate a specified number of cylinders for a desired time. This technology is called selective or fixed CDA. A contrast to this model is presented by the dynamic or rolling CDA in which each of the cylinders can be deactivated at any time [7]. Therefore, it is possible to change the number of active cylinders from cycle to cycle. The main part of this technology is the algorithm. One of the most developed rolling technologies is Dynamic Skip Fire (DSF).

2. HISTORY

The first application of CDA is considered to be the one-cylinder 'hit-and-miss' engine from the nineteenth century, which was used in tractors to control their speed [8]. After that, there were some successful attempts to incorporate CDA, like the Sturtevant 38/45 hp from 1905 [2] or the Enger Twin-Unit 12 from 1917 [9]. To deactivate one engine bank, the driver had to push a lever. This mechanism closed a butterfly valve in the intake manifold and moved a camshaft, so that all the exhaust valves on one engine bank remained open.

In 1981, Cadillac introduced its 'modulated displacement' engine V8-6-4 with a switchable rocker arm. Highway fuel consumption was improved by around 30% [7]. In the same year, Alfa Romeo tried using CDA on the Alfetta CEM. Mitsubishi released their 1.4 l four-cylinder Orion-MD one year later. The fuel consumption benefit was 11% in the city traffic [7]. The first electronically controlled deactivation system dates back to 1987 when Ford incorporated the hydraulic rocker arm from Eaton. In 1999 and 2001, Mercedes offered the 5.0 l V8 and 6.0 l V12 engines with CDA. This CDA system with switchable rocker arms produced a 7% improvement in fuel consumption in city driving and 20% at a steady cruise [7]. Honda was the first to use CDA technology in a hybrid vehicle in 2002, specifically the Accord Hybrid V6 [10]. Currently, many car manufacturers incorporate CDA. The trend is to implement CDA in downsized engines.

3. EFFECTS OF CDA

3.1 Transition processes

CDA can be classified according to the charge trapped inside the inactive cylinder. Trapping exhaust gas leads to higher irregularities on the crankshaft. The pressure stabilises after approximately ten cycles [11]. The deactivation must be maintained for more cycles to achieve the fuel consumption benefit because of the increased initial losses caused by friction. The advantage is that the cylinder cools down more slowly which is beneficial for reactivation. The second option is to deactivate the cylinder with fresh air inside. The trapped charge loses its tumble or swirl motion. However, the pressure in the cylinder is lower, which leads to lower irregularities on the crankshaft. Both exhaust gas and fresh air act as a gas spring. The third option is to leave the cylinder empty (the inlet valves no longer open after the exhaust gas is expelled). This shows the greatest benefit in simulations, but it could lead to oil being sucked into the combustion chamber [12].

3.2 Challenges

Despite the fuel consumption benefit, CDA still has many challenges. There are thermodynamic losses resulting from motoring deactivated cylinders [13]. One of the biggest challenges is frictional losses with their nonlinear dependence on engine load [14]. There is even a possibility of mixed lubrication occurring because of the higher temperatures and pressure on the bearings [15]. CDA can affect the compressor surge line of the turbocharger [16]. Another consequence of CDA is an increase in the temperature of the components [13] and increased engine oil consumption caused by

lower in-cylinder pressure during the intake stroke and the lower temperature of the piston rings [17].

CDA changes the NVH characteristics of an engine. All methods lead to greater linear and torsional vibrations, which means higher amplitudes and lower resonance frequencies [18]. The current trend is to implement CDA in downsized engines with few cylinders, where the problem with NVH is even more serious. Some of the problems can be solved by dynamic CDA. It is possible to avoid the firing frequencies that would generate high levels of vibration. Therefore, the NVH characteristics of the engine can be improved in CDA mode. The dynamic method also prevents the uneven wear caused by selective CDA. There is no problem with oil suction into the combustion chamber because the cylinder is not deactivated for such a long time.

4. TECHNICAL IMPLEMENTATION

There are many ways to implement CDA. The easiest way to incorporate CDA is to deactivate the fuel injection. However, the fuel consumption benefit is rather low. The most common way to incorporate CDA is to use switchable elements like roller finger follower [19] shown in Figure 3. It consists of two main parts, i.e. an inner and an outer arm, which are connected by the roller pin and a latch. This latch can be hydraulically disengaged and no valve lift is provided.

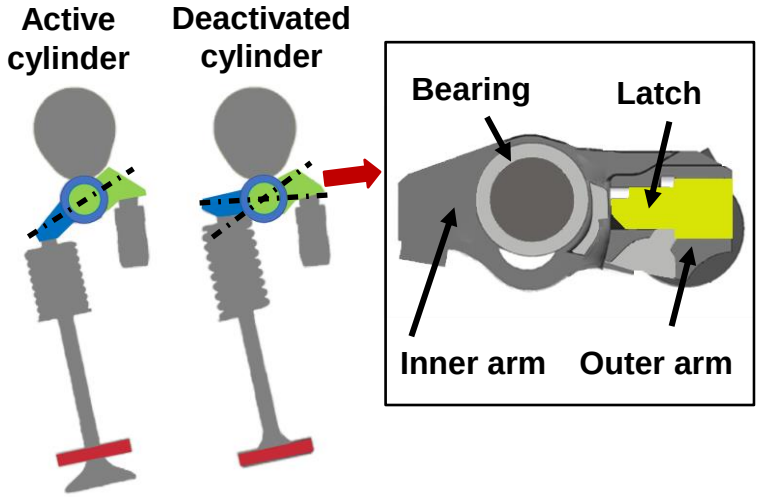

Figure 3: *Switchable roller finger follower*

Even engines with hydraulic valve tappets can implement this technology [20]. The slide pin could be moved by the oil pressure to disengage the valve stem from the lifter. The valve stem falls into a through hole created in the slide pin. Another way to implement CDA can be a switchable pivot element [11]. This consists of an inner and an outer part. In CDA mode, the inner part can be telescopically collapsed into the outer part to absorb the cam lift. The arrows in Figure 4 mark the place where the oil pressure must be applied. The same mechanism as for the switchable pivot element can be applied in the switchable roller tappet of an OHV engine [21].

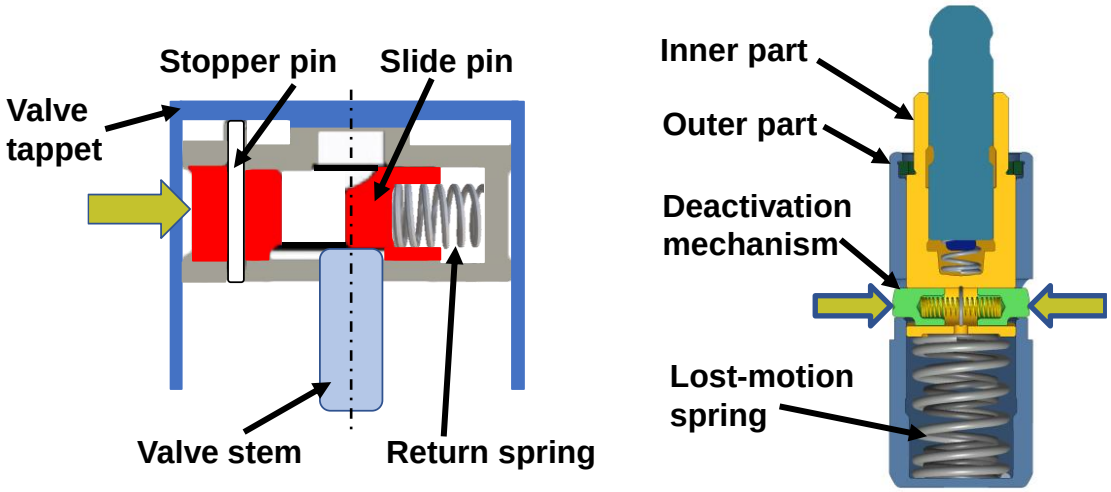

Figure 4: *Switchable valve tappet (left) and switchable pivot element (right)*

Most of the systems are electro-hydraulically controlled. However, there are also electro-mechanically controlled systems, like electro-mechanical roller follower or switchable rocker arm shown in Figure 5 [22]. The rocker arm is pivoted on an eccentric ring with a finger. This finger is locked or unlocked by the ELD (Electromagnetic locking device). An electrical signal releases the eccentric ring and the ring converts the cam lift into a rotation around its eccentricity centre. The rocker arm is pivoted on the point of contact with the valve stem and, therefore, the cylinder is deactivated.

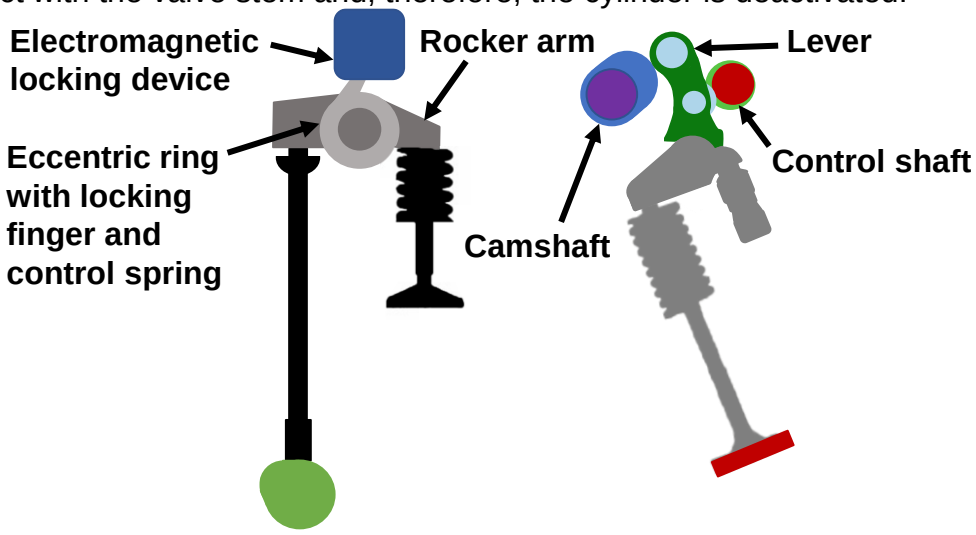

Figure 5: *Switchable rocker arm (left) and UniValve system (right)*

The Volkswagen group uses an electro-mechanical system of movable cam sections to deactivate the cylinders [4]. These cam sections can move axially and there is a zero-lift cam next to every cam with a full profile. The two-pin electro-mechanical actuator is located above the Y-shaped spiral grooves and slots the pin into the groove, which forces the section to move and the zero-lift cam to operate the valve. The second pin is used in a similar way when the cylinder is to be activated again. The system can be seen in Figure 6. The arrows in the lower part of the figure mark the position of the followers.

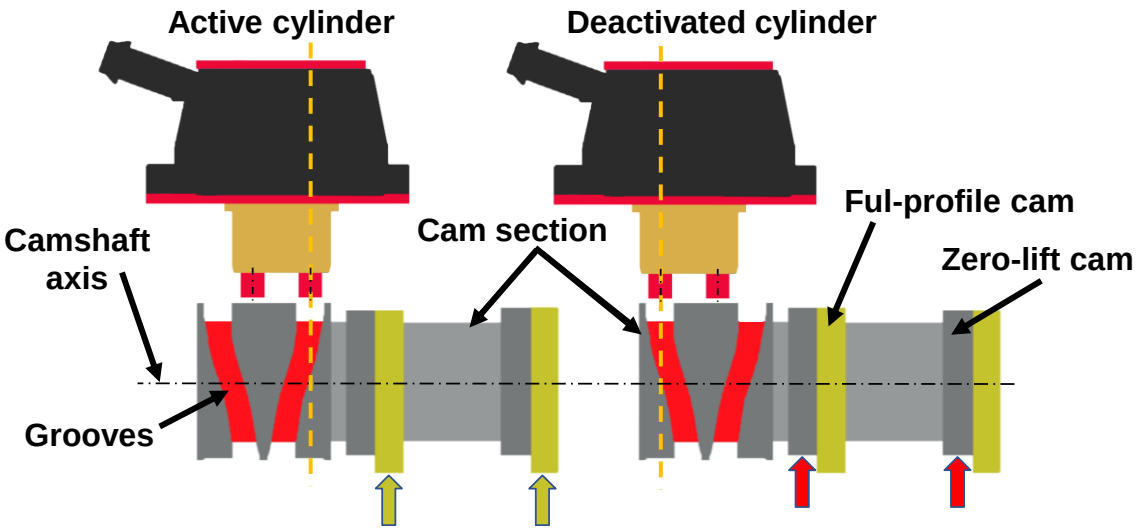

Figure 6: *Movable cam sections*

The implementation of CDA in engines with VVA is very easy. It is necessary to implement CDA into the ECU, and there are usually only slight design changes in the valvetrain. An example is the UniValve system [23] shown in Figure 5: *Switchable rocker arm (left) and UniValve system (right)*
. Each valve is operated by two shafts, i.e. the camshaft and the eccentric control shaft. Both shafts are in contact with a lever part that is in contact with the finger follower. The control shaft affects the reaction of the lever to the first conventional camshaft.

However, there are many other approaches to CDA implementation like using additional rotary valves or sliders placed on the inlet and exhaust channels [24]. This systems suffered from air leakage, insufficient fuel–air mixing and evaporation under higher pressure conditions. Some of the fixed CDA systems use separated intake and exhaust manifolds.

5. COMBINATION WITH OTHER TECHNOLOGIES

Even better fuel economy can be achieved by combining CDA with other technologies. One of these is λDSF, which combines CDA and homogeneous lean burn [25]. Homogeneous lean burn cannot be used under low loads because of the instability of combustion. CDA can broaden the operation zone of lean burn. Another benefit can be achieved by implementing CDA in hybrid vehicles. The eDSF technology combines rolling CDA with hybridisation [26]. The synergy is achieved by expanding the DSF operation zone through using hybrid torque assist and torque smoothing. Torque smoothing means generating countering waveforms to smooth the engine output. It allows more flexibility in DSF operation and better NVH. CDA also shows good synergy with the Miller cycle [27]. This technology is called mDSF. The CO_2 emissions of technologies mentioned above are compared in Figure 7.

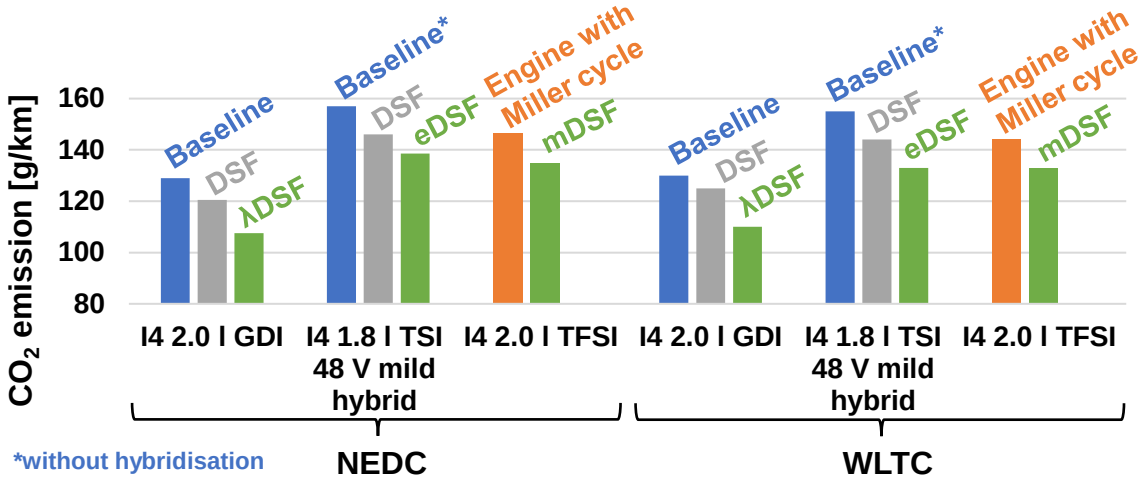

Figure 7: *Carbon dioxide emissions improvement of engines with λDSF, eDSF and mDSF*

Implementing also piston deactivation technology could significantly reduce frictional losses that are higher due to CDA [28]. This technology is based on piston decoupling. A combination of these two technologies on a V8 spark ignition engine with displacement of 4.6 l led to a decrease in fuel consumption of 30%. CDA can also improve the combustion stability of High Fuel Stratification Gasoline Compression Ignition at low loads [29].

Even though CDA is more beneficial for SI engines, it has some advantages for CI diesel engines too. Implementing this technology lowers fuel consumption at very low load [30]. The most significant benefit of CDA in CI engines is higher exhaust gas temperature for improved aftertreatment. Higher temperatures help the catalytic converter to increase its efficiency [31] and they also enable diesel particulate filter regeneration [32].

A completely different approach is cylinder activation. Cylinder activation can reduce the number of switching events as the deactivated mode is the main operating mode. For example, a four-cylinder engine should be converted into a three-cylinder engine in a four-cylinder crankcase [33]. The fourth cylinder is operated in parallel with one of the other cylinders. This cylinder is used only for stronger acceleration. The biggest problem is an unbalanced crankshaft. The BSFC improvement in the four-cylinder engine with a displacement of 1.4 l is 8.2% at 3 bar BMEP and an engine speed of 2000 rpm. According to the RDE drive cycle, the engine was operating 95% of the time in the three-cylinder mode.

6. COMPARISON

It is difficult to quantify the fuel economy benefit obtained by CDA in general. The results depend on the engine specification, used test drive cycle, type of CDA etc. **Chyba! Nenalezen zdroj odkazů.** summarises the fuel economy benefits of CDA for various implementations.

Engine specification	Ref.	Year	CDA type	Test cycle/ conditions	Fuel economy benefit
V8 6.2 l OHV VVT CR: 10.4 : 1 switchable roller tappet	[7]	2013	Rolling (DSF)	U.S. FTP HFET	Up to 21%, 14% with NVH supres.
V6 3.9 l OHV 2007 GM Impala Switchable roller tappet	[34]	2007	One bank deactivated (cylinders1, 3, 5)	EPA City	5.5%
				EPA Highway	7.5%
I4 1.8 l TSI VW Jetta	[35]	2019	Rolling (DSF)	US-City Highway	7.8%
				WLTP	6.4%
I4 1.6 l CR: 10.0 : 1	[36]	2005	Fixed, two cylinders deactivated	NEDC	10%
I4 1.6 l Direct injection Turbocharged Univalve	[23]	2013	Fixed, two cylinders deactivated	2000 rpm, 2 bar BMEP	18.5%
				2000 rpm, 3 bar BMEP	15%
I4 1,4 l TSI VW EA211 CR: 10.5 : 1	[37]	2018	Fixed, 1 cylinder deactivated (no valve deactivation)	25 different speeds and loads	1.23% (cumulative)
I4 1.4 l TSI Movable cam sections	[4]	2012	Fixed, two cylinders deactivated	NEDC	0.4 l/100 km (city traffic of up to 1 l/100 km)
I4 1,1 l motorcycle CR: 11.0 : 1 Switchable valve tappet	[20]	2010	Fixed, two cylinders deactivated (outer cylinders)	NEDC	24.7 % ECO 46.4 % (CDA when idling)
I3 1.0 l EcoBoost Ford Focus turbocharged Switchable roller finger follower	[38]	2016	Fixed, 1 cylinder deactivated	On-road commuter's test (near Cologne)	4%
			Rolling		6%
I3 1.0 l	[13]	2016	Fixed, 1 cylinder deactivated	NEDC	3.6%
				FTP-75	3.5%
				WLTC/ CADC	1% or less

Table 1: *Summary of fuel economy benefits for SI engines*

The fuel consumption reduction caused by CDA implies emission reduction, especially CO_2 emissions that rely mostly on the amount of burnt fuel. NO_x emissions are strongly dependent on combustion temperature, load and oxygen concentration. When the load is higher, the temperature rises and NO_x emissions increase. However, higher thermal efficiency helps reducing these emissions and the increase of NO_x emissions in the deactivation mode can be compensated by an enlarged EGR rate [22]. Higher concentration of NO_x can also be reduced by proper aftertreatment. The conversion efficiency of catalysts increases at higher temperatures which is an effect of CDA. Four-cylinder 1.6 l engine showed 28% reduction of NO_x emissions over NEDC [36].

CDA can significantly reduce CO emissions through improving thermal efficiency at low loads and complete combustion. Tests conducted on GM L94 V8 with displacement of 6.2 l with DSF showed that at BMEP lower than 1 bar, the reduction of CO emissions was approximately 60%. Higher thermal efficiency also led to 70% reduction of CO_2 emissions and significant decrease of unburned hydrocarbons at low loads [39]. Hydrocarbon emissions decrease with rising wall temperature, which is caused by higher combustion temperature. The analysis of four-cylinder SI engine with the deactivation of two cylinders has shown that CDA reduces CO emissions by as much as 8.5%, the NO_x emissions by nearly 10% and HC emissions by 8.7% [40].

7. CONCLUSION

Increasing environmental awareness and emission limitations forces car manufacturers to implement new emission-reduction technologies like CDA. Even though the idea is rather old, it was not widely used until the 2000s, because of reliability issues. This technology helps to decrease fuel consumption and emissions. However, CDA has some negative consequences too. The most significant ones are poorer NVH and higher frictional losses. Other consequences are higher engine oil combustion and an increase in temperature of the engine components. Some of these problems can be mitigated by using the dynamic method. CDA exhibits good synergy with other technologies, mostly due to broadening their operation zone. It is expected that modern engines will be produced with a combination of these technologies to reduce emissions and satisfy the required limits. However, this makes them more complex and more expensive.

REFERENCES

[1] ZHAO J, Xi Q, WANG S, WANG S. Improving the partial-load fuel economy of 4-cylinder SI engines by combining variable valve timing and cylinder-deactivation through double intake manifolds. Applied Thermal Engineering 2018;141:245–256.

[2] PETERS G. Cylinder deactivation on 4-cylinder engines: A torsional vibration analysis [thesis]. Eindhoven: Eindhoven University of Technology; 2007.

[3] YÜKSEK L, ÖZENER O, SANDALCI T. Cycle-skipping strategies for pumping loss reduction in spark ignition engines: An experimental approach. Energy Conversion and Management 2012;64:320–327.

[4] MIDDENDORF H, THEOBALD J, LANG L, HARTEL K. The 1.4-l TSI gasoline engine with cylinder deactivation. MTZ Worldwide 2012;73(3):4–9.

[5] LEONE T, POZAR M. Fuel economy benefit of cylinder deactivation - sensitivity to vehicle application and operating constraints. SAE Technical Paper 2001-01-3591; 2001.

[6] MUHAMAD SAID M, LATIFF Z, ZAINAL ABIDIN S, ZAHARI I. Investigation of intake valve strategy on the cylinder deactivation engine. Applied Mechanics and Materials 2016;819:459–465.

[7] WILCUTTS M, SWITKES J, SHOST M, TRIPATHI A. Design and benefits of dynamic skip fire strategies for cylinder deactivated engines. SAE International Journal of Engines 2013;6(1):278–288.

[8] MERY M. Explosive engine, United States patent 157 543. 1895 Jul 23.

[9] DUNNE J. Two-in-one engine. Popular Science 1977;210(1):70–72.

[10] INDRA F. Zylinderabschaltung für alle Hubkolbenmotoren? MTZ-Motortechnische Zeitschrift 2011;72(10):712–715.

[11] IHLEMANN A, NITZ N. Cylinder deactivation: A technology with a future or a niche application? 10th Schaeffler Symposium; 2014 3-4 Apr; Baden-Baden, Germany. Schaeffler Technologies AG & Co. KG; 2014. 172–187.

[12] FAUST H, SCHEIDT M. Potentials and constraints of cylinder deactivation in the powertrain. MTZ Worldwide 2016;77(6):72–77.

[13] BECH A, SHAYLER P, MCGHEE M. The effects of cylinder deactivation on the thermal behaviour and performance of a three-cylinder spark-ignition engine. SAE International Journal of Engines 2016;9(4):1999–2009.

[14] MORRIS N, MOHAMMADPOUR M, RAHMANI R, JOHNS-RAHNEJAT P, RAHNEJAT H, DOWSON D. Effect of cylinder deactivation on tribological performance of piston compression ring and connecting rod bearing. Tribology International 2018;120:243–254.

[15] SHAHMOHAMADI H, RAHMANI R, RAHNEJAT H, GARNER C, DOWSON D. Big end bearing losses with thermal cavitation flow under cylinder deactivation. Tribology Letters 2015;57(1):1–17.

[16] VIJAYAKUMAR R, AKEHURST S, LIU Z, REYES-BELMONTE M, BRACE C, LIU D, COPELAND C. Design and testing a bespoke cylinder-head pulsating-flow generator for a turbocharger gas stand. Energy 2019;189:116291.

[17] MA Z. Oil transport analysis of a cylinder deactivation engine. SAE Technical Paper 2010-01-1098; 2010.

[18] BAYKARA C, AKIN KUTLAR O, DOGRU B, ARSLAN H. Skip cycle method with a valve-control mechanism for spark ignition engines. Energy Conversion and Management 2017;146:134–146.

[19] RADULESCU A, ROBERTS L, YANKOVIC E. Durability and reliability demonstration for switching roller finger follower in cylinder deactivation systems. SAE Technical Paper 2015-01-2816; 2015.

[20] MAEHARA H, KITAWAKI S, ABE T, SAITO S, TSUKUI T. Development of variable cylinder management system for large motorcycles - An effective way of reducing output change at switching of the number of working cylinders. SAE Technical Paper 2010-32-0117; 2010.

[21] FALKOWSKI A, MCELWEE M, BONNE M. Design and development of the DaimlerChrysler 5.7L HEMI® engine multi-displacement cylinder deactivation system. SAE Technical Paper 2004-01-2106; 2004.

[22] KREUTER P, HEUSER P, REINICKE-MURMANN J, ERZ R, STEIN P, PETER U. Meta - CVD System: An electro-mechanical cylinder and valve deactivation system. SAE Technical Paper 2001-01-0240; 2001.

[23] FLIERL R, LAUER F. Mechanically fully variable valve-train and cylinder deactivation. MTZ Worldwide 2013;74(4):50–57.

[24] FIORENZA R, PIRELLI M, TORELLA E, PALLOTTI P, KAPUS P E, KOKALJ G, LEBENBAUER M. VVT port deactivation application on a small displacement SI 4 cylinder 16V engine: An effective way to reduce vehicle fuel consumption. SAE Technical Paper 2003-01-0020; 2003.

[25] ORTIZ-SOTO E, WANG R, NAGASHIMA M, YOUNKINS M, MÜLLER A, TEWS S, BALAZS A, THEWES M. λDSF: Dynamic skip fire with homogeneous lean burn for improved fuel consumption, emissions and drivability. SAE Technical Paper 2018-01-0891; 2018.

[26] WILCUTTS M, NAGASHIMA M, EISAZADEH-FAR K, YOUNKINS M, CONFER K. Electrified Dynamic Skip Fire (eDSF): Design and Benefits. SAE Technical Paper 2018-01-0864; 2018.

[27] ORTIZ-SOTO E, YOUNKINS M. Advanced cylinder deactivation with Miller cycle. MTZ Worldwide 2019;80(5):58–63.

[28] BORETTI A, SCALCO J. Piston and valve deactivation for improved part load performances of internal combustion engines. SAE Technical Paper 2011-01-0368; 2011.

[29] BABU A, KOKJOHN S. Cylinder deactivation strategies to stabilize high stratification gasoline compression ignition down to idle. SAE Interantional Journal of Engines 2021;14(4):1-25.

[30] PILLAI S, LORUSSO J, VAN BENSCHOTEN M. Analytical and experimental evaluation of cylinder deactivation on a diesel engine. SAE Technical Paper 2015-01-2809; 2015.

[31] BASARAN H, OZSOYSAL O. Effects of application of variable valve timing on the exhaust-gas-temperature improvement in a low-loaded diesel engine. Applied Thermal Engineering 2017;122:758–767.

[32] LU X, DING C, RAMESH A, SHAVER G, HOLLOWAY E, MCCARTHY J, RUTH M, KOEBERLEIN E, NIELSEN D. Impact of cylinder deactivation on active diesel particulate filter regeneration at highway cruise conditions. Frontiers in Mechanical Engineering 2015;1:9.

[33] SCHURR A, GUENTHNER M, FLIERL R, WOIKE D, MUELLER F. Investigation of a cylinder activation concept for a turbocharged direct-injection gasoline engine. SAE Technical Paper 2018-01-1713; 2018.

[34] STABINSKY M, ALBERTSON W, TUTTLE J, KEHR D, WESTBROOK J, KARBSTEIN H, KUHL M. Active Fuel Management™ technology: Hardware development on a 2007 GM 3.9L V-6 OHV SI engine. SAE Technical Paper 2007-01-1292; 2007.

[35] WILCUTTS M, SCHIFFGENS H, YOUNKINS M. CO2 reduction with dynamic cylinder deactivation. MTZ Worldwide 2019;80(4):20–27.

[36] DOUGLAS K, MILOVANOVIC N, TURNER J, BLUNDELL D. Fuel Economy Improvement Using Combined CAI and Cylinder Deactivation (CDA) - An Initial Study. SAE Technical Paper 2005-01-0110; 2005.

[37] KOUBA A, HNILICKA B, NAVRATIL J. Downsized gasoline engine cylinder deactivation MiL development and validation using real-time 1-D gas code. SAE Technical Paper 2018-01-1244; 2018.

[38] KÜPPER K, LINSEL J, PINGEN B, WEBER C. Cylinder deactivation for three-cylinder engines. MTZ Worldwide 2016;77(12):46–51.

[39] EISAZADEH-FAR K, YOUNKINS M. Fuel economy gains through Dynamic-Skip-Fire in spark ignition engines. SAE Technical Paper 2016-01-0672; 2016.

[40] TURNBULL R, DOLATABADI N, RAHMANI R, RAHNEJAT H. Energy loss and emissions of engine compression rings with cylinder deactivation. Proceedings of the Institution of Mechanical Engineers, Part D: Journal of Automobile Engineering; 2021. 1-14.

ACKNOWLEDGEMENT

The authors gratefully acknowledge the funding from the Specific research on BUT FSI-S-20-6267.

52. MEZINÁRODNÍ VĚDECKÁ KONFERENCE ČESKÝCH A SLOVENSKÝCH UNIVERZIT A INSTITUCÍ ZAMĚŘENÁ NA VÝZKUMNÉ A VÝUKOVÉ METODY SPOJENÉ SE SPALOVACÍMI MOTORY, ALTERNATIVNÍMI POHONY A DOPRAVOU

22.-23. ZÁŘÍ 2021, PRAHA
ČESKÁ ZEMĚDĚLSKÁ UNIVERZITA V PRAZE, TECHNICKÁ FAKULTA,
KATEDRA VOZIDEL A POZEMNÍ DOPRAVY

THE ROLE OF AUTOMOTIVE THERMAL MANAGEMENT ON THE PATH TO CARBON NEUTRALITY

Guillaume HÉBERT[1]

Abstract
Transportation, and specifically personal transportation, accounts for a large extend of the European Union CO2 emission balance. Two extreme different approaches are competing to reduce it: larger electrification of the transport means and improvement of Internal Combustion Engines (ICE). Both technologies have to be investigated holistically, including the effect on energy infrastructure and both present or future advantages and disadvantages. The author will further discuss the role of thermal management, both powertrain and cabin, as a key enabler for future progress on energy consumption of passenger vehicles. Some specific examples will be quoted to illustrate the discussion.

1. INTRODUCTION

Fight against Climate Change is probably one of the most significant challenge seen by the industry at present time. It is taken as granted that a positive correlation between anthopogenic Green House Gases (GHG) emissions and average atmospheric temperature exists [1]. As transportation in general, and road transportation specifically, represents an important share of global GHG emissions (Fig.1), the goal fixed by the Paris Agreement to limit average atmospheric temperature rise below 2°C as compared to pre-industrial times, leads therefore to some necessary adaption in the transportation sector. In the rest of this article we will focus on road transportation and, more specifically, on Light Duty Vehicles (LDV), sometimes also called Passengers Vehicles (PV).

[1] Guillaume HÉBERT, Hanon Systems, Závodní 1007, 687 25 HLUK, Czech Republic, ghebert4@hanonsystems.com

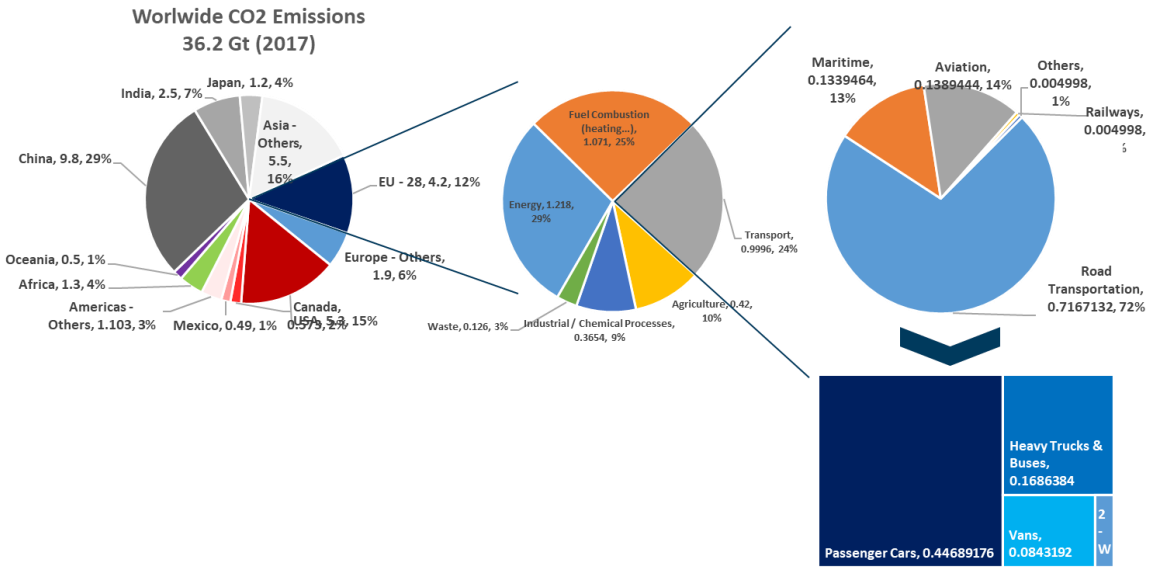

Figure 1: *Distribution of GHG Emissions in 2017*[2]

If Paris Agreement goal has to be linearily transfered to each aspect of human activities, then it means that we need to reduce LDV vehicles GHG emissions by, at least, 5% every year until 2050. The problematics is not new and there were already multiple attempts to reduce these emissions, by means of technology and / or legislation. Therefore, one may find interesting to look at backward data and understand what the industry as a whole was able to achieve by now (Fig.2 & 3),

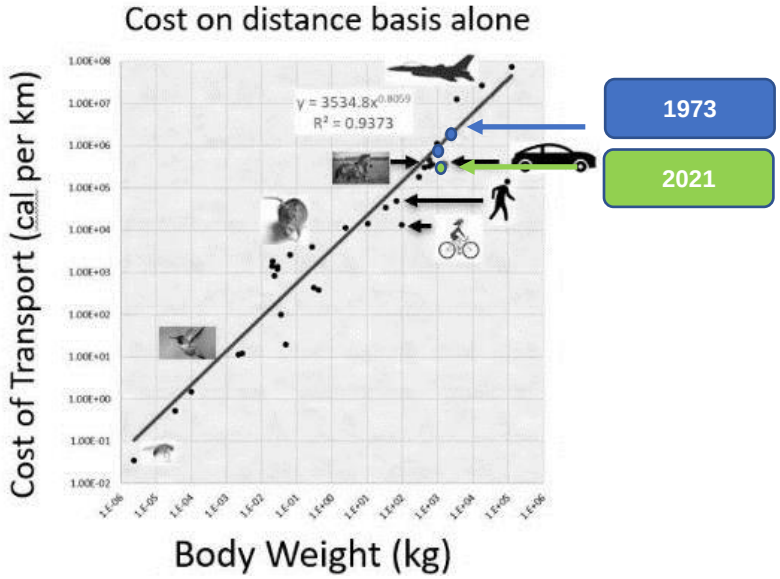

Figure 2: *Energy Cost of Transportation per Distance* [2].

[2] Data source: https://ec.europa.eu/eurostat/cache/infographs/energy/bloc-4a.html. Graphics: G.HEBERT

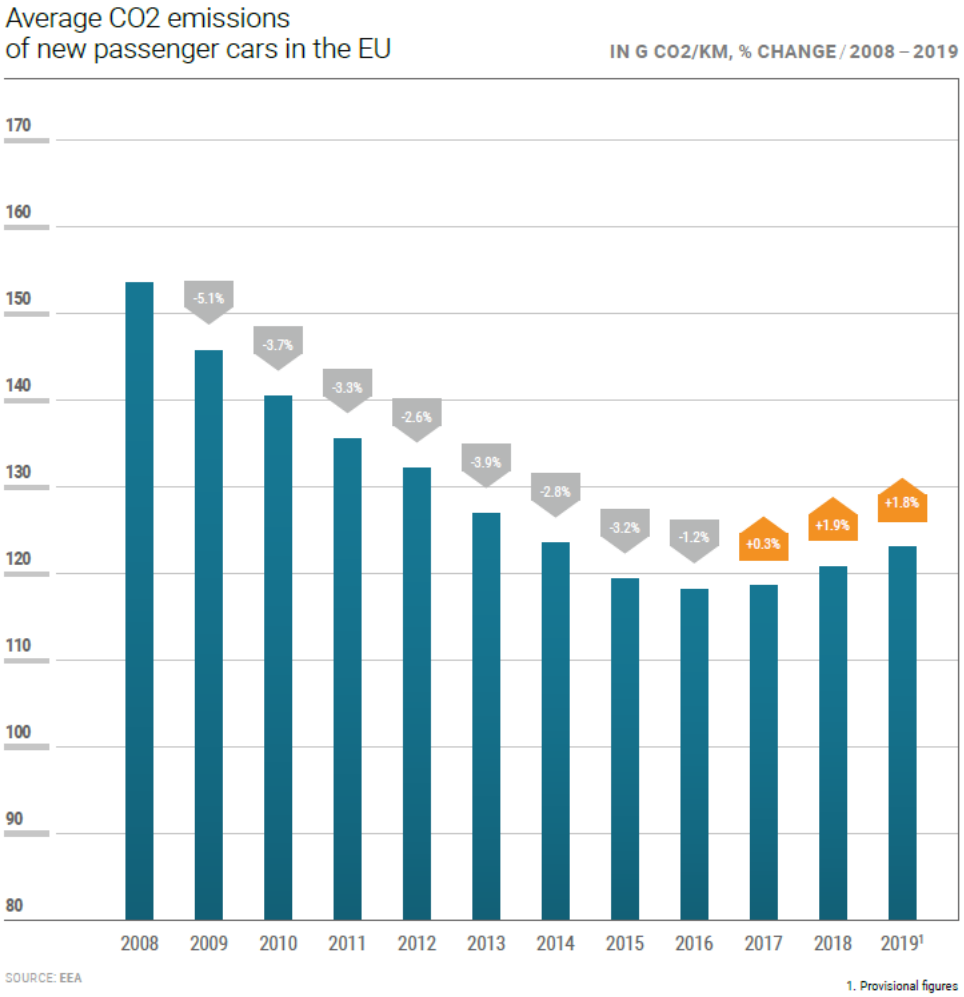

Figure 3: *Average CO2 Emissions of New Passenger Cars in the EU* [3].

From Fig. 2, it can be seen that cars have clearly become more efficient, reaching today the same energy consumption level as horse transportation! However, as shown in Fig.3, the progress has slow-down and even reversed since a couple of years due to mainly more sales in gasoline engines (which are still less efficient than diesel powertrains they replaced), increase weight of new sold vehicles, deterioration of aerodynamics linked to the success of SUV and bigger car architectures.

To better understand which levers can be activated to further reduce GHG emissions, one may find interesting to express those as proposed by the Japanese economist Yoichi Kaja [4] (1):

$$Carbon\ Emissions = \frac{Carbon\ Emissions}{Energy\ Consumption} * \frac{Energy\ Consumption}{Gross\ Domestic\ Product} * \frac{Gross\ Domestic\ Product}{Total\ Population} * Total\ Population \quad (1)$$

From an engineering perspective, we can focus on the first two ratios. Translated to the use case of car, the first ratio represents fuels and energy carrier carbon intensity. The second ratio is then related to vehicles energy efficiency. In the rest of this article,

we will focus on ways to improve the second ratio, specifically speaking of powertrain efficiency and energy needed to ensure passengers comfort.

2. ENERGY USAGE OPTIMIZATION THROUGH ADVANCED THERMAL MANAGEMENT

Most of GHG emissions of cars can be correlated to its energy consumption. In a conventional powertrain, a significant part of the energy consummed is being released to the atmosphere as heat, due to the relatively low efficiency of the energy transformation proces from chemical carrier (fuels) to mechanical work. On the other hand, alternative powertrain like Battery Electric Vehicles (BEV) often suffer of lack of thermal energy and require incremental energy (electricity) consumption to fulfill basic functions as cabin heating for example. Fig.4 shows an overal summary of the need for heating and cooling of various car sub-systems.

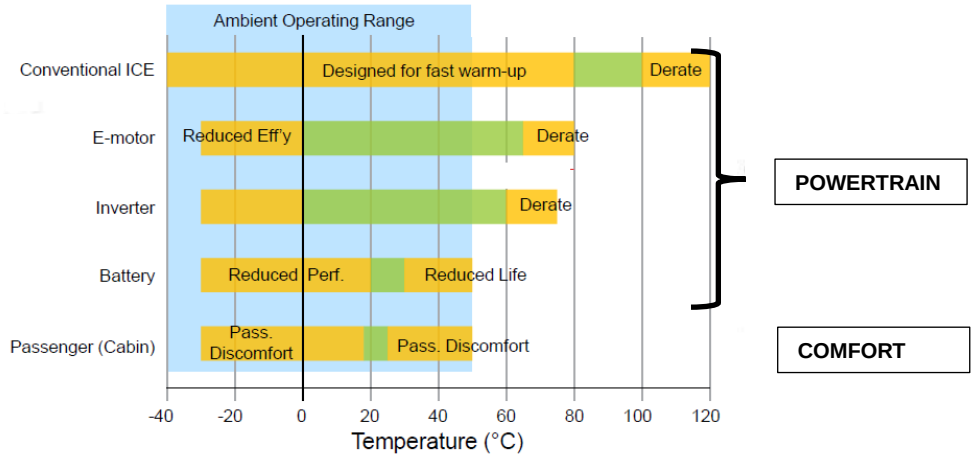

Figure 4: *Temperature Operational Range of Vehicles Sub-Systems* [5].

It appears that the most critical items can be grouped in two categories, powertrain and comfort, and both need to be addressed.

2.1 POWERTRAIN

2.1.1 Internal Combustion Engines (ICEs)

Despite recent „hype“ to alternative powertrains, ICEs are still the predominant powertrain and will still be present in most markets for upcoming decades. It is therefore fundamental to continue improving them toward better Brake Thermal Efficiency (BTE). On Fig.5, the maximum thermal efficiecny of available modern gasoline engines is displayed as function of the engine specific power. 40% maximum BTE is now getting achievable and further advanced studies tend to show that 50% can be achieved with full map λ=1 combustion (stoichiometric engine) [7] & [8].

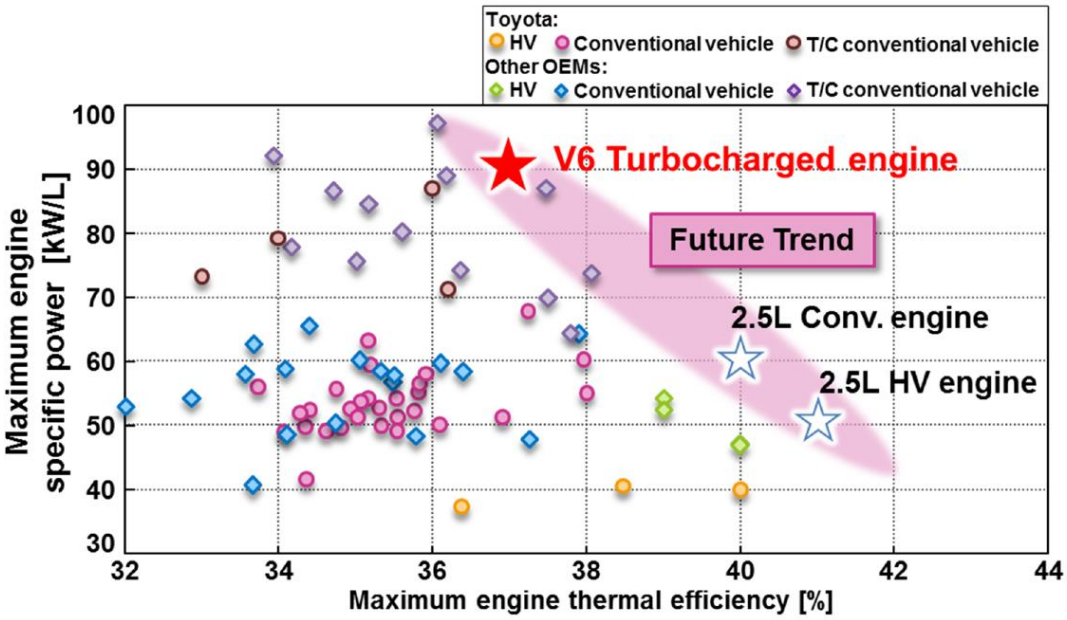

Figure 5: *Temperature Operational Range of Vehicles Sub-Systems* [6].

What these efforts have in common is, among others, the use of advanced thermal systems, as:

- Increase Compression Ratio (CR). Dilution of the gas mix in the combustion chamber is necessary to avoid knock; that can be achieved by various means out of which higher rate of Exhaust Gas Recirculation [9] and Water Havesting / Injection involved advanced thermal systems [10]. The effect on overal fuel consumption for various driving cycle can be seen on Fig. 6.
- Usage of exhaust waste heat, as an immediate heating source or with time dephasing through storage [11].
- Drag Reduction linked to reduction of Front End Cooling Module area. This can be achieved by adopting a higher nominal cooling liquid temperature [12], and peak heat accumulation. It can be noticed that this will have a secondary effect of limiting internal engine friction, as per the „no-flow strategy“ described by Dr. Johann Himmelsbach.

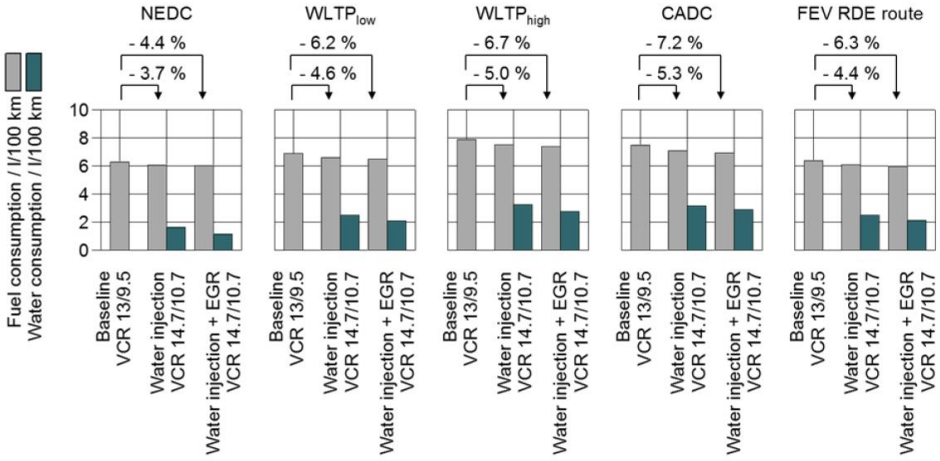

Figure 6: Fuel consumption benefits of EGR and WI for various drive cycles [13].

On top of optimizing the ICE itself, hybridation can enable to make a better use of the engine, as described in Fig. 7, by cancelling the need of engine run at area of the map which are far from the optimal, e.g. low load.

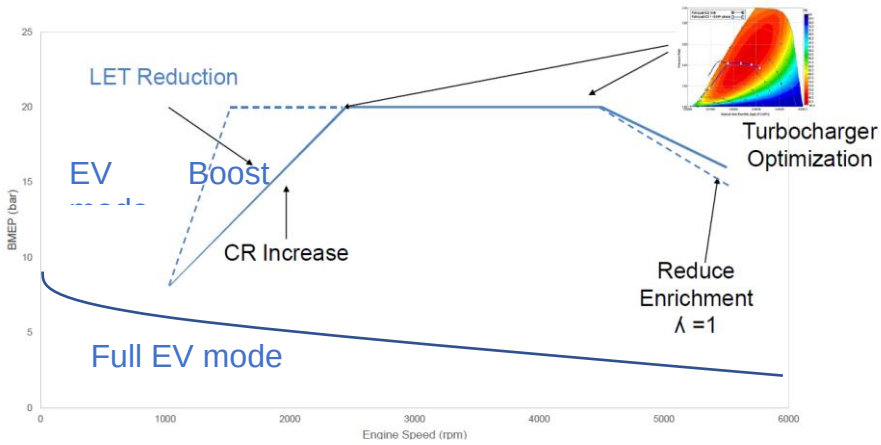

Figure 7: *Operating Strategies for Hybridation*[3]

When considering hybrids, thermal systems as heat recovery and storage can also help faster achieving the cooling liquid temperature threshold and therefore enabling longer and more often pure electric drives.

2.1.1 Battery Electric Vehicles (BEVs)

As far as BEV are concerned, the main powertrain thermal challenge remains battery thermal management, as described in Fig. 8. When lowered temperature can prevent

[3] Adapted by Guillaume HEBERT from Graham CONWAY, SwRI, April 2021

a full capacity charging, higher temperature creates safety issues, e.g. thermal runaways.

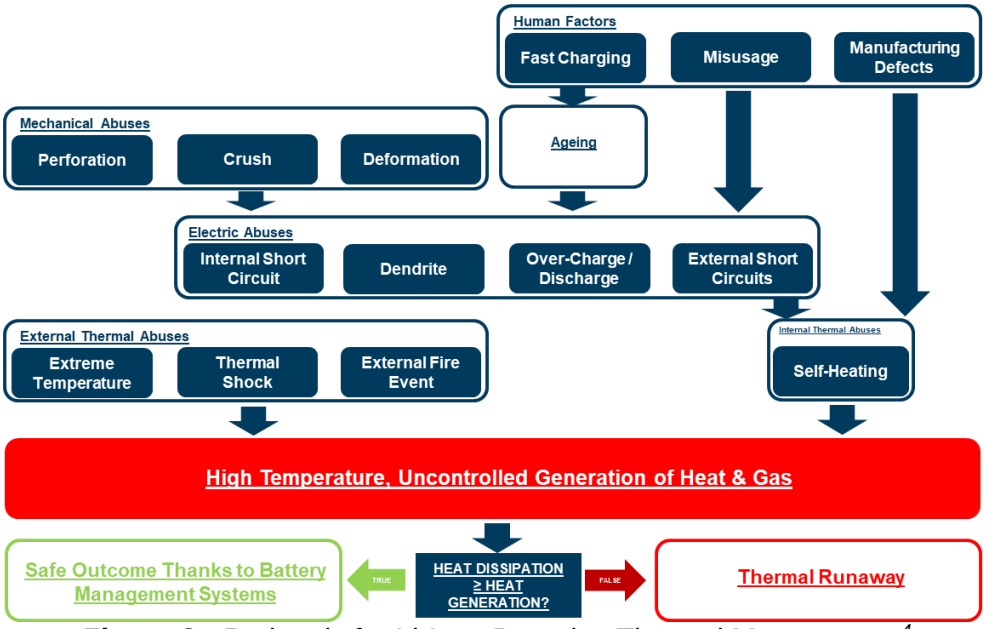

Figure 8: *Rationals for Li-Ions Batteries Thermal Management*[4]

Several concepts for battery thermal management are known and have been implemented on various BEVs, for the so-called „Li-ion“ batteries currently in production:

- Air cooling. This is the easiest and most cost effective solution but presents limited heat dissipation, especially at no / low-speed, if no blower is used (i.e. passive air cooling). It can be found on either low performance BEV (e.g. Nissan Leaf) or hybrid vehicles (e.g. Toyota Prius).
- Refrigerant cooling. In this case the caloriferic medium is refrigerant which flows through a bundle of extruded tubes in contact with the batteries. This is a system which was widespread by car maker as BMW. On top of adding some heat in the Air Conditioning (AC) loop it also presents significant hurdle in terms of heating at low temperature, which requires direct resistance electric heating and therefore negatively impacts the BEV range.
- Liquid cooling / cold plate is the most widespread system available in various shapes from cold plates (e.g. VW ID3) ort he so-called „cooling snake“ from Tesla. Despite the fact that moving to higher voltage charging system can help to reduce current (and therefore dissipated heat), the main hurdle comes from limited capacity to absorb peak heat, up to 12 kW, during fast charging.
- Therefore, immersion / di-electric cooling is seen as a promising technology to garantee a narrow range of temperature even for the most demanding use cases. There are various technical principles (e.g. 1 or 2 phases pumped, spray, pool boiling or vapor chambre, gap filler, static bath) which involve oil or fluorinated liquids. Applications out of automotive are known for transformaters

[4] Adapted by Guillaume HEBERT from Cecile PERA, OROVEL, 2021

or fighter aircraft radars for example but can also be seen in Formula 1 or Hypercar BEVs, e.g. RIMAC, McLaren. Out of the benefits, a faster charging time can be achieved, higher power/energy ratio, increased safety (no fire propagation possible as heat can be easily dissipated cancelling the need for charging power limitation), compatibility all cells shape factors and longer battery life time due to narower temperature range being kept [14].

2.2 COMFORT

Comfort function, i.e. cabin tempering in attempt to meet passenger termperature expectations, is now one of the most limiting factors in term of energy usage optimization, for both cold and hot conditions (see Fig. 9).

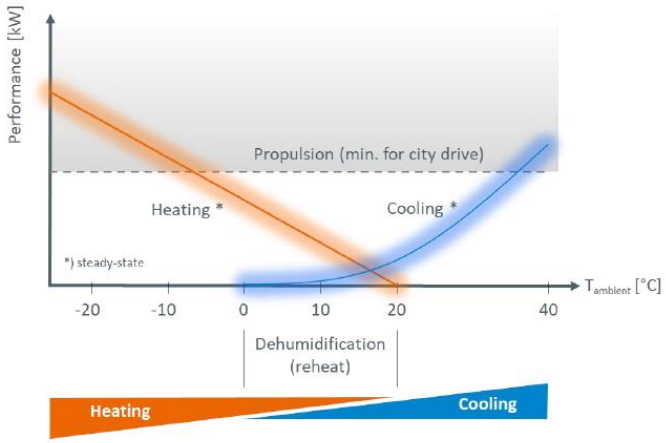

Figure 9: *Required Heating and Cooling Performance* [15]

In case of an ICE equipped vehicle, including hybrids, the cold condition heating can be in most cases ignored, except at start, because of the excess of heat energy provided by the combustion process. Cold starts are generally handled through Positive Temperature Coefficient heaters (PTC), sometimes suppleting by various systems as supplemnetal fuel burner or Exhaust Heat Recovery Systems (EHRS) [11]. However, this is not possible with BEV, where heating / cooling and necessary calorific fluid movement consume electricity, i.e. have a direct negative impact on the range of the vehicles as displaid on Fig. 10.

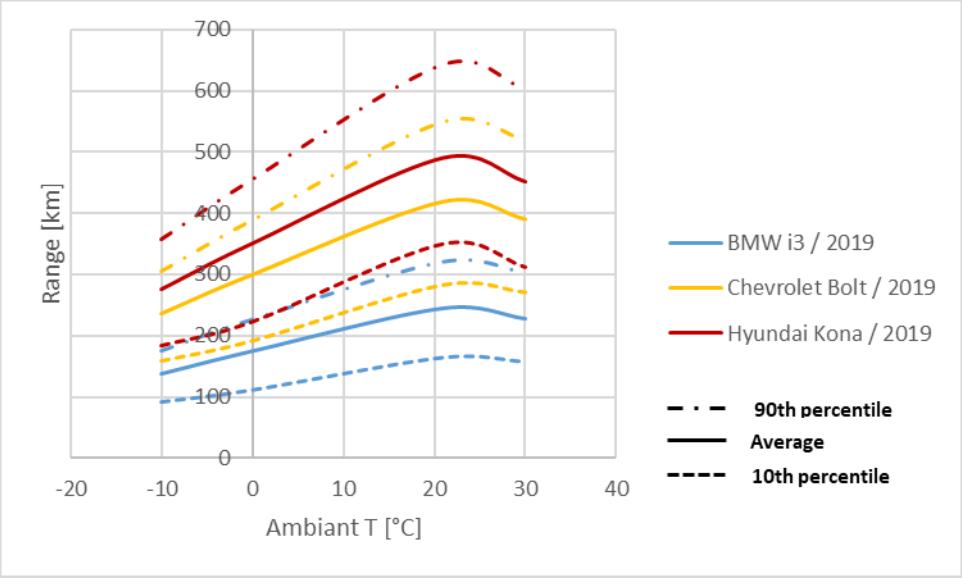

Figure 10: *Variation of Various BEV Range as a Function of Ambiant Temperature*[5]

Different thermal management technologies can there being used to reduce the impact. The most common approach will be usage of Heat Pump (HP) which efficiency can be optimized by moving from regular R1234yf refigerant to R744 (CO2) or R290 (Propane). However, usage of those alternative refrigerant is not neutral for the thermal management system:

- CO2 requires to work at higher pressure, which means that every single component needs to be re-designed and comes with extra cost.
- Propane, on the other hand, is having a higher flammability, which is problematic in a close environment cf civil engineering where the unit can be positioned on the roof, i.e. propane diluted under the lower flammability limit in case of leak. This can be walked around by limiting the charge in the system, i.e. the amount of refrigerant. One way of achieving it is to reduce the overal size of the circuit by bringing all component into a compact unit. The refrigerant to ambiant Heat Exhanger (HEX), i.e. condenser, is then replaced by a water cooled one, the electric compressor, as well as the evaporator are closely assembled leading to a significant reduction of the Fluid Transport (FT) lines enabling the charge reduction at iso system performance. It has to be noticed that this approach is also very convenient for OEMs as it offers a full AC/HP as a „black box“, with only electric and cooling liquid interface, limiting the problems of refrigerant fittings and leakage.

Looking at standard cabin heating system architecture, one can assess that this is not really optimized to minimize the energy consumption. Especially in mid-cold condition, ambiant air needs to be dehumidified before being blown which results in first cooling air down to force water content to condensate and then heating it to target temperature. In parallel the air in the cabin, which is already tempered, is being extracted in order to

[5] Guillaume HEBERT, 2021, data https://www.geotab.com/blog/ev-range/

limit the concentration of pollutants and water vapour in the cabin. A walk around solution could be in to increase the recirculation rate, which can be achieved by adding different filtering and dehumidification systems into the Heating Ventilation & Air Conditioning system (HVAC). Nowadays, in time of pandemics, one can also think of adding various UV and ionizer units to decontaminate the cabin air. It can be seen in Fig.11 that an extreme recirculation approach combined with an HP circuit can significantly improve the drive range of BEV, i.e. the energy consumption.

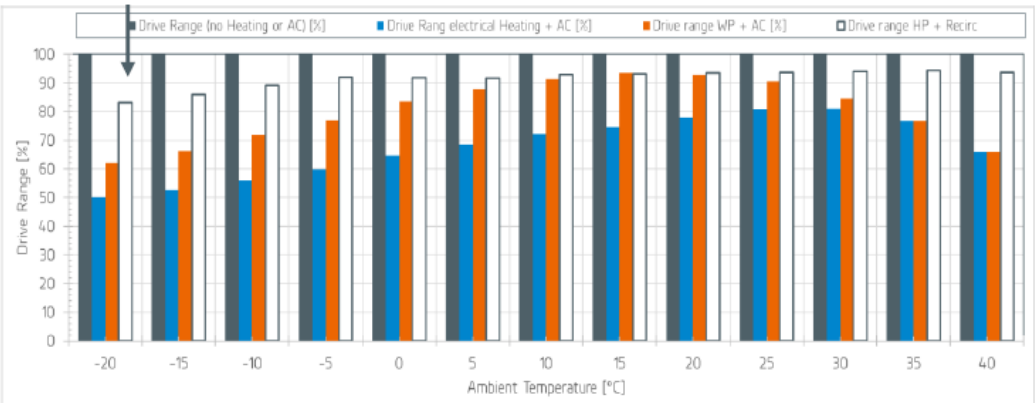

Figure 11: *Heat Pump & Recirculated Air Effect on BEV Range* [15]

Analysis of customer usage shows that in most of the cases, the mean number of passengers in the car is limited [16]. The rational of heating the full cabin volume (e.g. up to 4 m^3 for a MPV) is therefore questionable. Alternatives can be local heating / cooling system targeting the most impacting body parts of the passengers to provide a „feeling“ of comfort, as shown in Fig. 12. Among those systems are e.g. steering wheel heating, seat heating and cooling, radiative surfaces, heat absorbing materials.

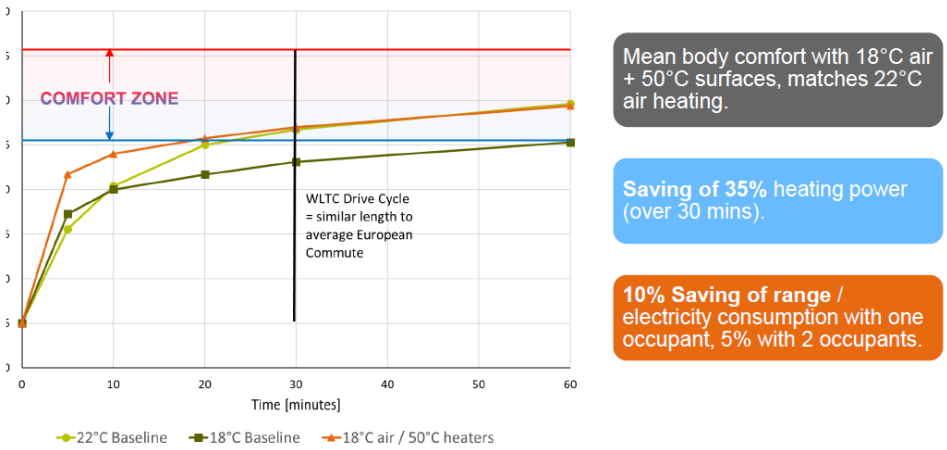

Figure 12: *Improved Comfort and Reduced Energy through Heated Surfaces*[6]

[6] Source : Autoneum. https://www.autoneum.com/innovation/research-and-development/

Very recent material research has even demonstrated the theoretical possibility to transform the cabin heat wave length to mid infrared spectrum, for which the atmosphere is prooven not being absorptive. At the end of the day, that could provide a „cabin to space“ HEX, taking advantage of the higher temperature difference possible, providing an economical solution for supplemental cabin cooling during hot days [17].

2.3 ELECTRIFICATION OF ACCESSORIES

A category which should not ignored to optimize the overal energy consumption is composed of accessories, e.g. coolant pumps & valves, Electronic Refrigerant Valves (ERV). With the increasing trend for electrification, these accessories are also being electrified. It is difficult to seggregate them between powertrain and comfort related, as the different loop are nowadays often connected as it can be seen on Fig. 13.

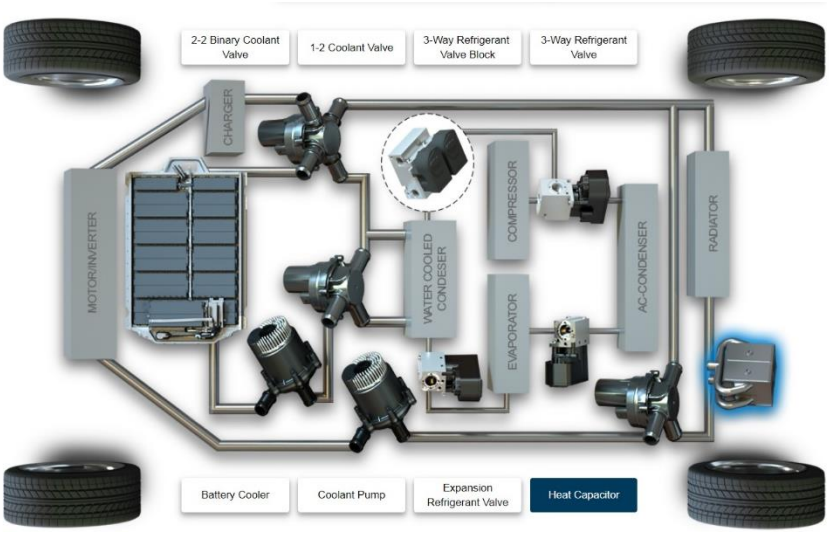

Figure 13: *BEV Thermal Management System Lay-Out*

All these mechatronics devices need to be optimized to limit their energy consumption Compared to previous system generation (e.g. mechanical pump, more simple coolant valve), it comes with more precise temperature control and provide energy on demand. The energy savings may not seem at first glance significant [18], but this is part of a „snow-ball effect“: every minor contribution enables better energy optimization of the whole systém and can drive to further savings, leading to overal remarkable results.
Fig. 14 displays an example of saving achievable when switching from a standard electric coolant pump to a dual mode one, i.e. size for lower power output but capable of peak higher power for limited period of time.

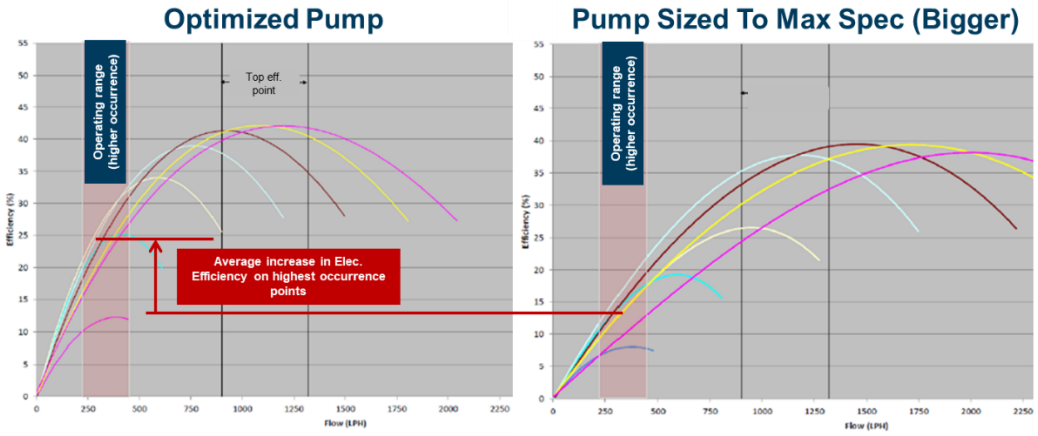

Figure 14: *Pump Size Efficiency Effect* [19]

As far as coolant valves are concerned the two main trends are the usage of efficent Brush-Less Direct Current (BLDC) motors and multi-wet sides architecture, i.e. changing from simple on / off valves to variable flow, multi-directional and multi-coolant circuits. It can be noticed that the different architectures can be obtained by just adapting the „wet side“ on standardized „dry-side“, therefore limiting the development and validation required for each application as well as simplyfying the control interfaces. The refrigerant valves can follow the same approaches. This results in simplification of the circuit (thanks to combination of functions, one unit can then replaced different products, e.g. 1 refrigerant valve = Shut-Off Valve –SOV- + Expansion Valve –EXV-), reduction of the electric consumption. Compare to a standard valve actuated with solenoid, the energy consumption is reduced by 99,5% as the holding current is 0. This second effect (reduced energy consumption) is amplified by the first one (reduction of the amount of components), as described in the example from Fig. 15.

	Traditional Configuration	Hanon Systems
System	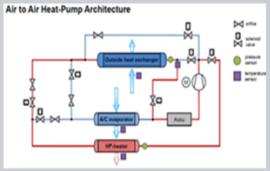	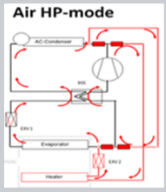
shut-off Valves	7 x E-Sol. Valves	4 x ERV
Expansion Valves	4 x Orifice	2 x ERV
Average electric Consumption	(7+4) * solenoid conso = 100%	(4+2) * BLDC conso = 0,3%

ERV vs. Orifice / solenoid is providing maximum degree of freedom:
- **Position Control and regulation accuracy**
- **System design and setup under all conditions**
- **Reduce Valve amount from 11 to 6**

Figure 15: *Example of System Optimization (HP) through Upgraded Components* [19]

3. CONCLUSION

At the end of the day, both powertrain and comfort thermal management is at the heart of the further automotive energy optimization, therefore a „must“ step toward a real Life Cycle Analysis (LCA) „Net Zero“ carbon footprint in this sector. Current transformation, including fairly quick outphasing of ICE in Europe, is being underlied with 5 key customer drivers, all of them are highly impacted by thermal management:

- How to provide current level of comfort function at the minimal energy cost
- BEV acceptance will be linked to their „user friendliship” : limit energy consumption through aerodynamics improvements via advanced cooling system may helps fight the „range anxiety” by limiting the charging frequency
- Autonomous driving, when it will come, will bring additional sensors and components (e.g. radar, LIDAR, cameras...) to be thermally managed. This additional power to be dissipated can be estimated in the range of 10-12 kW
- Cars haring is most likely to change durability expectation, as the vehicles will be considered as investments and the avoidance of parking costs may lead to run the cars almost 24/7. Then it can be expected that the usefull lifetime of a LDV, today considered being 250 000 km, may raise to the level for Heavy Duty Vehicle, i.e. 1 200 000 km. This will also apply to thermal management components
- Finally, transition to new vehicles can only be sucessful is they remain affordable, which is still a challenge for BEV regarding tot the total cost of Li-Ion batteries. Efficient thermal management, when optimizing the energy consumption, can significantly helps reducing the amount of batteries needed to support a given mission profile.

REFERENCES

[1] STOCKER, T.F. *et al*. IPCC, 2013: Climate Change 2013: The Physical Science Basis. Contribution of Working Group I to the Fifth Assessment Report of the Intergovernmental Panel on Climate Change, Cambridge University Press, 2013, p. 28 ISBN 978-1-107-05799-1

[2] JOSHI A., Cost of transportation on Distance Basis, on LinkedIn, 2021

[3] The Automobile industry Pocket Guide, ACEA (European Automobile Manufacturers Association), 2021, p. 65. https://www.acea.auto/publication/automobile-industry-pocket-guide-2020-2021/

[4] KAYA Y., KEJICHI Y. Environment, energy, and economy : strategies for sustainability *in* Tokyo conference on Global Environment, Energy and Economic Development, United Nations Univ. Press, 1997, 381 p. ISBN 92-808-0911-3

[5] ROUAUD C., Battery cooling, energy optimisation through advanced control methods *in proceedings* 2nd Annual Automotive Thermal Management Conference, BCF group, 2019, p. 4

[6] MORI, A. *et al*., The New Toyota V6 3.5L Turbocharged Gasoline Engine *in proceedings* 26th Aachen Colloquium, ika & vka RWTH AACHEN UNIVERSITY, 2017, pp. 895-920, ISBN 978-3-00-054182-7

[7] CONWAY, G. *et al*., Achieving 50% BTE at Lamba 1, Southwest research Institute, 2021
[8] Nissan's next generation e-POWER technology update, Nissan, 2021, https://global.nissannews.com/en/releases/210226-01-e
[9] Alger, T. and Mangold, B., "Dedicated EGR: A New Concept in High Efficiency Engines," SAE Int. J. Engines 2(1):620-631, 2009, https://doi.org/10.4271/2009-01-0694.
[10] HEBERT, G. *et al*., Exhaust Gas Condensate as an Enabler for Self-Contained Water Injection Systems *in proceedings* 28th Aachen Colloquium, ika & vka RWTH AACHEN UNIVERSITY, 2019, pp. 1080-1101, ISBN 978-3-00-060311-2
[11] HEBERT, G., Waste Heat Recovery *in proceedings* 5th International Conference Diesel Powertrains 3.0, FEV, 2019, pp. 64-67,
[12] WILL F. *et al.*, OVER8™ - Affordable thermal management innovations to achieve the 2020 fuel consumption limits in China, *in proceedings* 39. Internationales Wiener Motorensymposium, 2018
[13] THEWES, M.; BAUMGARTEN, H.; SCHARF, J.; BIRMES, G.; BALAZS, A. et. alt., 2016 Water Injection - High Power and High Efficiency combined in: 25. Aachener Kolloquium Fahrzeug- und Motorentechnik
[14] Webinar on Immersion Cooling, company EXOES & Dr. Cecile PERA, 2021
[15] GRAAF, M., Recirculation in Cold Climate: Challenges & Opportunities *in proceedings* 2nd Annual Automotive Thermal Management Conference, BCF group, 2019, p. 8
[16] ALONSO-MORA *et al.*, On-demand high-capacity ride-sharing via dynamic trip-vehicle assignment. Proceedings of the National Academy of Sciences. 114. 201611675. 10.1073/pnas.1611675114
[17] Karl Joulain, Refet Ali Yalçin, Jérémie Drévillon, Etienne Blandre. Refroidissement radiatif diurne par revêtement de fibres de silice. Photoniques, EDP Sciences, 2020, pp.28-31. 10.1051/photon/202010528. hal-03083238
[18] BATTEH J., RAVI A.K., PICKELMAN D., Diesel Cooling System Modeling for Electrification Potential, 2018
[19] CROWTHER D., HEBERT G., Optimization of Electric Vehicle Thermal Management System Through Mechatronics Components *in*: proceedings of MMT Tech Days, 2018

THANKS

This article has been developed on the basis of a guess lecture provided by an author at Brno Technical University (VUT v Brně) in March-June 2021 thanks to the support of Prof. Ing. Josef ŠTĚTINA, Ph.D. (director of ÚADI institute) and Ing. Pavel RAMÍK (assistant lecturer ÚADI institute).

52. MEZINÁRODNÍ VĚDECKÁ KONFERENCE ČESKÝCH A SLOVENSKÝCH UNIVERZIT A INSTITUCÍ ZAMĚŘENÁ NA VÝZKUMNÉ A VÝUKOVÉ METODY SPOJENÉ SE SPALOVACÍMI MOTORY, ALTERNATIVNÍMI POHONY A DOPRAVOU

22.-23. ZÁŘÍ 2021, PRAHA
ČESKÁ ZEMĚDĚLSKÁ UNIVERZITA V PRAZE, TECHNICKÁ FAKULTA,
KATEDRA VOZIDEL A POZEMNÍ DOPRAVY

COMPARISON OF 12 V NETWORK POWER SUPPLY STRATEGIES IN A CONVENTIONAL VEHICLE AND THE EFFECT ON FUEL CONSUMPTION

Jolana Heřmanová[1], Rastislav Toman[2]

Abstract
The main purpose of 12 V onboard electric network is to power several key vehicle systems and number of other onboard consumers. For this purpose, the Internal Combustion Engine Vehicles (ICEVs) are equipped with an alternator and a 12 V battery. As the number of vehicle systems and control units in vehicle is increasing and the start-stop system is widely implemented, much higher demands are placed on the alternator and 12 V battery. With stricter limits on CO_2 emissions, it is necessary to focus on the 12 V network power supply strategy. The aim of this work is to compare several approaches to powering the onboard network. The first variant is a strategy of maintaining a constant voltage of the 12 V battery. The second variant distinguishes several voltage targets for different driving modes based on the actual SOC, Internal Combustion Engine (ICE) speed and actual required power necessary to drive the vehicle. For this purpose, a 1D simulation model of a conventional car was built in the SW GT-Suite, charging strategies were implemented and the effects on fuel consumption were compared.

1. INTRODUCTION

The pressure on the automotive industry has led the car manufacturers to search for any possible ways to lower their fleet fuel consumption, i. e. CO_2 emissions. Because of the penalties for each gram of CO_2 emissions exceeding the stated limit, even solutions that promise CO_2 emissions reduction in the order of 1 gram or a fraction of gram are very valued. In recent years, it was one of the reasons that led to wider implementation of the intelligent alternator regulation in conventional vehicles. With little additional hardware costs the fuel savings can range between 1-4 % of CO_2 emissions (according to the [1]).

[1] Jolana Heřmanová, Czech Technical University in Prague, Technická 4, 166 07 Praha 6, Jolana.Hermanova@fs.cvut.cz
[2] Rastislav Toman, Czech Technical University in Prague, Technická 4, 166 07 Praha 6, Rastislav.Toman@fs.cvut.cz

Today these levels of fuel savings are no longer sufficient, and the fleet has to contain a large part of BEVs and Plug-in HEVs to be able to lower their fleet CO_2 emissions under the stated limit. Nevertheless, the portion of ICEV vehicles produced still prevails and the study of the intelligent alternator regulation is relevant.
The aim of this work is to build a 1D simulation model of a conventional vehicle with detailed on-board electric network and to compare an intelligent alternator regulation strategy with a simple one.

- The first modelled strategy aims to simply maintain constant voltage of the 12 V network.
- The second modelled strategy is based on set of voltage targets, that vary depending on the actual ICE (actual required power and speed) and battery (actual SOC) conditions.

The second aim of this work is to use this model and developed methodology to quantify the effects of additional 100 W of electric on-board consumption on the fuel consumption.
All simulations are using the WLTP speed profile and gear shifting points.
The structure of the article is as follows: The first chapter – the introduction, is focused on the state of the art, it briefly describes the 12 V system components and then the common control strategies. The second chapter describes the methodology, the simulation model and implemented strategies. The third chapter presents the results of performed simulations and the fourth discusses the obtained results.

1.1 12 V system

The function of the 12 V system is to ensure that the vehicle network always can meet the power demand of all consumers – that is firstly to always ensure that enough power is stored in the battery to start the ICE. Secondly it has to supply power to other consumers that are necessary to drive the ICE and vehicle during operation, and thirdly it supplies power to other safety, convenience and comfort on-board consumers.
For this purpose, the network consists of these main components: Alternator, Starter, Battery, and on-board consumers.

1.1.1 Alternator

Alternator is an AC electric generator with rectifier diodes to supply DC to the vehicle electric network. The main task of the alternator is to supply the network with enough power to meet the demand of electric consumers, and to charge the battery. It should be able to maintain constant voltage throughout the ICE operating speed and load range. Other requirements are these: high efficiency, low operating noise, robust design, long service life, low weight, compact dimensions. [1]
The alternators should be used in higher motor speeds, therefore the gear ratio to ICE should be used accordingly. Usually it is around 1:2.2 or 1:3 in passenger cars. The nominal power varies from 1 to 3 kW and their efficiency is around 70-80 %. [1]

1.1.2 12 V battery

The main purpose of 12 V battery in conventional vehicle is to supply power to start the ICE and then to supply power to the other consumers when the ICE is not operating, or the actual alternator power output is lower than the actual demand.

To supply power for the ICE start and to power other vehicle consumers – those are two very different requirements. The ICE start means load of around 300 to 500 A for a very short period of time. During other periods only small loads are necessary – the battery works like “general-purpose electric supply”. The battery design is always a trade-off between high output (high power density) and high capacity. [1]
Battery’s performance differs in dependence on the ambient temperature and its location in the vehicle. In cold ambient temperatures, the battery that is located in the ICE compartment can be warmed up more quickly, than in the luggage compartment. Also, the battery located in the ICE compartment has to be shielded from the higher temperatures from ICE. Negative aspects of positioning the battery in the luggage compartment are higher losses in the wires and higher voltage drop. [1]
There are two types of lead acid batteries, that can be used in vehicles with start-stop system and the intelligent alternator regulation. Those are AGM (absorbent glass mat) and EFB type (enhanced flooded battery). Both can operate in lower SOC level than the standard wet-flooded batteries, can absorb higher charging currents and have higher cyclic durability. The AGM are usually used in higher specification vehicles that have functions like start-stop, regenerative braking, and passive boost. [1]

1.1.3 Starter

Starter is a DC electric motor with rated power up to 2.5 kW, current load varying from 200 to 1000 A. The gear ratio between the ICE and the starter is usually between 1:10 or 1:20. As its purpose is to start the ICE, the main demands are focused on convenience, safety, quality, and low noise levels. Higher demands are placed on the starter when it is equipped in a vehicle with start-stop system. It needs quicker and lower-noise level starts. Also features that prolong its life are necessary.[1]

1.1.4 On-board Consumers

According to duration of load, the consumers can be divided into these groups: the continuous loads (electric fuel pump, ECUs…), long-term loads like lights, car radio, electric radiator fan, and the short-term loads like electrical seats adjustment, power-window units, turn-signal lamps. The consumers are also divided according to the terminal to which they are connected. The first group is powered only when the ignition is on. The second group can operate even when the ignition is off. Those are for example: car radio, or auxiliary heating. There is also a group of “no-load-current systems”. One example is the anti-theft alarm system. Typically, the current for these systems in passenger cars should be under 3-10 mA.[1]

1.2 Common strategies:

The basic control strategy is to keep constant system voltage to ensure that battery is fully charged. The output of alternator is regulated by excitation field by pulse-width-modulated PWM current in the rotor winding. The regulation must work in the whole operating range of speed and load.[1]
The general ways to reduce fuel consumption are these:

- avoid ICE idling by using the start-stop system,
- increase efficiency of power generation – generate power during fuel-cut off periods,
- isolate the accessories from the ICE and power them from the electrical system,

- integrate the electrical energy management system, so it can be switching off or reducing power demand when it is convenient. [1]

The vehicle fuel consumption can be lowered also by adapting the strategy to actual driving conditions. These systems can be called like Intelligent Alternator Activation, Load-response driving, or Intelligent alternator regulation and recuperation, passive boost… [1]
Main functions of the electrical energy management are these: no-load mode, switching of consumers, increasing alternator output. The no-load mode monitors the battery state to ensure the startability when ICE is off. When necessary it can reduce power consumption of the consumers. The switching of consumers is used to reduce power demand peaks, or when the battery SOC is low, then to recharge it quickly. The consumers that can be turned off or their power supply can be reduced are the convenience and comfort consumers. But these situations should occur rarely. The increasing of alternator output is used especially during vehicle deceleration (during overrun fuel cut-off) to recuperate the vehicle kinetic energy. In this moment the electrical power is generated without the increase of fuel consumption. On the other hand, if the alternator works with low efficiency, its output can be lowered. Another case of alternator increased output occurs if the battery SOC is too low. Then the ICE stays idling during the stop phases and the idling engine speed is increased, to charge the battery. Unlike in ordinary voltage control, the battery is not operated at its maximum SOC. The recuperation function requires that the battery is in a “partial state of charge” to be able to absorb the power from recuperation. These functions generally increase thy cyclical variation of the battery. The AGM batteries (absorbent glass mat) are better suited to such operating conditions. Usually, the fuel savings can be between 1-4 %. [1]
The fuel savings depend on the vehicle type and the implemented strategy. In [2] the authors achieved by optimizing the control strategy the fuel savings of 1,7 % compared to traditional voltage control (but without the balanced battery SOC). In [3] there is a similar comparison (using the Pontryagin’s Minimum Principle), the improvements in fuel consumptions were around 1 % - small in absolute value but possible to achieve without additional hardware costs. Similar results were achieved in [4] using the ECMS method.

2. METHODOLOGY

In this chapter firstly the GT-Suite simulation model of a conventional vehicle is described. Second part of this chapter is focused on implementation of charging strategies into the model. The third describes the methodology behind the sensitivity analysis of on-board electric energy consumption.

2.1 Vehicle

The vehicle chosen for this article is a A0 Class conventional vehicle (fully equipped) with manual transmission, front-wheel drive. The chosen driving cycle is WLTC and the gear shifting points are calculated according to the WLTP regulation.

2.2 GT-Suite model

The simulation model was built in GT-Suite 0D/1D simulation software. It is a basic ICEV model with detailed 12 V electric system (figure 1).

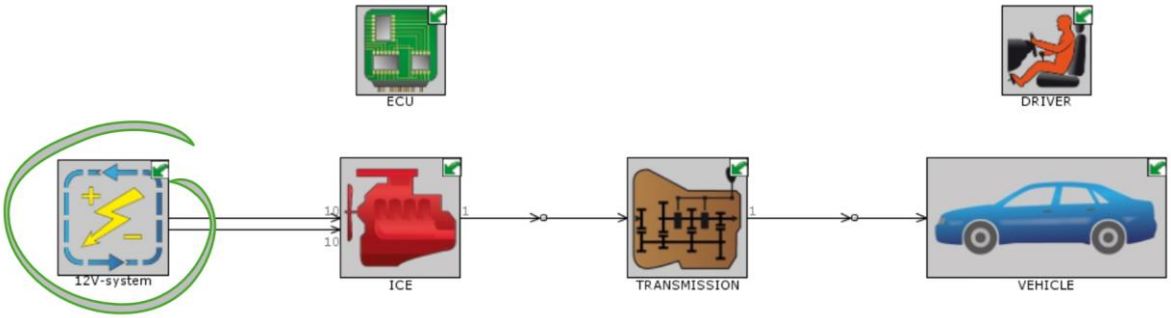

Figure 1: *Basic ICEV model*

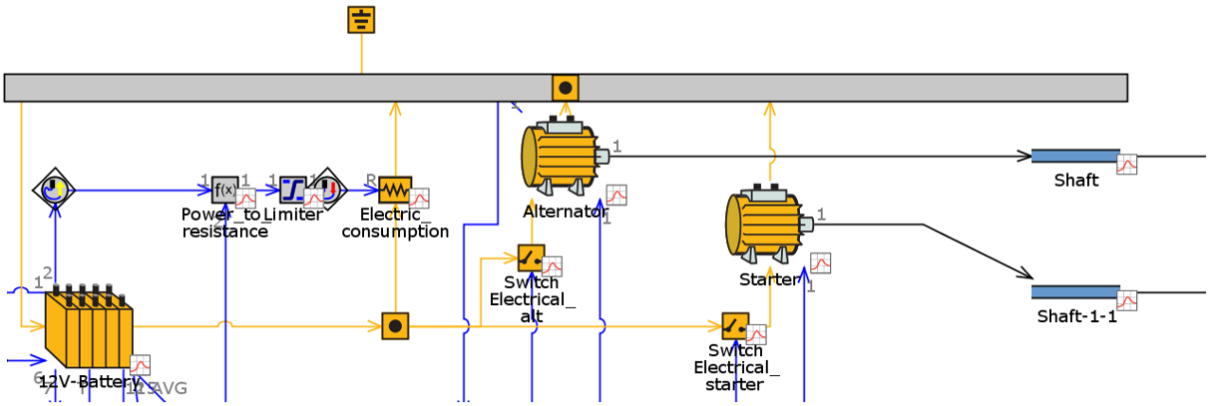

Figure 2: *Detailed 12 V system model*

The modelled 12 V electric system (figure 2) consists of these main parts: 12 V battery model, starter electric motor, alternator electric motor, and on-board consumers modelled with electrical resistor.

2.2.1 12V battery

The battery is modelled with a resistive electrical-equivalent battery model based on open-circuit voltage and internal resistance characteristics – both differs for charge and discharge. The battery data used in this model comes from measurement. The internal resistance is dependent on the duration of load – 1, 2, 4, and 10 seconds. The temperature dependency is neglected. It was verified in a measurement that the temperature changes of the battery in the ICE compartment during the WLTC cycle are low.

The battery is connected to the electrical circuit via electrical connection, also the required load is expressed via voltage and current. The battery type used in this model has capacity of 49 Ah, and it is a lead acid battery of the EFB type.

2.2.2 Alternator

The alternator is modelled as a map-based electromechanical Motor/Generator. The inputs are the efficiency map and line of minimum torque dependent on RPMs. It is connected to the ICE via mechanical link with a given gear ratio and then to the electrical system circuit with electrical connections (Voltage, Current). The demanded electric power is transmitted to the alternator via the signal from the strategy.

2.2.3 Starter

The starter is also modelled by the mapped electromechanical motor/generator. Its purpose is to start the ICE after every stop phase and therefore to allow simulation of the start-stop functionality. It is modelled with constant efficiency and constant maximum torque. After the ICE is turned on the starter is disconnected.

2.2.4 On-board Consumers

In electrical circuit in GT-Suite the on-board consumption can be modelled as an electrical resistor that dissipates electric power. The electric consumption can be entered like a constant value through the driving cycle or like a time dependent profile.

2.3 Control Strategies

In this article there are two strategies that are compared. – the Constant Voltage Control and the Variable Voltage Control. Both are implemented using a PID controller that is targeting to a voltage target and its output is the required electric power demand, that is sent to the Alternator.

2.3.1 Constant voltage control

The first strategy is a simple strategy that aims to maintain the same system voltage during all conditions. The target voltage is lowered when the battery SOC is higher to prevent overcharging. It is necessary for comparability of variants to assure that that the initial battery SOC equals to the end SOC. That is ensured by the level of the voltage targets (figure 3).

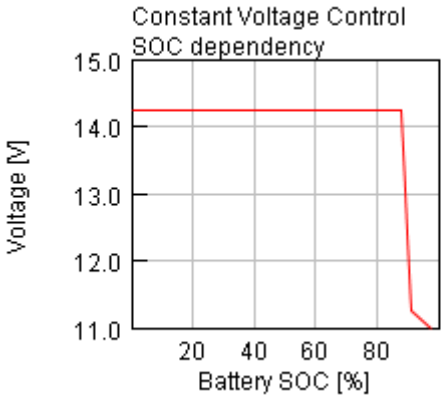

Figure 3: *Constant Voltage Control: SOC dependency*

2.3.2 Variable Voltage Control

The second strategy is based on variating the voltage targets according to the actual driving conditions. Those are the actual battery SOC, actual ICE power demand and actual ICE speed (figure 4).

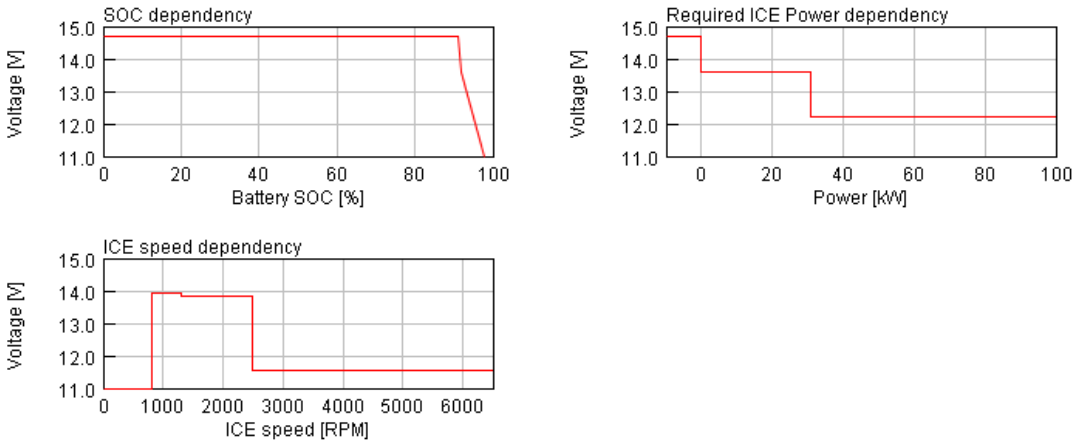

Figure 4: *Variable Voltage Control: SOC, ICE speed and ICE power dependencies*

The target voltage is chosen from these 1D lookups as the minimum value. With these exceptions: 1) if the ICE is turned off, then the PID controller is also turned off, 2) during ICE start (until ICE reaches idle speed, the PID is turned off, 3) if the required ICE power is negative, then the strategy ignores the ICE speed dependency and choses the limit dependent only on SOC and required ICE power.
It is a rule-based strategy that contains dependency limits that can be used in an optimization task. As it is difficult to “guess” the limits or chose them from previous experience so well to achieve the balanced battery SOC (the same SOC level at the beginning and the end of simulation), it is convenient to use the integrated design optimizer that GT-Suite offers. In this case an optimization task was run to find the above-mentioned limits, that can meet the balanced SOC condition, and also minimize the fuel consumption. The fuel consumption is the main objective of this strategy and the second objective of this optimization – the balanced SOC – ensures that the results are comparable with each other.

2.4 Sensitivity analysis

The above-described model with the methodology to achieve balanced battery SOC can be used to quantify the fuel consumption increase with 100 W on-board electric power consumption increase. The levels of on-board electric power consumption that were evaluated are these: 100 W, 200 W, 300 W, 400 W, 500 W and 600 W. In every variant the consumed power stays constant during the whole cycle, even during the stop phases. The model with variable voltage control was used for this purpose and each variant has its own set of voltage targets to achieve the balanced battery SOC.

3. RESULTS

This chapter presents the obtained results. Firstly, there is a description of the simulation settings – the vehicle, on-board network and strategy settings. Then there are the results from the WLTC cycle simulation in GT-Suite with the two implemented strategies – the Constant Voltage Control and Variable Voltage Control. These results are presented in graph of time profiles (strategy inputs and outputs), the set of operating points in ICE fuel consumption map and in alternator efficiency map, and the final fuel consumption – the achieved CO_2 emissions savings. The last part shows the results of the sensitivity analysis of ICE fuel consumption on the on-board network energy consumption.

3.1 Additional simulation settings

Every simulation starts with the battery SOC of 89 %.
The simulations of the constant voltage control and variable voltage control have an additional input for the base on-board electric power consumption. This consumed power was chosen based on the measurement of the same vehicle in WLTC. The values are filtered and then used as a time profile dependency in both strategy focused simulation variants (figure 5).

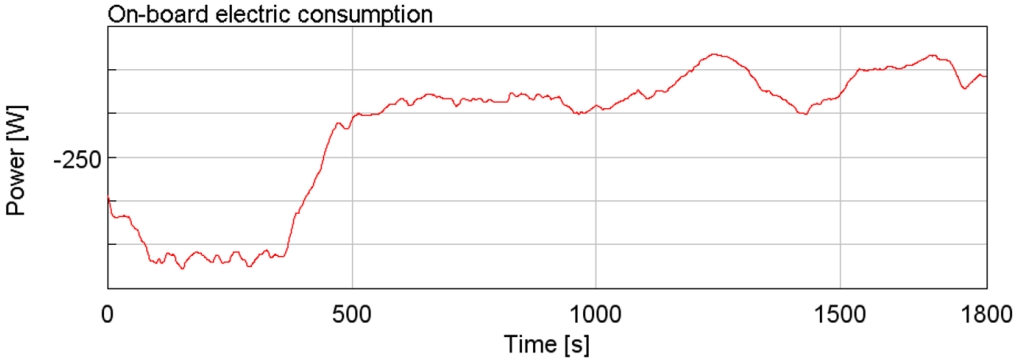

Figure 5: *On-board electric consumption*

3.1.1 Constant voltage control strategy simulation

The simulation runs firstly with a manually chosen voltage target. To obtain the result with balanced battery SOC the voltage target has to be modified. For this purpose, the integrated optimizer in GT-Suite was used and the modified voltage targets were obtained. The final voltage target for this variant is shown in the figure 3. In this case the target voltage is 14.2 V under battery SOC of 88%, for higher SOC it decreases to 11 V.

3.1.2 Variable voltage control strategy simulation

The same approach was taken in case of the variable voltage control strategy simulation. In addition to the battery SOC dependency, there is a dependency on ICE speed and ICE required power. The voltage targets that are the output of the optimizer are shown in the figure 4. The maximum voltage target is 14.7 V and can be applied only if the SOC is lower than 91 % and the required ICE power is negative (in phases of deceleration). During normal driving condition the voltage target is very low (11.6 V)

for the ICE speed higher than 2500 RPM. No charging will occur during these moments.

3.1.3 Sensitivity analysis

For the sensitivity study, the time dependent power curve (of on-board electric consumption) is replaced with constant values from 100 W to 600 W. The optimization step is also necessary to ensure the balanced battery SOC.

3.2 Comparison of control strategies

The figure 6 and figure 7 show the simulation results in WLTC cycle. The figure 6 shows the inputs to the strategy – ICE speed and ICE power. The second one – figure 7 shows the outputs of the strategy – the system voltage, that is the controller input, that is targeted and – the alternator power – that is the output of the controller. In the second graph the main difference between the strategies can be seen. The constant voltage control targets to one voltage target that varies only with battery SOC to prevent overcharging and ensure balanced battery SOC. On the other hand, the variable voltage control varies the system voltage according to the actual driving conditions and thus changes the required load of the alternator to the ICE.

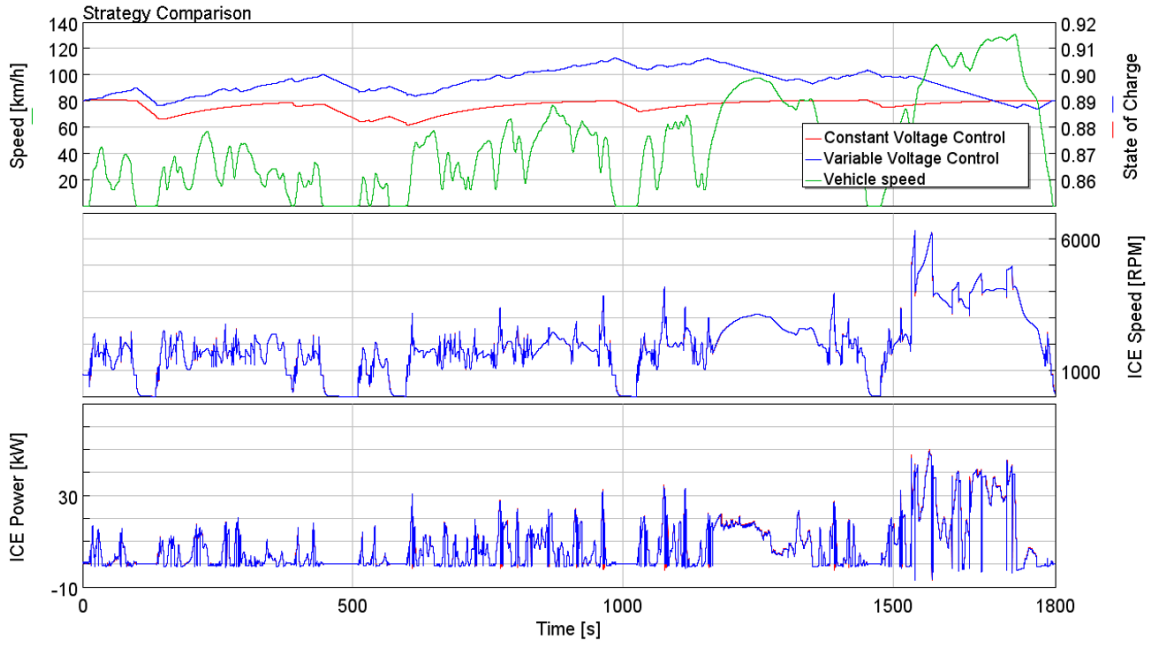

Figure 6: *Strategy comparison: inputs*

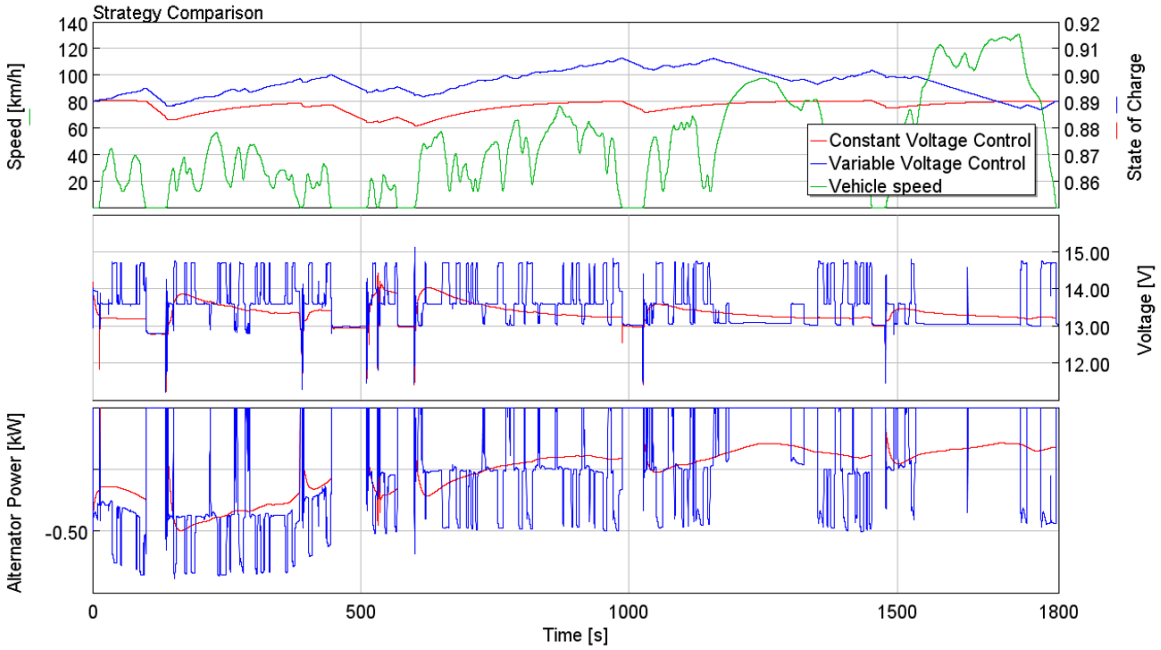

Figure 7: *Strategy comparison: outputs*

The figure 8 shows then how the operating points of both ICE and alternator look like. The main visible difference between the two strategies can be seen in the alternator efficiency map. Nearly no operating points are located in the alternator higher speed areas (above 10 000 RPM) – in case of the variable control strategy. Also, the operating points from area of low speed are shifted to areas with higher loads and better efficiency.

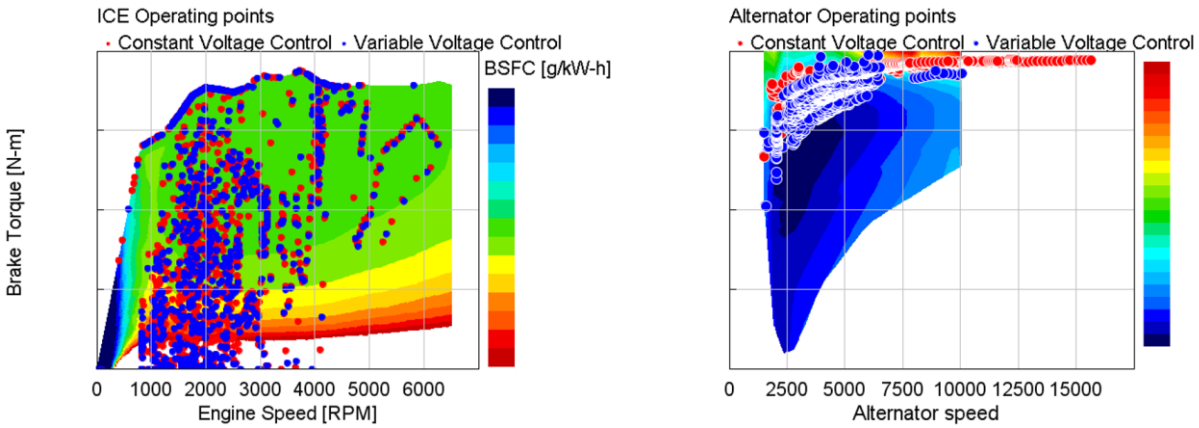

Figure 8: *ICE fuel consumption map, Alternator efficiency map*

The table 1 shows the comparison of WLTC fuel consumption of both variants. The fuel savings achieved by variable voltage strategy are around 1 gCO_2/km (0,8 %).

	WLTC Fuel Consumption [l/100km]	[gCO_2/km]	Δ [gCO_2/km]
Constant Voltage	[illegible]	[illegible]	-
Variable Voltage Strategy	[illegible]	[illegible]	-1,07

Table 1: *Constant Voltage vs. Variable Voltage strategy comparison: fuel consumption results*

3.3 Sensitivity analysis – On-board consumption variants

The figure 9 shows results of variants with different levels of onboard consumption. Only variants of 100 W, 300 W and 500 W are shown, to maintain clarity.

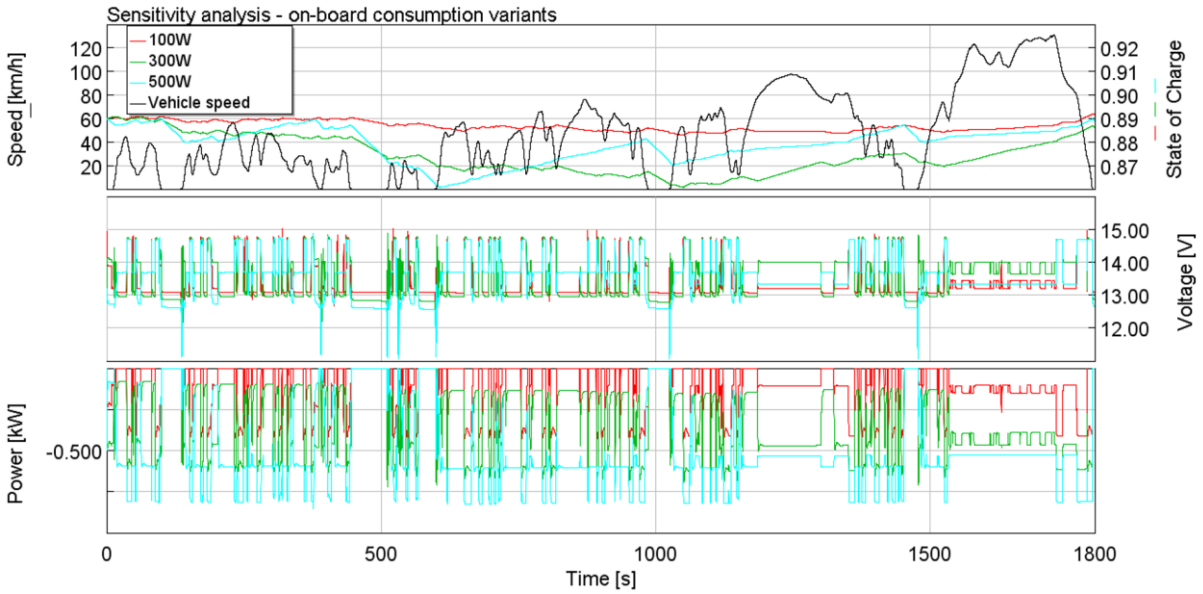

Figure 9: *Sensitivity analysis results*

The table 2 then contains complete results with differences between subsequent variants. The average difference per additional on-board electric consumption of 100 W is 1.6 gCO_2/km.

On-board electric consumption	WLTC Fuel Consumption [l/100 km]	[gCO_2/km]	Δ [gCO_2/km]
100 W	[illegible]	[illegible]	
200 W	[illegible]	[illegible]	1,8
300 W	[illegible]	[illegible]	1,4
400 W	[illegible]	[illegible]	1,8
500 W	[illegible]	[illegible]	1,9
600 W	[illegible]	[illegible]	1,1

Table 2: *Sensitivity analysis results*

4. CONCLUSION

The aim of this work was to build a conventional vehicle model with detailed 12 V network, implement one basic power supply strategy and one intelligent control strategy and compare their results. The second aim was to quantify the impact of higher on-board electric consumption on the fuel consumption.
For this purpose, 1D simulation model of ICEV vehicle (A0 Class) in GT-Suite software was built. The detailed 12 V network model consists of electrical circuit with these components: 12 V battery, alternator, starter, and electrical resistance to model the on-board energy consumption. The first strategy that was implemented is a simple constant voltage strategy. The strategy is based on a PID controller that ensures that the target voltage is achieved. The target voltage is one constant value and is lowered when high SOC is reached. The second strategy is the variable voltage strategy based on variable voltage target dependent on actual ICE conditions (ICE speed and power) and battery SOC. Both strategies have to achieve a balanced battery SOC (the SOC at the beginning equals to the SOC at the end) in order to be comparable, for this reason the voltage target values are tuned. With this variable voltage strategy, the WLTC fuel consumption (in CO_2 emissions equivalent) can be lowered by about 1 gCO_2/km in comparison to the simple strategy. Using the optimal control methods, the fuel savings achieved can probably be a little higher, but the applicability of such methods in real vehicles is very difficult.
The second aim of this work was to quantify the effect of higher on-board electric consumption on the fuel consumption. The simulations of several electric power consumption levels were performed (100 W to 600 W). The outcome of this sensitivity analysis is that the 100 W increase in electric on-board consumption has effect of on average 1.6 gCO_2/km (in CO_2 emissions equivalent). Although this number corresponds to the specific vehicle and ICE, for a different vehicle the value is expected to be similar. Also, the model and methodology that was developed can be easily applied to another vehicle.

REFERENCES

[1] Bosch Automotive Handbook: 8th Edition, 8th Edition. Plochingen: Robert Bosch GMbH, 2011.
[2] Y. WANG, H. HU, L. ZHANG, N. ZHANG and X. SUN, "Real-Time Vehicle Energy Management System Based on Optimized Distribution of Electrical Load Power", Applied Sciences, vol. 6, no. 10, 2016.
[3] C. WALDMAN, S. GURUSUBRAMANIAN, L. FIORENTINI AND M. CANOVA, "A model-based supervisory energy management strategy for a 12 V vehicle electrical system", Control Engineering Practice, vol. 44, pp. 20-30, 2015.
[4] J. COUCH, L. FIORENTINI AND M. CANOVA, "An ECMS-Based Approach for the Energy Management of a Vehicle Electrical System", IFAC Proceedings Volumes, vol. 46, no. 21, pp. 115-120, 2013.

ACKNOWLEDGMENTS

This work was realized using support of:

- Technological Agency, Czech Republic, programme National Competence Centres, project # TN01000026 Josef Bozek National Center of Competence for Surface Vehicles.
- The Grant Agency of the Czech Technical University in Prague, grant No. SGS21/155/OHK2/3T/12.

This support is gratefully acknowledged.

ABBREVIATIONS

AC	alternating current
AGM	absorbed glass mat
BEV	battery electric vehicle
DC	direct current
ECMS	equivalent consumption minimization strategy
ECU	electronic control unit
EFB	enhanced flooded battery
HEV	hybrid electric vehicle
ICE	internal combustion engine
ICEV	internal combustion engine vehicle
PID	proportional–integral–derivative controller
PWM	pulse-width-modulated
SOC	state of charge
WLTC	Worldwide Harmonized Light Vehicles Test Cycle
WLTP	Worldwide Harmonized Light Vehicles Test Procedure

LII. INTERNATIONAL SCIENTIFIC CONFERENCE OF THE CZECH AND SLOVAK UNIVERSITY DEPARTMENTS AND INSTITUTIONS FOCUSED ON RESEARCH AND TEACHING METHODS RELATED TO COMBUSTION ENGINES, ALTERNATIVE DRIVES AND TRANSPORT
SEPTEMBER 22 – 23, 2021, PRAGUE
CZECH UNIVERSITY OF LIFE SCIENCE PRAGUE, FACULTY OF ENGINEERING,
DEPARTMENT OF VEHICLES AND GROUND TRANSPORT

THE INFLUENCE OF ENGINE OIL DEGRADATION ON ENGINE BEARING PERFORMANCE

E. Jankes[1], C. Besser[2], A. Agocs[3], C. McAleese[4], L. Loveček[5], B. Ronai[6], A. Ristic[7], N. Dörr[8]

Abstract
The influence of interaction of bearings with engine oils at different degradation grades (fresh versus artificially altered according to selected parameters) on the tribological performance was evaluated. The investigation was focussed on the influence of oil degradation on tribochemistry and overall bearing performance under various test conditions for a high-performance bearing material. Evaluation of the bearing-lubricant-interactions with suitable surface analysis of the worn bearings was carried out by X-ray photoelectron spectroscopy (XPS). The bearing material functioned with only a small change in tribological performance between fresh and heavily degraded engine oils under the applied test conditions.

1. INTRODUCTION

For evaluation of material performance in tribological contacts, various lubricants are commonly used for testing and fundamental studies. These lubricants are usually “fresh” and can be base oils without additives (such as ZDDP, MoDTC, etc.) or formulated oils which contain various additives, e.g. antioxidants for a better ageing behaviour or anti-wear and friction modifiers to improve the oil performance in the tribological contacts, to name a few. However, lubricants which are used in the application may contain unwanted contaminants. Furthermore, lubricants degrade by mechanical stresses and chemical changes caused by thermal and oxidative impact during operation. Thus, the oil condition

[1] E. Jankes, Daido Metal Co., Ltd – organizační složka, The European Technical Center, Švédské valy 1309/6, 627 00 Brno, Czech Republic, jankes@daidometal.com
[2] C. Besser, AC2T research GmbH, Wiener Neustadt, Victor-Kaplan-Straße 2/C, Austria, charlotte.besser@ac2t.at
[3] A. Agocs, AC2T research GmbH, Wiener Neustadt, Austria, adam.agocs@ac2t.at
[4] C. McAleese, Daido Metal Co., Ltd – organizační složka, The European Technical Center, Brno, Czech Republic, colin.mcaleese@daidometal.com
[5] L. Loveček, Daido Metal Co., Ltd – organizační složka, The European Technical Center, Brno, Czech Republic, lovecek@daidometal.com
[6] B. Ronai, AC2T research GmbH, Wiener Neustadt, Austria, Bettina.ronai@ac2t.at
[7] A. Ristic, AC2T research GmbH, Wiener Neustadt, Austria, andjelka.ristic@ac2t.at
[8] N. Dörr, AC2T research GmbH, Wiener Neustadt, Austria, nicole.doerr@ac2t.at

may change significantly over its operating duration. It is therefore important to understand the influence of oil degradation on component performance in applications such as bearings. In this project, the focus was on the performance evaluation of bearings lubricated with relevant commercially available engine oils. Accordingly, several candidate oils were chosen for a pre-study to benchmark them regarding their thermo-oxidative stability characterized by conventional oil parameters. Based on these results, two engine oils (oil A and oil B) were selected for subsequent artificial alteration [1]. Altered engine oils were produced in large amounts (~ 100 litres) for subsequent bearing testing. As next step, different bearing bench test procedures were carried out with oil A and oil B, each oil in fresh and in altered condition. After this tribotesting, the resulting oils and bearings were again evaluated.

2. MATERIALS AND METHODS

2.1 Bearing material

The bearings used for this project are multilayer materials consisting of a steel back, aluminium alloy layer, and a surface layer (or overlay) consisting of an electroplated Ag interlayer and a Bi layer on top [2], as shown in *Figure 1*. This type of bearing material is used for high-performance automotive engines (such as V8 and V12 petrol engines) where lead-free material is required.

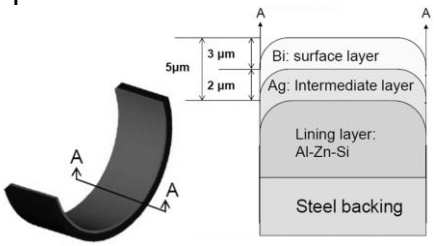

Figure 1: *Engine bearing model and schematic diagram of bearing cross section*

2.2 Oil selection and artificial alteration

Conventional oil analysis of the candidate oils was performed in fresh condition (basic characterization) and after carrying out artificial alteration to depict the simulated degradation behaviour. The large scale artificial alteration was performed in a 250 litre stainless steel jacketed chemical reactor, whose setup is displayed in *Figure 2*. This is a specially built reactor at AC2T research GmbH for the purpose of producing artificially altered oils under controlled conditions to simulate oil degradation in the field [1].

100 litres of fresh oil were inserted into the cold reactor tank, rapidly heated up, and kept at a specified temperature under constant stirring by a propeller stirrer at 480 rpm. During the storage period, the oil was brought in contact with dried compressed air. The oil temperature was constantly set at 180 °C and the air flow was held at a flow rate of 2 667 l/h, which was monitored by a flow controller. Exhaust gases were cooled down by a condenser system consisting of two steps, i.e., a stainless steel primary condenser utilized as a reflux condenser followed by a glass secondary condenser serving as an oil separator, both operating at 4 °C.

In constant time intervals, oil aliquots were sampled, and the oil condition was monitored in terms of oxidation and content of antiwear additive ZDDP as well as content of antioxidants by Fourier transformed infrared spectroscopy (FTIR), viscosity at 40 °C and 100 °C and viscosity index by Stabinger viscometer, Total base number (TBN), Neutralisation number (NN), and elemental content by optical emission spectroscopy equipped with inductively coupled plasma (ICP-OES).

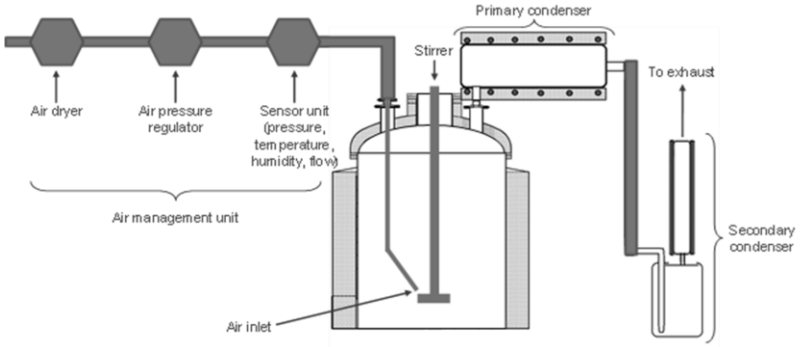

Figure 2: *Schematic set-up of the large scale alteration device*

2.3 Oil Rheology – Dynamic viscosity

In all fluids, the molecules are showing relative motion between each other, and this process is always combined with internal frictional forces. Therefore, for all fluids in motion, a certain flow resistance occurs which may be determined in terms of the dynamic viscosity. Oils typically behave as Newtonian liquids, i.e. dynamic viscosity is stable with changes in shear rate, but rheological parameters change with temperature [3]. Therefore, the measurement of dynamic viscosity at different temperature was carried out with a rheometer (Anton Paar MCR502 TwinDriveReady, with software RheoCompassTM) with double gap geometry.

Oil A, oil B and Renolin DTA05 (as reference oil for the wear test) were used for dynamic viscosity determination. Oils A and B were measured in double gap geometry at several different temperatures, 25 °C, 40 °C, 80 °C, 100 °C and 130 °C, Renolin DTA05 only at 25 °C. Analysis was performed at shear rates between 0.1-100 s^{-1} in a linear ramp over 50 points with a measurement time of 275 s at each temperature. Viscosity determination was repeated at least 2 times for each oil and each temperature.

2.4 Engine bearing tribometer

Three types of tests were carried out during this project: wear, seizure and fatigue. The test rig used for these tests is a tribometer developed for the evaluation of tribological properties of engine half bearings. A schematic diagram of the system is shown in *Figure 3* below. The system is composed of a driving part where the shaft rotation can achieve up to 10 000 rpm, with loading and lubrication systems. The oil quantity required for the lubrication unit is 60 litres. A clutch is integrated to disengage the motor from the test shaft in overloading conditions, such as when seizure occurs. The loading system is applied by

a hydraulic aggregate able to simulate static and dynamic testing conditions with a force amplitude of 100 kN and a frequency up to 60 Hz.

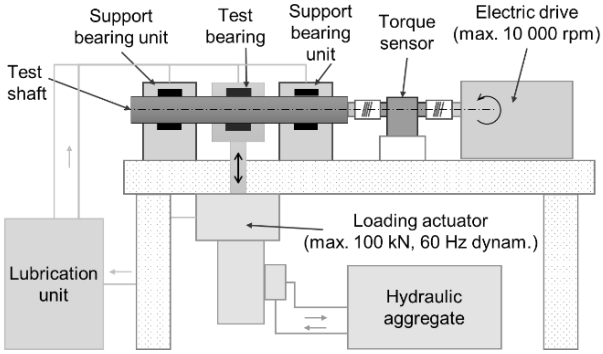

Figure 3: *Schematic diagram of bearing test rig*

2.5 Tribotesting and surface analysis

2.5.1 Wear test

Wear test conditions are described below in *Table 1*. The test machine was set for repeated start/stop cycling conditions for the rotation of the shaft, to simulate conditions of a hybrid vehicle or start-stop engines, i.e. with frequent start-ups when the oil film is sparse and, hence, promotes bearing wear. The constant static load was set to the specific load (or nominal contact pressure) of 5 MPa with the small inlet of lubricant at room temperature.

The wear amount is determined from the bearing thickness before test minus the bearing thickness after the test at the main loaded area of the bearing (i.e. at the 90° position from the half bearing joint face).

Parameter	Value	Unit	Test pattern
Test pattern	Start – Stop	-	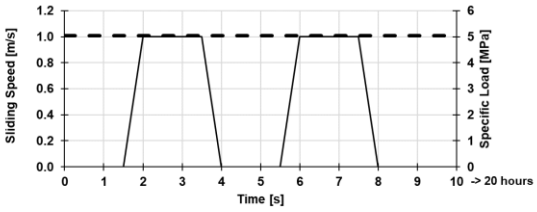
Sliding speed	360 (1)	rpm (m/s)	
Test specific load	5 (4)	MPa (kN)	
Test duration	20	hours	
Lubricants	oil A and oil B	-	
Oil inlet temperature	Room temperature	-	
Oil flow	2	ml/min	
Shaft material	DIN 16MnCr5, HRC 50-60	-	
Shaft roughness	Rz <1.0	µm	

Table 1: *Test conditions for wear test*

2.5.2 Seizure test

Test conditions of the seizure test are shown below in *Table 2*. In this test, cumulative step-up loading was applied with a shaft rotating at a constant speed. The seizure resistance was evaluated from the specific load at seizure. The bearing back temperature was measured during the entire test and seizure was judged to have occurred

when the temperature reached 230 °C, or when the torque in the drive motor reaches a predetermined value.

Parameter	Value	Unit	Test pattern
Test pattern	Step-up loading	-	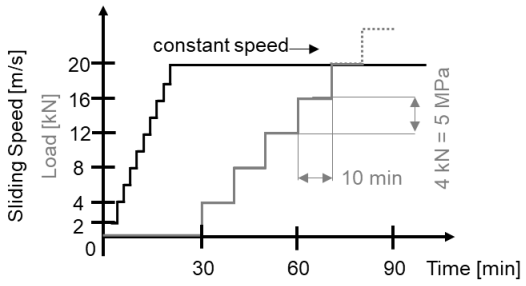
Sliding speed	7 200 (20)	rpm (m/s)	
Initial load	0	kN	
Specific load step	5 (4)	MPa (kN)	
Time per step	10	min	
Lubricants	oil A and oil B	-	
Oil inlet temperature	100-110	°C	
Oil flow	150	ml/min	
Shaft material	DIN 16MnCr5, HRC 50-60	-	
Shaft roughness	Rz <1.0	µm	

Table 2: *Test conditions for seizure test*

2.5.3 Fatigue test

The purpose of the fatigue test is to evaluate the resistance of the material against fatigue. It was applied in the project to evaluate the effect of engine oil degradation on the surface in harsh conditions. The test conditions are shown in *Table 3*. The tribometer applies a cyclic dynamic load to the test bearing from the hydraulic cylinder. High housing rigidity ensures excellent stability, and this test can be performed under heavy specific loads that are two to three times the load in an actual engine. The test was stopped after a significant rise in bearing temperature from fatigue crack formation. After the test, the bearings were taken out, cleaned, visually examined with an optical microscope.

Parameter	Value	Unit	Test pattern
Test pattern	Dynamic loading	-	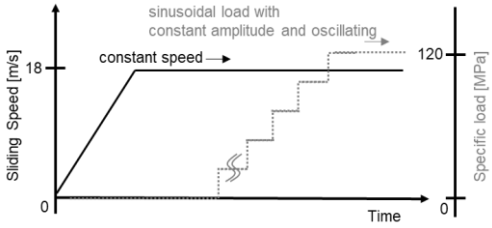
Sliding speed	6 500 (18)	rpm (m/s)	
Specific load	120	MPa	
Load cycle frequency	60	Hz	
Test duration	Until Fatigue is detected or Seizure of bearing occurs	-	
Lubricants	oil A and oil B	-	
Oil inlet temperature	80	°C	
Oil flow	290-310	ml/min	
Shaft material	DIN 16MnCr5, HRC 50-60	-	
Shaft roughness	Rz <1.0	µm	

Table 3: *Test conditions for fatigue test*

2.5.4 Bearing sliding surface chemistry analysis

The surface analysis was carried out with a Thermo Fisher Scientific Theta Probe using a monochromated Al Kα X-ray source with an X-ray spot resolution of 400 µm. The survey scans were carried out applying a step size of 1 eV and 200 eV pass energy, and for the narrow scans a step size of 0.1 eV with a pass energy of 50 eV was applied. The Avantage v5.976 software was used for evaluation. The depth profiles were obtained by sputtering with Ar+ ions with a beam energy of 3 kV, a sputter current of 1 µA and a sputter area of 2×2 mm.

3. RESULTS AND DISCUSSION

3.1 Oil alteration results

Properties and difference between fresh and altered oils are summarised in *Table 4*. The alteration conditions were selected to guarantee a heavy degradation degree of the final oil sample in terms of high oxidation values and almost complete depletion of antioxidants [1]. Furthermore, a significant decrease of TBN and a steep rise in NN and water content is observed. Additive elements such as Ca, P, Zn, Mo, Ti, and B did not change to a strong extent, only S experienced a decrease which can be linked to the evaporation of volatile sulphur containing degradation products.

Oil parameter	Method	Fresh oil A	Altered oil A	Fresh oil B	Altered oil B	Chemical composition	Method	Fresh oil A	Altered oil A	Fresh oil B	Altered oil B
Oxidation [A/cm]	FTIR	0	90	0	93	Ca content [ppm]	ICP-OES	2000	2200	2700	2800
ZDDP content [%]		100	22	100	19	P content [ppm]		920	930	850	820
Phenolic Antioxidant content [%]		-	-	100	6	S content [ppm]		2100	1300	2600	1700
Aminic Antioxidant content [%]		100	3	100	1	Zn content [ppm]		960	1070	880	930
Viscosity 40 °C [mm²/s]	Stabinger Viscometer	48.0	55.6	54.2	54.5	Mo content [ppm]		< 10	< 10	59	60
Viscosity 100 °C [mm²/s]		9.0	9.4	10.4	8.7	Ti content [ppm]		56	67	< 1	1
Viscosity index [-]		171	151	176	136	B content [ppm]		69	66	2	< 1
Density 15 °C [g/cm³]		0.84	0.86	0.84	0.86						
Total base number [mg KOH/g]	Titration	7.7	2.8	8.7	4.3						
Neutralisation number [mg KOH/g]		1.7	10.4	1.3	8.7						
Water content [ppm]		130	640	200	860						

Table 4: *Properties and investigation methods of altered engine oils A and B after large scale alteration*

3.2 Dynamic viscosity

The results from both dynamic and kinematic viscosity measurements show that the viscosity at ambient temperature of both oils is increased slightly as a result of the artificial alteration. However, at higher temperatures the viscosity of oil A increases as

a result of the alteration, whereas the viscosity of oil B shows the opposite behaviour, and decreases to similar or even lower values than the altered oil A.

	Oil temperature [°C]					Kinematic viscosity		
	25	40	80	100	130	(treated at large scale alteration)		
Oil type	**Dynamic viscosity [mPas]***					**v 40 °C [mm²/s]**	**v 100 °C [mm²/s]**	**SAE**
fresh oil A	76.4	40	11.3	7.2	4.2	48	9.01	0W-20
altered oil A	92.6	47.5	12.7	7.8	4.3	55.6	9.35	0W-20
fresh oil B	86.6	45.7	12.8	8.1	4.7	54.2	10.1	5W-30
altered oil B	95.1	47	11.9	7.2	4	54.5	8.69	5W-30
Renolin DTA05	4.3	-	-	-	-	4.6**	1.6**	ISO-VG 5
*average value of at least 2 measurements								
**values from technical data sheet								

Table 5: *Dynamic and kinematic viscosity at different temperatures of fresh oils and oils after artificial alteration*

3.3 Wear test

During the wear test, the start mode distributes oil in the entire contact area, but during the stop part of the cycle, oil leaks out from between the shaft and test bearing. This reduced oil film coverage causes metal-metal contact and higher wear of the softer sliding partner. The oil leakage is mainly influenced by viscosity and density. All selected oils show lower wear amount compared to a base oil Renolin DTA05, which is used as reference. Both tests with altered oils show the same values, and both result in the lowest bearing wear amount ~3 µm. Thus, when the test was finished, wear amount had progressed to around interface Bi-Ag layer. The tests with fresh oils refer to wear amount > 5 µm, so the latest part of this test was running on the aluminium lining layer and the sliding coating was mostly removed. The reason for this could be the difference in dynamic viscosity at 25 °C, see *Figure 4*. The wear amount decreases with higher dynamic viscosity of oil, which significantly influences the result for these test conditions. Another important parameter could be friction modifiers such as molybdenum compounds in oil B and anti-wear additive titanium in oil A, which may be activated by the alteration. This hypothesis has to be verified with additional analytical means.

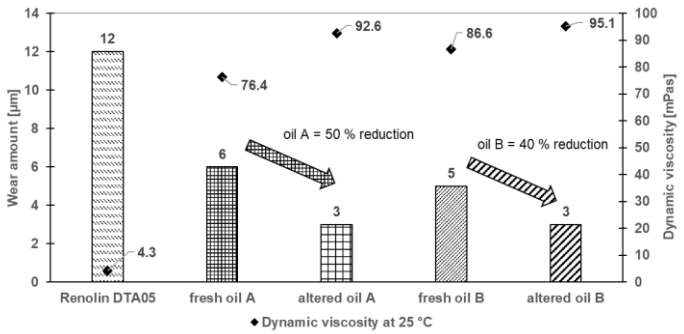

Figure 4: *Comparison of wear amount with dynamic viscosity of different oils (at shear rate 50 s^{-1})*

3.4 Seizure test

During the testing, several parameters were measured – torque on the driving part, oil lubrication pressure and temperature of support bearings as well as the test bearing. Test bearing temperature measurements were performed on both sides close to the edge to also detect a potential edge contact. There are two thermocouples which measure back steel temperature during the entire seizure test. These thermocouples are used as an indicator to identify the beginning of seizure phenomena.

Tests with both altered oils have different temperature growth compared to fresh oils, with the altered oils showing more unstable temperature behaviour. This may indicate that the oil performance is worse after alteration. The two fresh oils show almost the same load at seizure. The altered oil A shows the highest minimum load compared to the other oils and the altered oil B shows the lowest load (by 10 MPa) at seizure. Therefore, we can say that seizure was not dramatically affected by the oil alteration as can be seen in the chart below (*Figure 5*). The bearings were seized under similar loads, therefore from this test, no great influence of oil alteration was observed, although the altered oil B shows a slight decrease. For this test, the results are influenced more by the bearing material properties than the oil type, and even with the altered oils which are heavily degraded, the bearing still performs well under these conditions.

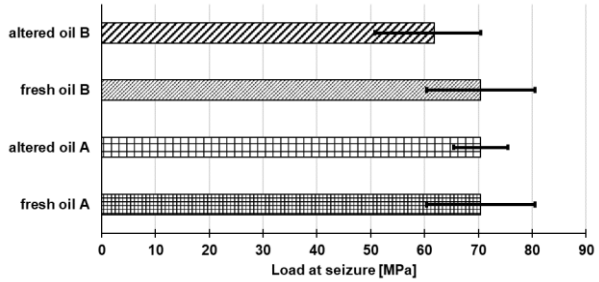

Figure 5: *Load at seizure: same bearing material, but four different oils*

Altered oils generally showed higher coefficient of friction (CoF) during seizure test than fresh oils, but all tests reached similar maximum load for this comparison. Another interesting fact about temperature is that back steel temperature during seizure tests at high loads with both altered oils show higher temperature than seizure tests with fresh oils (up to 30 °C difference), although it doesn't have a large effect on the final seizure load for this material. Thus, it seems that an altered oil is not able to transport heat from the shaft-bearing contact very well. The dynamic viscosity measurements at 130 °C of the altered oils are not so different from that of the fresh oils, but the conditions at the tribological contact in this test on the oil viscosity also need to be considered (high temperature, high shear) to better determine the difference in behaviour between the oils during this test. There could be other parameters such as specific heat conductivity of the oil and additives in the oil which could also have some effect under these test conditions.

3.5 Fatigue test

The better fatigue resistance response to tests is found with oil B, for both fresh and altered oils. The better performance of oil B could be the effect of additives contained in fresh oil B. The bearings tested with altered oil A show worse fatigue performance than with the fresh oil A, although there is some variation, and bearing samples with altered oil A show the worst performance for fatigue test. The difference between fresh and altered oils is about 50 000 cycles for both oils, which is not a large difference. In general, the effect of the alteration on the fatigue performance does not seem to be large for these test conditions.

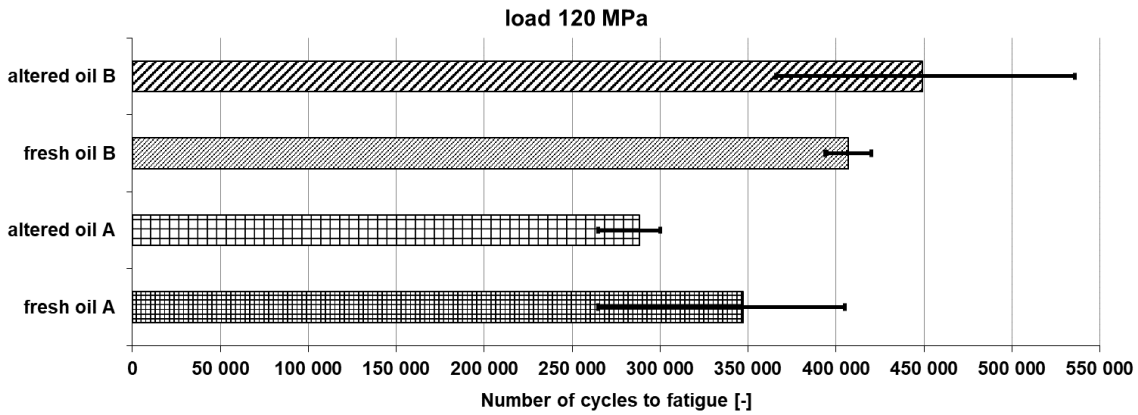

Figure 6: *Number of cycles to fatigue at test load 120 MPa*

3.6 Bearing sliding surface chemistry

Three bearings after Wear test with fresh and altered oil A and one bearing tested with altered oil B were analysed by means of XPS. The bearings tested with each oil were cut and the measurement spots were at different zones (a mirror-like zone and scuffing zone in the worn region around the main loaded area in the middle of the bearing, and the transition zone). For comparison with the original coating, a reference position was visually chosen in a spot with low tribological stress.

Both had a mirror-like zone in the middle, with the Bi layer worn off and mainly Ag present, along with traces of Zn, Ca, S and P assigned to the engine oil. On both bearings, there is a transition zone from the mirror-like zone to the unworn Bi layer, where Ag is decreased or not present, but mostly Bi oxides and some elements originating from engine oil like Ca, Si, and Zn are found. The thickness of contaminants and tribolayers was clearly less than 10 nm, probably in the range of few nanometres. The analysis of the bearing tested with fresh oil A revealed overall little or no presence of elements originating from the engine oil (Zn, Ca) for the Bi layer, the transition zone and the mirror-like zone. The scuffing zone with fresh oil A, which does not appear on the other two bearings, shows a different composition. Al, Si, and Zn originating from the substrate were detected along with some elements coming from engine oil (Ca, P). Generally, no evidence for the presence of Mo or Ti, components of friction modifiers in the engine oil, was found on any analysed surface, and no S was found on the bearing tested with fresh oil A.

4. CONCLUSION

Bearings tested with all selected oils have relatively low wear amount after the wear test. Altered oils A and B show the same values and bearings tested with these oils have the lowest wear amount. This is probably caused by degradation products and increased viscosity of both altered engine oils. Significant bearing-lubricant-interactions were not detected by XPS on the bearing surfaces after test.

Seizure test with fresh oils show almost the same load at seizure, although the altered oil B shows a slight decrease. Therefore, we can say that seizure under the applied test conditions was not dramatically affected by the oil alteration. Altered oils have higher CoF during seizure test than fresh oils. Altered oils also show higher temperature and rapid rise and fall in temperature when the load is increased, although it doesn't have a large effect on the final seizure load for this material.

The best fatigue resistance response to tests is found with altered oil B, but this oil also has the biggest variation. Tests with oil A show smaller maximum number of cycles to fatigue than tests with oil B. Bearing samples with altered oil A show the worst performance for fatigue test. However, the difference between fresh and altered oils is about 50 000 cycles, which is not a large difference, and the effect of oil alteration on these bearing fatigue tests does not seem to be large.

In general, despite the heavy degradation of the altered oil, the change in the performance of this bearing material compared with the fresh oil was relatively small, and the bearing was still able to function under the applied test conditions. However, further investigation of the influence of engine oil degradation on the bearing material under different conditions is required.

REFERENCES

[1] Charlotte Besser, Adam Agocs, Bettina Ronai, Andjelka Ristic, Martin Repka, Erik Jankes, Colin McAleese, Nicole Dörr, Generation of engine oils with defined degree of degradation by means of a large scale artificial alteration method, Tribology International, Volume 132, 2019, Pages 39-49, ISSN 0301-679X, https://doi.org/10.1016/j.triboint.2018.12.003.

[2] Nirasawa, T., Yasui, M., Ishigo, O., Kagohara, Y. et al., "A Study of Lead-free Al-Zn-Si Alloy Bearing with Overlay for Recent Automotive Engines," SAE Technical Paper 2009-01-1054, 2009, https://doi.org/10.4271/2009-01-1054.

[3] Mezger, Thomas G., The Rheology Handbook, 4th Edition, Hanover: Vincentz Network, 2014, European Coatings Tech Files, pp. 80-85. ISBN 3-86630-650-4, ISBN 978-3-86630-650-9

ACKNOWLEDGEMENT

The work presented was funded by the Austrian COMET program (Project InTribology, no. 872176) and carried out at the "Excellence Centre of Tribology" (AC2T research GmbH).

52. MEZINÁRODNÍ VĚDECKÁ KONFERENCE ČESKÝCH A SLOVENSKÝCH UNIVERZIT A INSTITUCÍ ZAMĚŘENÁ NA VÝZKUMNÉ A VÝUKOVÉ METODY SPOJENÉ SE SPALOVACÍMI MOTORY, ALTERNATIVNÍMI POHONY A DOPRAVOU

22.-23. ZÁŘÍ 2021, PRAHA
ČESKÁ ZEMĚDĚLSKÁ UNIVERZITA V PRAZE, TECHNICKÁ FAKULTA,
KATEDRA VOZIDEL A POZEMNÍ DOPRAVY

DOG CLUTCH WITHOUT CIRCULAR BACKLASH – SEQUENTIAL SHIFTING ADAPTATION

Michal Jasný[1], Michal Hajžman[2], Radek Bulín[3]

Abstract
Dog clutch without circular backlash was designed to be shifted by a standard MT/AMT gear selector mechanism. To make it compatible with selector mechanisms with kinematic endpoints (e.g., sequential shifting), additional springs between the sliding dog and sleeve were added. Two solutions using different spring types (wave and disc) are presented, including their properties and dimensions. A multibody simulation model with these additional springs was created and gearshifts examined.

1. INTRODUCTION

Dog clutch without circular backlash uses a unique and patented [1] mechanical blocking mechanism to secure it in all desired positions (engaged or neutral). This allows it to use dogs shaped in a way which would be otherwise impossible for a standard dog clutch – narrower tips than roots (Figure 1).

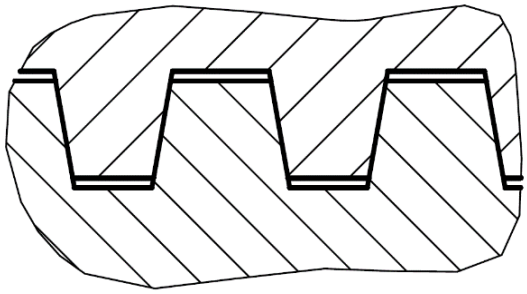

Figure 1: *Dogs with tapered sides – geometry basis.*

[1] Ing. Michal Jasný; Czech Technical University in Prague; Department of Automotive, Combustion Engine and Railway Engneering; Technická 4, 160 00 Praha 6; Michal.Jasny@fs.cvut.cz
[2] doc. Ing. Michal Hajžman, Ph.D.; University of West Bohemia; Faculty of Applied Sciences, Department of Mechanics; Univerzitní 8, 301 00 Plzeň; mhajzman@kme.zcu.cz
[3] Ing. Radek Bulín, Ph.D.; University of West Bohemia; Faculty of Applied Sciences; Department of Mechanics; Univerzitní 8, 301 00 Plzeň; rbulin@kme.zcu.cz

This allowed us to minimize the circular backlash typical for dog clutches and thereby improve the ride quality. Another advantage is the ability of disengagement under partial or full load to fasten the gearshift. However, using external synchronization is necessary. The initial design of the dog clutch with blocking mechanism was presented in paper [2]. This design was then improved based on testing and validation. An improved prototype of the dog clutch with blocking mechanism was then manufactured (Figure 2), successfully tested and proven functional.

Figure 2: *Prototype of the clutch without circular backlash.*

The clutch was initially designed to cooperate with gear selector systems based on manual or automated manual gearboxes. This paper presents a possible modification which would make the clutch compatible with sequentially shifted gearboxes.

2. DOG CLUTCH DESIGN

The clutch consists of the following parts (see Figure 3). The hub is fixed to the gearbox shaft, and the sliding gear can move axially on this hub to engage the selected gear. The gearshift sleeve controls the sliding gear movement, and finally, the blocking ring secures the sliding gear in the desired position. The sliding gear is divided into two halves and connected by screws because of assembly reasons. Just one blocking ring secures the sliding dog in all three positions (engaged/neutral/engaged) and the gearshift sleeve in the neutral position as well. No modifications of the standard gear selector mechanism are needed. The blocking ring is designed to withstand axial forces up to 3 000 N. This force arises at the dogs when transferring the maximal torque of 200 Nm. However, when acting on the gearshift sleeve, the force required for the dis/engaging the clutch is only ca. 45 N which is far less than are the permissible values and comparable with the lowest forces needed for manual shifting [3].

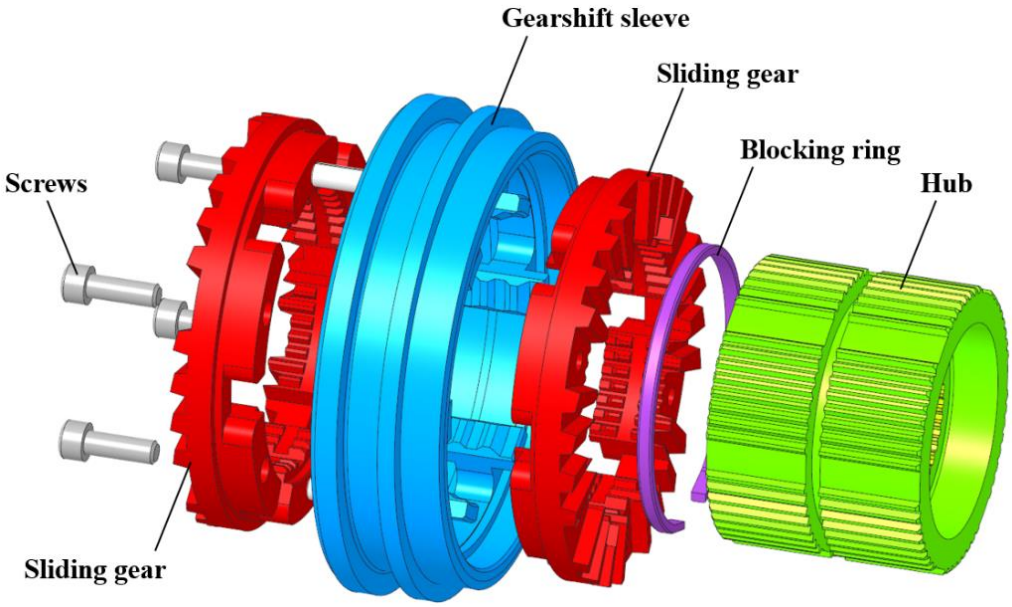

Figure 3: *Dog clutch with blocking mechanism.*

3. ADAPTATION FOR SEQUENTIAL SHIFTING

Shifting gear based on the standard MT or AMT system means that the driver or gearshift actuator acts on the gearshift mechanism until it senses that further movement is impossible, the gear is fully engaged. Only then the gearshift force is removed. This system ensures that the sliding dog is pushed to its furthest position possible and the blocking ring stretches into the desired shape. However, this scenario does not apply for a gear selector mechanism with kinematic endpoints – typically sequential shifting with a rotating gear selector drum. In this case, the furthest point of the sliding dog travel is given by the dimensional precision of many components, including the dog clutch, shaft, gearbox case, and gear selector mechanism.
The idea of adapting the dog clutch for sequential shifting is based on adding a flexible spring-like element somewhere between the sliding dog and the selector fork. As a result, the travel of the selector fork would always be longer than the travel of the sliding dog. The difference between them would be compensated by deformation of the flexible element to provide secure blocking under every circumstance.
The spring used for this purpose must meet specific requirements. Its size should be as small as possible to keep the current packaging dimensions of the clutch. It must allow large enough deformation to cover the required operating range (see Figure 4**Chyba! Nenalezen zdroj odkazů.**). The lowest deformation in the operating range must be greater than zero, otherwise the spring would provide very little force in this area. Overlap on the other side of the range is also required for safety reasons. Stiffness and force under deformation of the spring must correspond to the stiffness of the blocking ring. When the stiffness of the spring is lower than the resistance of the sliding dog against axial movement (caused mainly by the stiffness of the blocking ring at the beginning of the engagement), the spring reaches the maximal possible deformation during each shifting. This may negatively affect its service life. On the other hand, excessive stiffness would require a stronger and therefore heavier and more expensive gear selector mechanism and actuator.

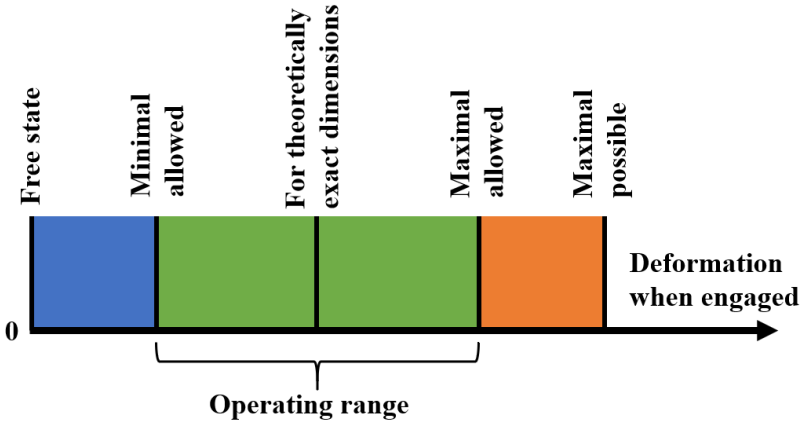

Figure 4: *Operating range of the spring.*

Investigation about the spring placement resulted in only one possible location – between the sliding dog and the gearshift sleeve. It meets the requirement of the dog clutch with the blocking mechanism being a system not requiring changes in the gear selector mechanism. For the prototype of the dog clutch and the gearbox, it is being tested in, the following parameters were selected:

- Operating range width 1.5 mm
- Maximal possible deformation 2.5 mm

4. ADDITIONAL WAVE SPRING

This solution uses two additional wave springs placed between the gearshift sleeve and the sliding dog (see Figure 5 and Figure 6). Wave springs offer high stiffness for small dimensions. On the other hand, the stress can be very high for the required maximal deformation and must be watched closely. The number of waves is three. Two waves would mean only two contact points between the spring and each adjacent component, leading to instability and uneven force distribution. More waves would lead to large stiffness and stress under deformation. Mean diameter of the spring is 66.5 mm.

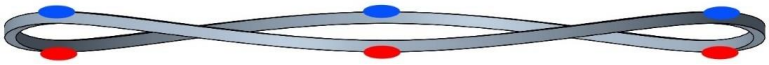

Figure 5: *Wave spring and its contact points.*

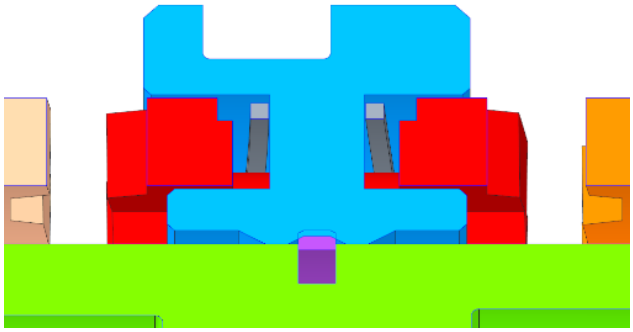

Figure 6: *Dog clutch with wave springs – cut section.*

To keep the production cost low, only single-profile springs as in Figure 5 were considered. Therefore, the design possibilities were reduced to different section

shapes and dimensions. The rectangular section was selected since it can be produced from sheet metal. Out of the various investigated dimensions, two square sections with dimensions 1 and 1.2 mm are depicted in the following figures as possibly suitable solutions. Figure 7shows the reaction force for different spring section dimensions during deformation. The force values for 1 mm deformation are equal to the spring stiffnesses, as the curves are clearly very linear. These results were obtained using a FEM model of the springs being squished between two rigid planes. The area near 2.5 mm is extrapolated – as the deformation comes to the maximal value, the stiffness rises rapidly since the spring theoretically shapes itself perfectly flat.

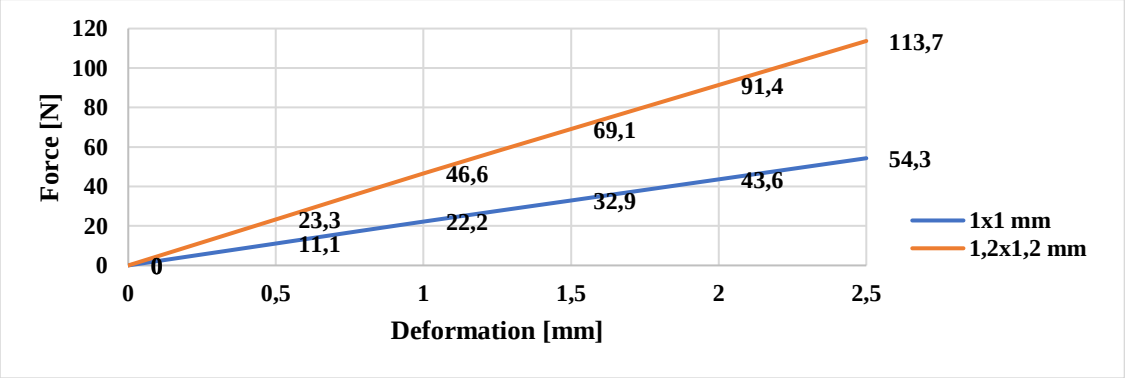

Figure 7: *Reaction force for different wave spring section dimensions during deformation.*

The 1.2 mm profile offers bigger stiffness and force, which seems more suitable since the force needed for overcoming the blocking mechanism is ca. 45 N as mentioned before. However, the stress value for the deformation of 2 mm (which is the maximal allowed value within the operating range) is quite high – around 1000 MPa for the 1.2 mm profile (see Figure 8). The 1 mm profile has smaller stress, but because of its low stiffness and reaction force, it would definitely reach its maximum deformation and stress during each shifting. Therefore, these springs would require using high-quality spring steel to secure sufficient service life.

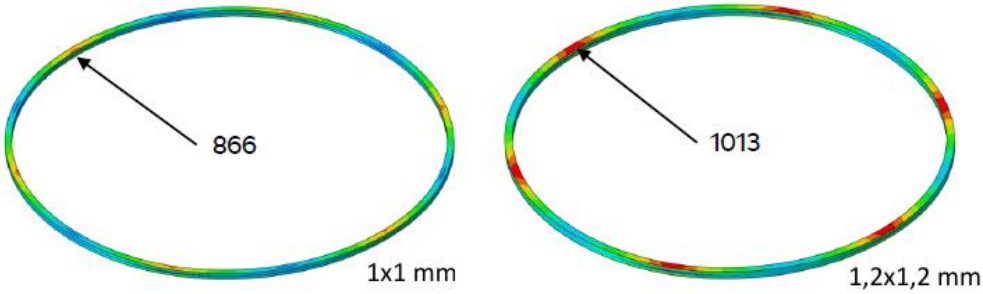

Figure 8: *Maximal stress values in [MPa] for different spring section dimensions and deformation 2 mm.*

5. ADDITIONAL DISC SPRING

This solution uses two or more additional disc springs placed between the gearshift sleeve and the sliding dog (see Figure 9 and Figure 10).

Figure 9: *Disc spring and its contact curves.*

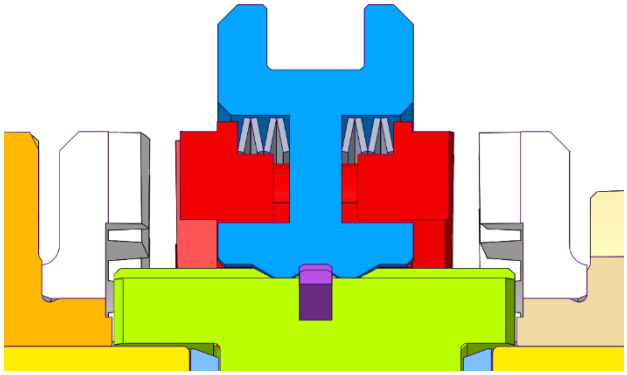

Figure 10: *Dog clutch with disc springs – cut section.*

Disc springs offer high stiffness for small dimensions as well. Probably their biggest advantage over wave springs is the possibility of using multiple disc springs in series stacking as in Figure 10. This stacking multiplies the maximal compression of one spring by the number of springs used. However, the force necessary for this compression stays the same as for one spring – visualised in Figure 11.

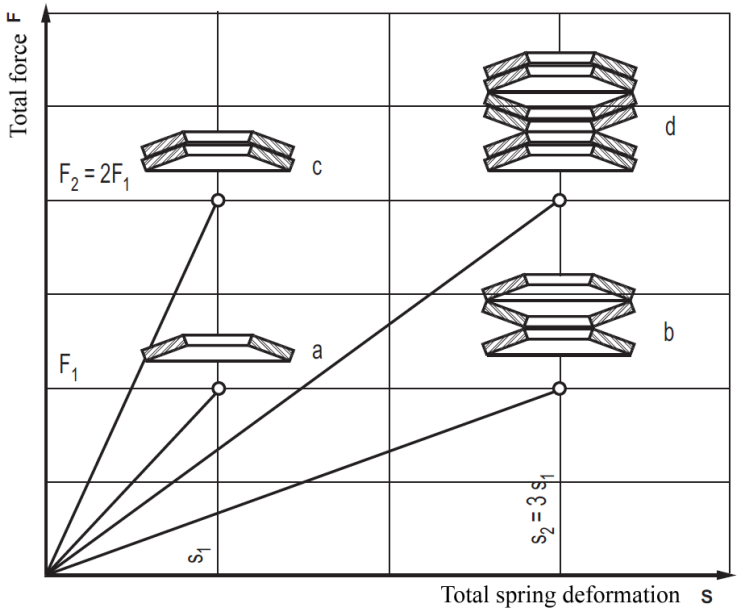

Figure 11: *Comparison of parallel and series stacking of disc springs; [4].*

This stacking is possible for the wave spring as well. However, for series stacking, the waves must be permanently connected at their contact points, otherwise they would rearrange themselves into parallel stacking because of instability. This makes disc springs a more cost-effective and versatile solution for different dog clutch designs and requirements. It also brings us to another advantage of the disc springs – better material under stress usage. Disc springs have complete contact curves around their

circumference. Their deformation is symmetric, and the stress, therefore, does not concentrate at local maximums but spreads equally instead.
Four-wave spring on each side was selected as a suitable solution. Their diameters are 70.7 mm (outer) and 65.3 mm (inner) with 0.5 mm thickness. Free height of one spring 1.125 mm gives us the required maximal deformation of 2.5 mm.

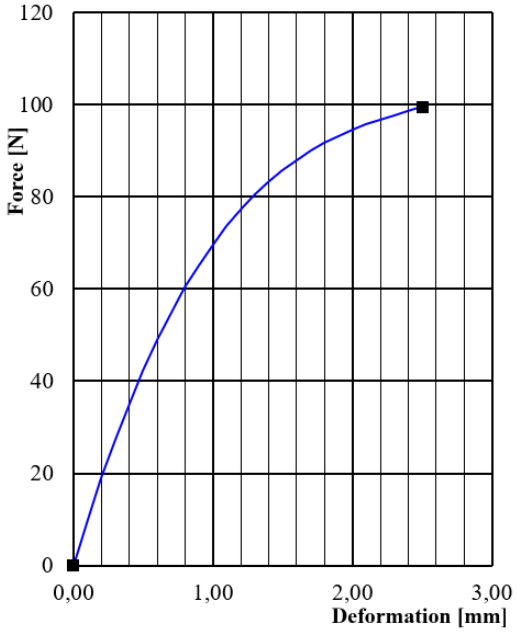

Figure 12: *Reaction force of the disc spring stack during deformation.*

Reaction forces and stress under deformation of disc springs were calculated regarding DIN 2092 – Calculation of Disc Springs. Figure 12 shows that the reaction force of the spring disc stack is not linear. However, this type of curve is favourable for our application since (a) the force in the engaged state throughout the operating range does not vary so much and (b) lower deformation is required to reach the force necessary for blocking ring compression. On the other hand, higher stiffness around the free state may result in a bigger conflict when setting the neutral position of the sliding dog.
The Neutral position of the sliding dog is affected by both the blocking ring and additional springs since both of these act on it. Our initial assumption was that the position of the engaged gearshift sleeve could vary. This means that the neutral position of the sleeve can vary as well, and the neutral position of the sliding dog will be a compromise. This effect was not examined throughout the paper, but generally, it can be said that it may be necessary to enlarge the gap between the sliding dog and shifted wheels to accommodate this neutral position uncertainty.
Stress values for 2 mm deformation find themselves between 600 and 650 MPa located on the inner and outer diameters. These values are much more favourable and can be optimized by tuning the stack properties. One disadvantage of the disc springs is bigger packaging. It may be necessary to enlarge the diameter of the dog clutch to accommodate all disc springs and still fulfil the strength requirements, especially of the sliding dog.

6. SIMULATION MODEL

The simulation model was created in the MSC Adams software based on multibody system dynamics. The multibody approach generally utilizes rigid or flexible bodies, which are connected by kinematic joints and affected by forces and torques. For details on various multibody approaches see, e.g., [5]. Figure 13 shows a kinematical scheme of the multibody simulation model. Bodies are depicted using rectangles, and joints are denoted using circles. Contact interaction between gears is introduced using nonlinear contact forces. The shifting is realized by the prescribed motion of the sleeve characterized by a constant translational velocity. The effect of the blocking ring is also defined using a nonlinear force acting on proper bodies. Linear spring is defined between the sleeve and sliding gears to represent the wave or disc springs. Further details about the model properties and its validation can be found in [6].

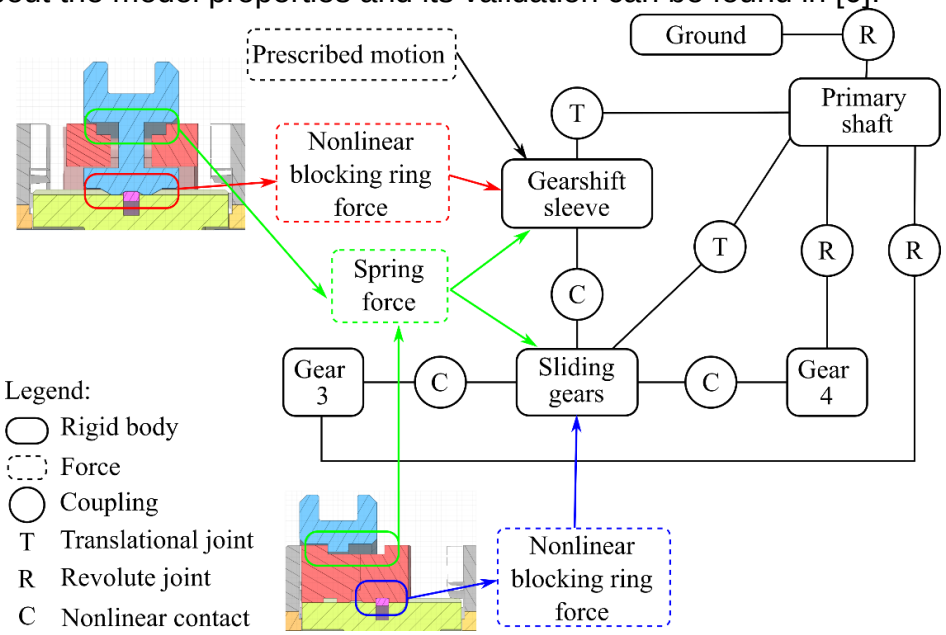

Figure 13: *Kinematical scheme of the multibody model.*

7. SIMULATION RESULTS

The following input parameters were varied:

- Additional spring stiffness 10/20/40/60 [N/mm]
- Maximal displacement of the gearshift sleeve 7/6.25/5.5 [mm]

The main target of the simulation was to confirm that the sliding dog always reaches the desired engaged position, and the blocking ring stretches to secure the engaged gear. According to the simulation, this happened successfully for all input parameters, which is a very encouraging result.

The secondary target was to investigate the effect of the input parameters on the engagement duration. The expected scenario of the sliding dog reaching the engaged position later because of additional spring compression is present. However, the highest observed delays in engagement are only roughly 0.01 s for the softest spring (see the left side of Figure 14). The oscillating movement of the sliding dog is tighter for the harder spring (see right side of Figure 14). These values are very low and lower

than expected. The negative effect of the additional spring on the engagement duration, therefore, seems to be negligible.

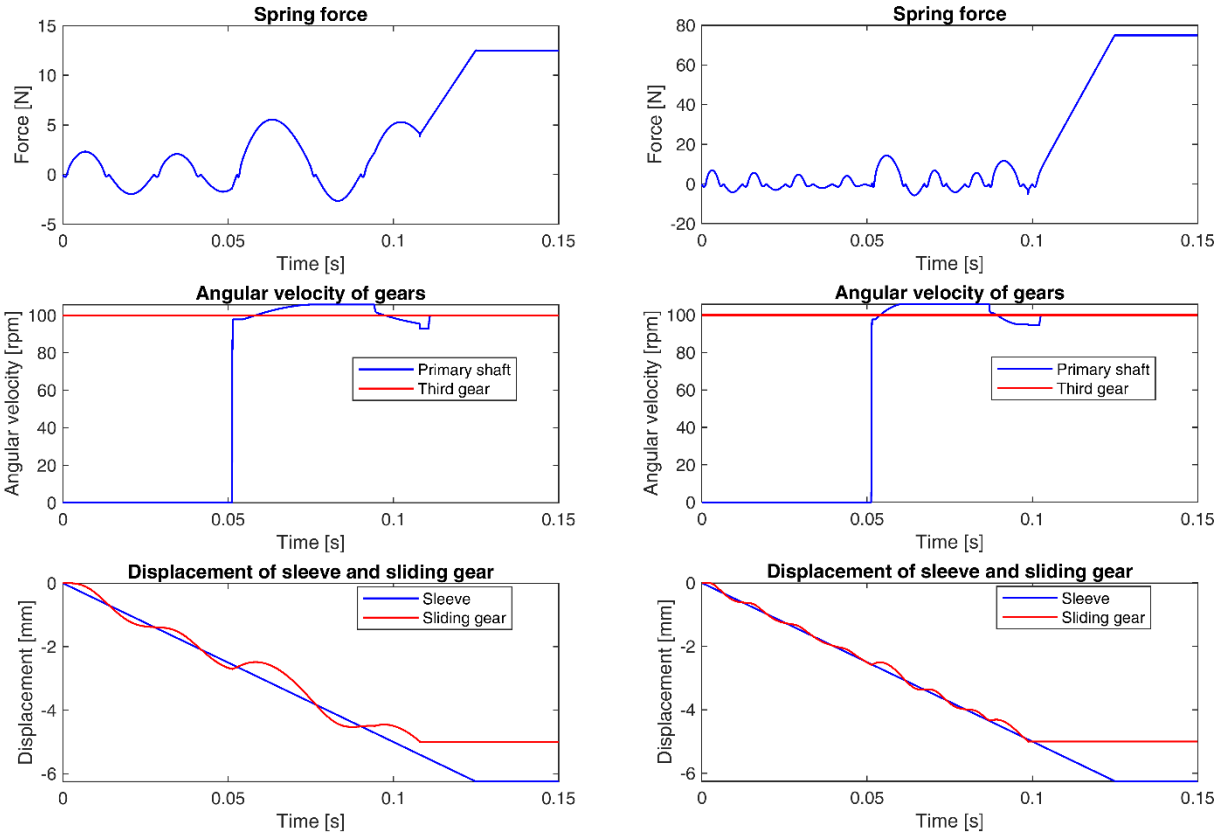

Figure 14: *Comparison of engagement with nominal gearshift sleeve displ. (6.25 mm). Left: Spring stiffness 10 N/mm. Right: Spring stiffness 60 N/mm.*

8. CONCLUSION AND FURTHER PROGRESS

Adaptation of the dog clutch to sequential shifting was proposed using two additional spring types. Disc spring seems to be more suitable than wave spring thanks to the possibility of simple and versatile stacking. This is favourable for the optimization of stiffness, maximal deformation, and stress. Results of the simulations are encouraging and indicate that the negative effect of the additional spring on the engagement should be minimal and only in terms of slightly longer duration.

However, these assumptions must be proved by testing a physical prototype. This would require changes to the dog clutch itself and modification of the test bench to make it possible to simulate the endpoints of sequential shifting.

REFERENCES

[1] ČESKÉ VYSOKÉ UČENÍ TECHNICKÉ V PRAZE, FAKULTA STROJNÍ. *Řadící spojka.* Inventors: JASNÝ, M., G. ACHTENOVÁ, J. PAKOSTA. Appl. 26. 06. 2017. MPT F 16 D 11/10. Patent No. 307443. 22. 08. 2018. Úřad průmyslového vlastnictví.

[2] ACHTENOVÁ, G., M. JASNÝ, J. PAKOSTA. *Dog Clutch Without Circular Backlash.* SAE Technical Paper 2018-01-1299, 2018, doi:10.4271/2018-01-1299.

[3] NAUNHEIMER, H., B. BERTSHCE, J. RYBORZ, W. NOVAK. *Automotive Transmissions: Fundamentals, Selection, Design and Application.* Berlin : Springer-Verlag, 2011. ISBN 978-3-642-16216-8.

[4] HENNLICH INDUSTRIETECHNIK. *Talířové pružiny - Technické parametry.* https://www.hennlich.cz/produkty/pruziny-talirove-pruziny-157/talirove-pruziny-din-2093.html.

[5] SHABANA, A.A. *Dynamics of Multibody Systems.* London : Cambridge, 2013.

[6] JASNÝ, M., HAJŽMAN, M. a BULÍN, R. *Dog Clutch Without Circular Backlash - Design Optimization Using Multi-Body Simulation.* In FISITA Web Congress 2020 - Technical Papers. https://www.fisita.com/f2020papers/f2020-adm-083.

ACKNOWLEDGEMENTS

The first author was supported by the Grant Agency of the Czech Technical University in Prague, grant No. SGS19/160/OHK2/3T/ and by Technological Agency, Czech Republic, programme National Competence Centres, project # TN01000026 Josef Bozek National Center of Competence for Surface Vehicles. This support is gratefully acknowledged.

The second and the third author were supported by European Regional Development Fund-Project „Research and Development of Intelligent Components of Advanced Technologies for the Pilsen Metropolitan Area (InteCom)" (No. CZ.02.1.01/0.0/0.0/17_048/0007267).

LII. INTERNATIONAL SCIENTIFIC CONFERENCE OF THE CZECH AND SLOVAK UNIVERSITY DEPARTMENTS AND INSTITUTIONS FOCUSED ON RESEARCH AND TEACHING METHODS RELATED TO COMBUSTION ENGINES, ALTERNATIVE DRIVES AND TRANSPORT
SEPTEMBER 22 – 23, 2021, PRAGUE
CZECH UNIVERSITY OF LIFE SCIENCE PRAGUE, FACULTY OF ENGINEERING,
DEPARTMENT OF VEHICLES AND GROUND TRANSPORT

MODELLING FRICTIONAL LOSSES OF TURBOCHARGERS DUE TO ROTOR-FLUID INTERACTION

Petr Kudláček[1], Pavel Novotný[2], Jiří Vacula[3]

Abstract
The mechanical efficiency of rotating machines is continuously increased due to improved rotor-bearing system designs. However, research activities are also gradually focusing on non-traditional sources of loss, such as frictional losses due to rotor-fluid surface interaction. The main analysis tools used are computational fluid dynamics, which evaluates the fluid flow in a lubrication system and the effect on rotating rotor walls, and analytical-empirical description of the rotating turbulent fluid flow around rotating elementary bodies. The results will allow further improvement of mechanical efficiency without increased manufacturing costs.

1. INTRODUCTION

The electric energy is a fundamental need of modern society. Any approach to achieving this need must meet the criteria of energy efficiency, safety, and long-term sustainability in addition to meeting customer requirements. The rotating machines, as a key element of the electric energy local generation, always have a significant impact on the fulfilment of these criteria. A key parameter describing the rotating machine is its efficiency of converting input energy in fuel into electric energy. The paper focuses on turbochargers (TC) considering losses due to rotating flows occurring due to rotor-fluid interaction.
In general, the total efficiency of the TC includes three components, one of which is the mechanical efficiency. The mechanical efficiency is thus an important parameter for achieving a high overall turbocharger efficiency. The mechanical efficiency of a TC includes various energy losses such as frictional losses due to friction in the oil-film bearings, the lubricant flow in the lubrication system or friction due to the rotor-fluid interaction.
The rotor-fluid interaction involves the interaction of the moving rotor surfaces with a mixture of lubricating oil, air and oil vapour. The resulting fluid, consisting of three components, is subject to three-dimensional turbulent flow. This interaction causes,

[1] Ing. Petr Kudláček, Brno University of Technology, Technická 2896/2, petr.kudlacek@vutbr.cz
[2] doc. Ing. Pavel Novotný, Ph.D., Brno University of Technology, Technická 2896/2, 61669 Brno, novotny.pa@fme.vutbr.cz
[3] Ing. Jiří Vacula, Brno University of Technology, Technická 2896/2, jiri.vacula@vutbr.cz

among other things, energy losses. These losses can be often neglected, but in some operating conditions they can reach significant values.
The aim is to analyze these losses on the rotor of a stationary engine TC by computational modeling. A description of these energy losses will allow design changes to be proposed leading to an increase in TC mechanical efficiency.

2. THEORETICAL BACKGROUND INTO ROTATING FLOWS

A fluid flow modelling for many applications is nowadays standardly performed using computational fluid dynamics (CFD). The use of CFD, as with any other modeling method, requires a critical evaluation of the physical model, boundary conditions, accuracy, and still computational cost issues. The computational cost of a CFD model is highly dependent on how many dimensions the flow is modeled and whether the flow is modeled as steady-state or transient. Other important factors are the flow characteristics, whether laminar or turbulent. Further, consideration must be given to whether it is also necessary to solve the energy equation and whether to model the energy flows across the fluid-solid boundary or multi-phase flows for example and many others.
If the phenomena can be considered steady-state and single phase, acceptable results can be obtained with relatively simpler calculations. Previous experience combined with appropriate model validation based on experimental data and theoretical solutions is useful in this assessment. CFD flow modelling is then carried out with some knowledge of the problem.
Prior to the advent of CFD, many advances in understanding related to the flow of bearings, rotating discs, or gaps between discs were achieved through a combination of theoretical, numerical, and experimental approaches. Many of the theoretical approaches have now been replaced by CFD, but only CFD approach has lost some general insight into the problem. In the following subsections, theoretical insights from laminar or turbulent flow around geometrically simple bodies rotating in fluid will be presented. This will form the basis for understanding the flow through a rotating disc for subsequent use and for evaluating results obtained by CFD.

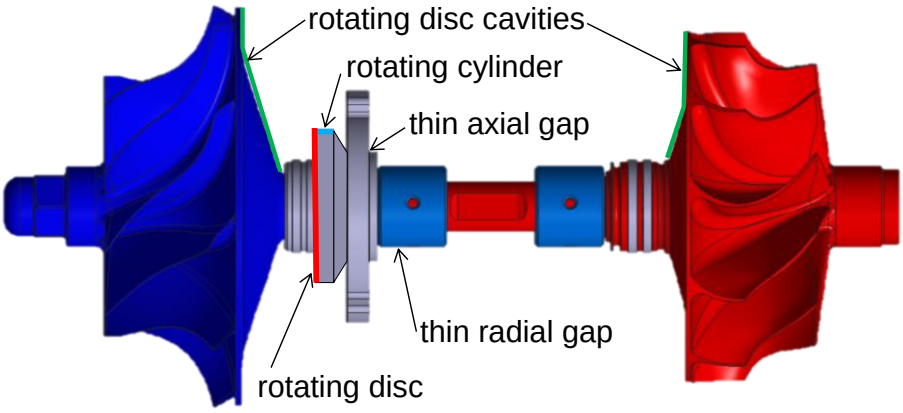

Figure 1: Identification of geometrically simple fluid-body interactions on a typical turbocharger rotor.

Geometrically simple fluid-body interactions can also be identified on the rotor of a typical TC as is presented in Figure 1. The larger diameter ring used for speed sensing can be characterized as a rotating disc in the fluid, the shaft as a cylinder rotating in the fluid, and the gap between the impellers and the stator part as a rotating gap between two discs. The lubricant flow in oil-film hydrodynamic bearings can also be described simplistically using analytical relations for thin radial or axial gaps derived for simplifying assumptions.
An overview of effects of base design dimensions and angular velocity on the power losses for geometrically simple bodies rotating in the fluid is presented in Table 1 and further described in the following subsections.

Table 1: Review of friction power losses P_f dependency on simple geometry dimensions including diameter d, width b, gap thickness c and angular speed ω assuming analytical and empirical equations.

	thin radial gap	axial gap	rotating disc	rotating cylinder
Schema	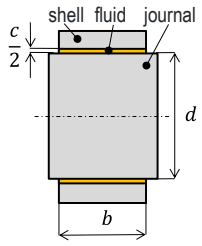	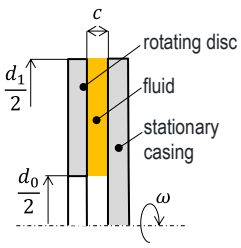	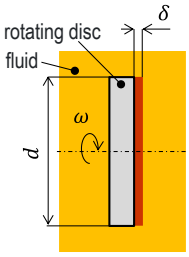	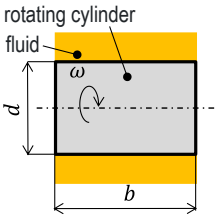
Friction power loses P_f	$\sim\omega^2 b d^3$	$\sim\omega^2(d_1^4 - d_0^4)$	$\sim\omega^{3.5} d^6$	$\sim\omega^3 b d^4$
Fluid flow	laminar	laminar	turbulent	turbulent
Reference	Stachowiak and Batchelor [1]	Childs [2]	Childs [2], Von Kármán [3]	Theodorsen and Regier [4]

2.1 Oil-film Bearings

Oil-film hydrodynamic bearings in many configurations are often used for TC rotor bearings. It is possible to use some simplification when the frictional losses are estimated and these losses can be described by analytical relationships.
A journal bearing consists of a shaft that rotates inside a housing. Due to the eccentricity of the rotating shaft, a wedge gap filled with a thin lubricating film is created and a hydrodynamic pressure is generated. A hydrodynamic film is formed between the moving surfaces of the shaft and the housing. With the simplification defined, for example, by Stachowiak and Batchelor [1], the following relation for the calculation of the friction power loss can be obtained

$$P_{\mathrm{f,jb}} = \frac{\pi\eta\omega^2 b d^3}{4c_{\mathrm{rad}}(1-\varepsilon^2)^{0.5}}, \tag{1}$$

where η is the dynamic viscosity, ω is the angular velocity of rotor, d is the journal diameter, b is the shell width, c_{rad} is the radial bearing clearance and ε is the journal eccentricity.
A similar procedure can be followed in the case of thrust bearings. To estimate the frictional power losses, the thrust bearing can be thought of as a ring rotating relatively to the non-moving wall and forming a thin lubricating gap. The shear stress component in the lubrication film due to the pressure gradient can be neglected and the resulting estimate of the power loss can be analytically derived in the form

$$P_{\mathrm{f,tb}} = \frac{\pi\eta\omega^2}{32c_{\mathrm{ax}}}(d_1^4 - d_0^4) \ . \tag{2}$$

Symbols d_0 and d_1 denote the inner and outer diameters of the bearing work surface and c_{ax} is the axial clearance.
Equations (1) and (2) are valid under the assumption of laminar flow, i.e. when the Reynolds number is less than approximately 1000. In general, for thin gaps of thickness c, the Reynolds number is defined as

$$R_{\mathrm{e}} = \frac{\rho c\omega d}{2\eta} \ . \tag{3}$$

where ρ is the fluid density.

2.2 Rotating Disc

Rotating discs are used in a variety of engineering applications such as gas turbine engines, flywheels, gearboxes and brakes. Assessment of the flow associated with the discs is also important in the case of TC rotors. The shear stress between the disc and the fluid in which it rotates determines the power required to drive the disc and overcome frictional drag. The local flow field also affects heat transfer. Unfortunately, several factors have to be also considered to use any universal analysis, the flow conditions and proximity of the local geometry must be taken into account. In the case of a free rotating disc with a radial outflow, the power loss can be determined using the relationship defined by Childs [2]

$$P_{\mathrm{f,d}} = \frac{1}{64}c_{\mathrm{m}}\rho\omega^3 d^5 \ . \tag{4}$$

In this case the symbol d denotes disc diameter and c_{m} the moment coefficient. The moment coefficient can be estimated for fully laminar flows by equation defined by Childs [2]

$$c_{\mathrm{m}} = 1.935{R_{\mathrm{e},\phi}}^{-0.5} \tag{5}$$

and in the case of turbulent flow over a free disk, the Von Kármán relation [3] can be used

$$c_{\mathrm{m}} = 0.073{R_{\mathrm{e},\phi}}^{-0.2} \ . \tag{6}$$

The symbol $R_{e,\phi}$ represents the rotational Reynolds number and can be defined as

$$R_{e,\phi} = \frac{\rho \omega d^2}{4\eta} \quad . \tag{7}$$

The transition between laminar and turbulent flow can occur locally if the local value of the rotational Reynolds number reaches the critical value $R_{e,\phi,crit} = 2 \cdot 10^5$.

2.3 Rotating Cylinder

Rotating cylindrical bodies in the fluid are also common parts of many machines. During the cylinder rotation, a boundary layer is formed due to a non-slip condition on the surface of the body. At low values of the rotational Reynolds number, the flow will be laminar. As the value of the Reynolds number increases, the flow regime will become transient and then turbulent. The approximate limit for laminar flow is a rotational Reynolds number somewhere between 40 and 60 [2]. The frictional losses of the rotating surface are negligible in most cases. However, if there is an increase in speed and diameter these losses can have a significant effect. Experimental investigations of frictional losses due to cylinder rotation have been carried out by Theodorsen and Regier [4], resulting in the following empirical relationship for the moment coefficient in the case of turbulent flow

$$c_{mc} = \left(\frac{1}{-0.8572 + 1.25 \ln(R_{e,\emptyset} \sqrt{c_{mc}})} \right)^2 \quad . \tag{8}$$

In this case, the moment coefficient must be calculated in an iterative manner. The resulting estimate of the power loss due to cylinder surface friction can be determined according to Childs [2] as

$$P_{f,c} = c_{mc} \rho \omega^3 d^4 b \quad . \tag{9}$$

3. MODELLING THE FLUID FLOW AROUND ROTATING ROTOR

A detailed CFD computational model of the TC lubrication system is used to verify mechanical losses under the preferred operating conditions and verify design changes on the TC rotor. The results are evaluated from a steady-state operating condition, including a combination of the maximum rotor speed and the corresponding lubricating gap thicknesses of thrust and journal oil-film bearings.
The operating conditions of the bearings have been obtained using the virtual turbocharger strategy introduced by Novotný et. al [5; 6]. The CFD computational modelling strategy for the bearings, i.e. turbulence modelling, boundary conditions, heat transfer lubricant properties etc., is adopted from the work presented by Novotný and Hrabovský [7]. Steady-state operating conditions used for the CFD solution of the TC lubrication system are presented in Table 2 and input and output quantities are graphically illustrated in Figure 2. The operating fluid is considered as three-phase

mixture of oil, air and oil vapour. The material properties of the mixture components are generally temperature-dependent; for a quantitative assessment, values are given in Table 2. The Rayleigh-Plesset model [8] is used to predict possible locations with cavitation occurrence. The material properties of the mixture components are generally temperature-dependent; for a quantitative assessment, values for 60°C (for oil) and 25°C (for air) are given in Table 2.

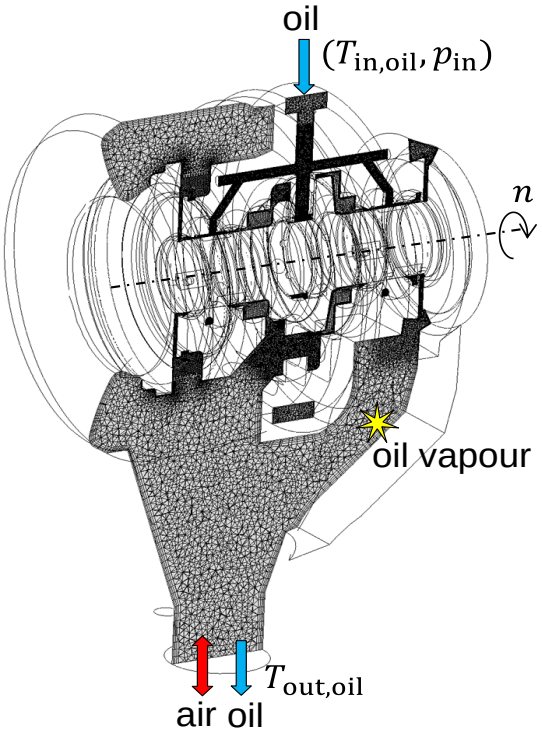

Figure 2: Scheme of input and output quantities defined for steady-state CFD simulations.

Table 2: Operating conditions and mixture component material properties defined for steady-state CFD simulations of the TC lubrication system under preferred design operating conditions at maximal rotor speed.

Operating condition and fluid material properties	Value
Oil temperature at inlet, $T_{\mathrm{in,oil}}$ [°C]	60
Oil absolute pressure at inlet, p_{in} [bar]	2.7
Oil density at 60°C [$\mathrm{kg \cdot m^{-3}}$]	805
Air density at 25°C [$\mathrm{kg \cdot m^{-3}}$]	1.185
Oil vapor density at 60°C [$\mathrm{kg \cdot m^{-3}}$]	0.0231
Oil dynamic viscosity at 60°C [$\mathrm{Pa \cdot s}$]	0.0384
Air dynamic viscosity at 25°C [$\mathrm{Pa \cdot s}$]	$1.831 \cdot 10^{-5}$
Oil vapour dynamic viscosity at 60 °C [$\mathrm{Pa \cdot s}$]	$9.863 \cdot 10^{-6}$

4. RESULTS

The CFD computational model allows to analyze the mixture formation in different parts of the rotor-fluid interactions. In principle, only the oil component is present in the lubricating system before entering the bearings, realistically with the exception of a certain proportion of air not separated at the inlet of the lubrication system. In the other parts of the lubrication system, mainly due to the rotation of the shaft, there is a significant mixing of all the fluid components with a strong influence of the air from the lubrication system outlet. The composition of the mixture in the vicinity of the rotating surfaces has a major impact on the frictional moment causing losses.

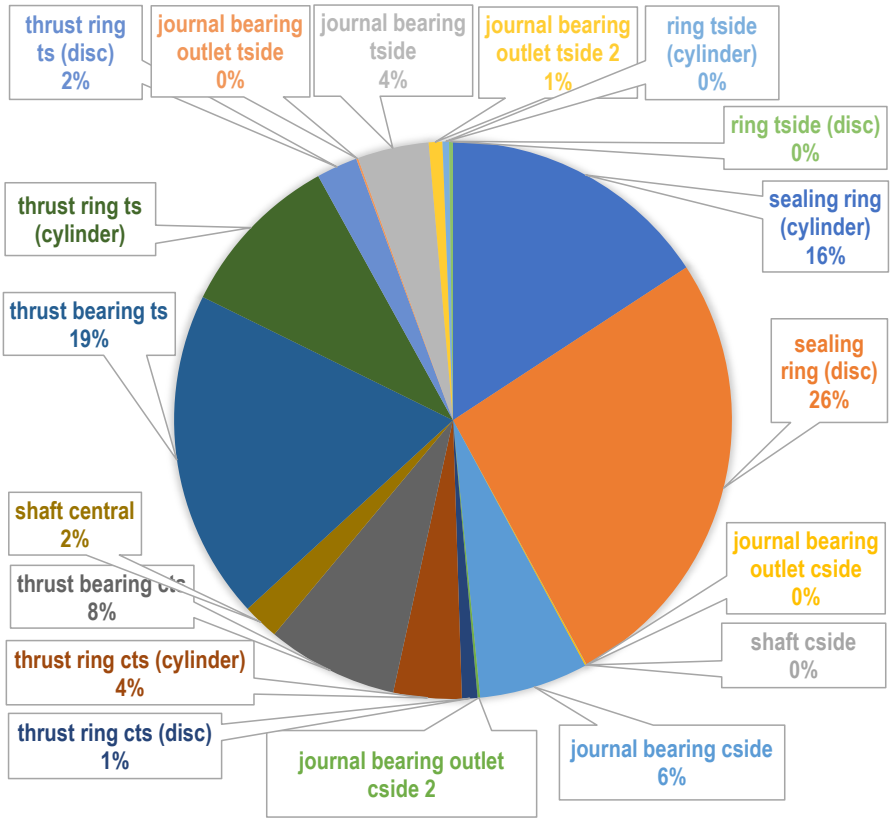

Figure 3: A distribution of friction power losses on rotating walls, shortcut ts denotes the thrust-side, cts the counter thrust side, tside the turbine side, cside the compressor side, a cylinder denotes cylindrical surfaces of the rotor components and a disc denotes axis normal surface of the rotor components.

The friction power losses can be evaluated for any rotating rotor wall, the friction losses ratios of the analysed TC are presented in Figure 3. Figure 4 presents the shear stress distribution on the rotor rotating walls interacting with the mixture. Figure 4 also presents the normalized velocity vectors of the oil component flow in the casing projected tangentially in the cutting plane.

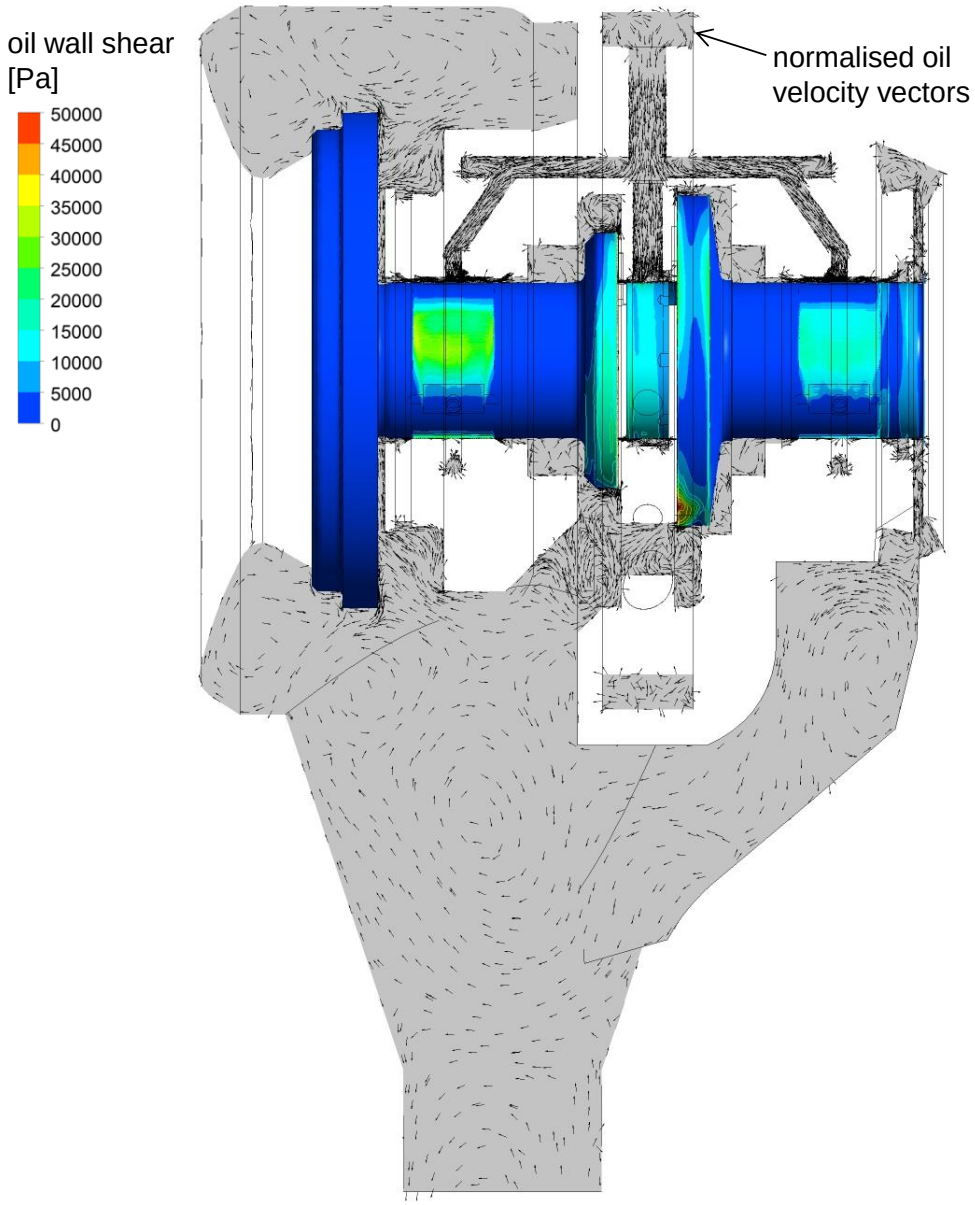

Figure 3: CFD solution results of design operating conditions at maximal rotor speed presenting a distribution of oil wall shear stresses on rotating rotor walls and normalised oil velocity vectors in cutting plane.

Computational methods generally assume some simplifications of the description of a given physical problem, including inaccuracies caused by a numerical solution. However, in practice, a factor that then determines the correctness of the lubrication system design is a technical experiment. Based on the measured lubricant temperature rise and lubricant flow rate, the power loss of the lubrication system is determined according to

$$P_{\mathrm{f,tc}} = \rho \dot{V}_{\mathrm{tc}} c_{\mathrm{p}} \Delta T_{\mathrm{tc}} + \dot{Q}_{\mathrm{w}} \,, \tag{10}$$

where ρ is the oil density, $\dot{V}_{\mathrm{tc}}$ is the TC volume flow rate, c_{p} is the specific heat capacity and $\dot{Q}_{\mathrm{w}}$ is the heat flux through surrounding walls.

The increase in lubricant temperature as it passes through the TC lubrication system is shown in Table 3 and compares the computational determination of values by means of a CFD model and the experimental determination of the lubricant heating by measuring the temperature of the lubricant at the inlet and the outlet TC by means of a measuring system.

Table 3: Computed and measured power losses by oil flow as it passes through the TC lubrication system under preferred design conditions.

Operating condition and fluid material properties	Value
Computation, $P_{\mathrm{f,comp}}$ [W]	12 755
Measurement, $P_{\mathrm{f,meas}}$ [W]	12 660

5. CONCLUSIONS

The results determined by the experimentally verified CFD model allow to focus on the key components of the TC rotor. If the oil-film hydrodynamic bearings are omitted, the important components are mainly the outer cylindrical surface of the thrust ring on the thrust side of the thrust bearing and the seal ring. This finding is not surprising since similar conclusions can already be drawn based on the analytics defined in the theory background.

ACKNOWLEDGEMENT

The research leading to these results has received funding from the Specific research program at Brno University of Technology, reg. no. FSI-S-20-6267 and has been realised with kind support of project Josef Bozek National Center of Competence for Surface Vehicles, reg. no. TN01000026.

REFERENCES

[1] STACHOWIAK, Gwidon W. and Andrew W. BATCHELOR. *Engineering Tribology*. Fourth edition. Waltham, USA: Elsevier, 2014. ISBN 978-0-12-397047-3.

[2] CHILDS, Peter R.N. *Rotating Flow*. 1st Edition. Oxford: Elsevier Inc., 2011. ISBN 978-0-12-382098-3.

[3] KÁRMÁN, Th. V. Über laminare und turbulente Reibung. *ZAMM - Journal of Applied Mathematics and Mechanics / Zeitschrift für Angewandte Mathematik und Mechanik*. 1921, **1**(4), 233-252. ISSN 00442267.

[4] THEODORSEN, Theodore and Arthur REGIER. Experiments on Drag of Revolving Disks, Cylinders, and Streamline Rods at High Speeds. *NACA Technical Report*. 1977, (793), 367-384.

[5] NOVOTNÝ, Pavel, Petr ŠKARA and Juraj HLINÍK. The effective computational model of the hydrodynamics journal floating ring bearing for simulations of long transient regimes of turbocharger rotor dynamics. *International Journal of Mechanical Sciences*. 2018, **148**, 611-619. ISSN 0020-7403.

[6] NOVOTNÝ, P., J. HRABOVSKÝ, J. JURAČKA, J. KLÍMA and V. HORT. Effective thrust bearing model for simulations of transient rotor dynamics. *International Journal of Mechanical Sciences*. 1, 2019, **2019**(157-158), 374-383.

[7] NOVOTNÝ, P. and J. HRABOVSKÝ. Efficient computational modelling of low loaded bearings of turbocharger rotors. *International Journal of Mechanical Sciences*. 2020, **2020**(174), 105505.

[8] BAKIR, F., R. REY, A. G. GERBER, T. BELAMRI and B. HUTCHINSON. Numerical and Experimental Investigations of the Cavitating Behavior of an Inducer. *International Journal of Rotating Machinery*. 2004, **10**(1), 15-25. ISSN 1023-621X.

LII. INTERNATIONAL SCIENTIFIC CONFERENCE OF THE CZECH AND SLOVAK UNIVERSITY DEPARTMENTS AND INSTITUTIONS FOCUSED ON RESEARCH AND TEACHING METHODS RELATED TO COMBUSTION ENGINES, ALTERNATIVE DRIVES AND TRANSPORT
SEPTEMBER 22 – 23, 2021, PRAGUE
CZECH UNIVERSITY OF LIFE SCIENCE PRAGUE, FACULTY OF ENGINEERING,
DEPARTMENT OF VEHICLES AND GROUND TRANSPORT

HEAT EXCHANGER THERMAL-CYCLE DURABILITY IMPROVEMENT

Josef Lapčík[1], Ľuboslav Kollár[2],

Abstract
Vehicle Heat Exchanger (HEX) used for engine cooling is facing increasing Thermal-Cycle durability requirement. This requirement is driven by changes like coolant loop electrification, more demanding drive cycle definition or non-homogeneity in airflow distribution. Demands are increased also with more frequent HEX U-flow configuration and HEX Combo-Cooler construction, where more than one cooling circuit are integrated. Current HEX construction technology (Controlled Atmosphere Brazing) is described including limitations. Design of HEX must be adapted to cope with these new requirements. Design combining current high efficient CAB technology with flexible mechanical assembly in critical places is described.

1. INTRODUCTION

Heat Exchanger is important part of engine cooling circuit. We can find HEX in all current types of vehicles – those with combustion engine, hybrid engine and electric engine as well. Current HEX are well optimized for heat performance efficiency and their construction is designed for mass production. HEX validation specification consist from several tests reflecting required vehicle durability.
Thermal-Cycle durability test is part of validation for several years. This requirement generally asked for cycling of hot and cold coolant or environment condition for several hundreds of cycles - testing this way HEX durability against dynamic temperature changes.
Especially German OEMs are increasing these requirements in recent years, which is driven by several factors:

- Coolant loop electrification - application of electric valves and electric pumps in cooling circuit -> sharper coolant switching
- Requirement for faster engine heating-up
- Driving conditions with more frequent Start-Stop operation
- Hybrid engine operation switching between combustion and electric engine
- Cooling module air-flow distribution non-homogeneity

[1] Josef Lapčík, Hanon Systems Autopal Services s.r.o., Závodní 1007 Hluk, jlapcik@hanonsystems.com
[2] Ľuboslav Kollár, Hanon Systems Autopal Services s.r.o., Závodní 1007 Hluk, lkollar@hanonsystems.com

There are two major Thermal cycle test procedures used by OEMs:

A. **Water-Water test procedure**, where is cycled hot and cold coolant and main parameters are defined as:
   - Coolant top and bottom temperature range (example 130 °C and -10 °C)
   - Coolant flow rate
   - Length of hot and cold cycle (not always the same time)
   - Speed of temperature ramp-up at beginning of hot cycle

   HEX is placed in chamber with stable ambient air temperature. Failure occurs once there is coolant leakage.

B. **Water-Air test procedure**, where cold cycle is driven by cold air passing through HEX core, while coolant flow is stopped:
   - Coolant temperature (example 130 °C)
   - Air chamber temperature (example -10 °C)
   - Coolant flow rate
   - Length of hot and cold cycle (not always the same time)
   - Speed of temperature ramp-up at beginning of hot cycle

   HEX is placed in chamber with defined low air temperature. Once hot cycle is finished, at defined time or at defined changeover criteria, hot coolant is stopped and FAN is turned ON cooling down HEX.

HEX must withstand particular number of cycles under specified test procedure. Between described test procedures can be made correlation, which is based on comparative results or on strain measurement at core critical areas and re-calculation.
HEX is built from components shown on Figure 1 and 2 below:

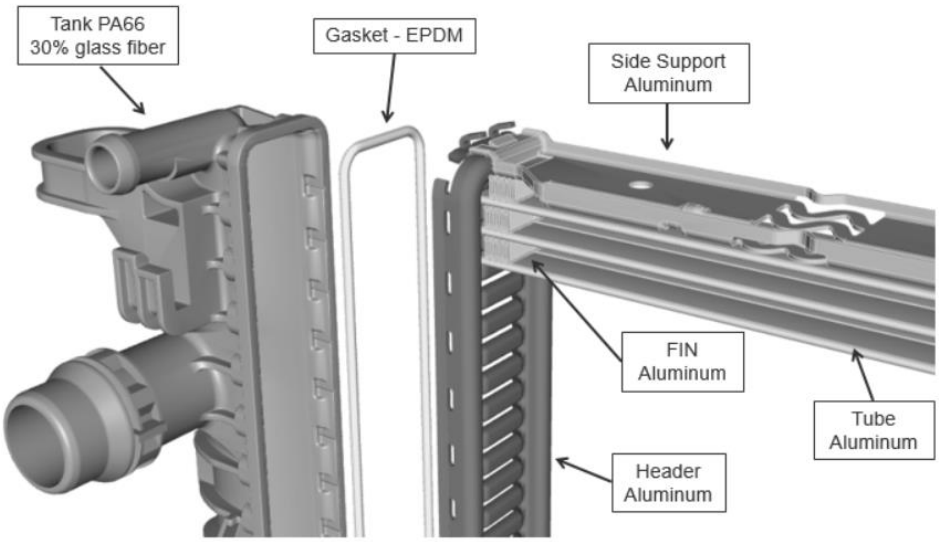

Figure 1: *HEX Assembly expanded view*

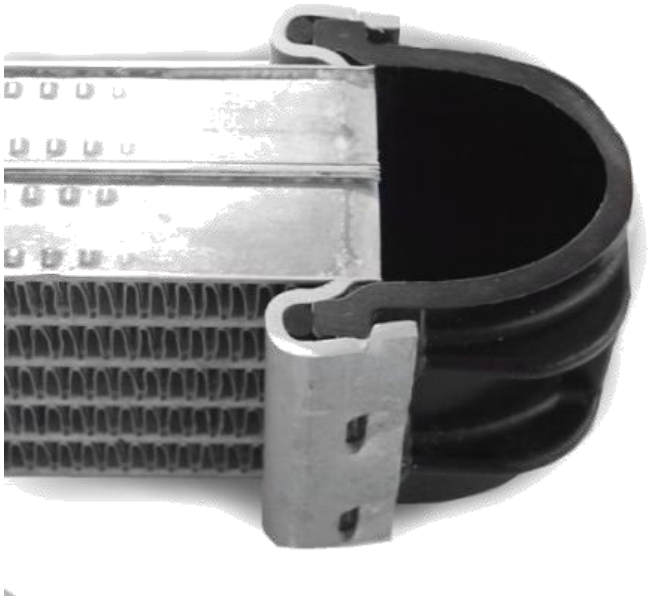

Figure 2: *HEX Sectional view*

Aluminum core is brazed by CAB (Control – Atmosphere - Brazing). During Thermal cycling tubes are spreading and shrinking with thermal expansion … thermal expansion rate directly correlates with heating-up / cooling-down profile on HEX core. This profile is not homogenous – is dependent on HEX flow configuration and on coolant flow footprint across core area. All tubes are brazed on both sides with headers = rigid components collecting all the tubes. With unequal tubes thermal expansion are inevitably emerging strains at tube to header brazed connection.
On Figure 3 below you can see examples of heating-up temperature footprint on various flow configurations … I-flow (coolant flows directly from one side to other), U-flow (coolant inlet and outlet are on the same HEX side) and Combo-Cooler.
From described flow configurations is obviously more sensitive U-flow version than I-flow as there are generated high strains in the middle of the core, where can be seen high thermal gradient at certain times of thermal cycle. And it is still not the worst possible scenario, which can be implemented. On the market are requested so-called Combo-Cooler heat exchangers, which combine two cooling circuits in single HEX core. In this special case must be simultaneously cycled temperature at both sections creating this way even more strain-critical areas. Combo-Cooler configuration can be seen on Figure 4 below.

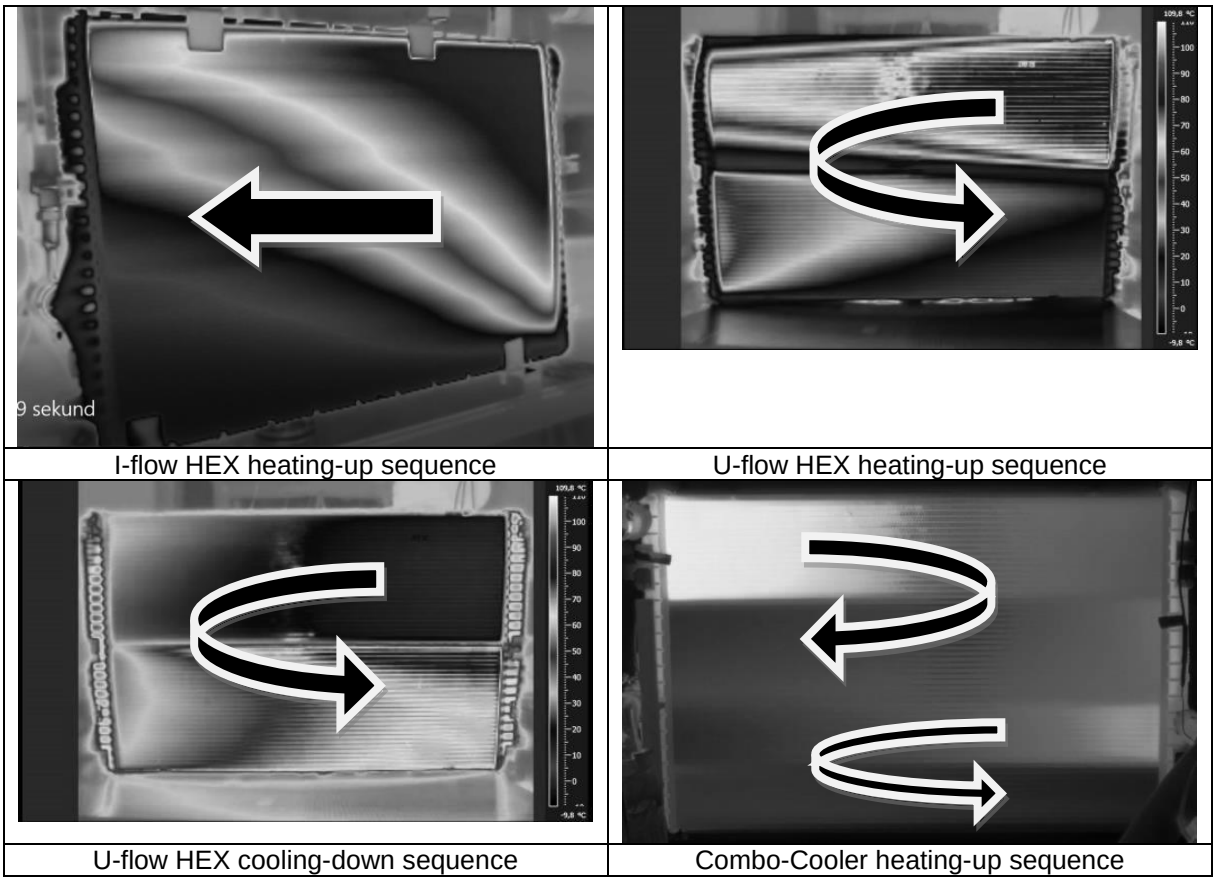

Figure 3: *Temperature footprint from thermal-camera on various HEX (water/water rig)*

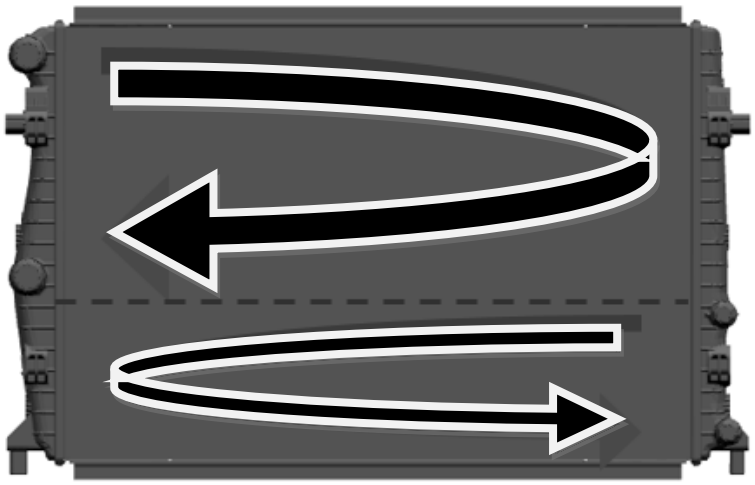

Figure 4: *Combo-Cooler HEX flow configuration example*

2. CAB TECHNOLOGY LIMITS

Current CAB technology is facing its physical limits and struggle with increasing thermal-cycle demands. This pressure is getting even more difficult consider the general market pressure on price leading to further material downgauge on components – especially on tubes. Tubes thinner material means shorter path for crack propagation. Thinner material is changing strains distribution across core as well – although we could consider thinner material as more flexible, higher flexibility means also higher deformations in area of connection with header and deformations are contributing to failure. Statistical data are supporting conclusion lower material thickness = lower durability on thermal cycle.

Higher thermal cycle requirements as one of the main life cycle parameter was evaluated together with its variability. There was indicated range of thermal cycles measured on same batch of samples with identical design features. This range is referred to as variability. All the measured sets of samples are evaluated by its average value of achieved thermal cycles and variability in percentage related to its initial design. This analysis allows to compare different radiator models and its modification shown on Figure 5.

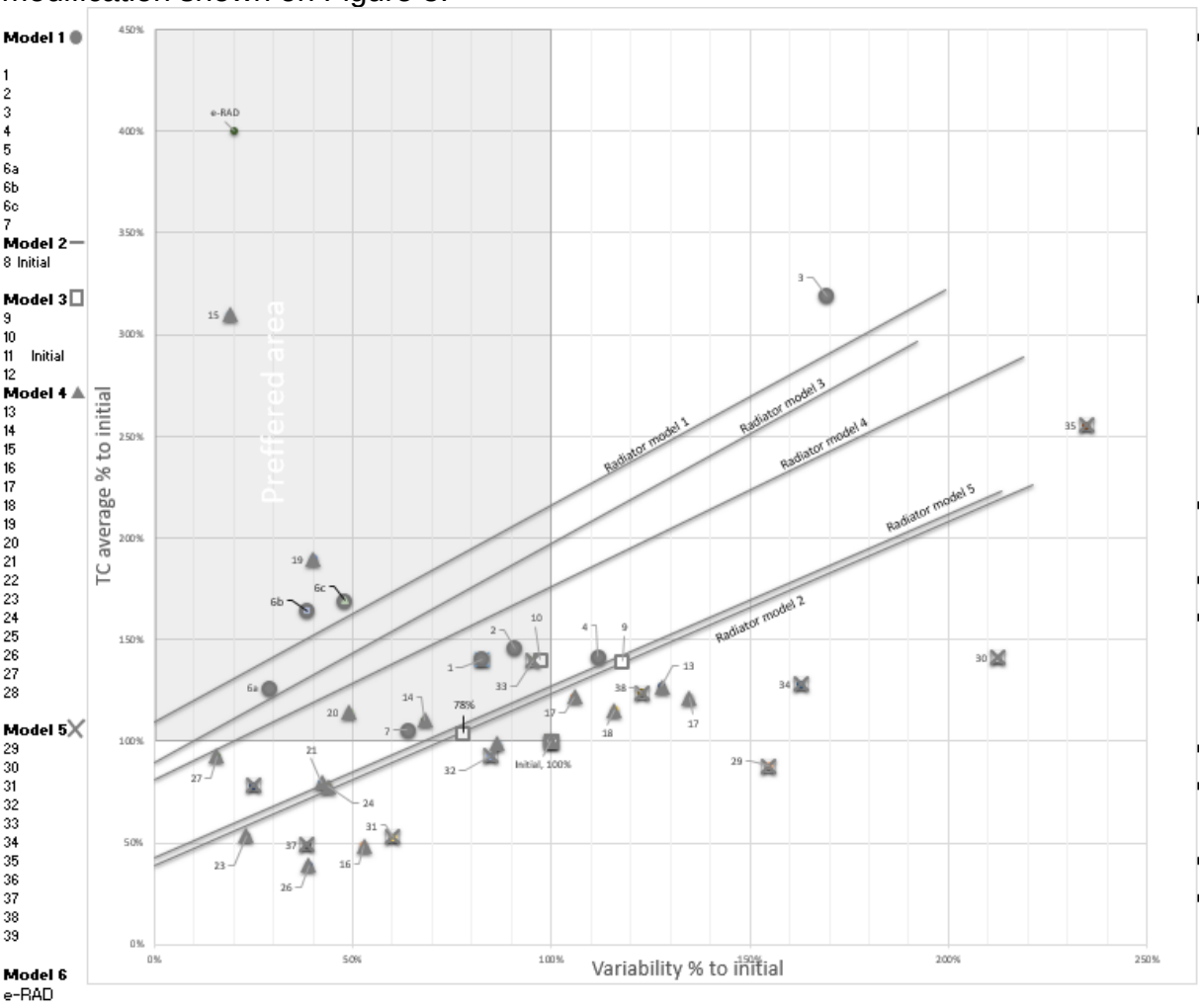

Figure 5: *Percentage thermal cycle vs. variability comparison chart of different radiator designs.*

Each line represents different radiator model produced by CAB technology. All the lines starts at minimum specified thermal cycle requirement TC_0 assuming 0% of variability. Which means all the samples of the batch achieve this value of thermal cycles as ideal case. Including the variability factor to the nominal value we get the linear function of

TC_v =f(variability) [%]. (1)

This define increase TC limit to reach required number of TCs all samples with specific level of variability.
Variability is defined as a standard deviation of thermal cycles std(TC) for sample batch with identical design features.
Assuming normal distribution of data we know 34% resp. 68% of values to be in ±1σ.
Determining of limit value thermal cycle including variability can be calculated as follow

$TC_v=TC_0+3*\sigma$ [cycle] (2)

where σ=std(TC) (3)

Acceptable level of achieved level of thermal cycles of identical design test batch is over the appropriate line. The area of the chart which is preffered for improvements is in variability less than 100% on x axis and TC on Y axis over the 100% compared to initial design and over the apropriate designe line.

Comparing all radiator models with all design modifications we can select only few with significant improvement regarding to thermal cycles level on CAB design technology. These are also demanding higher material or process cost. e-RAD™ technology, which will be described later, is shown on the same chart to compare with CAB. It represents highest TC level and promising results of this technology for difficult requirements of life cycle conditions.

2.1 Approach to solution

As already described HEX core critical places are located at Tube to Header brazed connection at areas, where core is facing high thermal gradient during certain times of Thermal cycle. You can see detail of tube failure on Figure 6.
Standard approaches to mentioned problem are mostly built on tube reinforcing by additional components, which is already increasing core assembly complexity.
OEMs are noticing issues with Thermal cycle requirement and there is increasing focus on question *how this can be solved fundamentally and how to overcome CAB technology limits.*

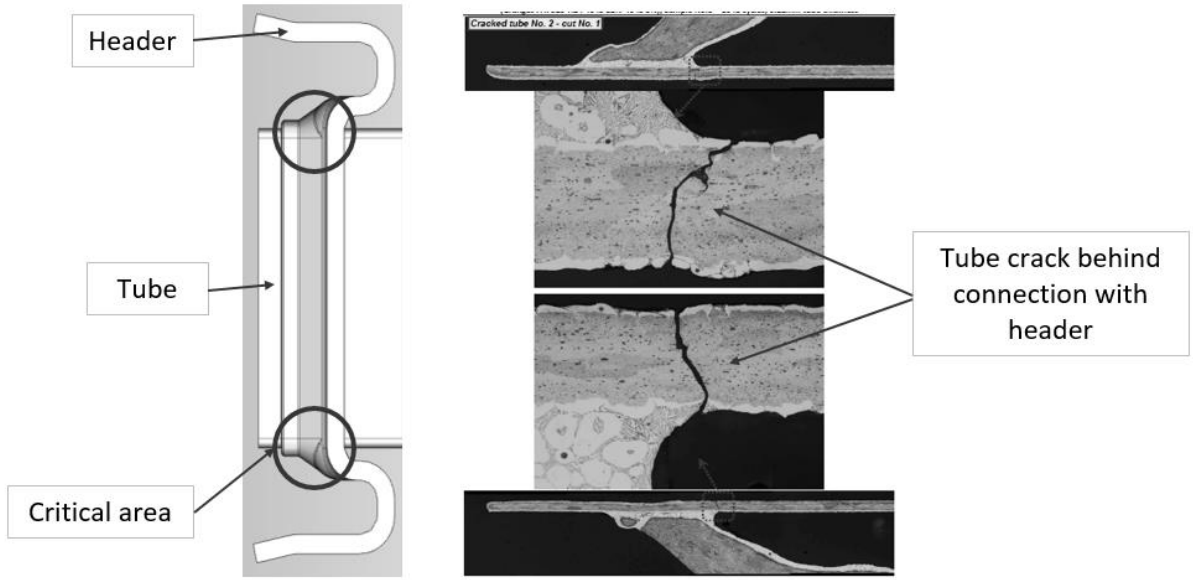

Figure 6: *CAB Core – detail of failure location*

Beside standard CAB Heat Exchangers, market knows also chronologically older MAAR technology (Mechanically Assembled Aluminum Radiator). *In MAAR Technology, there is no brazing at all* – connection between tubes and header is based on compressed gasket, which needs to be specifically designed. Tube / Gasket / Header connection, shown on Figure 7, has flexibility eliminating strains we know from CAB core. During tube thermal expansion and shrinking, tube can move in gasket and there is not generated tension causing failure with material fatigue.

On the other hand - MAAR technology is using mechanical connection also between tubes and FINs, which, together with some other design factors, means lower performance efficiency (through limited heat conduction between tubes and fins – non proper contact). Low performance efficiency (oversizing the HEX Core) is reason why MAAR technology, as we know it, is by some OEMs considered as obsolete.

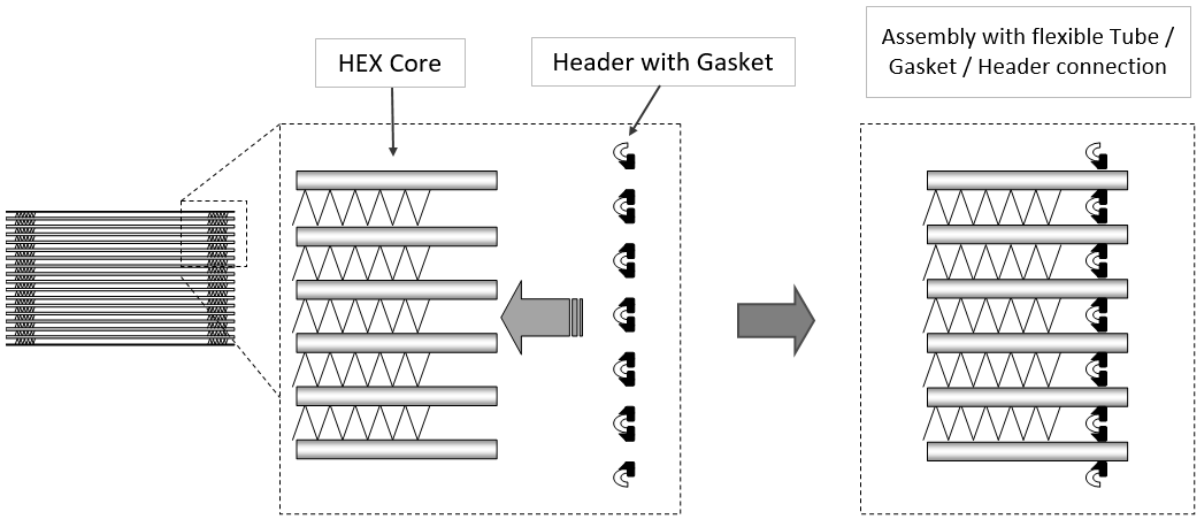

Figure 7: *MAAR construction concept*

To bring solution for Thermal cycling increasing requirements, while keeping current high CAB technology performance efficiency, Hanon is introducing technology combining brazed core with flexible Tube / Gasket / Header connection.

3. HANON E-RAD™

Hanon defined these basic expectations:

- Brazed connection between Tubes and Fins securing high thermal performance efficiency
- Flexible connection between Tubes and Headers made with integrated Gasket
- Keep comparable durability under all remaining validation tests

Although expectations seem simple, their integration is complicated task. HEX market is sector of automotive mass production, which is highly standardized, requires TOP level of serial production reliability and is under constant pressure to keep prices low.

There were several stages of e-RAD (enhanced-RAD) development:

3.1 Stage A: Tube selection and geometry

Not all tubes used in CAB technology can be integrated to mechanical connection through compressed gasket. Mainly tube capability to keep gasket in required compression is factor-influencing selection.
In CAB tube portfolio, welded and extruded tubes are optimal options providing smooth external surface and allow forming capable to keep gasket in compression.

Tube dimensions and particular tube-end forming were subject of FEA – see. Example on Figure 8.

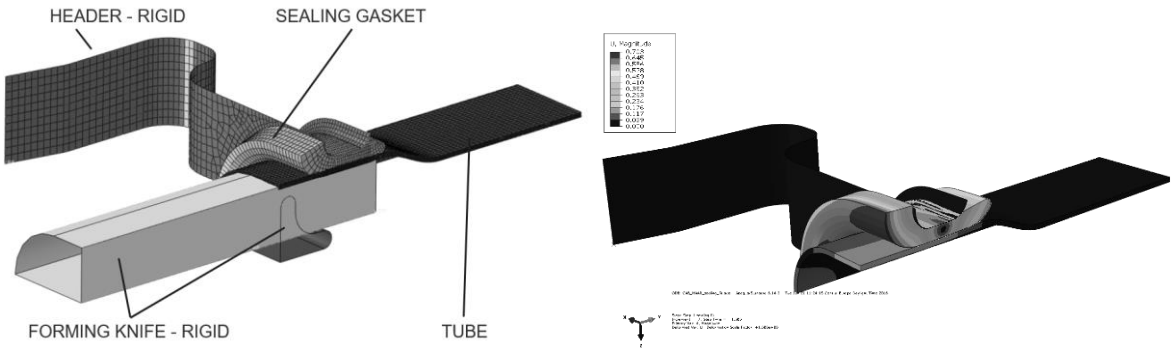

Figure 8: *FEA for gasket compression*

3.2 Stage B: Gasket compression and method of measurement

Optimal Gasket compression is given by material selection and by implemented gasket design. Optimal tube geometry (which is directly connected with geometry of header and gasket) is fixed by equations applicable on selected tube portfolio. Example of patented tube geometry design guideline can be seen on Figure 9.

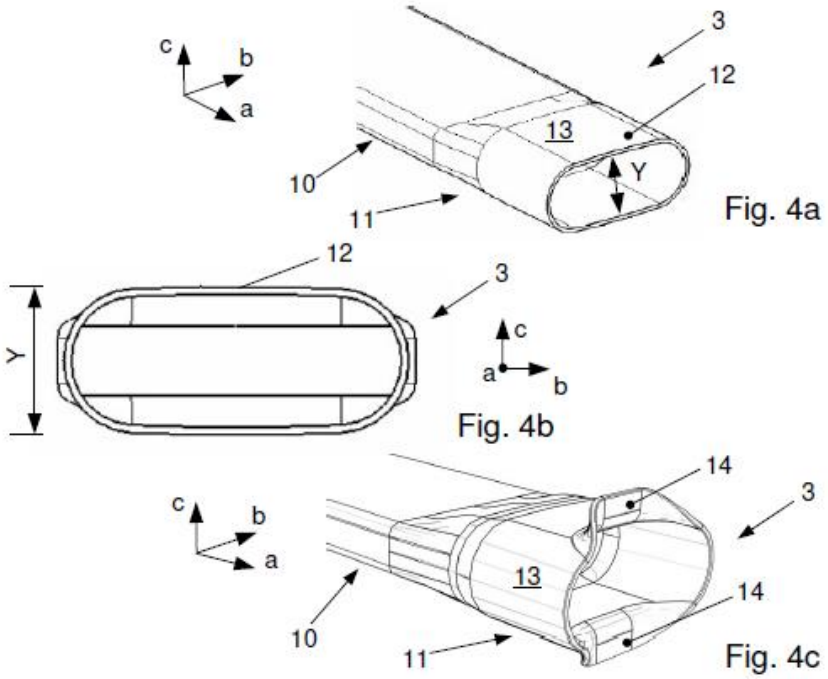

Figure 9: *Tube geometry design guideline*

Required gasket compression level is achieved with tube expansion by punch knives. Expansion level and knives design were subjects of several iterations as force generated by compressed gasket is causing tube flexing once knife is removed.
To get perfect control over resulted gasket compression CT scan analysis was used as a part of evaluation in each design iteration. On Figure 10 can be seen CT scan example.

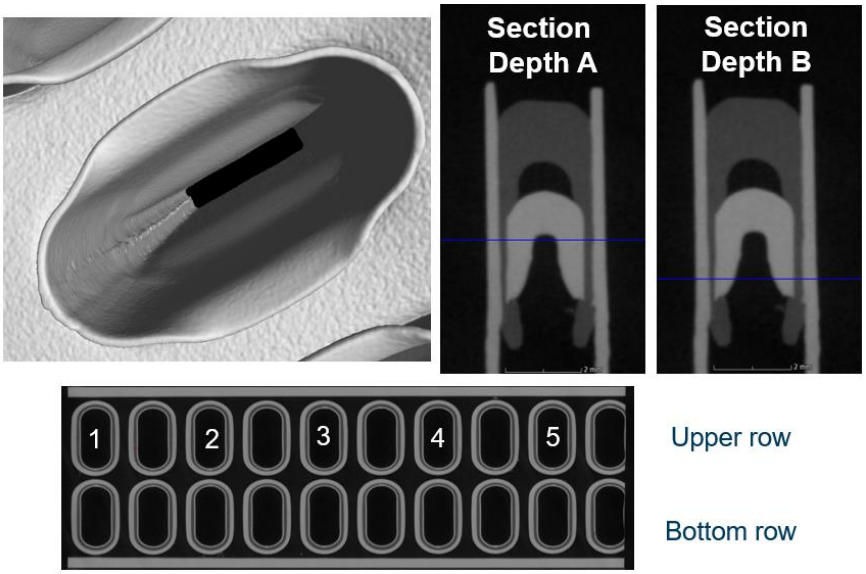

Figure 10: *CT scan analysis for gasket compression*

3.3 Stage C: Serial process readiness

Serial process readiness is for automotive industry important topic. Each new design must be carefully optimized for mass production. This part of development is often more demanding than design development itself.
Tools reflecting serial process assembly were developed and tested on batch of samples. This batch was observed for post-braze dimensional differences and occurrence of any major / minor defect caused by assembly tools / process. Example of assembly tool is shown on Figure 11.

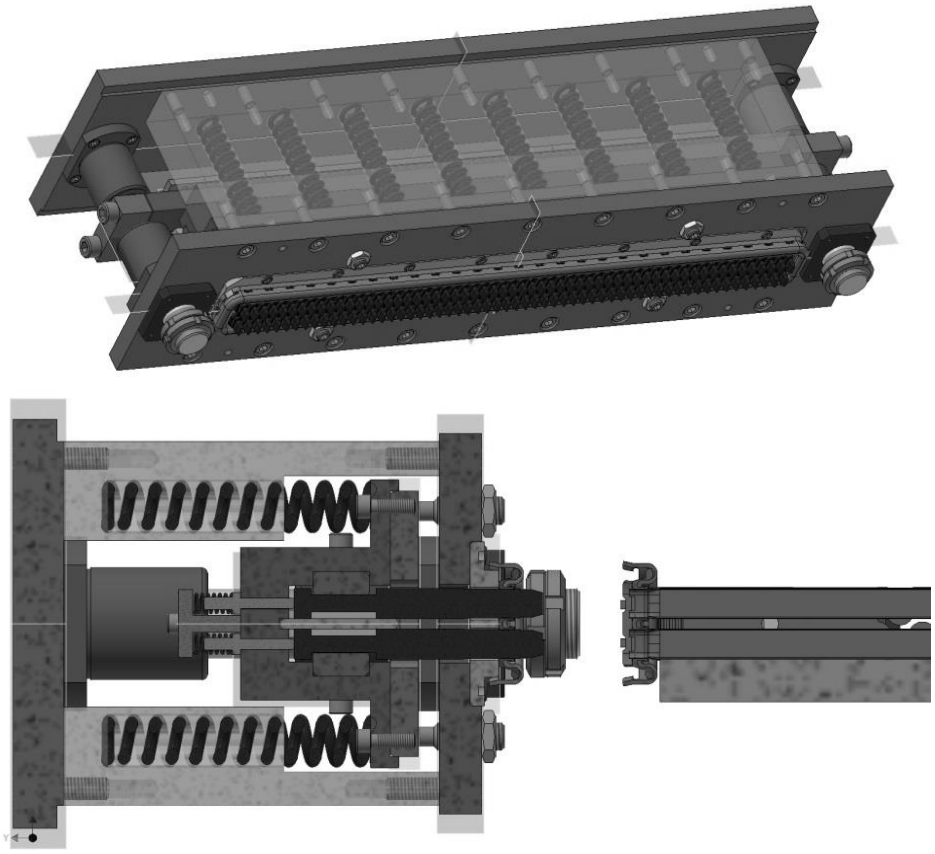

Figure 11: *Example of assembly tool for serial process*

3. CONCLUSION

Validation test matrix is defined to cover OEMs requirements, while selected are the most demanding to cover majority of potential market.
Test matrix was successfully passed including 4-times higher requirement for Thermal-Cycle durability (in comparison with the best design using current CAB technology). Analysis on samples does not show any damage - so we can conclude principle of flexibility in connection between tube – gasket – header works - there are not generated strains.
Addressed CAB heat exchangers problem of limited Thermal-Cycle durability - was solved.

REFERENCES

ACKNOWLEDGEMENT
This work describes Hanon internal development focused on solving technological obstacle for increasing thermal cycle durability requirement. Work was done in cooperation between several Hanon departments.

LII. INTERNATIONAL SCIENTIFIC CONFERENCE OF THE CZECH AND SLOVAK UNIVERSITY DEPARTMENTS AND INSTITUTIONS FOCUSED ON RESEARCH AND TEACHING METHODS RELATED TO COMBUSTION ENGINES, ALTERNATIVE DRIVES AND TRANSPORT
SEPTEMBER 22 – 23, 2021, PRAGUE
CZECH UNIVERSITY OF LIFE SCIENCE PRAGUE, FACULTY OF ENGINEERING,
DEPARTMENT OF VEHICLES AND GROUND TRANSPORT

TRIAL EXPERIMENTS ON LGW 702T GAS ENGINE

Minárik Matej[1], Polóni Marián[2], Chríbik Andrej[3], Šlauka Michal[4]

Abstract
The article deals with experimental results of turbocharged engine LGW 702T. The natural gas (96% vol. CH4) was evaluated for various performance and economic parameters as it will be used as reference fuel in the future research. Also state quantities before and after both the charger and turbo were measured to estimate the operating region of the turbocharger.

1. INTRODUCTION

One of the ways to increase performance as well as economic parameters of combustion engines is charging with turbochargers. Such field is well explored in case of gasoline and natural gas engines. The low efficiency of syngas combustion can be increased by implementing a turbocharging as their lower heating value tend to be much lower than those of a natural gas or methane. In case of LGW 702, the authors found that by decreasing the volume of inert gases under 25% with simultaneous increase of hydrogen above 25% the engine started to manifest signs of abnormal combustion. This possesses an interesting opportunity for future research as the turbocharging increase the charge temperature as well as pressure which makes the engine more prone to signs of abnormal combustion. It also possesses an interesting challenge as the turbocharging of uneven firing 2-cylinder engine tend to negatively affect the performance parameters of the turbocharger [1].

[1] Minárik Matej, Slovak University of Technology, Nám. Slobody 17, 812 31, Bratislava, matej.minarik@stuba.sk
[2] Polóni Marián, Slovak University of Technology, Nám. Slobody 17, 812 31, Bratislava, marian.poloni@stuba.sk
[3] Chríbik Andrej, Slovak University of Technology, Nám. Slobody 17, 812 31, Bratislava, andrej.chribik@stuba.sk
[4] Šlauka Michal, Slovak University of Technology, Nám. Slobody 17, 812 31, Bratislava, michal.slauka@stuba.sk

2. LGW 702T ENGINE

LGW 702T engine is an inline 2-cylinder, water cooled spark ignition engine which design is based on the compression ignition LDW 702 engine. Head of the LDW 702 unit was swapped for LGW 523 spark ignition engine head to allow mounting of ignition plugs. Also, the piston heads were machined to achieve a lower compression ratio. The overall compression ratio in this case was lowered to the value of 12.5 from the former 22.8. Mixture preparation takes place in external diffuser before the charger. The feedback narrow-band lambda controller drives the stepper unit which in turn chokes the flow of gaseous fuel. That in turn keeps the engine operation at stoichiometric parameters. Such system was utilized mainly for its simplicity, whereas various Syngases can reach an Air to Fuel ratio as low as 1.2. Drawback of such fuel system is mainly a high susceptibility to various forms of abnormal combustion. [2] The most evident of these is intake flashback where the mixture is present in whole intake system up to the diffuser. Such combustion is much more dangerous in case of turbocharged engine, where the flame propagating from the combustion chamber is causing strain on charger wheel. Various parameters of the LGW 702T engine can be found in Table 1.

Engine type	Spark Ignition
Number of cylinders and arrangement	Inline 2
Crankshaft throw angle [°]	180
Engine displacement [cm^3]	686
Bore / Stroke [mm]	75 / 77,6
Compression ratio [-]	12,5:1
Valve train	OHC, Toothed belt
Mixture preparation	External in diffuser, feedback regulation of stoichiometry controlled with stepper motor
Cooling	Thermostat controlled dual cooling system, forced air flow through radiator, fan with electric motor drive
Fuel	Methane, Natural Gas, Synthesis Gases
Lubrication	Full Pressure Lubrication with Filtration
Ignition System	Brisk10DS plugs Coil On Plug, Bosch P-65T, 65mJ ignition coils IMF Soft ECUMaster, Engine control unit
Dry weight [kg]	66

Table 1: *LGW 702T engine parameters*

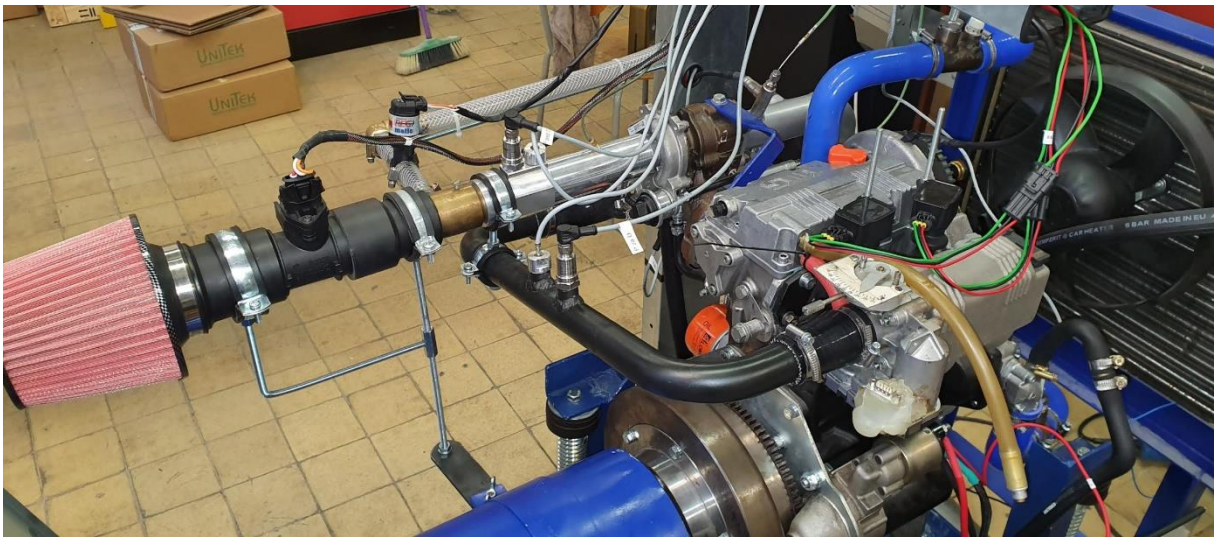

Figure 1: *LGW 702T test stand*

2.1 Data acquisition system

Data acquisition is being carried out with National Instruments c-RIO system. Various physical quantities were measured using the input modules. List of the modulesand type can be found in Table 2.

c-RIO module	Physical quantity	Place of measurement
NI 9205 – Analog input	Pressure	Intake before and after Charger and Turbine
	Pressure	Oil
	Mass Airflow	Intake
	Turbocharger RPM	Turbocharger
	Battery voltage	Battery (5:1 voltage divider)
	Lambda	Wide band before catalyst
NI 9217 – RTD sensors	Temperature	Cooling system in/outlet, Mixture before and after charger (RTD)
NI 9211 – Thermocouples	Temperature	Before and after turbine

Table 2 *Types of measurements carried out on LGW 702T engine*

At the moment indicated pressure is being traced with external digital oscilloscope which is connected to the Kistler SCP platform. In the future whole data acquisition system is planned to be overhauled. This includes incorporation of NI 9263 module which consists of 4 analog input channels. Such module incorporates 100 kHz simultaneous sampling speed. Also, various triggering events are planned to be incorporated with NI 9402 digital input module.

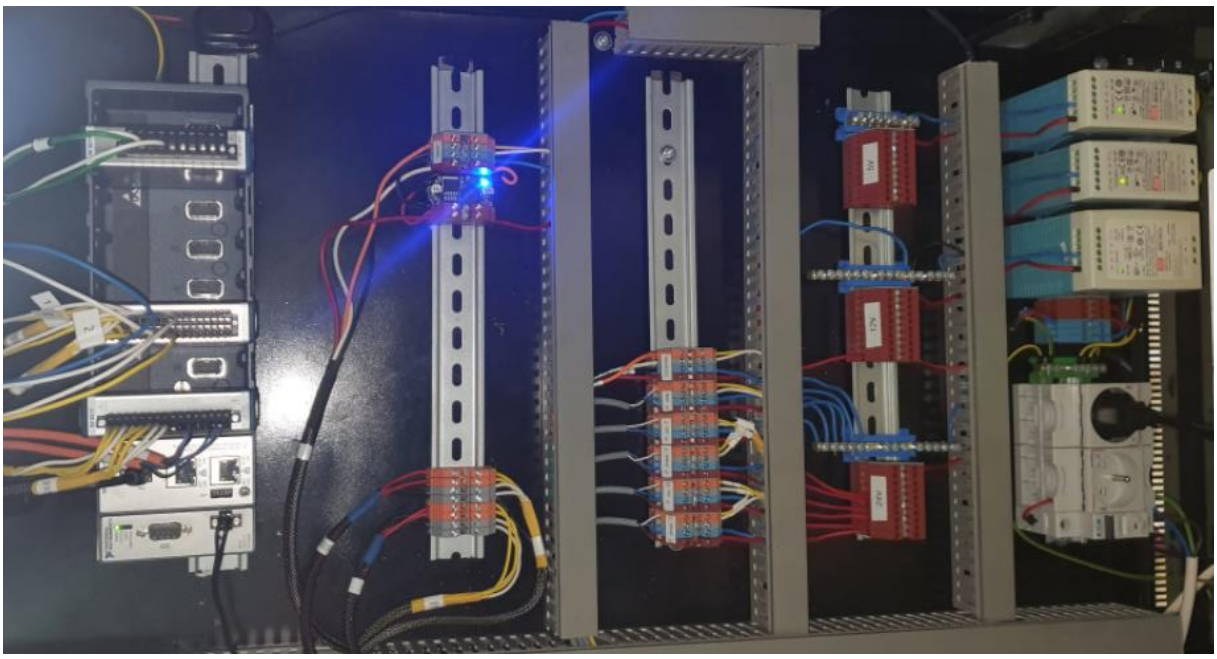

Figure 2 *Rack containing main parts of the measurement system*

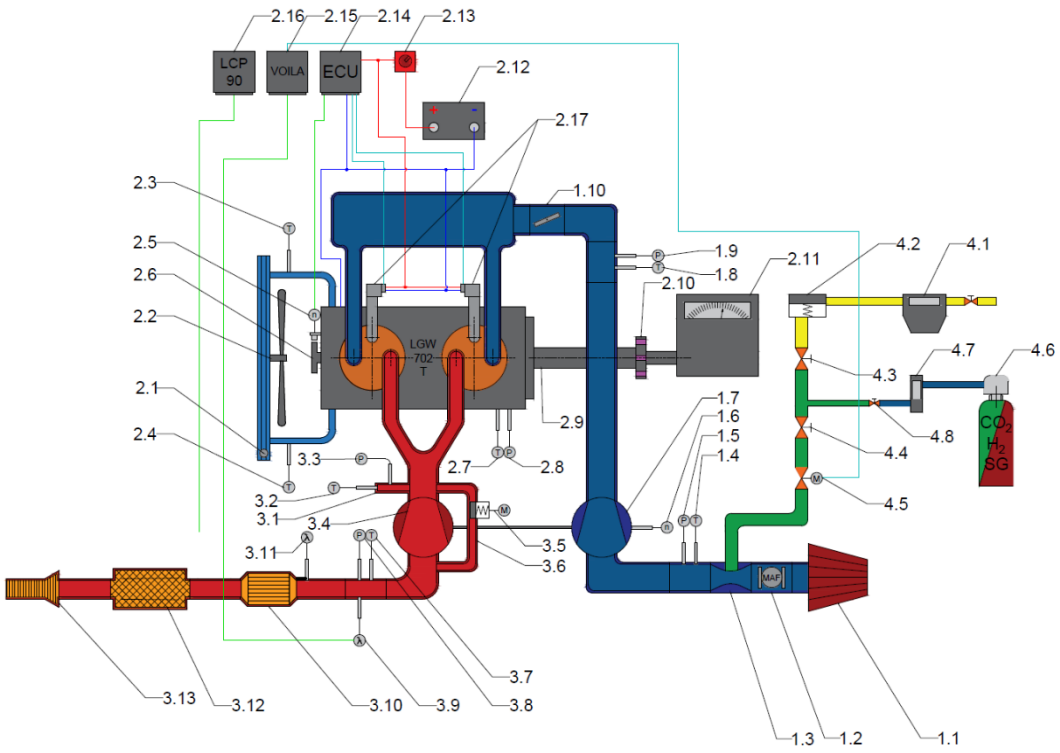

Figure 3 *LGW 702T layout*

Intake	
1.1	Air filter
1.2	Mass air flow sensor
1.3	Diffuser
1.4	Intake air temperature sensor (before charger)
1.5	Intake air pressure sensor (before charger)
1.6	Turbocharger RPM sensor
1.7	Charger
1.8	Intake air temperature sensor (after charger)
1.9	Intake air pressure sensor (after charger)
1.10	Butterfly valve
Engine accessories	
2.1	Engine radiator
2.2	Electric fan
2.3	Engine coolant temp. sensor (engine inlet)
2.4	Engine coolant temp. sensor (engine outlet)
2.5	Camshaft RPM sensor
2.6	Camshaft trigger wheel
2.7	Oil temperature sensor
2.8	Oil pressure sensor
2.9	Connecting shaft (engine – dynamometer)
2.10	Elastic Clutch
2.11	Dynamometer
2.12	Accumulator
2.13	Safety switch button
2.14	ECU
2.15	Narrowband lambda controller
2.16	Wideband lambda controller
2.17	Ignition coils

Table 3 *Legend for figure 3 (Part 1)*

Exhaust	
3.1	EGR reduction
3.2	Exhaust gas temp. sensor (before turbine)
3.3	Exhaust gas pressure. sensor (before turbine)
3.4	Turbína
3.5	DC motor-controlled waste gate
3.6	Waste gate
3.7	Exhaust gas temp. sensor (after turbine)
3.8	Exhaust gas pressure. sensor (after turbine)
3.9	Narrowband lambda sensor
3.10	3-way catalyst
3.11	Wideband lambda sensor
3.12	Silencer
3.13	Exhaust tip
Engine accessories	
4.1	Gas meter
4.2	Zero pressure regulator
4.3	Natural gas regulating valve
4.4	Stoichiometry regulating valve
4.5	Stoichiometry regulating stepper motor
4.6	High pressure gas cylinder
4.7	Mass gas flow sensor (for N2)
4.8	Flow regulation screw

Table 4 *Legend for figure 3 (Part 2)*

3 EXPERIMENTAL RESULTS

Measurements were performed on AVL DynoPerform 80 eddy current dynamometer. Engine was operating at full load and stoichiometry was maintained with narrow-band lambda controller. Ignition angle was set to 25° CA BTDC. Such angle is the optimal for engine speed of 1500RPM. Measured RPM ranged from 1200 up to 2000. Performance and economic parameters were evaluated for each mode of operation of the engine. As it was mentioned before, state quantities of the mixture in the intake and exhaust gas in the exhaust were collected with in-house software built with the LabView environment. As the research is focused on combined heat and power system engines, the main emphasis and focus is laid on engine RPM of 1500 or 1800 respectively.

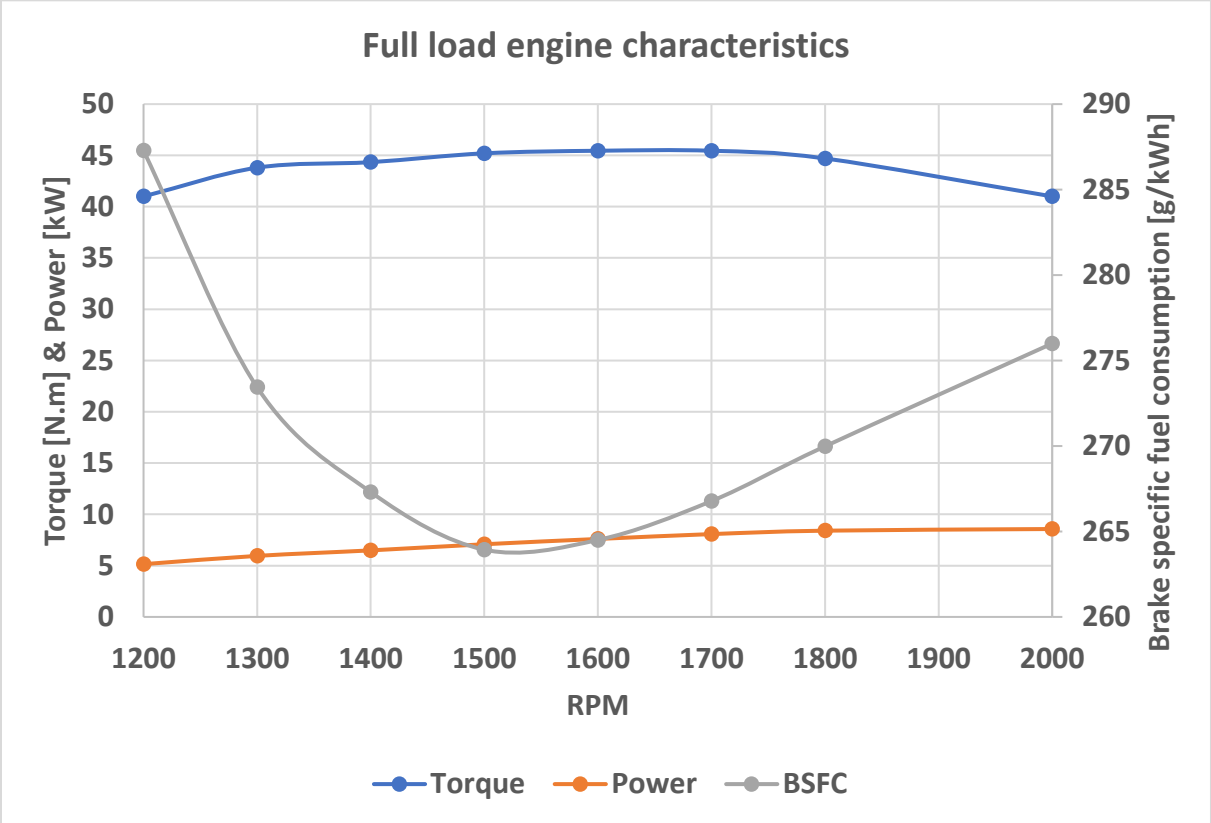

Figure 4 *Full load engine characteristic (Full load, stoichiometric ratio, ignition angle 25° CA BTDC)*

Engine achieved maximum power of 8.57kW at 2000 RPM. This corresponds to a torque of 41 Nm. The torque figures for 1500 RPM reached value of 45.2 Nm and 44.7 Nm for 1800 RPM. These represents power output of 7.09 kW and 8.4 kW. The minimum brake specific fuel consumption was 263 g/kWh at the RPM of 1500. This is mainly due to a fact that optimal ignition angle for 1500 RPM was used throughout the whole measured RPM region. At the point of 1800 RPM the brake specific fuel consumption 269 g/kWh.

3.1 Turbocharger

The turbocharger used in this experiment was Garrett GT0632SZ. It is the commercially smallest turbocharger available on the market. As it was expected, the RPM of turbocharger rose steadily from approximately 90 000 at engine RPM of 1200 to 160 000 at engine RPM of 2000. The maximum pressure ratio of both, the charger and turbine has also been achieved at 2000 RPM. The ratio reached values of 1.36 for charger and 1.39 for the turbine. At the points of 1500 and 1800 engine RPM, the turbine reached ratio of 1.28 and 1.30, respectively. For the charger, the respective pressure ratios were 1.19 at 1500RP and 1.24 at 1800 RPM.

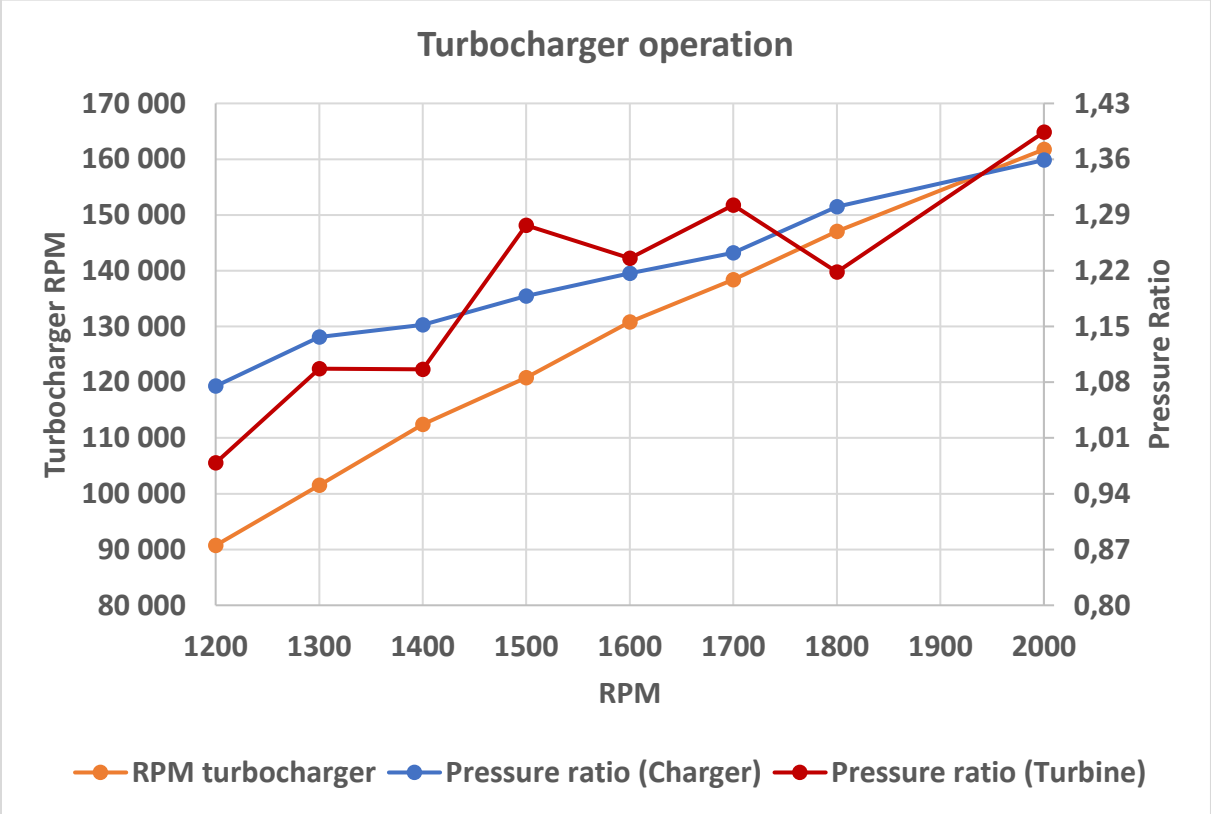

Figure 5 *Turbocharger RPM and pressure characteristic (Full load, stoichiometric ratio, ignition angle 25° CA BTDC)*

The temperatures of the exhaust gases before the turbine reached value of 501°C at 2000 RPM. This accounted for increase of 82°C compared to 1200RPM - at this point, the temperature before turbine was lower than after turbine. This is mainly accounted to uncertainty of measurement as well as unfavourable region of operation of the turbocharger. For the charger side, the fresh mixture after the charger reached temperature of 59.5°C at 2000 RPM and 53.5°C at the RPM of 1200. As the room was well vented throughout the whole experiment, the temperature before the charger was maintained between 33-34°C. The temperature of exhaust gas after exiting from the turbine at 1500 RPM reached value of 450°C. For the 1800 RPM the measured temperature was 460°C. The heat drop on turbine at 2000 RPM was 43°C, 15,5°C at 1500 and 31°C at 1800 RPM.

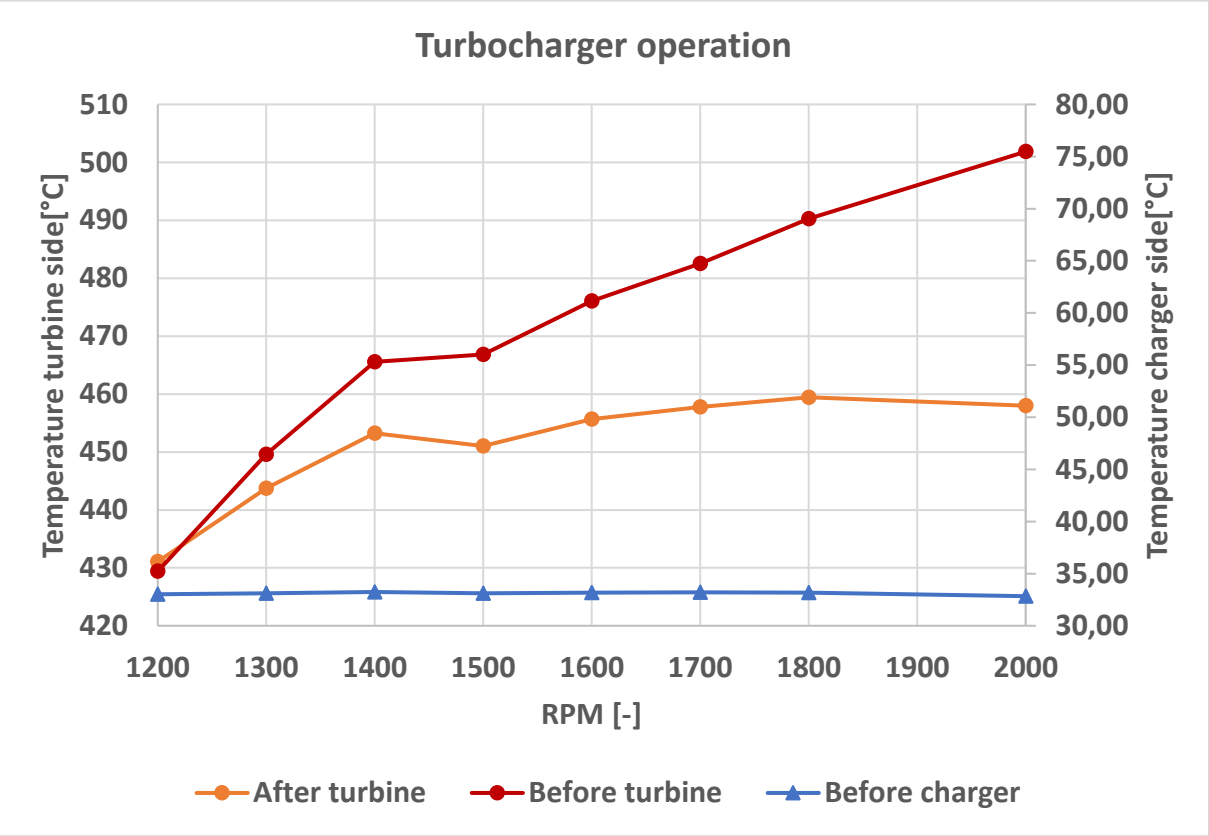

Figure 6 *Turbocharger temperature characteristic*

4. CONCLUSION

The most important findings found during the trial tests on LGW 702T engine can be summarized as follows:

- The combination of LGW 702 and of the turbocharger GT0632SZ needs to be re-evaluated as the expected performance were not met
- The expected effect of turbocharging is predicted to be even lower for the synthesis gases. This is mainly due to the fact that maximum in-cylinder pressure as well as exhaust gas temperature for these gases tend to be lower.
- The turbocharger operation for low RPM range could be better improved by even smaller turbocharger
- As the engine has a relatively small displacement volume, the bigger engine or engine with different number of cylinders [3] should be used to better understand the effect of turbocharging in case of synthesis gases

REFERENCES

[1] Wohlgemuth, S., Meiland, L., Wachtmeister, G., and Fledersbacher, P., Turbocharging of a Two-cylinder Lean-Burn Natural Gas Engine with Uneven Firing Order, SAE Technical Paper 2014-01-1652, 2014, ISSN: 0148-7191

[2] Polóni, M. and Chríbik, A., Low-Energy Synthesis Gases from Waste as Energy Source for Internal Combustion Engine, SAE Int. J. Engines, 2020, pp. 633-648, ISSN 1946-3944
[3] Georg K., Eberhard S., Horst M. Turbocharging of engines with low cylinder numbers: a thermodynamic consideration, Automotive and Engine Technology, 2019, pp. 153-167, ISSN 2365-5127

ACKNOWLEDGEMENT

This work was supported by the Slovak Research and Development Agency under Contracts-No. APVV-17-0006, APVV-20-0046, and was also supported by the Slovak Scientific Grant Agency under the Contracts-No. KEGA 050STU-4/2021 and KEGA 026STU-4/2018.

52. MEZINÁRODNÍ VĚDECKÁ KONFERENCE ČESKÝCH A SLOVENSKÝCH UNIVERZIT A INSTITUCÍ ZAMĚŘENÁ NA VÝZKUMNÉ A VÝUKOVÉ METODY SPOJENÉ SE SPALOVACÍMI MOTORY, ALTERNATIVNÍMI POHONY A DOPRAVOU

22.-23. ZÁŘÍ 2021, PRAHA
ČESKÁ ZEMĚDĚLSKÁ UNIVERZITA V PRAZE, TECHNICKÁ FAKULTA,
KATEDRA VOZIDEL A POZEMNÍ DOPRAVY

PROBLÉMY DOSAŽENÍ UHLÍKOVÉ NEUTRALITY U ELEKTROMOBILŮ

Josef Morkus[1], Jan Macek[2]

Abstrakt
Změny klimatu a globální oteplování jsou dnes velmi frekventovaná témata. Za příčinu těchto změn jsou považovány emise CO_2 pocházející z lidské činnosti. Evropská unie se zavázala do roku 2050 dosáhnout uhlíkové neutrality. Jednou z klíčových cest k tomuto cíli má být náhrada automobilů se spalovacím motorem elektromobily, přitom se předpokládá, že elektromobil je zcela bezemisní. Tento příspěvek se zabývá kritickým posouzením elektromobilů z hlediska emisí vznikajících při jejich výrobě včetně výroby baterií, výroby elektřiny pro jejich provoz a materiálové náročnosti přechodu na elektromobilitu a na bezemisní zdroje elektřiny. Jsou ukázány některé finanční nároky a výsledný vliv elektromobilů na klima.

1. ÚVOD

Evropský parlament výraznou většinou hlasů schválil Klimatický zákon, který mění dosavadní závazek EU snížit emise skleníkových plynů do roku 2030 o 55 % ve srovnání s rokem 1990 na zákonnou normu. Tento zákon, který se stává ústředním cílem EU, stanovuje postup, kterým by Unie měla do roku 2050 dosáhnout uhlíkové neutrality. Zákon musí ještě formálně schválit jednotlivé země. Cílem je zamezit globálnímu oteplování a klimatickým změnám. Přitom za hlavní příčinu těchto změn jsou považovány emise oxidu uhličitého (CO_2) pocházející z lidské činnosti.

Oxid uhličitý je přirozenou součástí atmosféry, je v ní obsažen v malém množství (obr. 1), ale jedná se o skleníkový plyn, který brání vyzařování tepla ze Země do vesmíru. Za období od průmyslové revoluce v 19. století vzrostla jeho koncentrace v atmosféře z 0,025 % na 0,04 % a právě skleníkový efekt vyvolaný tímto nárůstem je většinovým názorem považován za příčinu globálního oteplování. Z vývoje

[1] Ing. Josef Morkus, CSc. Centrum vozidel udržitelmé mobility, fakulta strojní ČVUT v Praze, josef.morkus@fs.cvut.cz
[2] Prof. Ing. Jan Macek, DrSc., Centrum vozidel udržitelmé mobility, fakulta strojní ČVUT v Praze, jan.macek@f..cvut.cz

v posledních desetiletích jsou odvozovány různé modely dalšího vývoje v závislosti na koncentraci CO_2 a katastrofické scénáře, hrozící nevratným přehřátím planety a

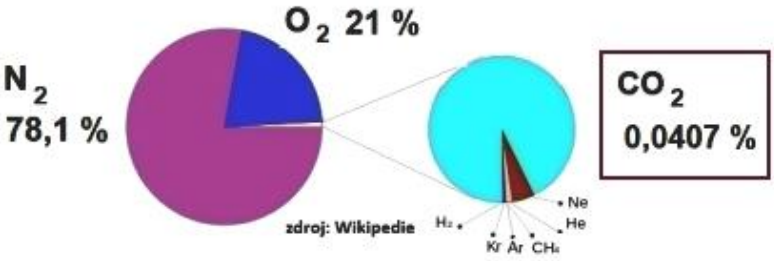

Obrázek 1: *složení atmosféry*

zánikem civilizace. Problémem některých modelů je, že neumí dobře vysvětlit minulost, např. oteplení Evropy ve středověku, kdy lidské emise CO_2 byly zanedbatelné. Rovněž v období 50. až 70.let minulého století docházelo k ochlazování [1] (obr. 2). Podle jiných, dnes menšinových názorů, je kauzální závislost mezi koncentrací CO_2 a oteplováním právě opačná, množství CO_2 následuje s jistým zpožděním změny teploty v důsledku periodických vesmírných cyklů [2] (obr.3).

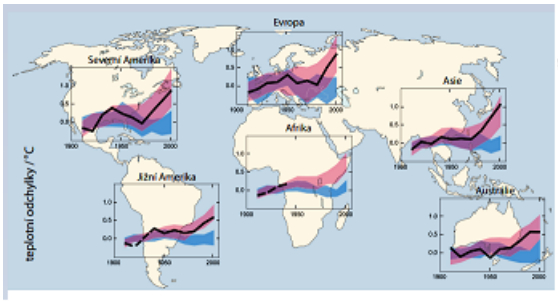

Obrázek 2: *vývoj teploty v období 1900 - 2000*

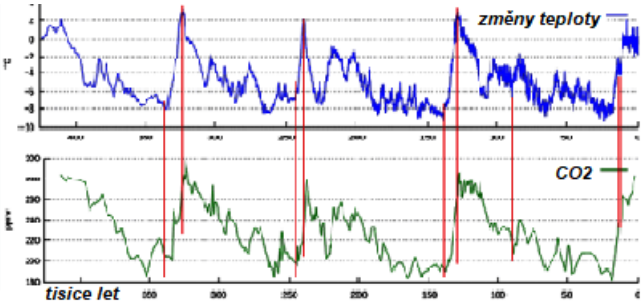

Obrázek 3: *závislost teploty a koncentrace CO2 v minulosti*

V každém případě není současná znalost vývoje klimatu dostatečně podrobná a predikce odvozené z relativně krátkého období několika desítek let mohou být zkreslené, i když jistý podíl lidské činnosti na růstu koncentrace CO_2 nelze popřít.

2. ELEKTROMOBILITA

Obecně snaha o snižování emisí jakéhokoliv druhu je správná. Otázkou však je její rychlost podmíněná stavem techniky. V současné době se různí představitelé a politici předhánějí v prohlášeních, kdy dosáhnou uhlíkové neutrality ještě před rokem 2050 bez ohledu na okolnosti, které s tím souvisí. Výrazná pozornost je přitom zaměřena na automobily se spalovacím motorem. Objevují se i termíny, od kdy má být prodej těchto vozidel zakázán.

2.1 Emisní předpisy

Evropská komise a parlament vydali požadavky na snižování emisí automobilů, které v praxi znamenají přechod na elektrický pohon (obr. 4). Přitom elektromobil je podle těchto regulí považován za zcela bezemisní. Podle plánu EU by do roku

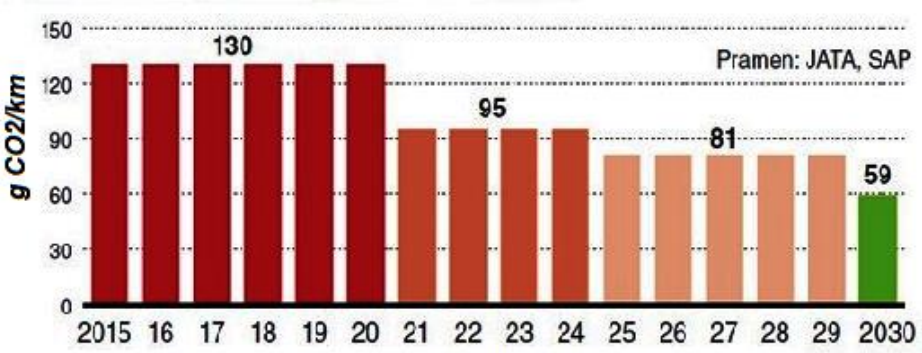

Obrázek 4: *limity emisí CO2 pro osobní automobily*

2030 mělo na evropských silnicích jezdit 30 milionů vozidel s nulovými emisemi [3] a do roku 2050 budou téměř všechny automobily bez emisní [4].

V Evropské unii dnes jezdí přibližně 260 milionů automobilů. V praxi splnění tohoto požadavku znamená prodat ode dneška do roku 2030 průměrně 3 miliony elektromobilů ročně a do roku 2050 průměrně 8 milionů elektromobilů za rok. V roce 2020 se v EU prodalo cca 770 tisíc elektromobilů. Výroba a prodej elektromobilů by tedy musely trvale výrazně růst.

V ČR podle Národního plánu čisté mobility [5] má v roce 2030 jezdit 220 800 až 500 000 elektromobilů. V roce 2020 se prodalo jen 3262 těchto vozidel.

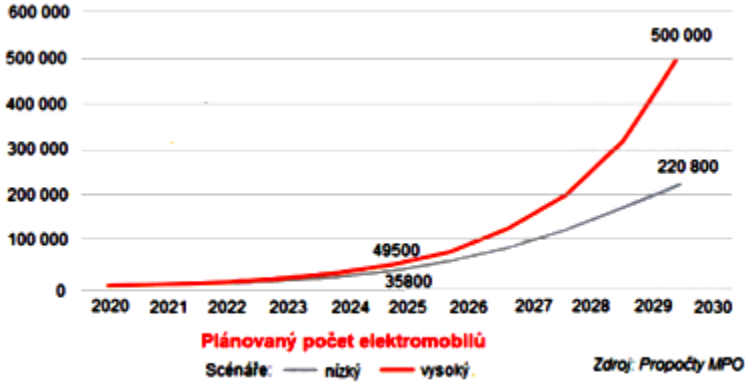

Obrázek 5 : *Národní plán čisté mobility ČR*

2.2 Kdy je elektromobil bezemisní

Předpisy EU berou v potaz pouze situaci za jízdy vozidla. Zcela pomíjí, že elektromobil je nutné vyrobit, vyrobit pro něj baterii a průběžně vyrábět elektřinu pro jeho provoz. Na konci životnosti by měl být každý elektromobil recyklován.

Z pohledu celoživotního cyklu (cradle-to-grave) bude elektromobil bezemisní, jestliže:

- při jeho výrobě nevzniknou žádné emise
- výroba baterie bude zcela bezemisní
- rovněž elektřina, na kterou bude jezdit, bude vyrobena bezemisně
- a na konci životnosti bude bez vzniku emisí rozebrán a recyklován

Je zřejmé, že pokud nebudou splněny všechny tyto podmínky, předpoklad, že elektromobil je bezemisní, neodpovídá skutečnosti.

2.3 Emise z výroby vozidel a baterií

Již při výrobě vozidla vzniká nezanedbatelné množství emisí. Některé automobilky uvádějí, že jejich výroba bude zcela bezemisní. Důležité však je, co vše bude započítáno: Zda pouze montáž vozidel, či výroba dílů nebo i těžba a zpracování surovin, ze kterých bude vozidlo vyrobeno. Švédská studie [6] uvádí, že při výrobě

automobilu vzniká v závislosti na jeho velikosti a vybavení 5 – 10 t CO_2, z toho cca 20 % připadá na spalovací motor. U elektromobilu tento motor není, tedy na výrobu vozidla zbývá 4 – 8 t CO_2.

Ale elektromobil má navíc baterii, jejíž výroba je energeticky náročná. Výsledky studií, které se emisemi při výrobě baterií zabývají, se dosti liší podle toho, jaké fáze výroby se týkají a kde se baterie vyrábí. IEA (International Energy Agency) v roce 2019

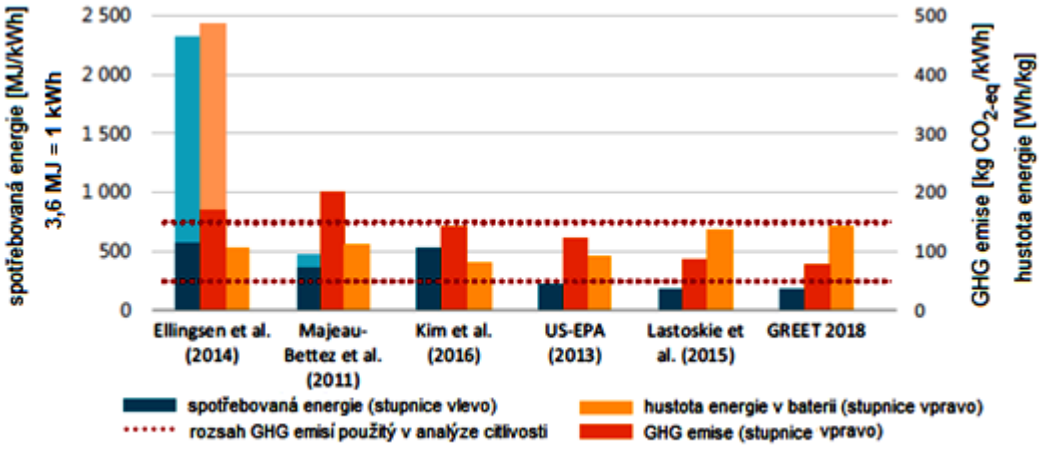

Obrázek 6: spotřeba energie a emise při výrobě baterií

publikovala graf [7] (obr. 6), který ukazuje množství spotřebované energie na výrobu 1 kWh baterie. Výsledky amerických studií, založené na metodě GREET vycházejí lépe než evropské studie, které uvádějí spotřebu energie kolem 500 MJ/kWh kapacity baterie. Obdobné hodnoty vycházejí i z dalších analýz. S uvažováním obvyklých velikostí baterií a energetického mixu Číny, kde se baterie převážně vyrábějí, se dá zjednodušeně říci, že při výrobě baterie vzniká zhruba stejné množství emisí CO_2 jako při výrobě celého zbytku elektromobilu.

2.4 Výroba elektřiny a obnovitelné zdroje

Za jízdy je elektromobil bezemisní. Ale elektřina pro jeho jízdu se musí někde vyrobit. Je potřeba si uvědomit, že z hlediska globálního oteplování a změn klimatu je v podstatě lhostejné, kde emise vznikají, zda při jízdě nebo v elektrárně. S uvažováním spotřeby elektromobilu 15 – 25 kWh/100 km, se započtením ztrát při výrobě elektřiny, ztrát v síti a ztrát při nabíjení elektromobilu (10 – 25 %) [8], ročního nájezdu 10 000 – 15 000 km a českého energetického mixu cca 0,5 kg CO_2/kWh, vznikají ročně přibližně 1 – 3 t CO_2 na každý elektromobil. Jinými slovy, téměř každý elektromobil má v českém energetickém mixu emise vyšší než je limit 95 g CO_2/km, za jehož překročení jsou výrobci vozidel se spalovacími motory pokutováni! Při počtu elektromobilů podle Národního plánu čisté mobility by v roce 2030 vzniklo pro provoz elektromobilů v ČR při nezměněném energetickém mixu 0,22 – 1,5 milionu tun CO_2.

Je vhodné podotknout, že v různých zemích jsou emise z provozu elektromobilů různé [9]. Každý elektromobil má zpočátku vyšší emise CO_2 než automobil se spalovacím motorem v důsledku emisí z výroby baterie. K vyrovnání emisí, t.j. od kdy začne být elektromobil emisně lepší záleží na tom, z čeho se elektřina vyrábí.

Například v Norsku, kde téměř všechna elektřina pochází z vodních elektráren, dojde k vyrovnání emisí po ujetí cca 40 000 km. Ve Francii, kde téměř ¾ elektřiny jsou z jaderných elektráren, nastane vyrovnání zhruba po 50 000 km. V ČR a podobně v Německu začne být elektromobil emisně lepší než auto s benzinovým motorem po cca 130 000 km, u auta s naftovým motorem po více než 200 000 ujetých km. A v Polsku, kde elektřina pochází převážně z uhlí, nebude elektromobil emisně lepší prakticky nikdy. Je pravda, že s uzavíráním uhelných elektráren a jejich náhradou nízkoemisními zdroji se bude situace lepšit.

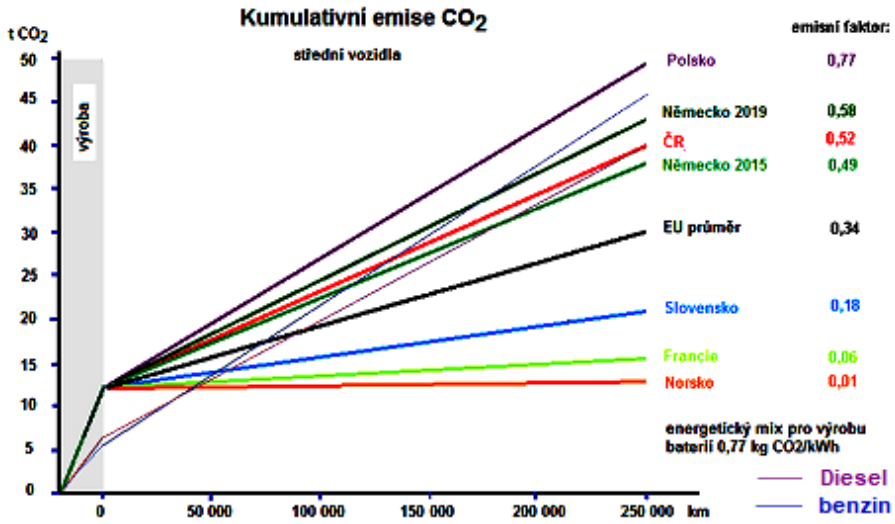

Obrázek 7: *vliv energetického mixu na emise elektromobilu*

Často se uvádí, že elektromobily budou jezdit na zelenou energii z obnovitelných zdrojů. Z hlediska emisí se jedná o podobnou situaci jako u elektromobilů. Když už je solární nebo větrná elektrárna v provozu a zanedbáme emise při údržbě, pak vyrábí elektřinu bezemisně. Ale pro stavbu větrné elektrárny se musí vytěžit železná ruda a uhlí, vyrobit surové železo a z něj ocel, cement pro betonové základy, měď a další prvky pro generátor, kabeláž a elektroniku. Podobně pro fotovoltaický panel je potřeba vytěžit křemíkový písek, v obloukové peci vyrobit surový křemík, z něho s použitím vzácných zemin polovodičové články a vše umístit do panelu se speciálním sklem. Celý proces je energeticky náročný a používá vysoké teploty. Ocel i panely se vyrábějí v Číně s využitím energie převážně z uhelných elektráren. IEA uvádí množství CO_2 vzniklé při těžbě a zpracování některých materiálů [10] (obr.8). Výstavba těchto elektráren rozhodně není bezemisní a vzniklé emise CO_2 je potřeba rozpočítat na dobu životnosti, přibližně 20 let. A po skončení životnosti se elektrárna musí nákladně recyklovat. Jak ukazuje situace v Německu, kde současně s masivní výstavbou obnovitelných zdrojů dochází k uzavírání jaderných elektráren, emise z výroby elektřiny se tím nelepší.

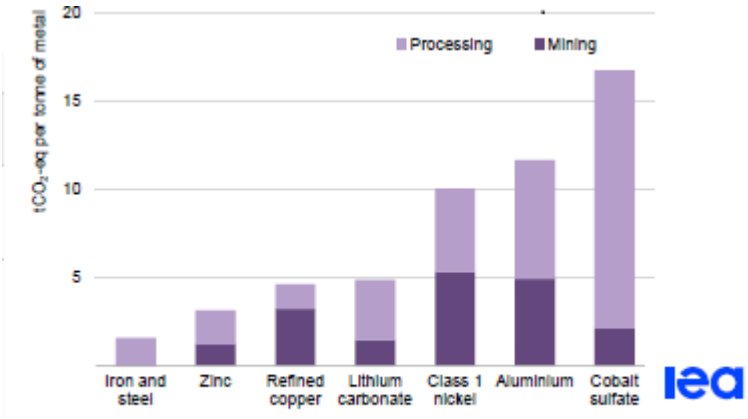

Obrázek 8: *emise při těžbě a zpracování materiálů*

Obnovitelné zdroje však mají ještě další problém: Jedná se o nestabilní zdroje s nepravidelným výkonem závislým na počasí. Když vítr nefouká a slunce nesvítí, nevyrábějí téměř nic. Proto je nutné tyto zdroje zálohovat jinými, jadernými, uhelnými a (paro)plynovými elektrárnami s obdobným výkonem a ty udržovat v pohotovostním režimu. Přitom nutno vzít v úvahu nemalé investiční náklady na tyto záložní zdroje, které budou využity poměrně málo (do 30 %) a u fosilních paliv také náklady kvůli prudce rostoucím cenám uhlíkových povolenek, vyvolané umělými zásahy EU. Emise z těchto elektráren pro nutnou stabilizaci sítě se však často do energetického mixu nezapočítávají, neboť vznikají až „mimo trh se silovou elektřinou“... Odběrateli elektrické energie je vcelku jedno, zda je zaplatí v silové či distribuční složce ceny energie, ovšem propagandisticky lze pak argumentovat s nízkými cenami z elektřiny OZE (občasných energetických zdrojů).

Zdánlivě lze tento problém řešit bateriovými úložišti, která by akumulovala energii, když je jí přebytek, a uschovala ji na dobu, kdy příznivé podmínky nebudou. I kdybychom si chtěli uložit průměrnou denní výrobu solárních elektráren v ČR v roce 2020, která byla cca 6 GWh [11], stačila by tato energie na necelou 1 hodinu průměrné spotřeby v ČR (7,5 GW). Přitom by úložiště stála částky v miliardách Kč (např. úložiště v Plané n/Lužnicí s kapacitou pouhé 2.5 MWh a životností 10 let stálo 70 milionů Kč [12]). Bateriová úložiště mají smysl pro krátkodobé pokrytí výkonu, než naběhnou jiné záložní zdroje, ne pro uschování energie na několik dnů i více.

Při předpokládaném využití baterií elektromobilů jakožto záložní bateriové kapacity lze první nadsazeně optimistický odhad udělat pro průměrné hodnoty. Záleží nejen na použitelné kapacitě baterie (využití cca 50 % odhadované kapacity baterií dává pro síť asi 20 kWh), ale i na výkonu nabíječky, upravené jako střídač pro obrácený tok proudu. Při 5 kW výkonu wall-boxu bychom pokryli z cca 1 500 000 automobilů sice celý průměrný příkon sítě ČR (asi 7,4 GW), ale jen po dobu 1,4 h. Ve skutečnosti by bylo zajímavé pokrýt špičku. Na průměrný příkon a na nabíjení pro průměrnou jízdu by bylo zapotřebí více než 500 000 nabíječek, pokud by každé vozidlo během dne bylo připojeno pro dorovnání sítě a nabíjení ve stejné lokalitě, což není pravděpodobné. Při nabíjení v cíli cesty by počet nabíječek samozřejmě stoupl. Pro všechna osobní auta (6 000 000) po jejich elektrifikaci by jejich kapacita stačila na trochu více než 5 h, ovšem za předpokladu jejich pravidelného střídání na více nabíječkách, kde by jedno vozidlo pobylo asi 9 h denně. Při snížení odebíraného výkonu pro využití všech těchto vozidel by však bylo pro nabíjení ve stejné lokalitě zapotřebí asi 5 000 000 nabíječek, doba

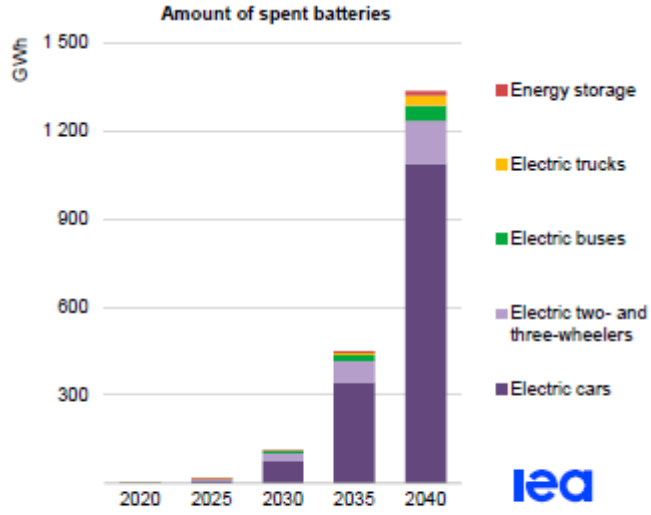

Obrázek 9: *potřebná kapacita baterií do r. 2040*

připojení by byla ovšem 20 h. Období s malým výkonem OZE se tím ovšem nevyřeší, trvají často déle než několik dní, a to v zimě i v létě.

2.5 Materiálová náročnost

Pokud je elektromobilů málo, zdá se otázka spotřeby materiálů banální. Ale s rostoucím počtem elektromobilů výrazně nabývá na významu a může se stát limitem rozvoje elektromobility. Data ukazují rostoucí nesoulad mezi ambicemi v oblasti klimatu a dostupností kritických nerostů, které jsou nezbytné pro realizaci těchto ambicí. IEA vydala v tomto roce obsáhlou zprávu [10], která podrobně analyzuje potřebu různých minerálů pro předpokládaný rozvoj elektromobility. Enormní nárůst potřeby baterií pro plánovaný počet elektromobilů ukazuje obrázek 9. Na výrobu elektromobilu a jeho baterie je potřeba několikrát více minerálů ve srovnání s výrobou automobilů se spalovacím motorem (obr. 10).

Podstatnou část nalezišť těchto materiálů vlastní nebo má pod kontrolou Čína. A podíl Číny je ještě větší při zpracování těchto prvků – Čína kontroluje až 70 % světové produkce kobaltu a lithia a až 90 % vzácných kovů [10]. Vzácné kovy jsou klíčovou součástí řady moderních technologií od spotřební elektroniky až po vojenské a zelené technologie: mobilní telefony, počítače, stíhačky, řízené střely, solární panely, větrné turbíny a elektromobily. Poptávka po vzácných kovech roste a Čína je prakticky jejich výhradním světovým producentem. Čína je také dominantním dodavatelem polykrystalického křemíku pro výrobu solárních panelů [14], spolu s Ruskem pokrývá 70 % spotřeby antimonu potřebného pro baterie, solární panely, polovodiče i větrné turbíny [13], atd. Rovněž výroba oceli se přesouvá do Číny, kde její cena není zatížena až 50 % navýšením emisními povolenkami jako v Evropě. Green Deal (Zelená dohoda pro Evropu) tak vede k závislosti Evropy na dodávkách surovin z Číny a dalších zemí.

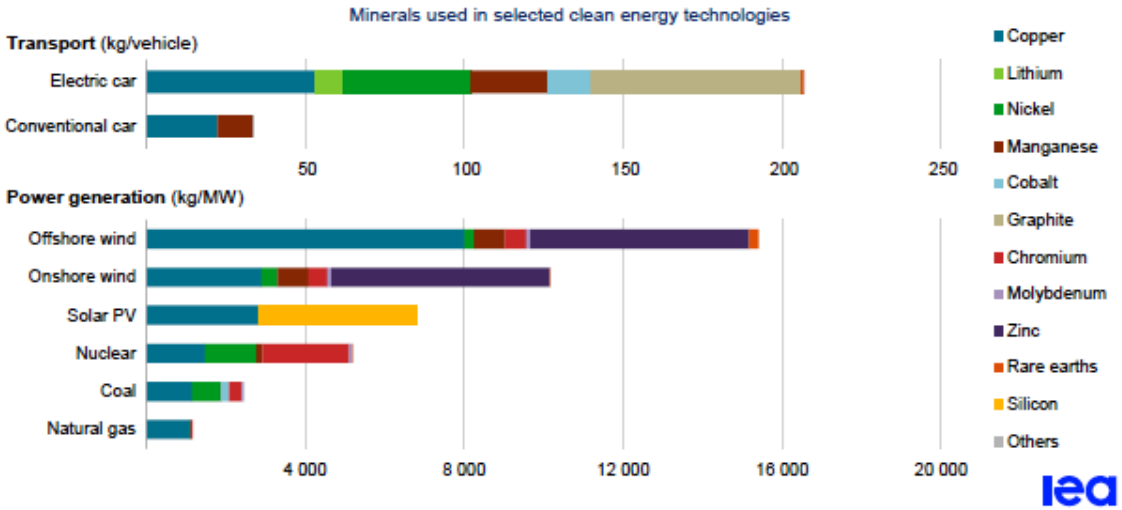

Obrázek 10: porovnání potřeby materiálů pro automobily a elektromobily a pro různé technologie výroby elektřiny

Rostoucí potřeba minerálů jak pro výrobu elektromobilů, tak i obnovitelných zdrojů energie vede k násobné potřebě surovin (obr. 11) a tím k další rozsáhlé devastaci přírodních zdrojů Země. Podle IEA by do roku 2040 potřeba lithia vzrostla více než 40x

a potřeba dalších materiálů cca 20x. Protože těžba probíhá v rozhodující míře mimo Evropu, emise vznikající při těžbě a dopravě surovin se do bilance CO_2 v Evropě nezapočítávají !

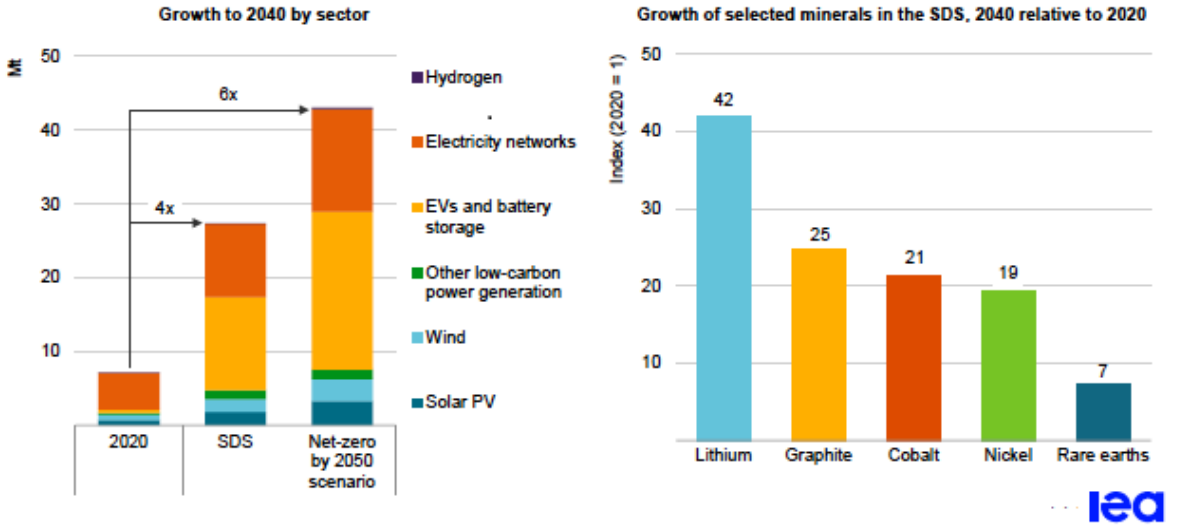

Obrázek 11: *Nárůst mateiálové náročnosti pro scénář udržitelného rozvoje (SDS) a uhlíkovou neutralitu a násobný nárůst potřeby vybraných materiálů pro SDS do roku 2040*

Lze předpokládat, že růst počtu elektromobilů bude limitován dostupnými zdroji surovin. Navíc zde hraje roli časový faktor: Otevření nových nalezišť trvá delší dobu, např. zprovoznění měděného dolu cca 10 let [15], což je v rozporu s plány rozvoje elektromobility v Evropě.

2.6. Recyklace

Teoreticky by potřeba těžby nových materiálů mohla být omezena recyklací použitých baterií elektromobilů, resp. solárních a větrných elektráren po skončení jejich životnost. Recyklace je v současné době v počátcích a je technologicky a energeticky náročná. V Evropě dosud není dostupná kapacita pro recyklaci většího množství baterií. V současné době se recyklací získává méně než 1 % lithia a vzácných zemin. IEA předpokládá, že v roce 2040, kdy již bude k dispozici značné množství vyřazených baterií, by recyklované množství mědi, lithia, niklu a kobaltu mohlo snížit požadavky na tyto minerály asi o 10 % [10].

2.7 Co to přinese ekonomicky

Často se uvádí, že cena elektromobilů bude s rostoucí sériovostí klesat a dojde k vyrovnání cen automobilů se spalovacím motorem a elektromobilů. Je pravděpodobné, že k vyrovnání dojde, ale ne na současných cenách automobilů, nýbrž na cenách elektromobilů. Důvody k tomu jsou jednak připravované znevýhodnění spalovacích motorů uhlíkovou daní a zejména rostoucí materiálové a energetické náklady na výrobu elektromobilů. Obrázek 12 ukazuje vývoj ceny některých materiálů v posledním roce [16]. Je pravděpodobné, že s rostoucí potřebou

těchto matriálů může cena dále růst. Roste nezanedbatelně i cena oceli, základního materiálu pro výrobu vozidel.

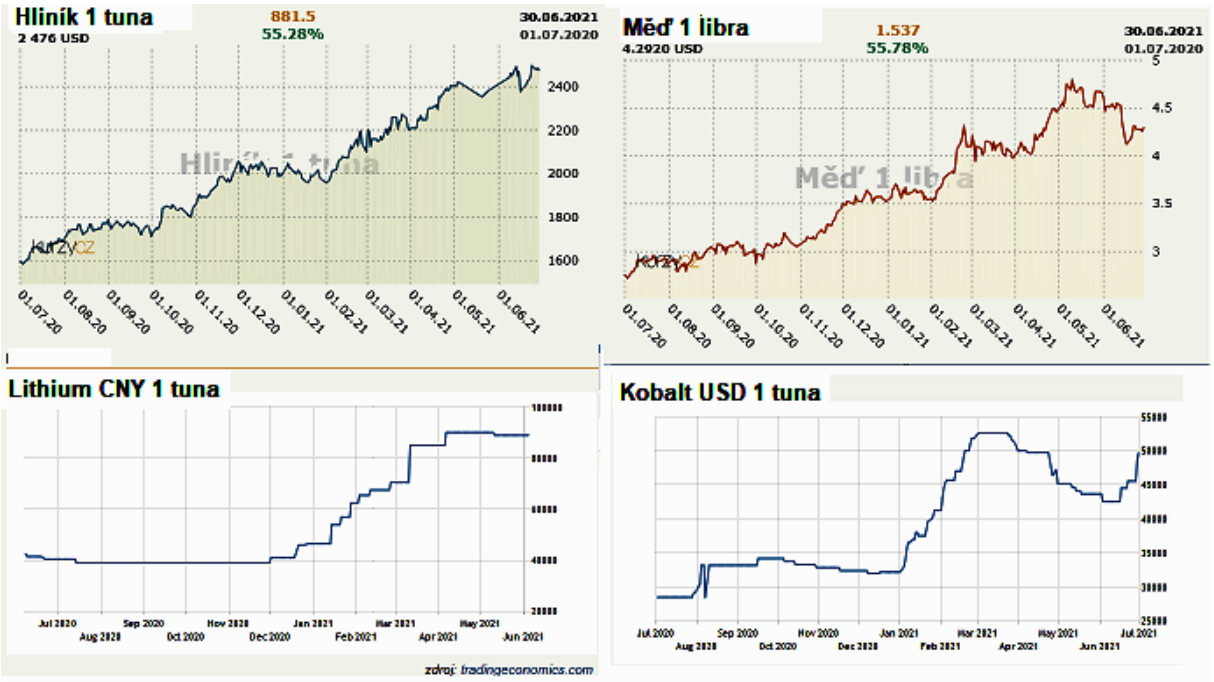

Obrázek 12: vývoj cen vybraných materiálů

Obrázek 13: vývoj ceny elektřiny

Dalším problémem je vývoj ceny elektřiny [16] (obr. 13). Obecně se na jejím růstu podílí snahy o snížení emisí CO_2, zejména rostoucí ceny emisních povolenek, uzavírání uhelných elektráren, dotace na výstavbu a provoz OZE a komoditní platby na záložní zdroje elektřiny. Např. dotace českých solárních elektráren od roku 2010 do 2030 se blíží 1 bilionu Kč, což je částka, za kterou by bylo možné postavit několik bloků jaderných elektráren se stabilními dodávkami elektřiny. Další růst OZE tyto částky ještě zvýší. Přitom v ČR solární elektrárny vyrábějí pouze cca 3 % a větrné necelé 1 % roční produkce elektrické energie. Rostoucí cena elektřiny se dotýká nejen domácností, zejména těch s nižšími příjmy, ale i průmyslu, kde zvyšuje náklady a tím snižuje jeho konkurenceschopnost a vede k obecnému zvyšování cen.

Ceny elektromobilů obecně jsou dotovány. Například v Německu je dotace na nákup elektromobilu 9000 €, ve Francii 7000 € [17]. Dotace mohou pocházet od státu (tedy od daňových poplatníků) nebo od automobilky, která na ně získává prostředky zdražením automobilů se spalovacími motory. Tento proces – zdražování automobilů

již probíhá. Čím více bude elektromobilů a méně automobilů se spalovacími motory, tím větší bude nárůst ceny automobilů pro kompenzaci dotací na elektromobily.

Rozvoj elektromobility vyvolává další nutné investice v řádech miliard EURO na budování nabíjecí infrastruktury, posílení rozvodných sítí atd. Masivnější růst počtu elektromobilů vyvolá v příštích letech růst spotřeby elektřiny, která bude muset být zejména v obdobích, kdy OZE nedodávají dostatek výkonu zajištěna patrně novými plynovými (t.j. fosilními) zdroji.

2.8 Co to přinese pro klima

Emise z lidské činnosti představují cca 3,5 % celkové tvorby CO_2 na Zemi, převážná většina CO_2 pochází z přírodních zdrojů. Za předpokladu, že by všechny automobily se spalovacím motorem v Evropě byly nahrazeny elektromobily a s uvážením podílu dopravy v Evropě na tvorbě CO2 celkem, z toho podílu silniční dopravy a podílu osobních automobilů je zřejmé, že se evropské osobní automobily podílejí na celkové tvorbě CO_2 v Evropě 5 – 10%. S uvážením podílu EU na tvorbě CO_2 ve světě se evropské osobní automobily podílejí na globálních emisích CO_2 z lidské činnosti pouze zlomkem procenta (obr. 14) ! A to ještě za předpokladu, že by elektromobily byly vyráběny zcela bezemisně a jezdily na čistou, bezemisně vyráběnou elektřinu. Tedy ve skutečnosti bude tento podíl ještě výrazně nižší v závislosti na reálných emisích při výrobě elektromobilů a baterií a výrobě elektřiny pro jejich provoz.

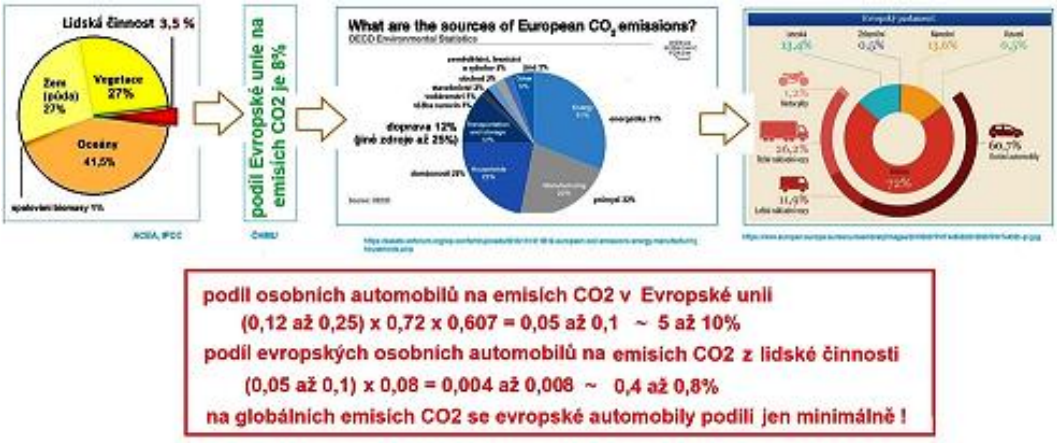

***Obrázek 14:** podíl osobních automobilů v Evropě na emisích CO2 z lidské činnosti*

V důsledku rostoucí životní úrovně v Číně a v dalších tzv. rozvojových zemích roste v těchto zemích spotřeba energie, která se vyrábí především z uhlí. Přes pokles spotřeby uhlí v Evropě a v USA jeho celková spotřeba ve světě neklesá [18] (obr. 15). V důsledku toho a v důsledku přesunu „špinavých“ výrob do Číny a dalších zemí celkové emise CO2 ve světě stoupají [19] a převyšují jejich úbytek v Evropě (obr. 16). Je zřejmé, že snaha o snižování emisí CO_2 náhradou automobilů elektromobily je velmi neefektivní a nevede k dosažení uhlíkové neutrality ve světě, nehledě na další problémy s tím souvisící. Za pozitivum lze považovat pouze snížení zdraví škodlivých emisí a hluku v ulicích měst.

S klimatickou změnou se musíme naučit žít, ne se ji snažit neúčinně a draze ovlivnit.

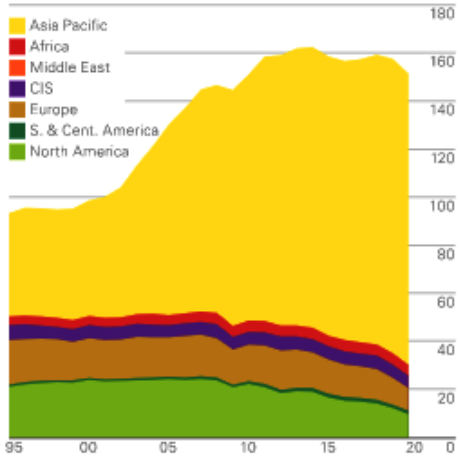

Obrázek 15: spotřeba uhlí ve světě

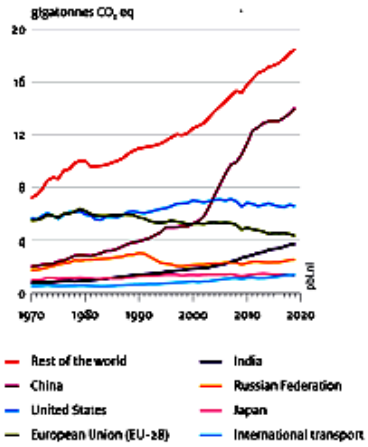

Obrázek 16: emise CO2 do r. 2019

3. ZÁVĚR

Elektromobil jako dopravní prostředek dává smysl zejména ve městech a při dojíždění do práce na krátké vzdálenosti, kde vystačí s malou baterií a lze jej dobít přes noc. Může být využit pro rozvážkové a jiné služby, dopravu po městě i jako druhý vůz v rodině, pokud majiteli nedělá problém vysoká cena. Násilné prosazování elektromobilů s cílem dosažení uhlíkové neutrality je neefektivní cestou, není lékem k ozdravění planety, nepřináší z hlediska klimatu prakticky nic a naráží na řadu problémů v oblasti výroby, materiálové náročnosti i v cenové politice. Vysoká cena omezuje mobilitu chudší části společnosti a nutí je udržovat v provozu stará vozidla s vysokými emisemi, což je v přímém protikladu se smyslem elektromobility. Dotace pokřivují trh a podporují bohatší část společnosti. Navíc zde vzniká riziko dovozu ojetých elektromobilů s následnými problémy s ekologickou likvidací vysloužilých baterií.

Budeme-li ve smyslu současných evropských předpisů považovat elektromobily za zcela bezemisní a podobně elektřinu vyráběnou v solárních nebo větrných elektrárnách za bezemisní, pak je možné, že do roku 2050 dosáhneme v Evropě uhlíkové neutrality. Ale jen na papíře, nikoliv ve skutečnosti, a to při značném poklesu současné kvality života.

POUŽITÉ ZDROJE

[1] Ccweb studie pro MŽP
https://www.chmi.cz/files/portal/docs/meteo/ok/klimazmena/files/cc_chap02.pdf

[2] Pascal Richet: The temperature–CO2 climate connection:
an epistemological reappraisal of ice-core messages
https://hgss.copernicus.org/articles/12/97/2021/hgss-12-97-2021.pdf

[3] EU chce mít na silnicích do roku 2030 nejméně 30 milionů aut bez emisí
https://www.auto.cz/eu-chce-mit-na-silnicich-do-roku-2030-nejmene-30-milionu-aut-bez-emisi-137087

[4] BRUSEL: Zelený úděl se vítězně valí vpřed
https://neviditelnypes.lidovky.cz/ekonomika/brusel-zeleny-udel-se-vitezne-vali-vpred.A210329_173419_p_ekonomika_nef

[5] Aktualizace Národního akčního plánu čisté mobility (NAP CM)2019
https://mdcr.cz/getattachment/Media/Media-a-tiskove-zpravy/Vlada-schvalila-aktualizovany-Narodni-akcni-plan-c/Aktualizace-NAP-CM.pdf.aspx

[6] ROMARE, Mia a Lisbeth DAHLLÖF. The Life Cycle Energy Consumption and Greenhouse Gas Emissions from Lithium-Ion Batteries:
https://www.ivl.se/download/18.5922281715bdaebede9559/1496046218976/C243%20The%20life%20cycle%20energy%20consumption%20and%20CO2%20emissions%20from%20lithium%20ion%20batteries%20.pdf

[7] Global EV Outlook 2019 [online]. Paris: IEA, 2019 [cit. 2020-06-04].
https://www.iea.org/reports/global-ev-outlook-2019

[8] Kosten für E-Autos: Ladeverluste nicht vergessen
ADAC e.V. | Technik | 22.07.2020
https://presse.adac.de/meldungen/adac-ev/technik/ladeverlust.html

[9] Morkus, Macek: Kam kráčíš, elektromobilito?
https://www.fs.cvut.cz/verejnost/pr-media/pribehy-z-ustavu/kam-kracis-elektromobilito/

[10] The Role of Critical Minerals in Clean Energy Transitions. IEA 2021
https://iea.blob.core.windows.net/assets/24d5dfbb-a77a-4647-abcc-667867207f74/TheRoleofCriticalMineralsinCleanEnergyTransitions.pdf

[11] ERÚ: Roční zpráva o provozu elektrizační soustavy ČR za rok 2020
https://www.eru.cz/documents/10540/6616306/Rocni_zprava_provoz_ES_2020.pdf/edc0cb03-700a-43a7-8c08-a1ccb3f2d173

[12] Největší bateriové úložiště v ČR zahájilo svůj provoz v Plané nad Lužnicí
https://oze.tzb-info.cz/akumulace-elektriny/19624-nejvetsi-bateriove-uloziste-v-cr-zahajilo-svuj-provoz-v-plane-nad-luznici

[13] Antimon. Prvek, kterým drží Čína a Rusko svět v šachu.
https://www.tydenikhrot.cz/clanek/antimon-cina-rusko-usa

[14) Silicon Data Sheet - Mineral Commodity Summaries 2020
https://pubs.usgs.gov/periodicals/mcs2020/mcs2020-silicon.pdf

[15] Jak se přechází na zelenou. Světu budou brzy chybět miliony tun mědi.
https://www.tydenikhrot.cz/clanek/jak-se-prechazi-na-zelenou-svetu-budou-brzy-chybet-miliony-tun-medi-zelena-ekonomika

[16] Kurzycz.
www.kurzy.cz/komodity

[17] Dotace na elektromobily v zahraničí
https://www.portalridice.cz/clanek/dotace-na-elektromobily-v-zahranici

[18] Statistical Review of World Energy
https://www.bp.com/en/global/corporate/energy-economics/statistical-review-of-world-energy.html

[19]Trends in global CO2 and total greenhouse gas emissions: 2019 Report
https://www.pbl.nl/sites/default/files/downloads/pbl-2020-trends-in-global-co2-and-total-greenhouse-gas-emissions-2019-report_4068.pdf

PODĚKOVÁNÍ

Tato práce byla financována z projektu Ministerstva školství, mládeže a tělovýchovy, programu NPU I (LO), projektu # LO1311 Rozvoj automobilového centra udržitelné mobility spolu s programy Technologické agentury ČR, NCK 1 a BETA , projekty Národní kompetenční centrum Josefa Božka, TN0100 0026, a Optimální využití obnovitelných paliv v dopravě, TIT SMZP 713. Tyto podpory jsou vděčně uznávány. Během diskusí s kolegy v think-tanku Realistická energetika a ekologie, https://realisticka.cz došlo k mnoha zajímavým závěrům.

LII. INTERNATIONAL SCIENTIFIC CONFERENCE OF THE CZECH AND SLOVAK UNIVERSITY DEPARTMENTS AND INSTITUTIONS FOCUSED ON RESEARCH AND TEACHING METHODS RELATED TO COMBUSTION ENGINES, ALTERNATIVE DRIVES AND TRANSPORT
SEPTEMBER 22 – 23, 2021, PRAGUE
CZECH UNIVERSITY OF LIFE SCIENCE PRAGUE, FACULTY OF ENGINEERING,
DEPARTMENT OF VEHICLES AND GROUND TRANSPORT

INNOVATIVE APPROACH TO REDUCE FRICTION LOSSES IN TURBOCHARGER THRUST BEARINGS

Pavel Novotný[1], Jiří Vacula[2], Petr Kudláček[3], Jiří Klíma[4], Vladimír Hort[5]

Abstract
The mechanical efficiency of turbochargers is mainly influenced by the lubrication system and can be increased by improving the performance of the thrust bearing. An innovative approach combines three levels of bearing computational models with optimization using genetic algorithms and effectively considers the multi-operating conditions. The strategy represents a 35% reduction in mechanical losses of the thrust bearing under preferred operating conditions. These savings result in a 20% energy saving in the lubrication system measured on the turbocharger of a stationary internal combustion engine without significant risk of lubrication system failure.

1. INTRODUCTION

Application sectors including marine, rail transport or distributed cogeneration are currently based on turbocharged internal combustion engines (ICE). Turbocharging technology makes it possible to achieve higher overall efficiency leading to lower specific fuel consumption and lower pollutant emissions [1], but, on the other hand, it introduces many issues, such as turbo-lag [2], failures [3], and noise and vibration [4]. Turbochargers (TCs) are machines with relatively high mechanical efficiency with values of about 90% at high speeds and correspondingly high loads. When the TC is operating at low speeds, the performance of the compressor is significantly reduced, and even the mechanical efficiency decreases to smaller values. Reducing mechanical losses is, thus, even more important. The mechanical losses are particularly important under TC transient operating conditions or under off-design operating conditions, such as, for example, compressor surge operating conditions.
Mechanical losses are mainly caused by the lubrication system and, thus, predominantly due to thrust and journal bearings when hydrodynamic oil bearings are used. Mechanical losses have been the subject of many research studies. The studies

[1] doc. Ing. Pavel Novotný, Ph.D., Brno University of Technology, Technická 2896/2, 61669 Brno, novotny.pa@fme.vutbr.cz
[2] Ing. Jiří Vacula, Brno University of Technology, Technická 2896/2, jiri.vacula@vutbr.cz
[3] Ing. Petr Kudláček, Brno University of Technology, Technická 2896/2, petr.kudlacek@vutbr.cz
[4] Ing. Jiří Klíma, PBS Turbo s.r.o, Vlkovská 279, 595 01 Velká Bíteš, jiri.klima@pbsturbo.cz
[5] Vladimir Hort, PBS Turbo s.r.o, Vlkovská 279, 595 01 Velká Bíteš, vladimir.hort@pbsturbo.cz

have analysed the effects of the lubrication system on mechanical losses and lubricant flow rates. Experiments performed by Deligant et al. [5] showed that thrust bearings make a significant contribution to friction losses and lubricant flow rates, which are more likely under increased rotor speeds.
Thrust bearings also have a fundamental effect on lubricant flow rate. Novotný et al. [6] presented lubricant flow rates of journal and thrust bearings on a heavy-duty truck's ICE TC and concluded that thrust bearing can have a much higher influence on the total lubricant flow rate; mainly, bearing axial clearance and lubricant inlet pressure is highly important. In another work, Novotný and Hrabovský [7] investigated a share of friction losses and flow rates between thrust-bearing sides. They found that, while the friction losses on the thrust bearing of the stationary ICE TC occurred mainly on the thrust side, the lubricant flow rates were higher on the counter-thrust side. The counter-thrust side was evaluated as mostly unloaded under design-operating regimes. This fact was further increased under operating conditions corresponding to higher compression ratios and rotor speeds.
TCs contribute positively to improving ICE performance, but they also have some disadvantages. For example, they significantly affect ICE failures. Nahim et al. [8] claimed 5 % of ICE failures are due to TCs. Moreira [9] also mentioned the great influence of TCs on diesel ICE failures in heavy-duty vehicles. There are many components of TCs that can lead to failure, but, most commonly, the lubrication system is the main source of technical failures. Dellis et al. [3] investigated TCs of passenger car ICEs and concluded that approximately 50 % of serious failures in a large group of samples were caused by the lubrication system. The failures mainly included the delay of lubricant entrance into the TC and a lack of sufficient lubrication. It can be stated that lubrication system failures are usually closely related to specific operating conditions and, unfortunately, are often associated with the human factor. When increasing the performance of the lubrication system, the design operating conditions are preferred, i.e. those conditions under which the TCs are operated most often. However, failures usually occur under off-design operating conditions and, therefore, these conditions must also be considered.

2. RESEARCH OBJECTIVE

The research objective is a development approach that will improve the performance of the lubrication system of TCs under the preferred-design operating conditions and guarantee its reliable functionality even under off-design operating conditions. The approach will be applied to find a new design for TCs' thrust bearing in a stationary natural gas ICE. The new thrust bearing must enable reduction of mechanical losses in the lubrication system. The main emphasis is on design operating conditions of TCs, including low loads and low rotor speeds. The following requirements must be met for an improved lubrication system, including the new thrust bearing:

- The energy losses of the lubrication system must be decreased by more than 5 % under preferred operating conditions at up to 60 % of maximal rotor speeds.
- The load capacity of the thrust bearing must not be decreased.
- The TC's lubricant flow rate must not be significantly higher.
- The bearing's lubricant temperature at the bearing outlet must not be higher.
- The minimal lubricating gap thickness must not be significantly reduced.

3. METHODOLOGY DESCRIPTION

An innovative approach is proposed to meet the defined research objectives. The innovative approach focuses on the thrust bearing as the most significant source of mechanical losses in the lubrication system and, at the same time, the source with the greatest potential for reducing losses. The approach assumes the definition of a specific bearing concept and an initial bearing design that satisfies that concept. Any bearing matching the bearing concept is subsequently evaluated for its integral characteristics, and these characteristics are used by an optimalisation approach. The principle is to work with relative changes between the initial and any bearing candidate. The innovative approach must not only find, but also verify, the new bearing as a key element of the entire lubrication system.

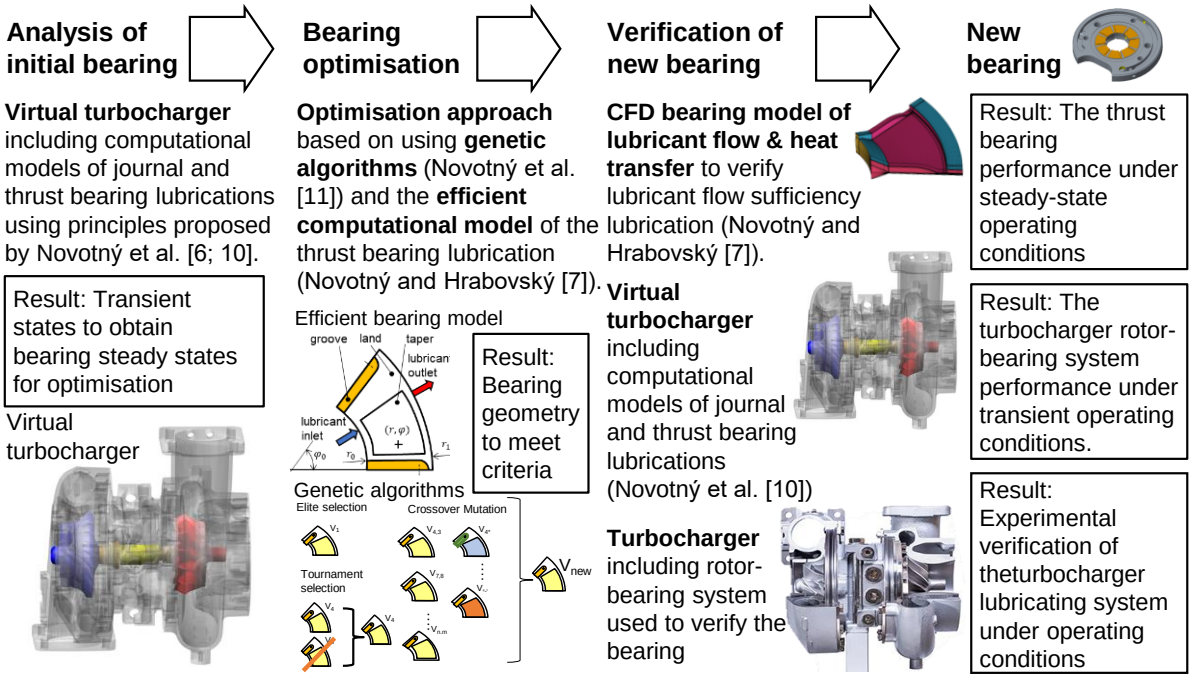

Figure 1: Scheme of the innovative approach including three steps: an evaluation of the serial bearing under transient operating conditions, a bearing optimisation and a verification of the new bearing.

The innovative approach consists of three consecutive steps:

- Evaluation of the rotor-bearing system, including the serial thrust bearing under the typical turbocharger operating conditions. This generates corresponding bearing kinematic conditions and loads for the preferred steady-state operating conditions. The transient dynamics of TCs is effectively solved using a nonlinear dynamic multibody model, called a virtual turbocharger and incorporating hydrodynamic bearing models developed by Novotný et al. [6; 10].
- Optimisation of the thrust bearing design parameters, utilising genetic algorithms (Novotný et al. [11]) and an efficient computational model of the thrust bearing (Novotný and Hrabovský [7]) under preferred operating conditions.
- Verification of the new thrust bearing using computational approaches for a solution of thrust bearing steady-states using CFD [7], transient dynamics of a rotor-bearing system [10] and final experimental verification of a TC, including a thrust bearing prototype.

This innovative approach also brings a certain loss of generality and undoubtedly requires a certain level of practical experience with the problem, but, on the other hand, partially limits the influence of computational modelling accuracy to describe a given physical problem. The proposed strategy is graphically illustrated in Figure 1.

4. RESULTS

The mechanical losses are evaluated by measuring the lubricant temperature rise after passing through the turbocharger lubricating system and measuring the lubricant flow rate in both the cold and hot operating conditions. From the principle of TC operation, it is clear that the heat dissipated by the lubricant does not occur only due to frictional losses in the bearings, but is also affected by heat transfer from the surrounding walls. Neglecting this effect may introduce some distortion of the measured lubricating system losses. To limit this influence, measurements are made on both the serial and the new thrust bearing installed on the same TC operated under the same operating conditions. The new bearing is then evaluated relative to the serial bearing and thus the effect of heat transfer through the walls is largely eliminated.
For a more detailed evaluation of the lubricant temperature rise at the thrust bearing outlet and to eliminate the effect of heat transfer the TC is operated under cold operating conditions. In this case, however, the maximum achievable rotor speed is reduced, as the cold conditions are limited by the maximum flow rate of compressed air supplied to the turbine by an external compressor.

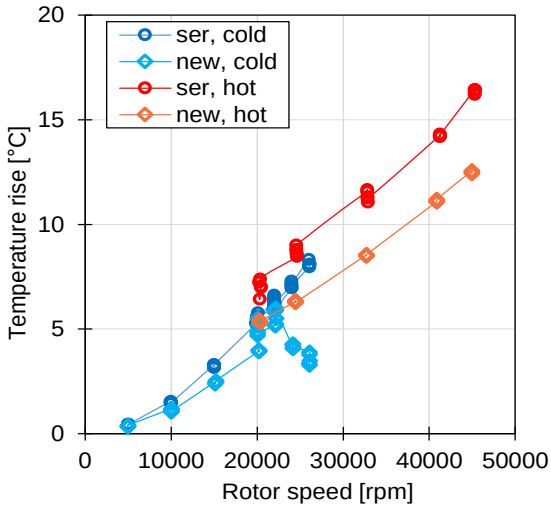

Figure 2: Rise in lubricant temperature between the inlet and the outlet of the TC operated under the cold and hot operating conditions for lubricant temperature at inlet, $T_{\mathrm{in}} = 60°\mathrm{C}$. The symbol ser indicates the serial design and new the new design of the thrust bearing.

The rise in lubricant temperature between the inlet and the outlet of the TC lubrication system is clearly visible in Figure 2. The effect of hot operating conditions on lubricant is also clearly visible in areas where the hot and cold operating conditions intersect at rotor speeds.
According to the measurements, the overall energy savings on the entire TC lubrication system when using the new thrust bearing design are on average 15 % in the TC's low speed range and under the cold operating conditions and on average 20 % in the full

speed range under hot operating conditions. The results of the measurements are shown in Figure 3, the mechanical loss ratio is defined as the power loss change using the new bearing relative to power loss of the serial bearing. The total energy savings determined by measuring the TC show the great influence of the thrust bearing on total mechanical losses of the lubricating system.

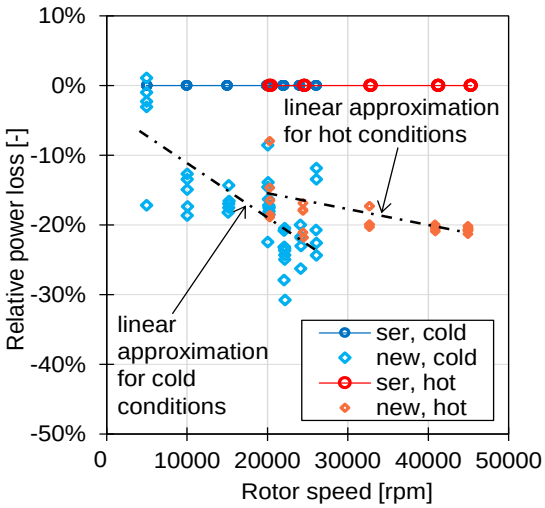

Figure 3: Mechanical loss ratio of the TC lubrication system comparing the new bearing relative to the serial bearing determined by measurements on experimental turbocharger under cold and hot operating conditions. Dashed lines present the linear approximation of measured results.

The requirement defined in the solution strategy also defines only a small increase in lubricant flow rates. The lubricant flow rates were slightly increased in line with the limit set in the solution strategy. There was an increase of 11% under cold operating conditions and 15% under hot operating conditions.

5. CONCLUSIONS

The proposed innovative approach has proven its effectiveness in reducing mechanical losses of the lubrication system of the considered TC under preferred operating conditions. The result was achieved by reducing the friction losses of the thrust bearing. At the same time, the approach eliminated thrust bearing designs that would lead to damage under off-design operating conditions. Application of the approach has made it possible to reduce mechanical losses of the thrust bearing by an average of 35 % under the preferred operating conditions. These partial savings resulted in approximately 9 % energy savings in the entire TC lubrication system without a significant increase in lubricant flow rates or a significant reduction in the risks of damage to the lubrication system components.

The strong point of the innovative approach strategy is the inclusion of several operating conditions to the optimalisation of the lubrication system, respectively, of the thrust bearing. The preferred operating conditions still have a dominant influence on the final shape of the bearing, but the off-design operating conditions enable the elimination of bearing variants, which are likely to reduce the bearing service life and, thus, the lubrication system failure.

REFERENCES

[1] TORREGROSA, A.J., A. BROATCH, R. NOVELLA and L.F. MÓNICO. Suitability analysis of advanced diesel combustion concepts for emissions and noise control. *Energy*. 2011, **36**(1), 825-838.

[2] PAGOT, A., A. DUPARCHY, X. GAUTROT, P. LEDUC and G. MONNIER. Combustion approach for downsizing: the IFP concept. *Oil and Gas Science and Technology*. 2006, **61**(1), 139-153.

[3] DELLIS, P., R. EVAGGELOS, G. ALCIBIADES and A. PESYRIDIS. Turbocharger Lubrication -Lubricant Behavior and Factors That Cause Turbocharger Failure. *International Journal of Automotive Engineering and Technologies*. 2013, **2**(1), 40-54.

[4] GALINDO, J., A. TISEIRA, R. NAVARRO, D. TARÍ and C.M. MEANO. Effect of the inlet geometry on performance, surge margin and noise emission of an automotive turbocharger compressor. *Applied Thermal Engineering*. 2017, **110**, 875-882. ISSN 13594311.

[5] DELIGANT, M., P. PODEVIN and G. DESCOMBES. Experimental identification of turbocharger mechanical friction losses. *Energy*. 2012, **39**(1), 388-394. ISSN 03605442.

[6] NOVOTNÝ, Pavel, Petr ŠKARA and Juraj HLINÍK. The effective computational model of the hydrodynamics journal floating ring bearing for simulations of long transient regimes of turbocharger rotor dynamics. *International Journal of Mechanical Sciences*. 2018, **148**, 611-619. ISSN 0020-7403.

[7] NOVOTNÝ, P. a J. HRABOVSKÝ. Efficient computational modelling of low loaded bearings of turbocharger rotors. *International Journal of Mechanical Sciences*. 2020, **2020**(174), 105505.

[8] NAHIM, H.M., R. YOUNES, H. SHRAIM and M. OULADSINE. Oriented review to potential simulator for faults modelling in diesel engine. *J. Mar. Sci. Technol*. 2016, **21**(1), 533-551.

[9] MOREIRA, M.F. Failure analysis in aluminium turbocharger wheels. *Wear*. 1999, **1999**(225-229).

[10] NOVOTNÝ, P., J. HRABOVSKÝ, J. JURAČKA, J. KLÍMA and V. HORT. Effective thrust bearing model for simulations of transient rotor dynamics. *International Journal of Mechanical Sciences*. 1, 2019, **2019**(157-158), 374-383.

[11] NOVOTNÝ, Pavel, Martin JONÁK and Jiří VACULA. Evolutionary Optimisation of the Thrust Bearing Considering Multiple Operating Conditions in Turbomachinery. *International Journal of Mechanical Sciences*. 2021, **195**. ISSN 00207403.

ACKNOWLEDGEMENT

The research leading to these results has received funding from the Specific research program at Brno University of Technology, reg. no. FSI-S-20-6267. The research has also been supported by the Technology Agency of the Czech Republic, in the project Thrust bearing load capability increasing, Reg. No.: TH03020426.

52. MEZINÁRODNÍ VĚDECKÁ KONFERENCE ČESKÝCH A SLOVENSKÝCH UNIVERZIT A INSTITUCÍ ZAMĚŘENÁ NA VÝZKUMNÉ A VÝUKOVÉ METODY SPOJENÉ SE SPALOVACÍMI MOTORY, ALTERNATIVNÍMI POHONY A DOPRAVOU

22.-23. ZÁŘÍ 2021, PRAHA
ČESKÁ ZEMĚDĚLSKÁ UNIVERZITA V PRAZE, TECHNICKÁ FAKULTA,
KATEDRA VOZIDEL A POZEMNÍ DOPRAVY

2021 - Trojnásobné jubileum

Ústavu automobilů, spalovacích motorů a kolejových vozidel Fakulty strojní ČVUT

Branko REMEK.

Abstrakt

Rok 2021 je pro současný Ústav automobilů, spalovacích motorů a kolejových vozidel, Strojní fakulty ČVUT v Praze mimořádně významný. V historickém vývoji pražské techniky se připomíná 100 let od založení Ústavu spalovacích motorů, 70 let od založení Ústavu automobilů, traktorů a zemědělských strojů a 55 let od sloučení obou ústavů. Celé toto období je kriticky zhodnoceno.

1707 - POČÁTEK HISTORIE

V roce 1705 poslal Christian Josef Willenberg Leopoldu I Habsburgskému supliku s žádostí o svolení k vyučování umění inženýrskému v Praze. Po dvou letech jeho následník Josef I nařídil českým reskriptem stavům, aby vše podpořily. Trvalo to 10 let a dvouletá výuka začala ve školním roce 1717/18. Vynález parního stroje v roce 1769 spustil technickou revoluci a význam pražské techniky vzrostl, když byl v roce 1805 jmenován ředitelem František Josef Gerstner. V první vlastní budově v Husově ulici na Starém městě pražském byl v roce 1812 uveden do provozu dar stavů, parní stroj Boulton&Watt 17HP. Stroj dodaný v dílech sestavil “mechanicus” techniky Josef Božek. Do dějin se Božek nesmazatelně zapsal prvním parním vozidlem ve Střední Evropě v roce 1815 a parolodí v roce 1817. Vůz je znám z rytiny, podle které udělal malý model František Rott počátkem 2. Světové války. První replika vozu byla postavena v roce 1950 jako pohyblivá maketa pro film o životě Josefa Božka, "Posel úsvitu". Druhou, plně funkční repliku, postavil v roce 1985 Josef Svoboda z Liberce a jeho samohyb je v Muzeu staré techniky v Žamberku.

Ing. Branko REMEK, CSc,, U12201, Fakulta strojní ČVUT v Praze, branko.remek@fs.cvut.cz

Obr. 01 Portál budovy politechniky

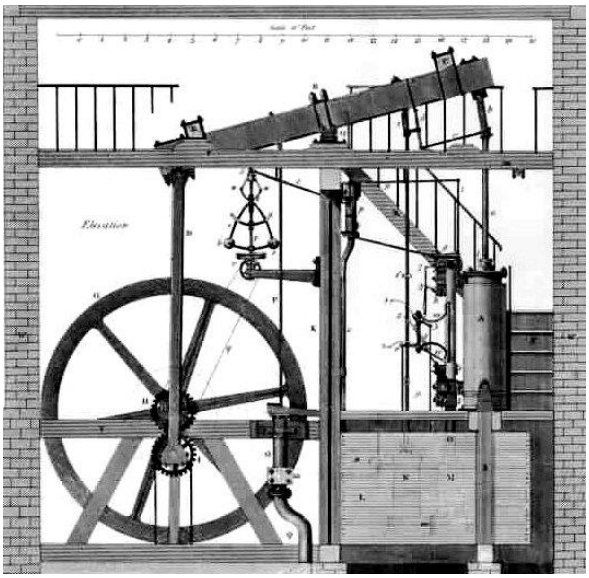

Obr. 02 Plnotlaký parní stroj Watt – 1769

Gerstner projektoval splavnění Vltavy a koněspřežnou dráhu z Českých Budějovic do Lince, později prodlouženou až do Gmundenu. Doprava na úseku do Lince v délce 130 km, byla zahájena roku 1827.

Obr. 03 Replika parovozu 2015

Obr. 04 Retro jízda koněspřežky, Kerschbaum

1864 - OBOR STROJNICTVÍ - MOTORY A VOZIDLA

Zrušení roboty v roce 1848 bylo hnací silou průmyslové revoluce 19. století. Obor strojnictví se samostatně rozvíjel od roku 1863/1864, kdy transformací inženýrské školy, resp. politechniky vznikla C. a K. Česká vysoká škola technická a byl zaveden

výkaz o studiu, index. Profesorské stolice byly zřízeny pro čtyři obory, Stavitelství pozemní, Stavitelství vodní a silniční, Strojnictví a Technická lučba (chemie). Bylo to v době páry a tak byla zaměřena i výuka, kde obor parních strojů a železničních vozidel dosáhl světové úrovně. Obor spalovacích motorů se zpočátku vyučoval v několika strojnických oborech. Výuka byla postavena na přednáškách „Technická mechanika a nauka o strojích“ profesora Hausmanna, „Stavba strojů a encyklopedie mechaniky“ profesora Salaby a „Všeobecná a technická fyzika“ profesora Zengera. Již v té době byla úzká spolupráce se strojírnami Ringhoffer, Breitfeld&Daněk a První česko-moravskou. Výnosem Ministerstva školství Československé republiky vzniklo v roce 1920 České Vysoké Učení Technické. Statut vytvářel školu, která zahrnovala původní obory, povýšené na Vysoké školy, později fakulty. Studium již bylo čtyřleté.

1921 – ÚSTAV SPALOVACÍCH MOTORŮ

V roce 1921 byl zřízen Ústav spalovacích motorů ČVUT profesora Jana Košťála, který po promoci v Praze a stáži na Polytechnice v Curychu pracoval jako konstruktér v Českomoravské továrně na stroje. Činost ústavu byla zaměřena na průmyslové motory, které postupně vytlačovaly parní stroje. Sídlo ústavu bylo ve starší budově Karlových kasáren. Laboratoř spalovacích motorů byla ve Strojní laboratoři zřízené v roce 1921 ve dvoře areálu ČVUT.

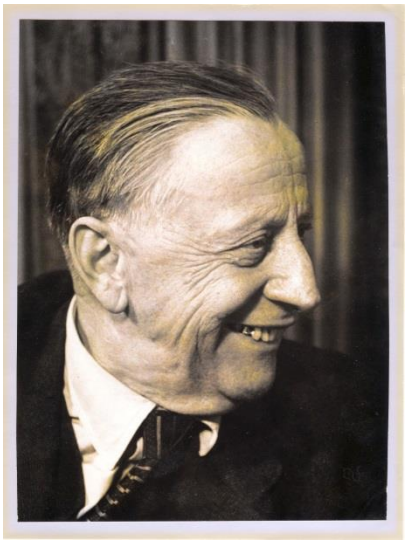

Obr. 05 Jan Košťál

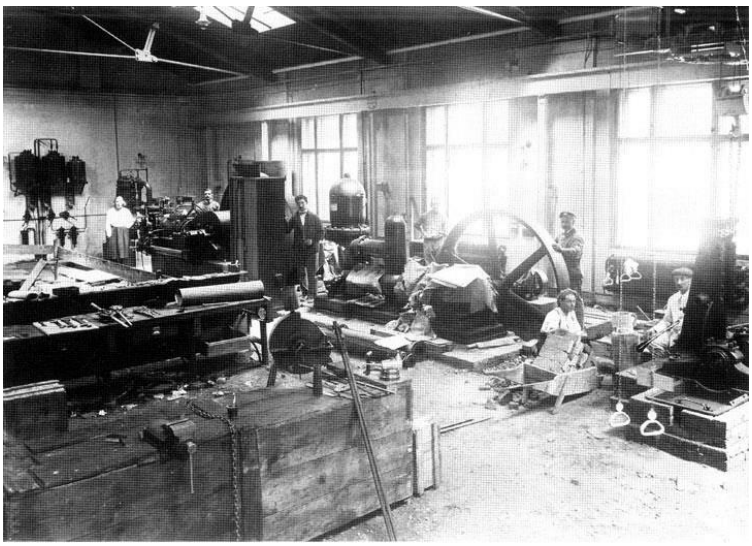

Obr. 06 Strojní laboratoř 1923

Strojní laboratoř byla vybavena parním kotlem Škoda Oschatz, který dodával páru pro turbíny a stroje. Prvními spalovacími motory byly vznětový jednoválec Škoda LW, zatěžovaný Pronyho brzdou a zážehový jednoválec Breitfeld&Daněk, zatěžovaný pístovým kompresorem. Po úmrtí profesora Zvoníčka v roce 1926 byl přednosta Ústavu spalovacích motorů Košťál pověřen i správou Ústavu parních motorů. V letech 1948-1949 byl rektorem ČVUT a ústav vedl až do roku 1960, kdy jej vystřídal profesor Alois Vrba. Pováleční asistenti Ladislav Reichert a Bohuslav Suk se rekrutovali z řad studentů, kteří začali studium před válkou a dokončili až po ní. Mladšími asistenty byli Václav Rychetník a František Holát.

1951 ÚSTAV AUTOMOBILŮ, TRAKTORŮ, ZEMĚDĚLSKÝCH STROJŮ

Po 2. Světové válce byl v rámci Dvouletého plánu obnovy národního hospodářství (1947-1948) stanoven výrobní program československých automobilových a motocyklových továren, který jim racionálně určoval jejich zaměření. Z plánu zbylo po Únoru 1948 sice jen torzo, ale na Vysoké škole strojního a elektrotechnického inženýrství byl v roce 1949/1950 vypsán obor „Stavba automobilů a traktorů“. Ústav pro tento obor byl zřízen pro školní rok 1951/1952 pro Jana Petránka, který byl již roku 1946 jmenován profesorem. Po roce 1948 byly ústavy, po sovětském vzoru, přejmenovány na katedry a školy na fakulty. Ze svazku ČVUT byly v roce 1951/1952 vyčleněny Fakulta zemědělská, Fakulta chemická a Fakulta komerčního inženýrství a vznikly z nich samostatné vysoké školy, Vysoká škola zemědělská, resp. dnes ČZU (Česká zemědělská univerzita), Vysoká škola chemicko-technologická a Vysoká škola ekonomická. Původně společná Vysoká škola byla rozdělena na Fakultu strojní a Fakultu elektrotechnickou. Petránek měl znalosti a zkušenosti jako konstruktér automobilů značky Praga a technický ředitel Automobilového oddělení koncernu ČKD (Breitfeld&Daněk). Prvními absolventy pětiletého studia byli v roce 1952 Milan Apetaur, Miroslav Hanke, Zdeněk Kostelecký, Václav Rektor, Čestmír Šalamoun a další. V areálu na Karlově náměstí pro ústav nebylo místo a tak sídlil v obecní budově ve Štěpánské ulici. Tento stav zůstal zachován až do stěhování sloučených původních ústavů v roce 1966 do nové budovy ČVUT v Praze 6.

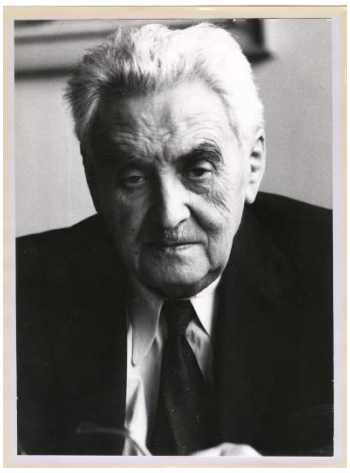

Obr. 07 Jan Petránek

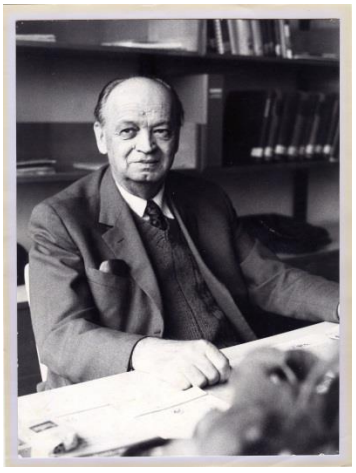

Obr. 08 Josef Kožoušek

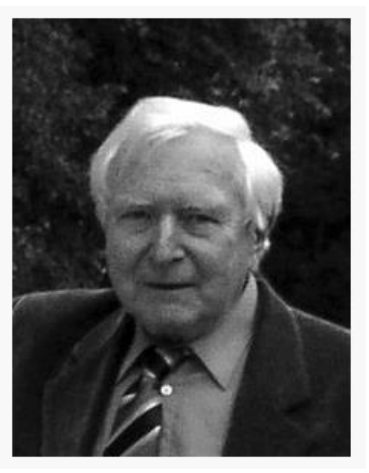

Obr. 09 Milan Apetaur

1966 – KATEDRA AUTOMOBILŮ A SPALOVACÍCH MOTORŮ *

Sloučením Katedry spalovacích motorů a části Katedry automobilů, traktorů a zemědělských strojů vznikla Katedra automobilů a spalovacích motorů pod vedením profesora Josefa Kožouška. Absolvent brněnské techniky a syn tamního profesora byl technik s praxí v konstrukci leteckých motorů u firem Škoda, Avia a Walter. Po 2. Světové válce odešel na bratislavskou techniku, kde k vědecké kariéře přidal i kariéru politickou. V roce 1962 byl povolán jako stranický kádr z Vysoké školy strojní a textilní v Liberci, kde od založení v roce 1953 byl rektorem a stal se i rektorem ČVUT. V oddělení automobilů, vedeném Petránkem, byli asistenti Zdeněk Kostelecký, Čestmír Šalamoun a od roku 1964 Vladimír Kosina, Zdeněk Trnka, Milan Rost, Jiří Svoboda, Mikoláš Hrubeš a později Jan Stejskal. V letech 1966-1970 nastoupili do oddělení motorů Pavel Douda, Daniel Hanus, Otakar Pilc, Branko Remek, Josef Wudy, Michal Takats a Pavel Baumruk. Kožoušek tak posiloval kádr katedry s ohledem na emigraci v letech 1968-1969 a se zřetelem na nové laboratoře. Součástí nové budovy ČVUT v Praze 6 byly “Lehké laboratoře”. Z hygienických důvodů v nich nemohly být některé laboratoře Strojní fakulty. Pro laboratoře turbín, kotlů, vodních strojů, transportních zařízení, zemědělských strojů, spalovacích motorů a automobilů byly postaveny “Těžké laboratoře” v Podbabě se sedmi halami. Do první haly, laboratoře motorových vozidel, byly přemístěny ze Strojní laboratoře 2 elektrické dynamometry a další dodaly podniky MEZ a VÚES. V podsklepené části byl umístěn vozový válcový dynamometr podle projektu docenta Kosteleckého.

Soustrojí bylo vyváženo pro rychlost 240 km/h a výkon na kolech hnací nápravy byl až 100 kW.

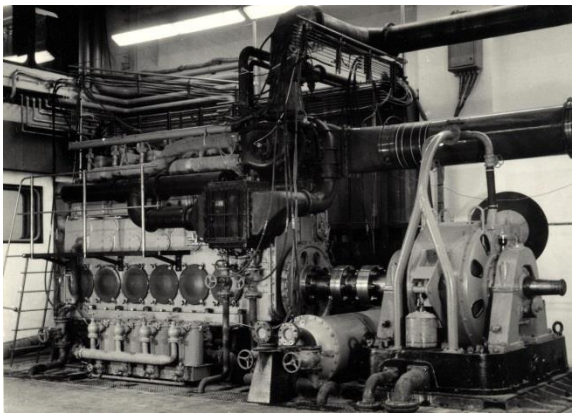

Obr. 10 Velký motor ČKD 6F275PV

Obr. 11 Hala vozidel a zkušební Nysa

Tento dynamometr byl roku 2015 nahrazen dynamometrem se stavitelným rozvorem pro vozy s pohonem 4x4. Unikátní českou konstrukci si německá firma Maha vyžádala výměnou pro své muzeum, protože to byl nejstarší dynamometr v provozu. V hale je i zkušební stav modelů železničních podvozků (1:3,5). Řeší se styk dvojkolí s kolejnicí a síly i pohyby podvozku při jízdě.

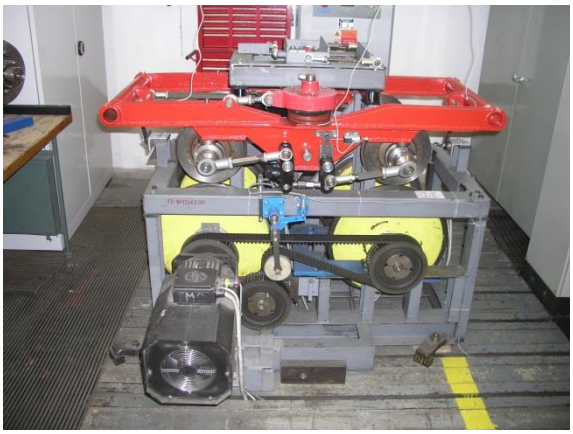

Obr . 12 Kladkový stav

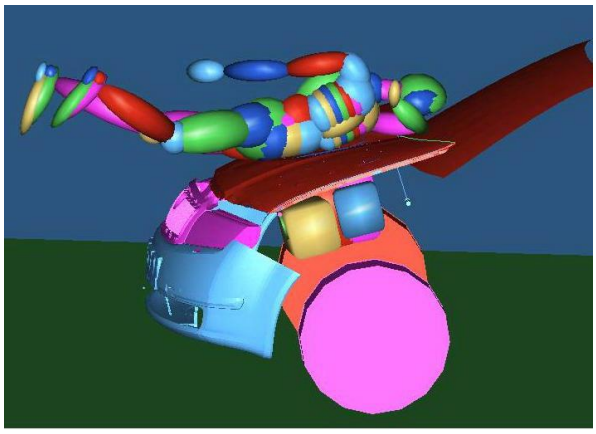

Obr. 13 Impact test - simulace

Sousední laboratoř, hala spalovacích motorů, je rozdělená na zkušební boxy. Do nejmenšího byl instalován elektrický dynamometr MEZ a zkušební jednoválec Tatra. V sousedním boxu byly vířivé dynamometry VÚES a v dalším dynamometry MEZ. V největším boxu byl k šestiválci ČKD, instalovanému v ještě nedokončené stavbě

koncem roku 1967, použit hydraulický dynamometr z východoněmeckého podniku VEB Schönefeld. Mezi zajímavosti tehdejší laboratoře patřila zkušební zařízení pro sledování paprsků paliva vstřikovaného do horkého prostředí dusíku.

1969 – NORMALIZACE

Po okupaci v srpnu 1968 byla katedra rozšířena o nové oddělení spalovacích turbín, resp. letadel. Ze Státního výzkumného ústavu pro stavbu strojů v Běchovicích přišel v roce 1969 profesor Jan Jerie. Vytvořením samostatné Katedry letadel v roce 1976 odešel Jerie a s ním asistenti Daniel Hanus a Václav Rychetník. V té době skončil profesor Kožoušek jako vedoucí katedry, jejímž vedením byl pověřen Jaroslav Šíba. Profesor Šíba byl povolán z lokomotivky plzeňské Škodovky, aby zavedl oddělení kolejových vozidel. Jeho asistenty byli Tomáš Heptner a Josef Kolář. Po odchodu profesora Šíby do důchodu v roce 1986 převzal vedení oddělení docent Kolář a vedení katedry profesor Milan Apetaur. V období let 1970 až 1990 probíhal v laboratořích vývoj spojky, samočinné převodovky, brzd a řízení pro Automobilové závody Mladá Boleslav (Škoda) a Ústav pro výzkum motorových vozidel a intenzivní výzkum a vývoj motorů značek Avia, LIAZ, Škoda, Tatra, Zetor a ČKD.

1989 – NOVÁ ÉRA

Čeští inženýři a konstruktéři byli vždy v kontaktu s vývojem oboru a po roce 1989 se jim znovu otevřel svět a začala spolupráce s výzkumnými centry. Milan Apetaur je jediným Čechem, kterého mezinárodní společnost automobilových inženýrů FISITA roku 2010 ocenila za práci v automobilkách Tatra a ROSS a pro ČVUT, prestižní „Gold Medal of Honour“. V roce 2015 dostal cenu FISITA Service Award i autor tohoto článku (obr. 3). Vedoucí oddělení spalovacích motorů docent Jan Macek přišel z Výzkumného ústavu ČKD, získal docenturu a roku 1991 vystřídal profesora Apetaura ve vedení ústavu a tím také začala nová éra, spojená s nástupem výpočetní techniky. Výuka byla historicky postavena na přednáškách profesorů Hausmanna, Salaby a Zengera. Z nich vzešla encyklopedická skripta „Spalovací motory“ profesora Košťála a Ústrojí automobilů“ a „Stavba automobilů“ profesora Petránka. Následovala exaktní skripta „Převody“ docenta Šalamouna a kniha profesora Kožouška „Teorie spalovacích motorů“ z roku 1968, která se stala

celostátní učebnicí. V době, kdy pro akademické pracovníky bylo vrcholem výpočetní techniky logaritmické pravítko a mechanická „kalkulačka“, si asistenti Remek a Takáts soukromě pořídili osmibitové počítače Sinclair ZX Spectrum, které byly vestavěny do klávesnice. Monitorem byl černobílý televizor a pamětí kazetový magnetofon. Stolní počítače byly jen z regulovaného dovozu za devizy. Prvním domácím dodavatelem bylo Jednotné zemědělské družstvo Slušovice s podnikavým předsedou (Ing. František Čuba), které je montovalo z komponent dovážených za devizy z exportu zemědělské výroby. Sálové počítače ČVUT z konce let šedesátých umožnily aplikaci programů pro simulaci pracovního oběhu motoru. Po doplnění o výpočty dynamiky vznikl tehdy ojedinělý systém VÚ ČKD pro konstrukci motorů a pro vyhodnocování zkoušek. Programy Jana Macka byly harmonizované s dalšími programy vyvíjenými v ÚVMV a na bratislavské technice. Po roce 1993 nabrala na intenzitě spolupráce se společností Škoda-Auto a.s. v rámci koncernu Volkswagen v oblasti motorů, převodovek a podvozků. Ústav pokračoval v činnosti a rozšiřování výzkumných aktivit s automobilovým průmyslem i s dodavateli příslušenství, PBS Turbo, ČZ a.s., Motorpal a.s. a dalšími. Pod vedením profesora Macka se katedra transformovala roku 1998 na velký Ústav vozidel a letadlové techniky. V roce 2003 se osamostatnil Ústav letadlové techniky. K zásadnímu posunu v zabezpečení vědy a výzkumu došlo v roce 2012, otevřením Centra vozidel udržitelné mobility ve VTP (Vědecko-technický park) Roztoky, které vzniklo na základě evropské i národní investiční dotace.

Obr. 14 Jan Macek

Obr. 15 Kolaudace VTP

Obr. 16 Zkušebna exhalací

Dnes centrum spolupracuje s mnoha partnery z výzkumu a průmyslu a patří mezi pracoviště vysoké světové úrovně. Ve spolupráci s TÜV-SÜD Czech byla v roce

2019 k emisní laboratoři přistavěna klimatizovaná přípravná hala, nutná pro splnění podmínek předpisů Evropské unie pro homologační zkušebny. Zkušebna umožňuje testovat a schvalovat automobily i motocykly a je připravena na nástup hybridních a elektrických vozidel. Výzkumné a vývojové práce jsou zaměřeny na ústrojí pohonu, tj. spalovací motory na kapalná i plynná paliva, elektrické a hybridní pohony. Dále probíhá výzkum a vývoj převodovek, odpružení, aerodynamiky karosérie a pasivní bezpečnosti. Výzkum motorů je zaměřen na termodynamiku, vnitřní aerodynamiku, přeplňování a snižování spotřeby paliv, včetně výzkumu spalování extrémně chudých směsí s příměsí vodíku. Centrum věnuje pozornost snižování emisí škodlivin a inteligentním systémům jejich řízení. K tomu slouží stanoviště pro zkoušení motorů, stanoviště pro mechanické a elektrické agregáty a specializované pracoviště pro numerické simulace s výkonnými servery a databázovým vybavením pro simulace účinnosti řízení a měření emisí. Kromě přístrojů pro laboratorní testování emisí je zkušebna vybavena vozidlem pro měření emisí CO_2 a NO_x v reálném provozu (RDE test). CVUM disponuje patentovaným přístrojem pro analýzu dosud nesledovaných škodlivin ve výfukových plynech naftových motorů při jízdě.

2021 - EPILOG

Ze série společných projektů Ústavu automobilů, spalovacích motorů a kolejových vozidel (U12120), Centra vozidel udržitelné mobility (U12201) a výzkumných institucí vzniklo Národní centrum kompetence Josefa Božka. Jeho zkušenosti se staly základem spolupráce s americkou softwarovou firmou Gamma Technologies Inc. absolventa ČVUT, Thomase Morela. Budoucnost oboru je v rukou mladé generace a v rozvoji výzkumných a vývojových center, podílejících se na teoretickém i praktickém vzdělávání studentů na úrovni bakalářské, magisterské a doktorské. Z tabulky je zřejmé, jak se za dobu existence oboru strojnictví změnily osnovy pro poslední roky výuky studentů v zaměření vozidla. V roce 1864 se jednalo pouze o parní stroje a železniční dopravu a studium bylo jen čtyřleté. O sto let později již byl rozvinut obor spalovacích motorů a automobilů, ale stále se jednalo o strojařinu. Dnes je dominantní nástup elektroniky, mechatroniky a informatiky.
Poznámka: Na ČVUT byl Výkaz o studiu, Index zrušen v roce 2015.

Tabulka: Historické porovnání studijních programů

	První rok zavedení indexu	Školní rok	Akademický rok
	1865/1866 (1867)	1965/1966/1967	2020/2021/2022
ZS	Hydraulika	Části strojů	Metoda konečných prvků
	Encyklopedie stavitelství	Elektrotechnika	Dynamická pevnost, životnost
	Encyklopedie inženýrského stavitelství	Transportní zařízení	Mikroelektronika
	Obecná mechan. technologie	Převody mechan. a hydraulické	Převodové ústrojí vozidel I
	Teoretická nauka o strojích	Základy měření, automatizace	Teorie vozidel
	Geodézie nižší	Vědecký komunismus	Mechanika mechanizmů
LS	Stavba strojů	Ekon., organizace a plánování	Převodové ústrojí vozidel II
	Speciální mechanická technologie	Spalovací motory	Experimentální metody
	Analytická mechanika	Pneumatické a hydraul. stroje	Kmitání mechanických soustav
	Stavitelství strojů	Tepelná technika	Elektrická zařízení vozidel
	Stavitelská mechanika	Zkoušení strojů	Spalovací motory II
	Účetnictví	Konstrukční praxe	Hybridní pohony
ZS		Laboratorní zkoušení	Zkoušení vozidel a částí
		Vozidlové spalovací motory	Výpočetní metody dopr. strojů
	čtyřleté studium	Ústrojí automobilů	Provoz a diagnostika vozidel
		Technologie výroby automobilů	Dynamika vozidel
		Elektrotechnika vozidel	Kompozitní materiály
		Převody	Mechanika tekutin
LS		Spalovací motory a paliva	Konstrukce karoserií
		Turbodmychadla a ventilátory	Konstrukce podvozků
	čtyřleté studium	Dynamika a pevnost	Pasivní bezpečnost vozidel
		Stavba motorových vozidel	Rozpočet a ekonomie projektu
		Elektrotechnika	Moderní techn. dokumentace
		Laboratorní zkoušení	Diplomový projekt

POUŽITÉ ZDROJE

[1] REMEK B. Výuka oboru spalovací motory a vozidla na pražské technice, ČVUT Praha 2020, ISBN 978-80-01-06763-5

[2] REMEK B. Obor spalovací motory a vozidla na pražské technice, FS ČVUT Praha 2021 ISBN (rukopis)

PODĚKOVÁNÍ - Práci podpořil děkanát FS a rektorát ČVUT

52. MEZINÁRODNÍ VĚDECKÁ KONFERENCE ČESKÝCH A SLOVENSKÝCH UNIVERZIT A INSTITUCÍ ZAMĚŘENÁ NA VÝZKUMNÉ A VÝUKOVÉ METODY SPOJENÉ SE SPALOVACÍMI MOTORY, ALTERNATIVNÍMI POHONY A DOPRAVOU

22.-23. ZÁŘÍ 2021, PRAHA
ČESKÁ ZEMĚDĚLSKÁ UNIVERZITA V PRAZE, TECHNICKÁ FAKULTA,
KATEDRA VOZIDEL A POZEMNÍ DOPRAVY

LAMINAR FLOW HEAT TRANSFER MODEL FOR 1D AND 3D MODELING

Kamil Šebela[1], Michal Janoušek[2], Josef Štětina[3]

Abstract
Heat transfer model for laminar flow is built in GT-Suite software. Proposed method is based on analytic heat transfer model for universal length channel and average heat transfer coefficient is applied to global model. Laminar flow heat transfer model is used in fluid to fluid heat exchanger numerical model. Heat exchanger is discretized to 1D fluid domain and 3D heat conduction in solid material. Both domains are solved together and are used for first design optimalisation before 3D CDF is used for final version assessment.

1 INTRODUCTION

Combustion engine cooling and general thermal management is crucial task in development of modern vehicles. Proper temperature regulation is important to keep all vehicle components at their operation temperatures and do not exceed these temperatures during vehicle usage. In current vehicles is heat transferred by cooling fluid from heat source to heat exchanger which transfer heat into ambient air. Engine accessories also require cooling and for cooling of engine and gearbox oil and steering oil is used the same coolant as for combustion engine. Heat is transferred from oil to coolant and dissipated to air. For cooling these accessories are usually used compact plate heat exchangers with large surface to volume ratio thus eliminating space inside the engine bay [1]. They have drawback in high pressure loss compared to shell and tube heat exchangers which have lower pressure loss and do not restrict flow in cooling circuit [2].
Shell and tube heat exchanger (HX) is described in next chapters for cooling oil by engine coolant circuit. Main benefit against plate HX is in implementing this HX directly on cooling tube downstream of coolant to air HX without need for additional cooling branch. There will be the lowest coolant temperature in whole cooling circuit thus utilizing the biggest coolant temperature difference to the oil. HX is also located

[1] Kamil Šebela, Brno University of technology, Technicka 2 Brno, 616 69, kamil.sebela@vutbr.cz
[2] Michal Janoušek, Brno University of technology, Technicka 2 Brno, 616 69, michal.janousek@vutbr.cz
[3] Josef Štětina, Brno University of technology, Technicka 2 Brno, 616 69, josef.stetina@vutbr.cz

downstream of cooling fan and s cooled by air flow inside the engine compartment. This factor is included in simulation as well.

2 LAMINAR FLOW HEAT TRANSFER CORRELATION

Heat transfer correlation depend on position from inlet into channel for classic heat transfer correlation for long straight tube. This fact complicates heat transfer modelling, because not only Reynolds and Prandtl number influences heat transfer coefficient (HTC). Laminar flow is common in small tubes where oil is used. In compact HX is desired to have small duct to have large surface area to transfer heat from the wall to cooling fluid. Nusselt number is determined by equation 1 [3]. for long straight pipe where hydrodynamic and thermal boundary layers are developing.

$$Nu = \left\{ {Nu_1}^3 + 0.7^3 + [Nu_2 - 0.7]^3 + {Nu_3}^3 \right\}^{\frac{1}{3}} \quad (1)$$

Nu_1 is asymptotes for the mean Nusselt number in tube with value 3.66 [4]. Nu_2 is obtained from equation 2 [5]. Re, Pr, d and l stand for Reynolds number, Prandtl number, hydraulic diameter, and segment length respectively.

$$Nu_2 = 1.615 \sqrt[3]{Re\ Pr\ DLRatio} \quad (2)$$

Nu_3 is obtained from equation 3 [6].

$$Nu_3 = \left(\frac{2}{1 + 22Pr} \right)^{\frac{1}{6}} (Re\ Pr\ DLRatio)^{\frac{1}{2}} \quad (3)$$

2.1 HTC MODEL IN GT SUITE

Nusselt number correlation is used for computing HTC in GT Suite. Fluid properties are sensed from the pipe and used to compute the mean HTC for straight section of rectangular pipe in HX. At Figure 1. is preview of the model, where HTC is feed back to the pipe.

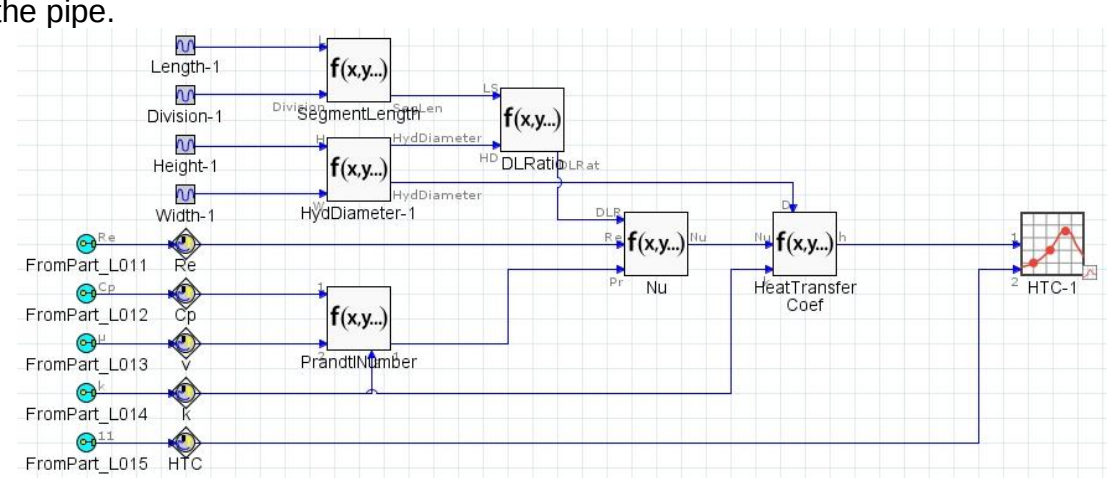

Figure 1. HTC model in GT Suite

Computation is done in multiple steps beginning with computing Prandtl number and hydraulic diameter for rectangle channel. Channels are divided to segments for increase HTC by disturbing flow and developing new thermal and flow boundary layer. Segments length is computed by dividing overall length by number of segments. Geometry parameters are sensed from model properties of HX.

$$DLRatio = \sum_{1 \le i \le 20} \frac{d}{0.05\ i\ l} \tag{4}$$

Hydraulics diameter ratio (DLRatio) is computed by equation 4. There are 20 segments used to approximate equation 4 to reduce the influence of overestimating inlet values. Nusselt number is computed by equation 1. and HTC by equation 5 [7]., where k is thermal conductivity of oil.

$$HTC = \frac{Nu\ k}{d} \tag{5}$$

Sensed properties are Reynolds number (Re), specific heat (Cp), kinematics viscosity (ν) and thermal conductivity (k). Geometry properties are based on CAD data including channel width, height and segment length (l).

3 HEAT EXCHANGER MODEL DESCRIPTION

Shell and tube heat exchanger for cooling oil by engine coolant located upstream of coolant pump is modelled in Creo Parametric at Figure 2. CAD model consist of inner tube for coolant and oil channels from outer side covered by outer shell. Oil flow in counter flow orientation to coolant.

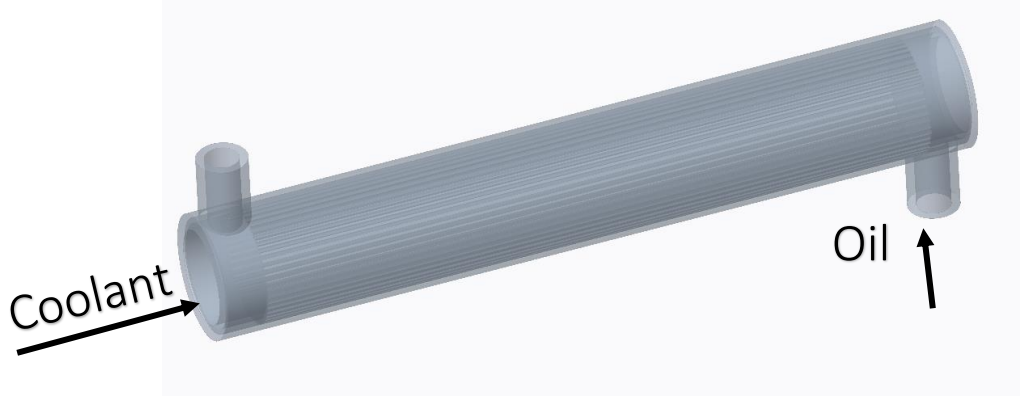

Figure 2. Heat exchanger

3.1 PRE-PROCESSING

CAD model is pre-processed in GEM3D, where internal fluid volumes are extracted. These volumes are discretized into GT components. Coolant volume is transferred to circular pipe with zero wall thickness and connected to shell mesh by convection connection. Housing and ribs are discretized to mesh object consisting of 172 780 elements with minimal size of 1 mm. Oil volume is discretized to inlet and outlet pipes,

flowsplits and cooling pipes with rectangle cross section. Geometry representation is depicted at Figure 3. including two ports for fluids. In pre-processor material characteristics and connections are set. There is also included surface for convection connection to surrounding air cooling.

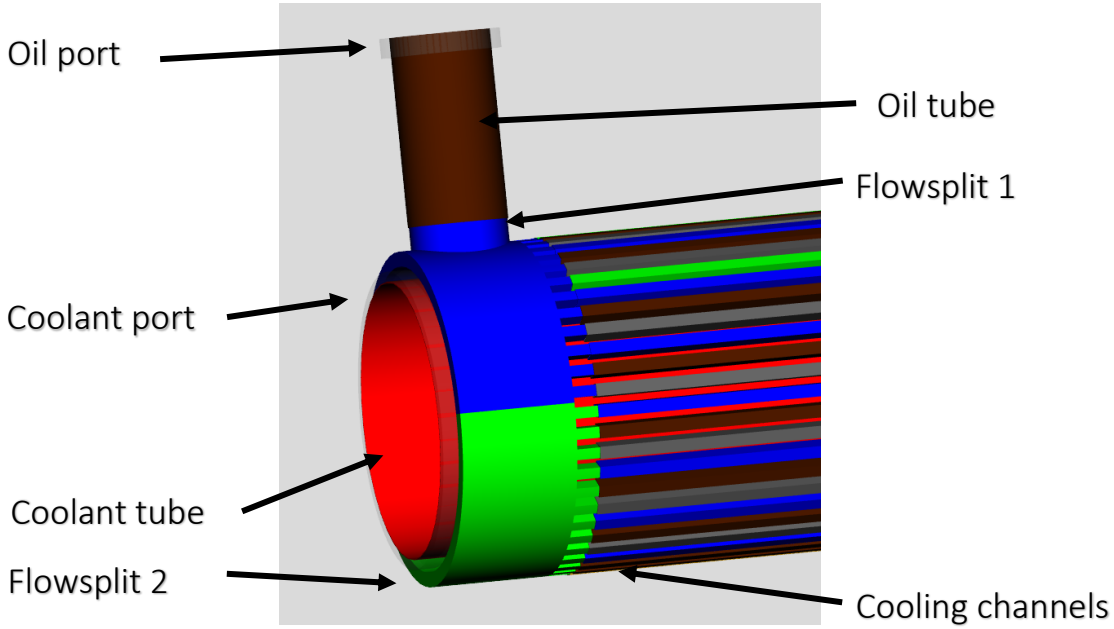

Figure 3. HX discretization

3.2 MODEL SETUP

Model is imported to the GT-ISE where boundary conditions and solver settings are defined. Model is simulated at steady state where after reaching steady state simulation is ended. Implicit solver is used with continuous simulation setup. Simulation runs for 0.8 to 1.2 seconds simulation time with real time 26 to 38 seconds. at office hardware. At Figure 4. is shown inlet section with HTC model. This THC is used in all other cooling tubes.

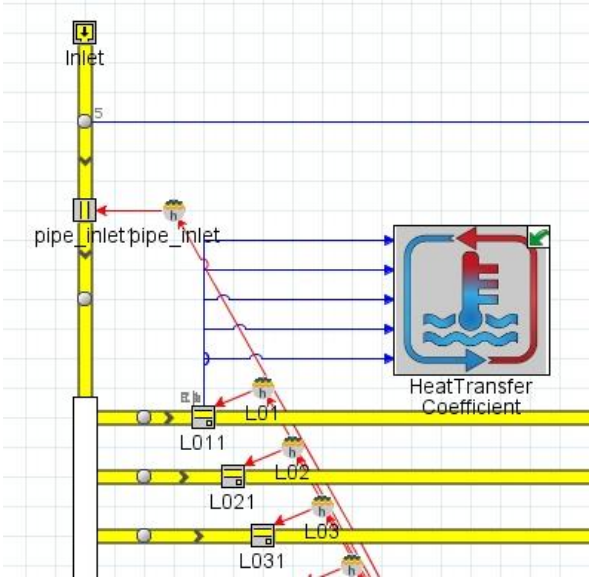

Figure 4. Detail of complete model

All components are connected by convection connection to housing mesh structure. For coolant model are used boundary flow template, round tube and boundary conditions. Coolant flow is turbulent thus default Colburn model for HTC is used. To mesh structure is also connected ambient air by external surface and constant HTC based at external flow around round tube. Constant air temperature is set as boundary condition. At Figure 5. is detail of the connections to the mesh structure. Complete model Figure is in appendix 1.

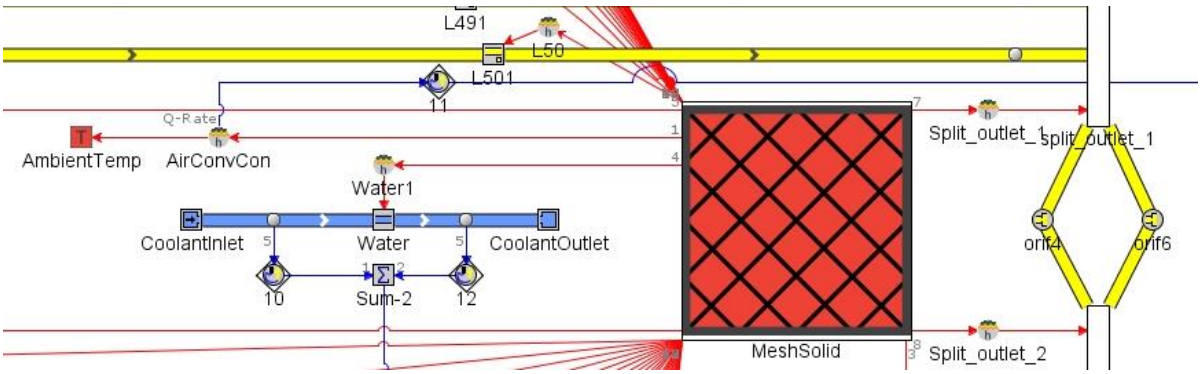

Figure 5. Mesh structure connections

Boundary conditions are set by mass flow of oil and coolant. For both liquids temperature is prescribed and pressure is computed based on boundary condition at outlet side. Geometry parameters are set by geometry, only number of divisions is to be defined by user, but not physically modelled.

4 RESULTS

Model is run at design point and at multiple points for complete characteristic. Main performance indicator for HX is cooling power. Heat is removed by coolant and air. At design point with coolant flow 80 l/min and 110 °C and 15 l/min and 135 °C for oil cooling power is 1 564 W where 1 488 W is cooled by coolant and the rest by air. Pressure drop for oil is 701 mbar and 3.2 mbar for coolant. Complete characteristic is presented at Figure 6.

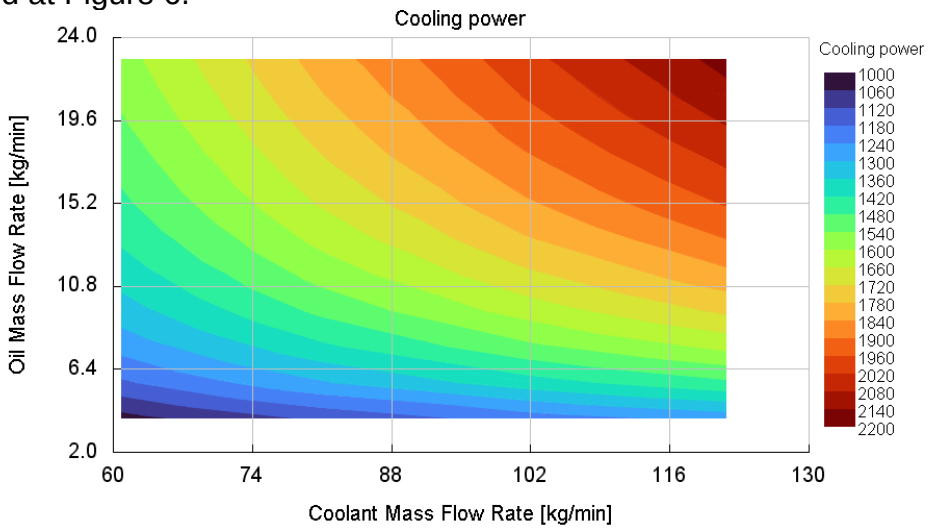

Figure 6. HX characteristic

Temperature distribution is presented at Figure 7. Surface temperature is highest at inlet port and at the opposite side to outlet is lowest temperature at housing. From temperature distribution is clear that oil is distributed evenly and there are no hot or cold spots except corners opposite to oil inlet or outlet tubes.

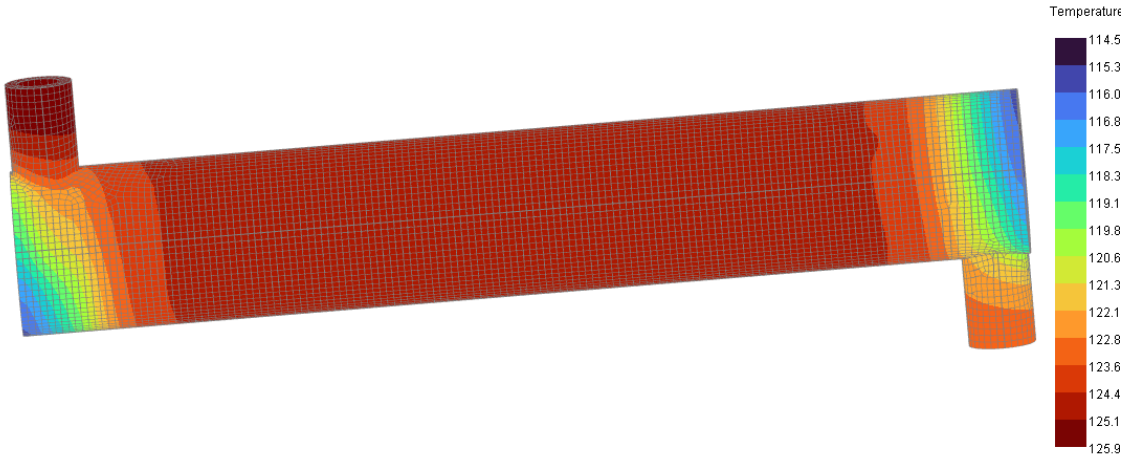

Figure 7. Temperature distribution at structure

From simulated characteristic simplified model is created based on the shell tube HX template depicted at Figure 8. Which specifies geometry data, fluid data and material characteristics. Cooling performance is based on detailed model where heat dissipated by coolant and air is combined. The simplified model runs 0.3 s in real time, which is 100 times faster than detailed model.

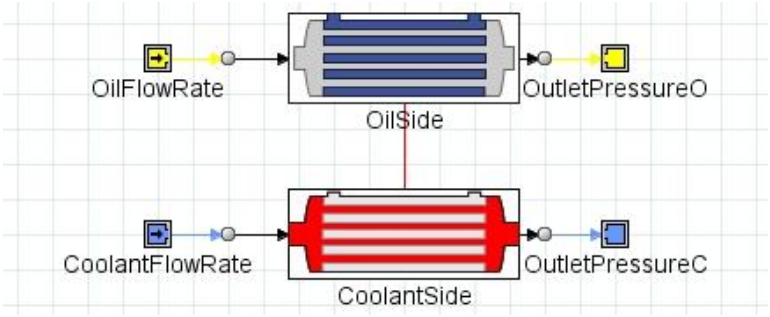

Figure 8 Shell tube HX template

5 CONCLUSION

Laminar HTC model is presented in GT Suite environment. This model is used to simulate oil cooling in long straight ducts of heat exchanger. Detailed simulation consist of laminar HTC model, coolant model, thermal conduction and air external convection. HTC is based at channel geometry and flow conditions from 1D flow model averaged along duct length. Mass flow is modelled equal for each cooling ducts. Detailed simulation can be further expanded to flow distribution at cooling channels, where inlet and outlet sections may be optimized to have better flow distribution among channels. Detail model can be used in cooling system simulation to model system performance with full details including temperature distribution and air-cooling dependent to speed and temperature. Detail simulation is simplified to performance based empirical model with computation time reduced to 0.3 seconds from 30 seconds for fast running optimalization simulations.

REFERENCES

[1] Bartlett, D. A. (1996). Fundamentals of heat exchangers. Industrial Physicist, 2(4), 18–21. https://doi.org/10.1016/b978-0-12-821923-2.00001-4
[2] ANNARATONE, Donatello. Handbook for heat exchangers and tube banks design. Berlin: Springer, c2010. ISBN 978-3-642-13308-4.
[3] Martin H (1990) Lecture on heat transfer II. Universitaet Karlsruhe (TH), Karlsruhe, Germany
[4] Sha RK, London AL (1978) Laminar flow forced convection in ducts. Academic Press, New York/San Francisco, CA/London
[5] Gnielinski V (1989) Zur Wärmeübertragung bei laminarer Rohrströmung und konstanter Wandtemperatur. Chem-Ing-Techn 61:160–161
[6] Stephan K (1959) Wärmeübergang bei turbulenter und bei laminarer Strömung in Rohren und ebenen Spalten. Chem-Ing-Techn 31:773–778
[7] VDI Heat Atlas: Gesellschaft Verfahrenstechnik und Chemieingenieurwesen (GVC). 2. Berlin: Springer, 2010. ISBN 978-3-540-77876-9.

ACKNOWLEDGEMENT

The authors gratefully acknowledge funding from the Specific research on BUT FSI-S-20-6267.

SYMBOLS AND ACRONYMS

d	Hydraulic diameter	[m]
DLRatio	Diameter to length ratio	[1]
HTC	Heat transfer coefficient	[W/(m^{2}K)]
k	Thermal conductivity	[W/(mK)]
l	Segment length	[m]
Nu	Nusselt number	[1]
Pr	Prandtl number	[1]
Re	Reynolds number	[1]

Acronyms

DLRatio	Diameter to length ratio
CAD	Computer aided design
GT	Gamma Technologies LLC.
HTC	Heat transfer coefficient
HX	Heat exchanger

APPENDIX

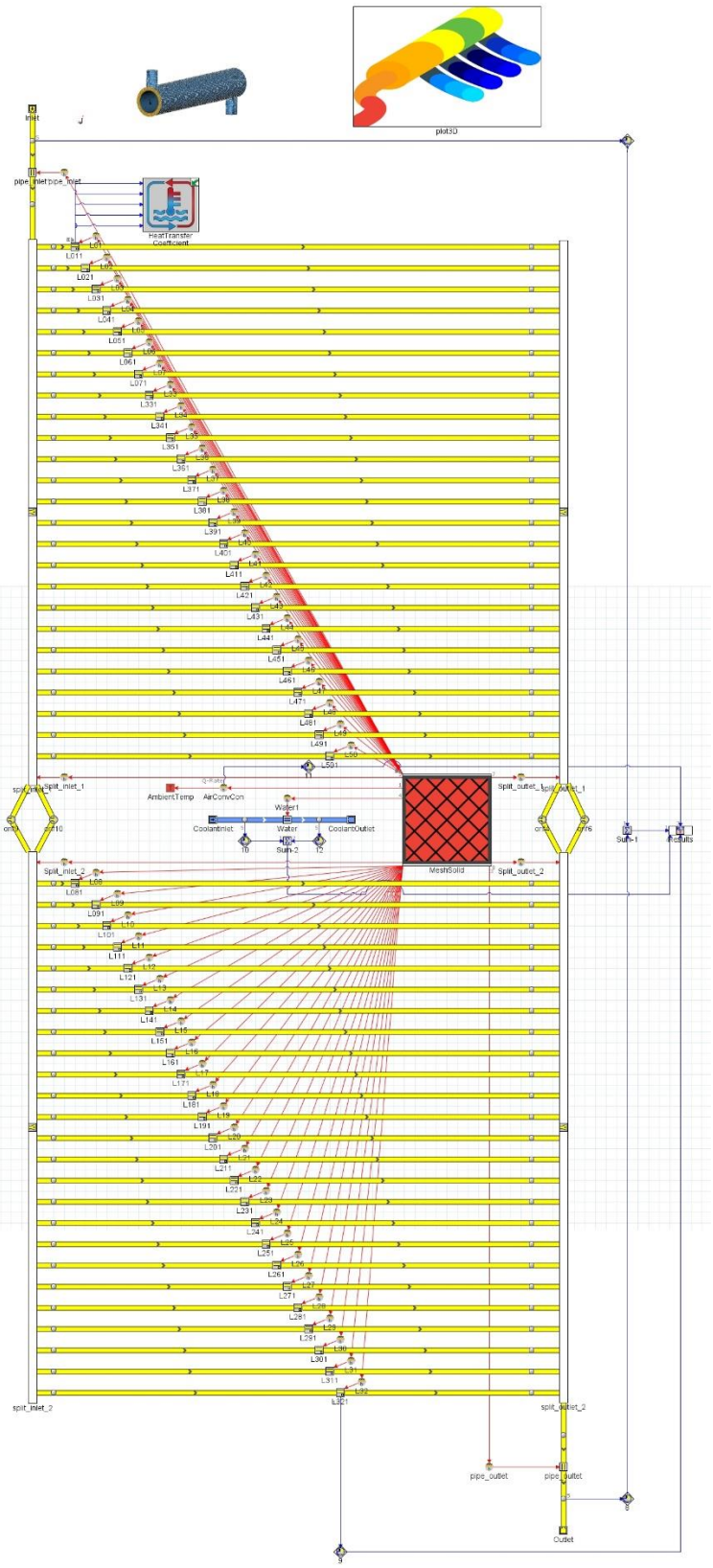

Appendix 1. Detail model in GT-ISE

52. MEZINÁRODNÍ VĚDECKÁ KONFERENCE ČESKÝCH A SLOVENSKÝCH UNIVERZIT A INSTITUCÍ ZAMĚŘENÁ NA VÝZKUMNÉ A VÝUKOVÉ METODY SPOJENÉ SE SPALOVACÍMI MOTORY, ALTERNATIVNÍMI POHONY A DOPRAVOU

22.-23. ZÁŘÍ 2021, PRAHA
ČESKÁ ZEMĚDĚLSKÁ UNIVERZITA V PRAZE, TECHNICKÁ FAKULTA,
KATEDRA VOZIDEL A POZEMNÍ DOPRAVY

VYUŽITÍ MATLAB LIVESCRIPT PRO DISTANČNÍ VÝUKU TEPELNÝCH CYKLŮ

Josef Štětina[1]

Abstrakt
Článek se snaží přiblížit přístup k výuce dvou klíčových předmětů, Termomechaniky pro bakalářské studenty a Teorie spalovacích motorů pro magisterské studenty. Výukou těchto předmětů prochází na Fakultě strojního inženýrství VUT v Brně všichni studenti magisterského programu Automobilní a dopravní inženýrství. Již před příchodem distanční výuky oba předměty měly elearningovou podporu na webu http://termomechanika.online . Distanční výuka vedla k myšlence více využít k samostudiu studentů schopnosti tzv. Live Scriptů v Matlabu, které umožňují kombinovat formátovaná text, rovnice v LaTeXu, obrázky a živé Matlab Scripty (tedy prakticky libovolně složité výpočty). Pro studenty takto vlastně vznikly živá skripta, které počítají a kreslí grafy. Druhá oblast, která se ukázala vhodná pro využití Live Scriptů je generování zkouškových příkladů. Každý student dostává individuální zadání minimálně co do číselných hodnot a podrobný výpočet příkladu v Live Scriptu umožňuje snadné opravení i při vyšších počtech studentů.

1. ÚVOD

Výuka školního roku 2020/21 byla jistě pro všechny učitele na technických vysokých školách výzvou s možností vyzkoušet nové přístupy a nástroje, a to jak pro vlastní distanční výuku tak i pro zkoušení. V tomto článku je snaha popsat, jak jsme k tomu přistupovali na Ústavu automobilního a dopravního inženýrství FSI VUT v Brně. Cílem je přiblížit přístupy, které mají obecnou platnost a je možno je využít i při klasické prezenční výuce. Jako příklad výuky byly zvoleny dva předměty a to předmět ***Termomechanika*** [1, 2] (bakalářský předmět, který měla zapsaná většina studentů fakulty cca 550) a předmět ***Teorie spalovacích motorů*** (magisterský předmět, který mělo zapsaný 97 studentů programu). Tento příklad je zajímavý tím, že na sebe předměty navazují s ročním rozestupem (předmět Teorie spalovacích motorů je obsahově aplikovaná termomechanika). Samozřejmě předměty mají standardní podporu v elernigovém systému university (Moodle), ale v tomto článku se podíváme na jiné přístupy než nabízí standardní elearnigový systém. Moodle má rozsáhlé

[1] Prof. Ing. Josef Štětina, Ph.D., Vysoké Učení Technické v Brně, Fakulta strojního inženýrství, Technická 2, CZ616 69 Brno, josef.stetina@vutbr.cz

schopnosti, ale údržba kurzu v něm je těžkopádnější a hlavně se zde špatně nastavuje přístup pro zájemce mimo studenty vlastní univerzity. Stále více zájemců nejčastěji absolventů má zájem o výukové materiály, takže je to i snaha jim vyhovět.

Obrázek 1: *Příklad webu http://termomechanika.online/*

2. CLOUDOVÉ SLUŽBY

Cloudový službami myslíme dva relativně porovnatelné produkty Office365 firmy Microsoft a Google Apps for Work. Oba balíky jsou ve svých funkcích velmi podobné a dají se využít prakticky stejně. Rozhodující je tedy zda má daný produkt univerzita integrovaný pro své zaměstnance a hlavně studenty ve svém informačním systému (jde zejména o přihlašování a nastavování práv). VUT má do informačního systému integrovány obě řešení rovnocenně. V tabulce 1 je jednoduché porovnání základních produktů, u kterých se předpokládá využití ve výuce. Z tabulky je patrné, že obě firmy se snaží pokrýt všechny činnosti. Výhodou produktů Microsoft je existence tzv. desktopových verzí, které lze nainstalovat na počítač, a které většinou mají vyšší funkčnost.

Služba	Microsoft	Google
Webovské stránky, intranetové řešení	SharePoint	Weby
Cloudové uložiště souborů	OneDrive	Google Disk
Textový editor	Word	Dokumenty
Tabulkový procesor	Excel	Tabulky
Prezentace	PowerPoint	Prezentace
Tabule	WhiteBoard	Jamboard
Komunikace	Teams	Meet, Chat, Classroom
Video streamování	Stream	Youtube
Zobrazení dat	PowerBI	Data Studio

Tabulka 1: *Porovnání Office 365 a Google Apps for Work*

Produkty firmy Microsoft mají výrazně více funkcí a celkově jsou více provázané, komplexnější a také více rozšířené. Produkty firmy Google obsahují jen základní funkce, ale ty dělají dobře a jsou více orientovány na spolupráci více uživatelů nad jedním úkolem. Jednoduchost produktů Google právě vedla k přechodu tvorby podkladů pro výuku v tomto cloudovém prostředí. Hlavní výhodou je, že studenti vidí vždy nejčerstvější verzi prezentací a více přednášejících stejného předmětu může snadněji připravovat prezentace a další podklady.

2.1 Webovské stránky

Weby od Googlu umožní vytvořit klasický statický web bez znalosti programování. V zásadě je tvorba webu stejně nenáročná jako tvorba prezentace např. PowerPointu. Obdobně snadná je tvorba webu v Microsoft produktu SharePoint. Příkladem možnosti výukového webu je http://termomechanika.online/ na obrázku 1, který vznikl jako alternativa k elearnigovému univerzitnímu systému. Výhodou je, že se relativně snadno dá nastavit, které materiály jsou dostupné všem a které vidí jen studenti a zaměstnanci univerzity. V současné době například vlastní výukové materiály v pdf formátu jsou veřejné a zdrojové prezentace, Matlab Live Scripty a přístup k elektronickým zdrojům v univerzitní knihovně [3, 4] je po přihlášení tedy jen pro studenty a zaměstnance univerzity.

2.2 Prezentace

Už několik roků pro přednášky místo PowerPointu využíváme Google Prezentace. Důvod je, že při více přednášejících mohou být prováděny úpravy všemi a zároveň studenti mají v době výuky vždy poslední verzi prezentace, která např. byla upravena pár minut před přednáškou. Další možností je přímo psaní dotazů a komentářů studenty k prezentaci, toto zatím využíváno moc nebylo, protože chat přímo v Youtube nebo Teams přenosu to nahrazuje lépe. Pro někoho mohou být možnosti Google Prezentací málo pokročilé, podle mne je to spáše výhoda. Vznikají tak jednoduché prezentace bez vizuálních efektů, které se dají i dobře vytisknout a dobře se z nich studuje a studenti mají prostor doplnění vlastními poznámkami. Jednou z limitujících vlastností Google Prezentací je chybějící editor rovnic, ale lze využít doplněk třetí strany zobrazující LaTeX rovnice. V zásadě lze tedy začleňovat rovnice vytvořené v Matlab LiveScriptu viz následující kapitola. Další možností je zakoupení editoru rovnic MathType, který má pokročilé vlastnosti a funguje i v produktech Microsoft.

2.2 Záznamy přednášek

Pro uložení záznamu přednášek jsme zvolili Youtube. Toto řešení je pro studenty uživatelsky přívětivé a lze i rozumně využít, jak pro veřejná videa tak i privátní. Na této adrese https://www.youtube.com/channel/UCT1gjfN5lg8ofb5la4_hm-A jsou záznamy přenášek za uplynulý školní rok. Na obrázku 2 vidíme jednu z předností Youtube a to pokročilé statistiky. Graf na obrázku 2 zachycuje posledních 365 dní. Jasně jsou tam vidět nárůsty sledovanosti ve zkouškovém období a vrcholy odpovídají dvěma zkouškovým termínům. Sledovanost v zimním semestru je větší, protože zde uváděné předměty Termomechanika a Teorie spalovacích motorů jsou vyučovány v zimním semestru. Jedním se zjištění je, že sledovanost záznamu přenášek klesá po nějakých 30 minutách. Tedy záznam tříhodinové přednášky znamená, že dvě třetiny přednášky

shlédne výrazně méně uživatelů. Proto byly přednášky sestříhány do kratších podle jednotlivých témat a v dalším kroku pro nastávající školní rok budou více se synchronizovány s ukázkovými příklady a podklady v prostředí Matlab. Pro střih videa a záznamy obrazovky prezentujícího je využíván software Camtasia firmy, který je přímo určen na tvorbu výukových videí na rozdíl od běžných video editorů.

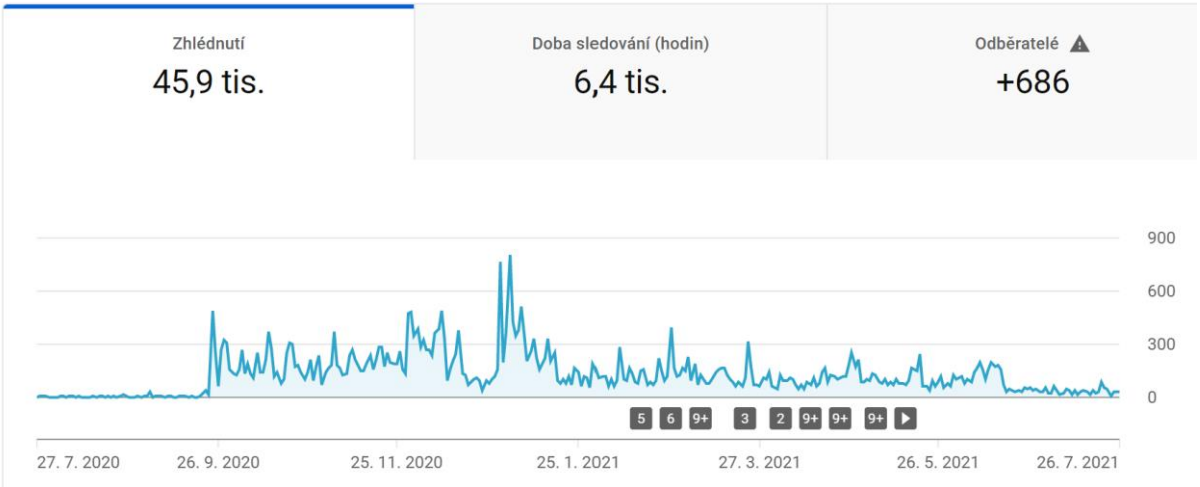

Obrázek 2: *Analytická data Youtube kanálu Josef Štětina za posledních 365 dní*

3. DOKUMENTY V MATLAB LIVE SCRIPT

Inženýři dlouhou dobu řeší problém čím nahradit papír, tužku a kalkulačku. Určitě nejrozšířenějším nástrojem je tabulkový procesor ***Excel***. Jeho hlavní výhodou je dostupnost a obecná znalost práce s ním. Na vysokých školách i ve firmách jsou využívány komerční programy jako jsou Matlab, Maple, Mathematica, MathCad, EES nebo volně šiřitelné například Jupyter Notebook, GNU Octave a další. Tento příspěvek si neklade za cíl je porovnávat nebo doporučovat. Kritériem pro použití je zejména dostupnost licence ve škole nebo firmě a také být v uvedeném nástroji efektivní, například vlastní databanka výpočtu a postupů z minulých let. Jinou otázkou je pokud mám za cíl připravit podklady pro studenty, kteří je nebudou používat jako black box, ale budou schopni jim porozumět, modifikovat a rozvíjet. Na FSI VUT v Brně se studenti v bakalářském studiu setkávají s Matlabem, Maplem a MathCadem, takže při rozhodování jak připravovat podklady jsem vybíral pouze mezi Matlabem a MathCadem.
Program MathCad v současné době rozvíjí firma PTC, která je známa svým CAD programem CREO. V současné době je jedinou podporovanou verzi PTC MathCad Primo 7.0. U uživatelů je populární zejména tím, že vlastně spojuje textový editor včetně zápisu rovnic blízký matematickému zápisu a velmi dobře pracuje s fyzikálními jednotkami. Samozřejmostí jsou grafy a tabulky. Existuje i verze Express, která je zdarma. Jeho nevýhodou je omezená možnosti programování, tedy cyklů a iteračních výpočtů. Čitelnost takto vzniklých dokumentů je výborná a přehledná, ale pro méně zkušené uživatele nemusí být úprava dokumentů přímočará. Proto jsme se rozhodli v maximální míře se orientovat na prostředí Matlab ve variantě souborů Live Script.

Výhodou je kombinace relativně jednoduchého textového editoru umožňující kombinovat formátovaný text obrázky a rovnice (vlastní editor nebo LaTeX) s programem v jazyce Matlab, kde výsledky a grafy jsou začleněny do textu. Výhoda je, že student základní syntaxi Matlabu znají a vlastní výpočet je klasický řádkový zápis, který snadno modifikují. Přehlednost zápisu záleží právě na doplnění doplňujícího textu a rovnic mimo program. Nevýhodou je, nízká podpora práce s fyzikálními jednotkami. Na obrázku 3 můžete porovnat zápis výpočtu příkonu kompresoru v MathCadu a Live Scriptu Matlabu. U Matlabu jsou pomocí vloženého souboru Include_Units nataženy přepočty jednotek a základní vztahy (komentáře) lze doplnit matematickým zápisem rovnice pomocí vestavěného editoru rovnic nebo LaTeXu.

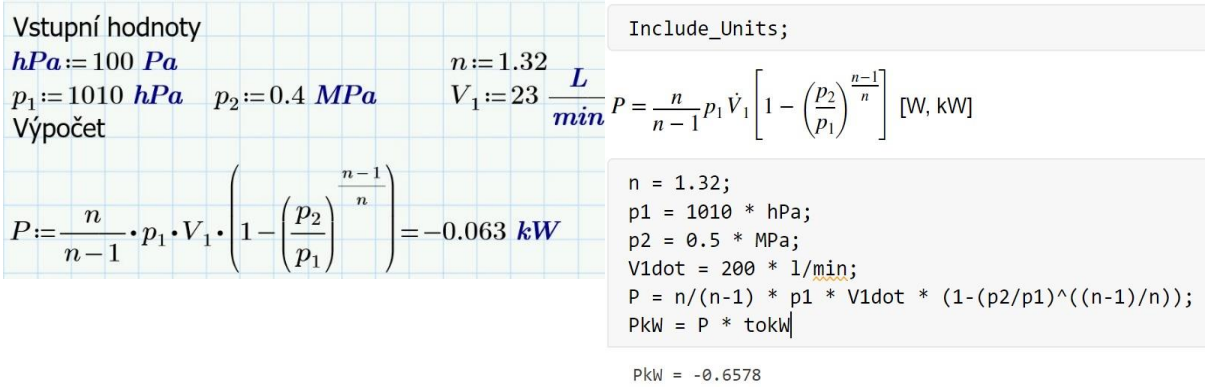

Obrázek 3: *Porovnání MathCad a Matlab*

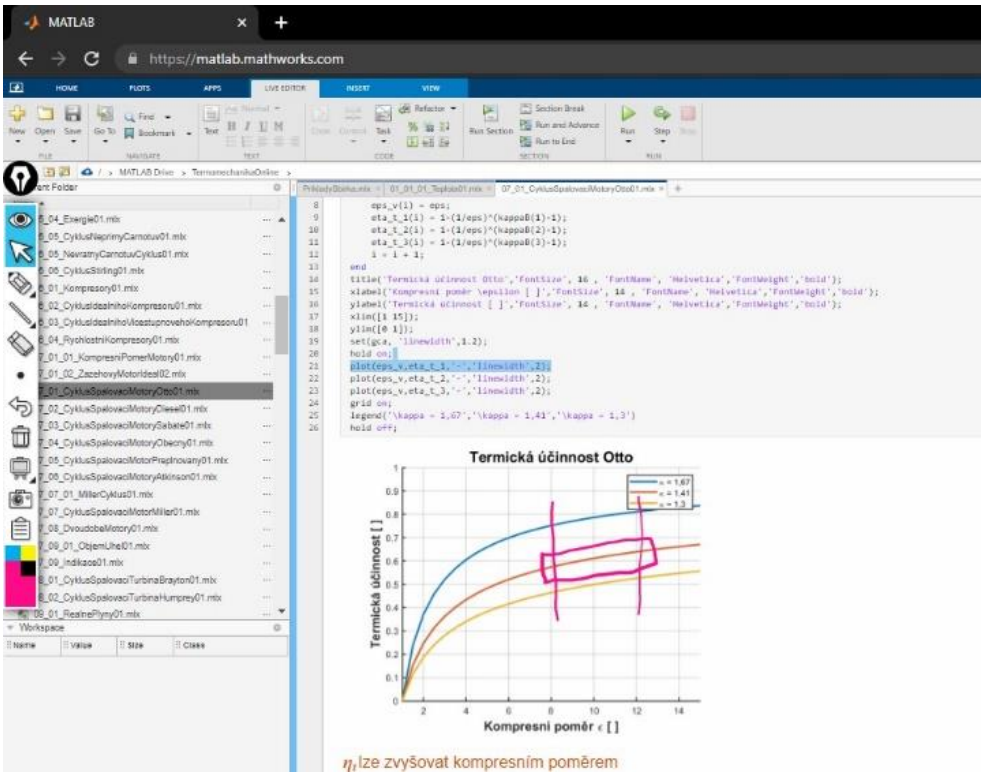

Obrázek 4: *Online Matlab a příklad scriptu na výpočet termické účinnosti Ottova cyklu*

Snaha nebylo v Matlabu vytvořit knihovnu (toolbox) na termomechanické výpočty, protože pak by studenti spouštěli výpočty aniž, by viděli podstatu výpočtu. Takže příklady a výpočty obsahují celý postup a jsou doplněny rovnicemi s matematickým zápisem rovnic v LaTeXu. Všechny soubory se odvolávají pouze na dva externí soubory a to na Include_Unit.m. který obsahuje definice jednotek a konstant a soubor xsteam.m, který obsahuje interpolační funkce pro vodu a vodní páru (IAPWS IF-97).
Live Scripty obsahují texty a obrázky stejné jako jsou v přednáškových prezentacích, dále rovnice v LaTeXu. Grafy a tabulky jsou tzv. živé, tedy jsou vykresleny z dat vypočtenými Matlabovským skriptem. Na obrázku 4 vidíme Matlab spuštěný v online režimu z adresy https://matlab.mathworks.com/, studenti tedy nemusí mít nic instalováno. Pro soubory je využit tzv. MATLAB Drive, kde každý licencovaný uživatel má 5 GB sdíleného prostoru a popisované skripty si mohou snadno do tohoto prostoru nakopírovat z dostupného odkazu. Je nutné, aby měli svoji kopii, protože se předpokládá, že soubory budou upravovat, ale tako mají možnost se vždy vrátit k původní verzi. Na obrázku vidíte typický graf účinnosti Ottova cyklu v závislosti na kompresním poměru, pro rozdílnou Poissonovu konstantu. Zároveň tento obrázek ukazuje využití dalšího programu Epic Pen, který na dotykové obrazovce umožňuje kreslit a tím lze doplnit výklad (natočená videa) o své kresby a poznámky (bohužel standardní nástroje Windows pro dotykové obrazovky nejsou příliš komfortní, proto řešení dalším programem). Zobrazení tabulek v Live Scriptech je možné, ale dosažení pěkných a přehledných tabulek je docela pracné, tady lze předpokládat vývoj v dalších verzích. Dobře se dá také využít vestavěný editor rovnic v Matlabu pro generování LaTeX kódu, který využijete jak v Matlabu, tak i prezentacích tak i např. v textu.
Velkou výhodou, která podporuje využívání Matlabu ve výuce je, že univerzita má licenci Campus Wide, která ho umožňuje využívat jak všem studentům i zaměstnancům.

4. ZKOUŠENÍ

Online nástroje pro zkoušení např. v elearningu vedou k zefektivnění zkoušení, ale špatně se podle nich rozlišují studenti, kteří umějí a ti co rozumějí problematice. Z toho důvodu kromě testů, které spíš slouží jako postupové kritérium než jako určující pro známku, stále využíváme zkoušení pomocí řešení relativně složitého komplexního příkladu a ústní zkoušky. Na obrázku 5, na kterém vidíte hodnocení studentů, dokladuje obtížnost předmětu Termomechanika. Z grafu je patrné, že zkouška byla nastavena příliš přísně, protože je zde výrazná dominance známky D, přičemž asi vhodnější by bylo větší rozprostření mezi C a D. Obrázek 5 je zároveň ukázka možností analytického nástroje Google Data Studio, který umožňuje takto snadno zobrazovat živá data z tabulek různého typu.
Live Scripty Matlabu jsou využity k tomu, že každý student u zkoušky a zápočtu obdrží individuální zadání příkladu, které je generováno z databáze cca 200 příkladů [2], kdy každý příklad má ještě individualizované číselné hodnoty. Všechna zadání příkladů jsou vygenerována programem v Matlabu a student obdrží zadání a zkoušející obdrží Live Script se správným řešením příkladu. Opravování je relativně snadné i při tomto větším počtu individuálních zadání. Problémem je a asi vždy rozdílná obtížnost

příkladů a to zejména z pohledu studentů, ale to lze opět řešit analýzou výsledků zkoušek.

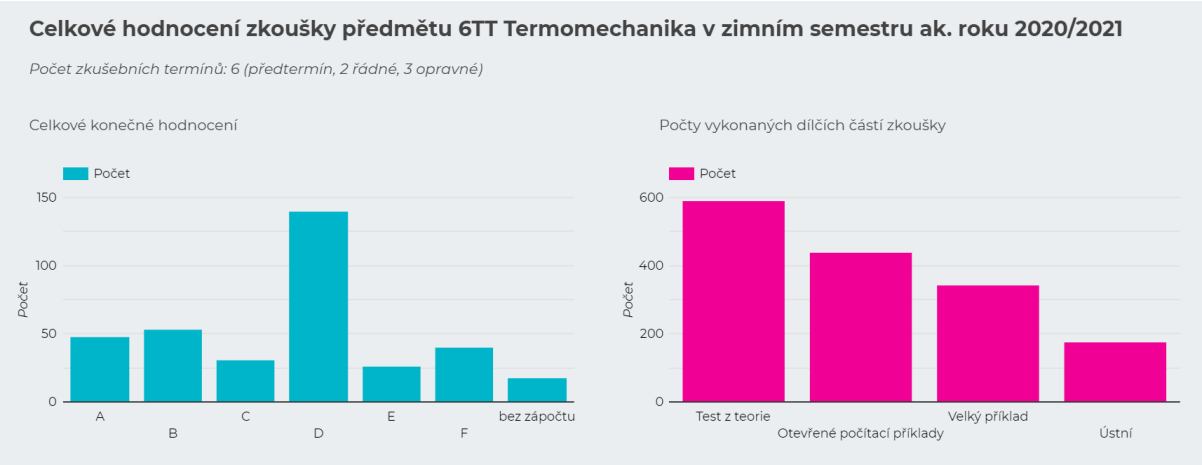

Obrázek 5: *Google Data studio pro prezentaci výsledků zkoušky z předmětu Termomechanika*

5. ZÁVĚR

Tento příspěvek se snažil přiblížit využití nových technologií k větší efektivitě výuky náročnějších teoretických předmětů, jak v bakalářském, tak i magisterském studium. Snaha byla, aby stejné podklady a přístupy mohlo využívat více přednášejících, cvičících a zkoušejících dá se říci v reálném čase. Zároveň, aby studenti měli dostupné online materiály, které jim podle zájmu umožní různě hluboko proniknout do problematiky termodynamiky, přenosu tepla, pracovních cyklů a spalování. Zároveň bych zmínil, že součástí výuky je i její propagace a motivování studentů k poznání. Zde hrají nezastupitelnou roli sociální média. Zde bych zmínil facebookovou stránku https://www.facebook.com/Termomechanika/, která tuto roli mezi studenty naší fakulty plní.

POUŽITÉ ZDROJE

[1] PAVELEK, Milan. Termomechanika. Brno: Akademické nakladatelství CERM, 2011, 192 s. ISBN 978-80-214-4300-6.
[2] JAROŠ, Michal a Josef ŠTĚTINA. Termomechanika: sbírka příkladů. Brno: Akademické nakladatelství CERM, 2020. ISBN 978-80-214-5885-7.
[3] ÇENGEL, Yunus A. a Michael A. BOLES. Thermodynamics an engineering approach. 8. New York: McGraw-Hill, 2015, 1115 s. ISBN 978-0-07-339817-4.
[4] INCROPERA, Frank, David DEWITT, Theodore BERGMAN a Adrienne LAVINE. Principles of heat and mass transfer. 7th ed., international student version. Singapore: John Wiley, c2013, xxiii, 1048 s. ISBN 978-0-470-64615-1.

PODĚKOVÁNÍ

Práce autorů vznikla za podpory projektu specifického výzkumu VUT FSI-S-20-6267.

LII. INTERNATIONAL SCIENTIFIC CONFERENCE OF THE CZECH AND SLOVAK UNIVERSITY DEPARTMENTS AND INSTITUTIONS FOCUSED ON RESEARCH AND TEACHING METHODS RELATED TO COMBUSTION ENGINES, ALTERNATIVE DRIVES AND TRANSPORT
SEPTEMBER 22 – 23, 2021, PRAGUE
CZECH UNIVERSITY OF LIFE SCIENCE PRAGUE, FACULTY OF ENGINEERING,
DEPARTMENT OF VEHICLES AND GROUND TRANSPORT

MAPPING OF A TURBOCHARGED ICE WITH ELECTRICALLY ASSISTED BOOSTING SYSTEM IN MIND

Rastislav Toman[1]

Abstract
The current turbocharged ICEs are usually matched with a turbocharger and mapped or calibrated with the aim to fulfil the low-end-torque (LET) requirement. The LET condition can be fulfilled only by using a smaller size turbine and compressor. However, this subsequently compromises the peak power output of the ICE at higher operating speeds, by limiting the maximum mass flow through the turbine. Electrically assisted boosting systems, such as eTurbos or eBoosters, allow for the fulfilment of LET condition with a bigger size turbocharger and therefore not limiting the peak power output of the ICE, also improving transient behaviour. This study presents a 3-cylinder spark ignition ICE mapping for different compression ratios with electrically assisted boosting system in mind. The results were obtained by the optimization of a virtual ICE in GT-Suite (0D/1D CFD approach), using genetic algorithm.

1. INTRODUCTION

Current hybrid electric powertrains' development at either mild level (48 V systems), full or optionally plug-in level (usually 300-400 V) enables the use of additional ICE electrification with electrically assisted boosting systems. These systems can help with the classic turbocharger matching dilemma of either matching relatively large turbocharger (TC) to achieve high ICE peak power, not concerning about the ICE's low-end-torque performance (LET) or matching a smaller TC to improve the LET conditions, while compromising the peak power. Modern passenger vehicle engines are usually mapped to achieve very good LET performance, but the electrically assisted boosting systems can compensate the LET also with relatively large TC, and even further improving the transient response.
Two main layouts are usually the focus of simulation and experimental research projects: a TC with electric motor/generator directly on shaft (*eTurbo*) or a conventional turbocharger combined with electrically driven compressor (*eBooster*). Research papers and projects usually target transient performance improvement, some study also the overall ICE efficiency improvement in the homologation driving cycles or the steady-state performance [1, 2, 3]. Some simulation research dealing with this topic was also published at author's department, focusing on finding the maximum thermodynamic potential of different electrically assisted boosting systems [4, 5].

[1] Rastislav Toman, CTU in Prague, Faculty of Mechanical Engineering, Technická 4, 166 07 Prague 6, Rastislav.Toman@fs.cvut.cz

1.1 Goals of the Paper

This paper focuses on the steady-state ICE mapping with electrically assisted boosting system in mind, comparing the thermodynamic potentials for three different compression ratio (CR) variants: *CR 9.5*, *CR 11.0*, and *CR 12.5*.
Then, the main goals of this paper are two – both for all CR variants:

- First, to find the peak performance limits of the ICE CR variants by optimal TC matching at high ICE operating speeds.
- Second, to optimize the full ICE operating maps, using the TC sizes obtained from the first goal.

2. ICE SIMULATION MODEL

ICE parameters are based on an existing ICE designs, although with some changes. Therefore, the studied and optimized ICE is a virtual one – a 3-cylinder long-stroke, with sweep volume of 1.12 L (Table 1). The simulation model is built in GT-Suite 0D/1D simulation environment [6].

Bore	[mm]	74.5
Stroke	[mm]	85.9
Compression Ratio	[-]	9.5 / 11.0 / 12.5
Engine Speed	[RPM]	1000-6500
Configuration		R3
Charging		Turbocharged
Combustion Mode		SI
Fuel		Indolene
Fuel Injection		Direct
Air Excess λ	[-]	1
External EGR	[%]	N/A
No. of Intake Valves	[-]	2 (VVT)
No. of Exhaust Valves	[-]	2 (VVT)

Table 1: *Main ICE parameters*

Figure 1 shows the ICE layout, with cooled low pressure EGR, waste-gate (WG) TC control, and charge-air cooler (CAC) upstream of the throttle. Although the simulation model is ready for the simulation of the electric assistance with *eTurbo* layout, this presented study does not account for it. Finally, the ICE also uses the integrated cooled exhaust manifolds.

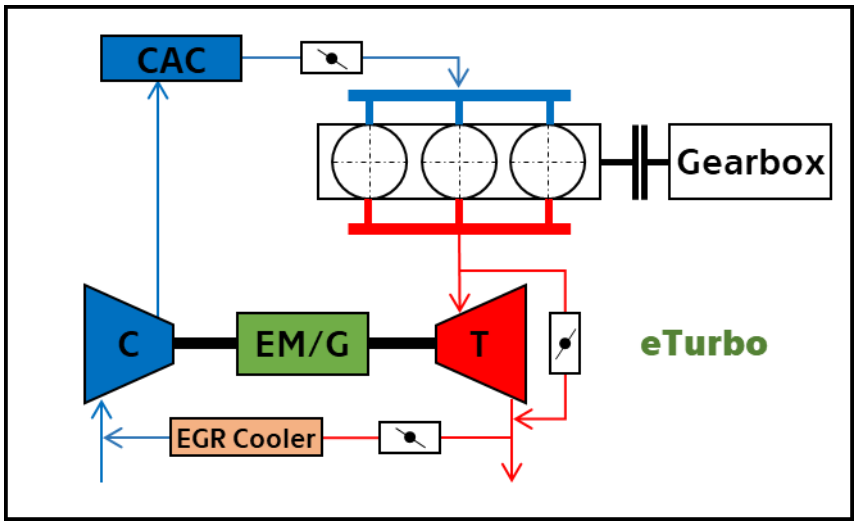

Figure 1: *ICE layout*

Also, the simulation sub-models were directly taken from existing calibrated ICE designs. All following sub-models have therefore high predictive abilities for our specific optimization task:

- Knock, and turbulent flame combustion models calibrated on a similar geometry cylinder unit for varied CRs (from 9.5 to 12.5), ICE loads, and speeds.
- Friction model formula is similar to the default GT-Suite's Chen-Flynn model, but our formula is enhanced by the dependencies (and interdependencies) on bore, stroke, ICE speed, mean piston speed, maximum and average cylinders' pressures. Model was calibrated using the in-house detailed mechanical losses model [7].
- Simplified FE model calculates the combustion chamber wall temperatures, and it is combined with classical Woschni correlation without swirl [8], that estimates the heat transfer coefficient between the in-cylinder gas and combustion chamber walls.

Turbocharger is simulated using a standard approach of lumped compressor/turbine model, with manufacturer-provided maps. These efficiency maps are scaled to achieve the peak total turbocharger efficiency of approximately 60 %. Turbine uses a fixed geometry, with maximum inlet temperature limit of 1100 °C. Then, the compressor map is widened, limiting the surge/choke behaviour. This way the modified TC represent a future advanced turbocharger design.

0D/1D ICE simulation model is controlled by a series of GT-Suite's enhanced PID based controllers:

- BMEP is controlled either by WG or throttle controllers, with automatic switching logic. WG controller also monitors TC over-speeding, however, automatic compressor surge control is not present.
- Combustion phasing and knock controllers adjust the CA50 position, avoiding knock behaviour.
- Lambda controller adjusts the stoichiometry to pre-set condition or to match the maximum turbine inlet temperature (however, our study only allows for the stoichiometric conditions).
- Finally, also there is also an EGR controller, for the cooled low-pressure EGR control.

3. OPTIMIZATION PROCESS

The multi-variable multi-constraint optimization problem is solved with the genetic algorithm that is available as a part of the GT-Suite SW package [6]. The whole optimization process is split into three distinct steps, that will be introduced in following sub-chapters. Each optimization step has slightly different optimization goals, and different set of optimization parameters.

3.1 TC Matching at ICE Full Load

First optimization step aims to find the optimal TC size for each CR variant at full load operation. So, the optimization parameters are turbine and compressor mass flow multiplier (2 parameters), intake/exhaust VVT (2 parameters), and combustion CA50 position.
Optimizer maximizes the average brake power for four ICE operating speeds: 4500 – 5000 – 5500 – 6000 RPM.
At this optimization step we have added one more optimization set: *CR 9.5 VVA* with full optimization of valve opening and closing events (4 parameters), to test for additional performance potential of the studied engine (the original valve lift profiles are somewhat limiting at high RPMs). However, this optimization set was not later used for the following optimization steps.
Note: the used valve-lift curves are the same for the three base variants, with 220 °CA opening (at 1 mm valve lift) for the intake valves, and 180 °CA for exhaust valve. Here, °CA does not represent the “crank angles” as per the whole document, but “cam angle”.

3.2 Full Load Performance

Then, at the second optimization step, the optimization goal is the maximization of BMEP at ICE full load, individually for each ICE operating speed of the whole RPM range.
The TC size here is fixed from the first optimization step, so the optimization parameters are intake/exhaust VVT (2 parameters), and position of combustion’s CA50.

3.3 Part Load Performance

Finally, at the third optimization step the GA minimizes the BSFC at different BMEP part load targets, for the whole RPM operating range. Part load BMEP steps are 2 – 6 – 10 – 14 – 18 – 22 – 26 bar.
The TC size is naturally also fixed, so the optimization parameters are again the intake/exhaust VVT (2 parameters), combustion phasing, but also the additional EGR rate.

3.4 Optimization Constraints

The optimization constraints are the same for all three optimization steps:

- Compressor surge behaviour;
- Maximum turbine inlet temperature: 1100 °C;
- Knocking behaviour;
- Maximum internal EGR: 30 %;

A design that violates any of these constraints (together with some other simulation convergence related constraints) is automatically discarded.

4. RESULTS

The results part is divided into three sub-chapters, accordingly to the optimization process's steps. At first, the TC matching at full loads results is shown, then the full load performances, and finally some of the full ICE maps for all three CR variants.

4.1 TC Matching at ICE Full Load

The results from the first optimization step show the performance potentials of the four optimized variants, with their respective optimal TC size. Table 2 contains the optimal turbine and compressor flow multipliers, average brake, and specific powers, that served as the objective function for the optimizer to maximize; Figure 2 then shows the BMEP and BSFC values on a case-by-case basis for all the variants.

	Turbine Flow Multi. [-]	Compressor Flow Multi. [-]	Avg. Brake Power [kW]	Specific Power [kW/L]
CR 9.5 VVA	3.25	2.15	142.48	126.83
CR 9.5	3.25	1.89	125.49	111.71
CR 11.0	3.49	1.68	110.72	98.56
CR 12.5	3.50	2.19	100.69	89.63

Table 2: *Optimal TC flow multipliers and ICE performance figures*

The optimal compressor and turbine flow multipliers lead to relatively large TC for all variants, compared to the original TC design. Especially the turbine map is enlarger substantially – as it was expected. These compressor and turbine sizes, together with VVT (or VVA) ensure reasonable performance values and specific power figures for a current downsized application.
The *CR 9.5 VVA* variant shows that there is further performance potential, the original valve lift curves were indeed restrictive. However, to improve the specific power even further would require redesign of intake ports, and cylinder bore enlargement.

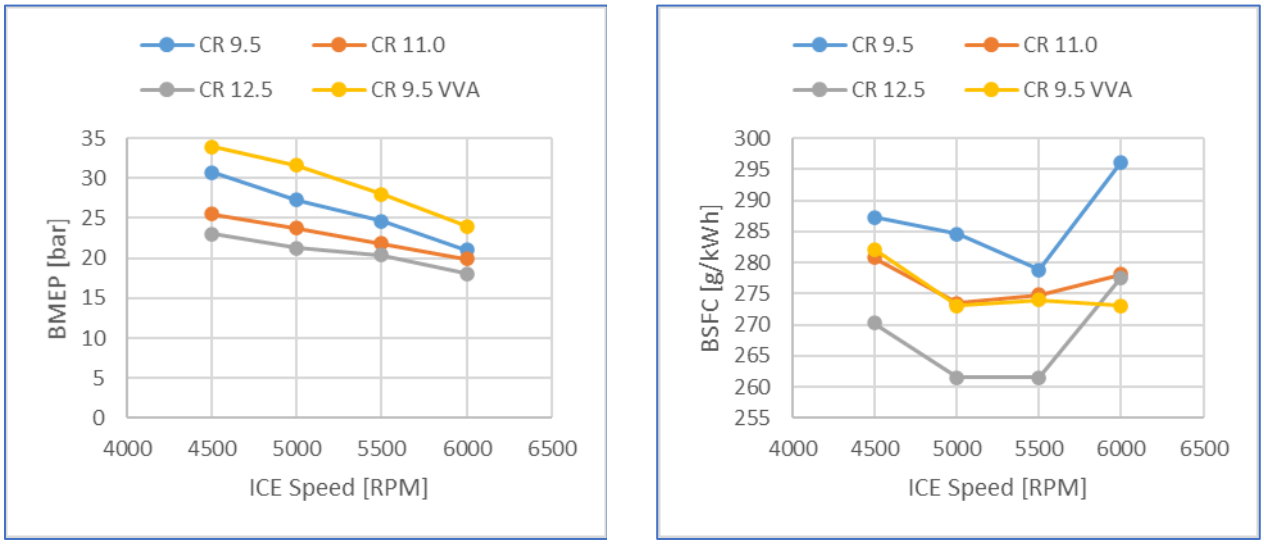

Figure 2: *ICE full load for TC matching step*

CR 9.5 VVA variant naturally reaches the highest BMEP value of almost 35 bar at 4500 RPM, and 25 bar at 6000 RPM. *CR 9.5 VVA* also improves on its BSFC figures in comparison to *CR 9.5*, which suggests possible beneficial use of e.g., cam switching system for high RPMs (such as Honda VTEC). *CR 12.5* reaches interesting BMEP and BSFC figures, even with the obvious knock limitations.

4.2 Full Load Performance

The second optimization step gives us the complete ICE full load performance (Figure 3). *CR 9.5* reaches a top BMEP of 32.0 bar at 4000 RPM; *CR 11.0* of 27.2 bar at 4500 RPM; and *CR 12.5* BMEP of 23.9 bar at 4500 RPM. These performance figures lead to a poorer LET performance – BMEP is limited bellow 3000 RPM for all variants.

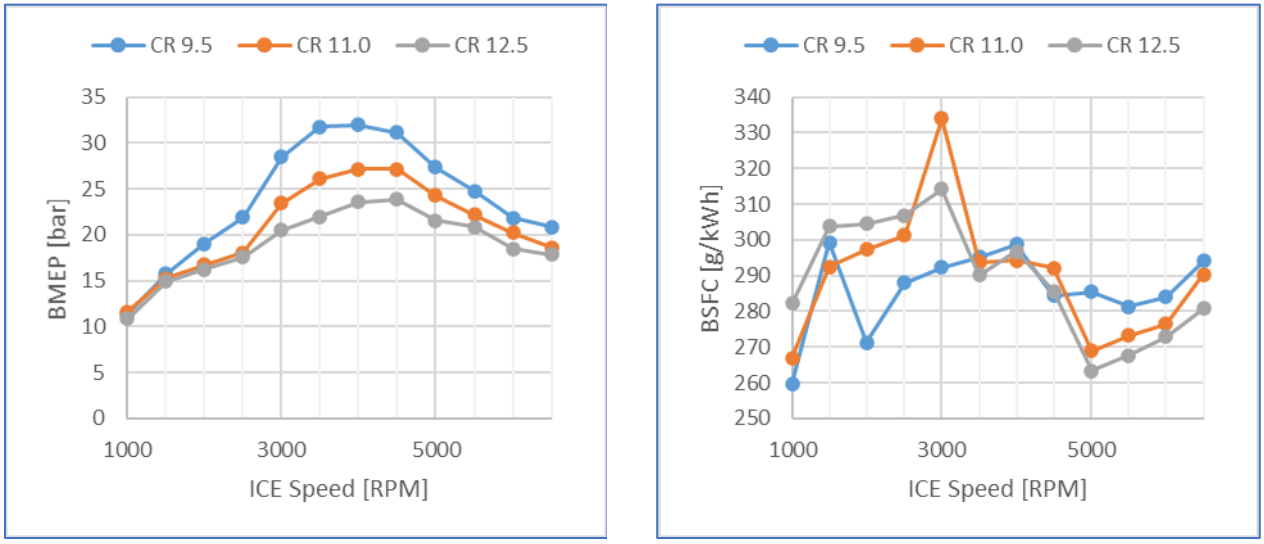

Figure 3: *ICE final full load performance*

A detailed analysis of other ICE quantities reveal, that probably the knock model's behaviour in the region of 2000-3000 RPMs for all variants leads to some questionable optimization outcomes: for example the BSFC figure of *CR 9.5* at 2000 RPM or *CR 11.0* at 3000 RPM are definitely strange. This means, that this model needs to be further studied and tested.

4.3 Full Maps

Optimized full maps contain a lot of information, however this chapter is limited to only few "most interesting" values. All variants feature Miller valve timings in broad spectrum of ICE operating points.

First, the study of the full map results confirms the correct function of the optimization process: all the optimization constraints are met as required, model controller components perform as expected (especially knock, EGR, and throttle with WG control logic), and the overall results are consistent through the individual ICE maps and comparison with each other.

Now, Figure 4 contains the full maps of *CR 9.5* variant (BSFC, CA50 position, maximum pressure, and EGR with residual gasses), Figure 5 the same maps for *CR 11.0*, and Figure 6 *CR 12.5* maps.

Best BSFC results (top left position in the figures) are naturally reached for the *CR 12.5* variant, although the top value is only about 6.5 g/kWh lower than for *CR 9.5* variant.

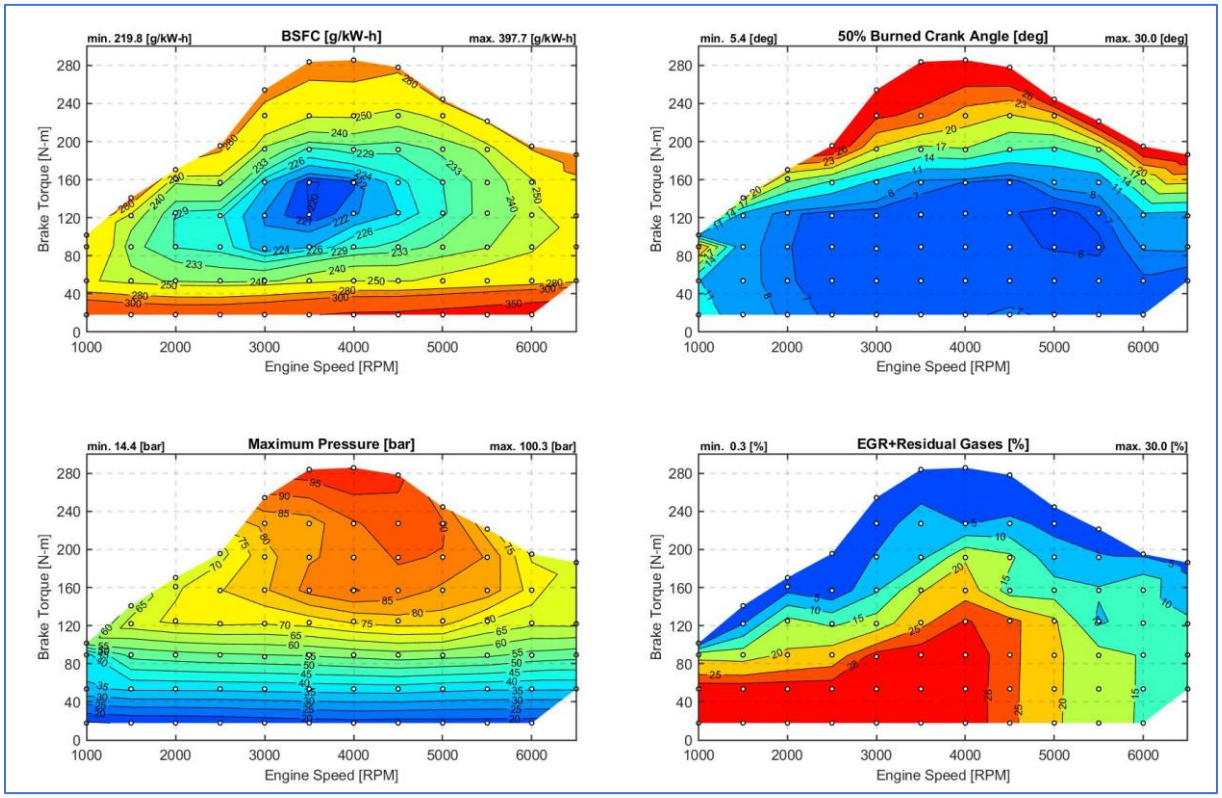

Figure 4: *CR 9.5 full maps*

Maximum cycle pressures (bottom left position) are highest for the *CR 9.5* (100.3 bar), whereas *CR 12.5* has maximum cycle pressures of about 20 % lower.

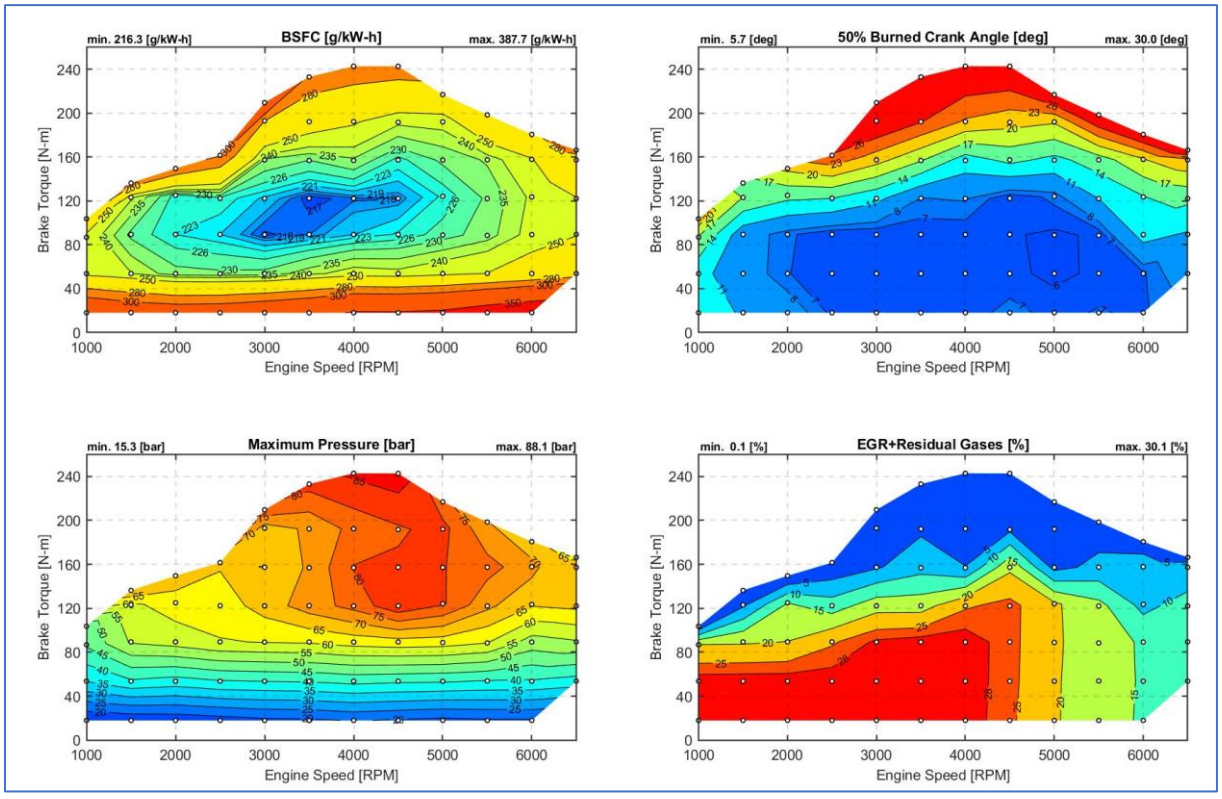

Figure 5: *CR 11.0 full maps*

CA50 positions (top right position) reach maximum allowable values of 30 °CA ATDC for all three variants around the ICE full load performance.
Finally, external EGR and residual gas content (bottom right position) is on the limit for a large spectrum of operating points. A detailed look on the external EGR without internal residuals show, that especially at very low speeds this is achieved with EGR valve almost closed.

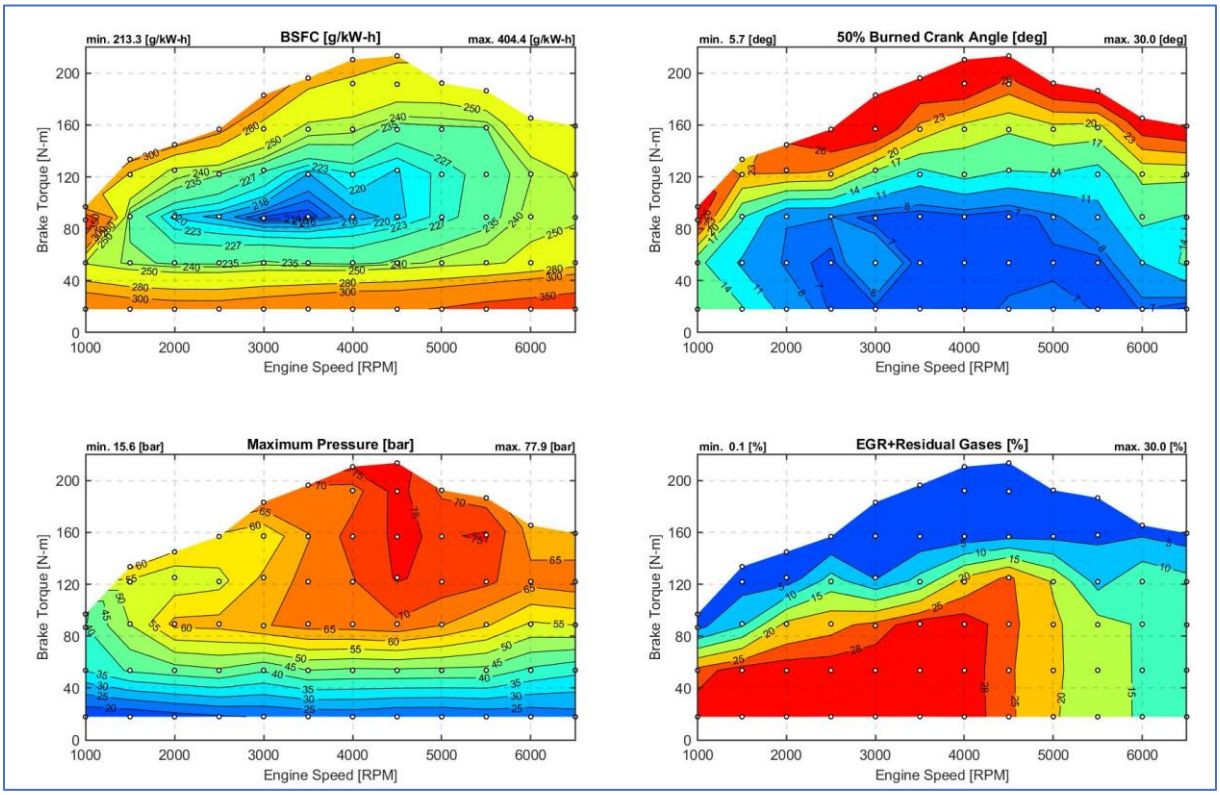

Figure 6: *CR 12.5 full maps*

5. CONCLUSION

The paper presented a detailed optimization study of a 3-cylinder downsized ICE, with a goal of achieving the best possible peak performance, having a future electrification of the boosting system in mind, that would compensate for the poor LET performance, and improve the transient behaviour.
Optimization considered parameters of a future advanced turbocharger (total efficiency of 60 %, improved temperature properties, wide compressor map), and was run for three different compression ratios (CR).
TC matching step of our study shows a specific power potential of 126.83 kW/L for the CR 9.5 variant with control of valve opening and closing events. The high CR variant reaches the lowest specific power of 89.63 kW/L. TC sizes were then fixed for the full operation map optimization.
The full map results show very good BSFC values for all three optimization variants (from 213.3 to 219.8 g/kWh), using Millerization when possible, and relatively high EGR overall content.
However, the optimizations show, that the knock model behaviour close to full load at 2000-3000 RPM may cause some uncertainty, affecting the optimal ICE setting and performance.

REFERENCES

[1] COOPER A., BASSETT M., HALL J., HARRINGTON S., HARTLAND J., HARRIS J., TAYLOR A., 2019. HyPACE - Hybrid Petrol Advance Combustion Engine - Advanced Boosting System for Extended Stoichiometric Operation and Improved Dynamic Response, SAE Technical Paper 2019-01-0325, doi: 10.4271/2019-01-0325.

[2] UHLMANN T., BAUMGARTEN H., FRANZKE B., SCHARF J., THEWES M., BIRMES, 2016. Extreme downsizing for gasoline engines – fun to drive with extremely low emissions, Proceedings of Internationaler Motorenkongress 2016, doi: 10.1007/978-3-658-12918-7_8

[3] BURKE R. D., 2016. A Numerical Study of the Benefits of Electrically Assisted Boosting Systems, Journal of Engineering for Gas Turbines and Power, Vol. 138, doi: 10.1115/1.4032764

[4] VITEK O., MACEK J., 2017. Thermodynamic Potential of Electrical Turbocharging for the Case of Small Passenger Car ICE under Steady Operation, SAE Technical Paper 2017-01-0526, 2017, doi:10.4271/2017-01-0526

[5] VITEK O., MACEK J., 2017. Electrical Turbocharging – Thermodynamic Potential under Steady State Operation, KOKA 2017 Conference

[6] GT-Power User's Manual, GT-Suite version V2018. Gamma Technologies Inc., 2018.

[7] MACEK J., FUENTE D., EMRICH M., 2011. A Simple Physical Model of ICE Mechanical Losses. SAE International 2011-01-0610. https://doi.org/10.4271/2011-01-0610

[8] WOSCHNI G., 1967. A Universally Applicable Equation for the Instantaneous Heat Transfer Coefficient in the Internal Combustion Engine. SAE International 670931. https://doi.org/10.4271/670931

ACKNOWLEDGEMENT

This work was realized using support of Technological Agency, Czech Republic, programme National Competence Centres, project # TN01000026 Josef Bozek National Center of Competence for Surface Vehicles. This support is gratefully acknowledged.

LII. INTERNATIONAL SCIENTIFIC CONFERENCE OF THE CZECH AND SLOVAK UNIVERSITY DEPARTMENTS AND INSTITUTIONS FOCUSED ON RESEARCH AND TEACHING METHODS RELATED TO COMBUSTION ENGINES, ALTERNATIVE DRIVES AND TRANSPORT
SEPTEMBER 22 – 23, 2021, PRAGUE
CZECH UNIVERSITY OF LIFE SCIENCE PRAGUE, FACULTY OF ENGINEERING,
DEPARTMENT OF VEHICLES AND GROUND TRANSPORT

CLASSIFICATION OF AERODYNAMIC INSTABILITIES IN A CENTRIFUGAL COMPRESSOR

Jiří Vacula[1], Pavel Novotný[2], Petr Kudláček[3]

Abstract
The formation of aerodynamic instabilities during centrifugal compressor operation is undesirable due to reduction in efficiency and increased vibration and noise. Based on the measurement of noise and casing vibration of a centrifugal compressor, an analysis of the obtained parameters is made and the individual sources of vibration and noise are classified. Taking into account the worldwide research carried out in this field, it is possible to assign the selected frequencies to a specific phenomenon. The significance of the individual sources of noise and vibration can be assessed for selected operating conditions and the potential to reduce them can be analyzed as well.

1. INTRODUCTION

Rotary machines are always designed to achieve maximum possible efficiency under the preferred operating conditions. The designers must often take these operating conditions into account and thus adapt the design accordingly. However, rotary machines can also be operated under off-design operating conditions. These operating conditions, although often negligible in terms of machine operating time, have a significant effect on vibroacoustic behaviour due to the occurrence of flow instabilities and often cause aerodynamic excitations. Increased vibrations can lead to a reduction in the service life of a rotary machine and, in combination with increased noise, lead to a reduction in the comfort of the people in contact with such a machine. Vibration and noise are thus often closely linked to the operating conditions of a compressor and to the typical dynamic flow phenomena in the compressor.
Rotary machines have operating characteristics that limit their operation to the conditions for which were designed. Generally, rotating machines are designed to obtain maximum efficiency for the design operating conditions. Nonetheless, the off-design operating conditions, under which the rotating machine can be operated, may lead to an increase in noise or vibration due to the generation of flow instabilities. Increased vibration can cause a reduction in the lifetime of the rotating machine and a

[1] Ing. Jiří Vacula, Brno University of Technology, Technická 2896/2, jiri.vacula@vutbr.cz
[2] doc. Ing. Pavel Novotný, Ph.D., Brno University of Technology, Technická 2896/2, 61669 Brno, novotny.pa@fme.vutbr.cz
[3] Ing. Petr Kudláček, Brno University of Technology, Technická 2896/2, petr.kudlacek@vutbr.cz

reduction in the comfort of persons occurs as well due to increase in noise. Aerodynamic phenomena producing vibration and noise of typical parameters are thus often closely linked to the operating conditions of the compressor. Typical frequency response range occurs if the centrifugal compressor is operated under typical conditions.
Centrifugal compressors are designed for one flow direction, one shaft rotation direction and so that the pressure value at their outlets is higher than at their inlets. A centrifugal compressor driven by a turbine allows operation at various speeds. Operation in such diverse conditions leads to a wide range of aerodynamic phenomena. It must be considered that the pressure ratio is roughly proportional to the square of the rotor speed and the change in pressure leads to a change in the temperature of the compressible medium, which leads to a change in the local speed of sound. Because centrifugal compressors are commonly operated at circumferential speeds that may exceed this local speed of sound, aerodynamic phenomena associated with supersonic flow may occur under some operating condition.
An intensive research has been carried out to describe the individual aerodynamic instabilities. Detailed information can be found for example in the work of Kushner [1], Japikse [2], Oaks et al. [3], Liśkiewicz [4].

2. RESEARCH OBJECTIVE

The research objective is to provide a guideline of typical and expected vibro-acoustic parameters in centrifugal compressor characteristic. Classification of the individual aerodynamic phenomena according to their frequency response ensures providing a reliable way to assess the risk of the individual excitation frequency. Vibroacoustic phenomena can help researchers identify aerodynamic phenomena and find suitable computational approaches to solve them. The classification of the individual aerodynamic phenomena takes into account the following:

- Operating condition in the compressor characteristics.
- Presence of vaned or vaneless diffuser.
- Frequency description of the vibroacoustic behaviour related to the aerodynamic instabilities.

3. METHODOLOGY DESCRIPTION

The aerodynamic phenomenon occurring in centrifugal compressors can be characterised by the excitation frequency of phenomenon f. This excitation frequency can be identified, for example, in the form of vibration, noise, axial force, etc. Rotor speed frequency f_{R} is one of the basic parameters of rotary machines. This frequency is often used as a base frequency for the description of aerodynamic processes.

The flow instabilities occurring in compressors usually consist of a rotating pressure field called a rotating stall. The instability can be characterised by the frequency of rotation of the rotating stall f_{S} and by integer number n, denoting the number of stall cells. The excitation frequency of such an aerodynamic phenomenon in a stationary coordinate system at a specific location can then be written in the form

$$f = f_S\, n\,. \tag{1}$$

Another important frequency that can be sometimes identified is a blade passing frequency defined as

$$f_{BPF} = f_R\, z_R\,, \tag{2}$$

where z_R is the number of impeller blades.

The excitation frequency of the aerodynamic phenomenon can be related to some characteristic frequency of the rotary machine and frequency ratio ε can be used to describe this dependence. Often, rotor speed or synchronous frequency is used as a base. Subsequently, the frequency ratio of the excitation of the given aerodynamic phenomenon can be defined as

$$\varepsilon_R = \frac{f}{f_R}\,. \tag{3}$$

The rotor speed ratio can take almost any value. In general, $\varepsilon_R < 1$ applies to sub-synchronous processes and $\varepsilon_R > 1$ applies to super-synchronous processes. However, in the literature, the frequency of the rotation of rotating stall f_S is often introduced under different designations. To avoid misinterpretation with ε_R and for the purpose of this work, the frequency ratio of rotation of rotating stall ε_S is defined as

$$\varepsilon_S = \frac{f_S}{f_R}\,, \tag{4}$$

where ε_S is typically less than 1.

The basic classification of aerodynamic phenomena occurring in centrifugal compressor can be described as:

- **Rotating stall**: The term rotating stall means a rotating flow separation characterised by rotating stall cells, especially those located in the impeller or diffuser. Frigne and Van Den Braembussche [5] and Zheng and Liu [6] mention that these flow instabilities can occur during compressor operation not only in the area of positive slope of the compressor characteristics.
- **Impeller rotating stall**: This instability is attributed to a destabilization of the impeller flow. Frigne and Van Den Braembussche [5] categorised the IRS phenomenon as Small/Mild IRS, Progressive IRS and Abrupt IRS.
- **Diffuser rotating stall**: Regardless the diffuser is vaned or vaneless, destabilization of the flow in the diffuser can occur. Marshall and Sorokes [7] and Frigne and Van Den Braembussche [5] distinguish whether DRS occurs at lower rotor speeds (low speed DRS) or at higher rotor speeds (high speed DRS).

- **Rotor-stator interaction**: Marshall and Sorokes [7] state that RSI can also occur at higher flow rates because the flow leaving the impeller has a more radial direction, resulting in higher energy transfer between rotor and stator.
- **Surge**: An operating condition during which flow is fully recirculated to the compressor inlet, accompanied mainly by flow pulsations. As Jansen [8] points out, surge can only occur in the case of compressible flow, when the resulting frequency of the pressure pulsations of fluid volumes in the inlet and outlet ducts of the compressor is related to the Helmholtz-type resonance. Therefore, it is not possible to speak about surge in pumps, because liquids are almost incompressible under normal conditions. An interesting fact is reported by Andersen et al. [9] that it is possible to detect an increased noise level, although the operation of the compressor is not under a near-surge condition. Therefore, for example, Kämmer and Rautenberg [10] distinguished 'surge line' and 'stall limit line' in compressor characteristics.

A general characteristic of a centrifugal compressor is graphically shown in Figure 1 with highlighted areas of the probable occurrence of specific aerodynamic phenomena and their properties. It is focused mainly on the aerodynamic instabilities in the area of low flow rates and the area of surge, as these off-design operating conditions occur most often during compressor operation

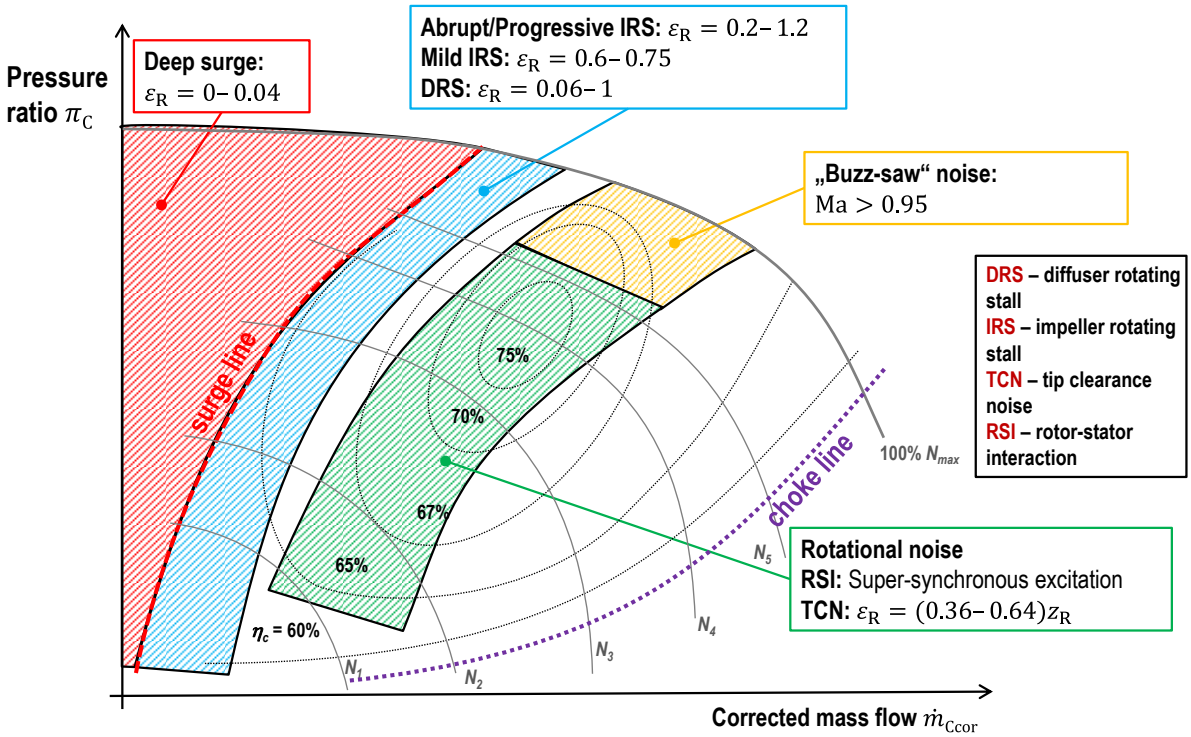

Figure 1: An indicative overview of the typical aerodynamic phenomena in a general characteristic of a centrifugal compressor.

4. RESULTS

A measurement of a compressor characteristic was performed including measurement of acoustic pressure by 8 microphones being at distance 1 m from the compressor. The evaluation of the measured signal was carried out by software Matlab. For each operational point of the compressor characteristic the far-field sound pressure level is obtained. Figure 2 presents A-weighted sound pressure level (SPL) values (dBA) measured by microphone located 1 m in front of the compressor in a compressor axis. The SPL values show significant increase at maximum speed line $u_{2\mathrm{red}} = 550\ \mathrm{m{\cdot}s^{-1}}$. In addition, at speed lines $u_{2\mathrm{red}} > 250\ \mathrm{m{\cdot}s^{-1}}$ the operational points at surge show the highest value of SPL.

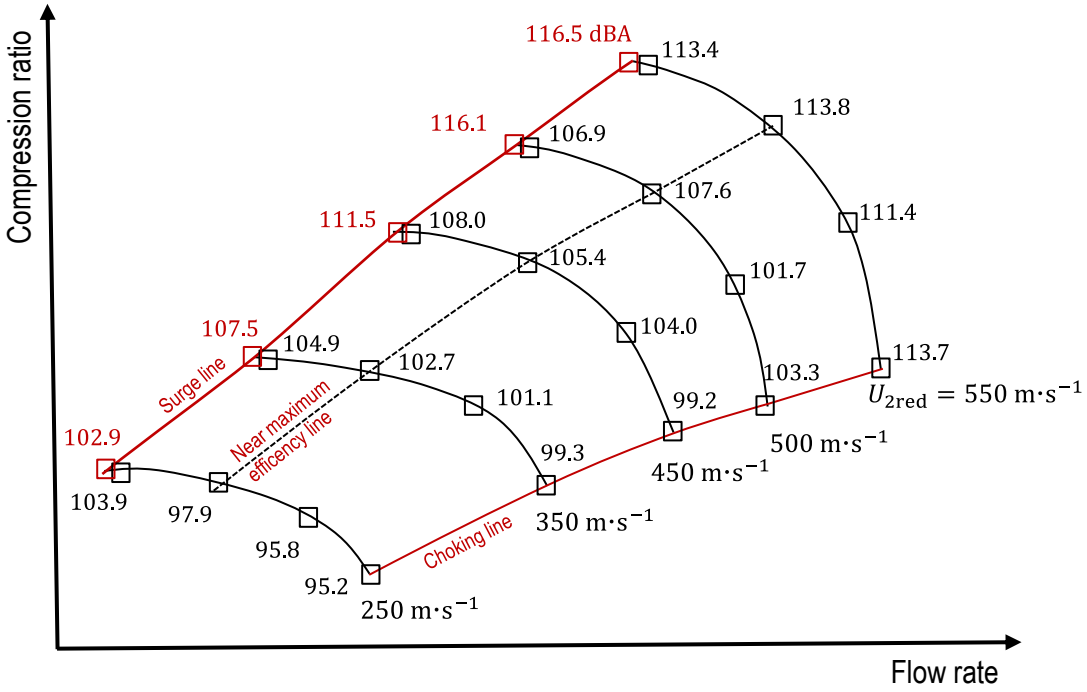

Figure 2: Sound pressure level measured for each operational point at a place 1 m in front of the compressor.

Pressure time history at operational point at surge line $u_{2\mathrm{red}} = 350\ \mathrm{m{\cdot}s^{-1}}$ is shown in Figure 3. The time period of pressure signal peaks excited by surge is approximately $0.4\ s$ creating excitation frequency $2.5\ \mathrm{Hz}$ ($\varepsilon_{\mathrm{R}} = 0.005$). Greitzer [11] derived the Helmholtz frequency in the form

$$f_{\mathrm{H}} = \frac{a}{2\pi}\sqrt{\frac{A_{\mathrm{duct}}}{V\, l_{\mathrm{duct}}}}, \tag{5}$$

where a is the average speed of sound of the system, A_{duct} is the equivalent cross-sectional compressor duct area, V is the volume of the compressed air and l_{duct} is the equivalent length of the duct. In the case of so-called deep surge, the arising frequency can be much lower than the Helmholtz frequency because the frequency is set by the plenum blowdown and refilling time, as shown by Fink et al. [12] and confirmed by Denher et al. [13]. According to equation (5) the Helmholtz frequency can be roughly estimated $f_{\mathrm{H}} = 9\ \mathrm{Hz}$. The measured frequency $2.5\ \mathrm{Hz}$ is lower than Helmholtz

frequency which is in accordance with conclusions created by Fink et al. [12] and Denher et al. [13].

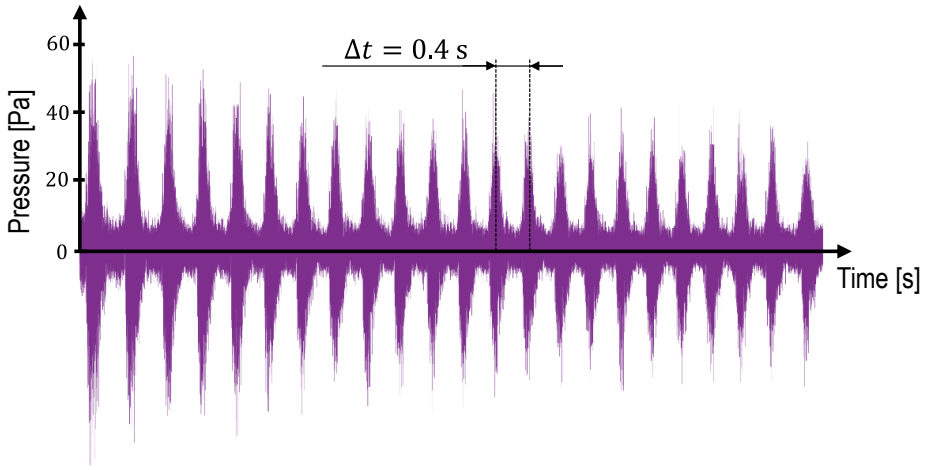

Figure 3: Pressure time history of operational point at surge line at speed line $u_{2red} = 350\ \mathbf{m{\cdot}s^{-1}}$.

In Figure 4 there is shown pressure spectra of operational point near maximum efficiency at each selected speed line.

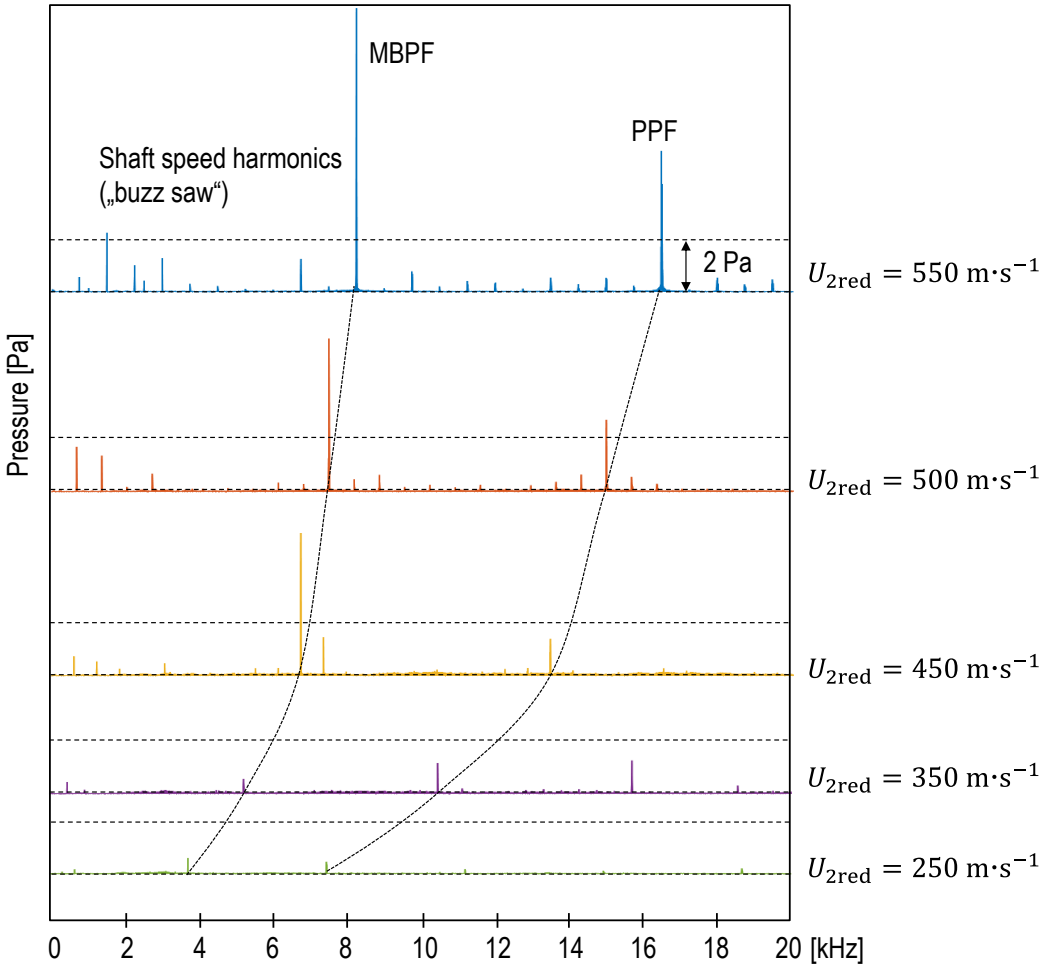

Figure 4: Far-field pressure spectra of the compressor operated at point near maximum efficiency at each speed line.

The maximum speed line $u_{2\mathrm{red}} = 550\ \mathrm{m{\cdot}s^{-1}}$ shows „buzz saw“ noise with dominant main blade passing frequency (MBPF) and passage passing frequency (PPF) taking into account the presence of splitter blades. The MBPF and PPF are dominant at each speed line.

5. CONCLUSIONS

The experimental results show reasonable accordance with data of prior research in centrifugal compressors. The acoustic pressure measurement confirmed the presence of buzz saw noise at maximum speed line, dominant MBPF and PPF at each speed line. It is also confirmed that frequency of excitation at operational points at surge can be reasonably estimated be Helmholtz frequency. The findings presented in this paper are consistent with many years of worldwide research on aerodynamic phenomena in the field of centrifugal compressors.

REFERENCES

[1] KUSHNER, Frank. Dynamic Data Analysis of Compressor Rotating Stall. *Turbomachinery and Pump Symposia*. 1996, **25**, 71-82.

[2] JAPIKSE, David. *Centrifugal Compressor Design and Performance*. Norwich,Vermont: Concepts ETI, Inc., 1996. ISBN 0-933283-03-2.

[3] OAKES, William, Patrick LAWLESS, John FAGAN and Sanford FLEETER. High speed centrifugal compressor surge initiation characterization. *AIAA Meeting Papers on Disc, AIAA Paper 96-2577*. 1996, , 1-11.

[4] LIśKIEWICZ, G., L. HORODKO, M. STICKLAND and W. KRYłłOWICZ. Identification of phenomena preceding blower surge by means of pressure spectral maps. *Experimental Thermal and Fluid Science*. 2014, (54), 267-278.

[5] FRIGNE, P. and R. VAN DEN BRAEMBUSSCHE. Distinction Between Different Types of Impeller and Diffuser Rotating Stall in a Centrifugal Compressor With Vaneless Diffuser. *J. Eng. Gas Turbines Power*. 1984, **106**(2), 468-474.

[6] ZHENG, Xinqian and Anxiong LIU. Phenomenon and Mechanism of Two-Regime-Surge in a Centrifugal Compressor. *Journal of Turbomachinery*. 2015, **137**(8), 1-7.

[7] MARSHALL, Fred and James SOROKES. A Review Of Aerodynamically Induced Forces Acting On Centrifugal Compressors, And Resulting Vibration Characteristics Of Rotors. *Proceedings of the 29th turbomachinery symposium*. 2000, , 263-280.

[8] JANSEN, Willem. Rotating Stall in a Radial Vaneless Diffuser. *Transactions ASME Journal of Basic Engineering*. 1964, **86**(4), 750-758.

[9] ANDERSEN, Johannes, Fredrik LINDSTRÖM and Fredrik WESTIN. Surge Definitions for Radial Compressors in Automotive Turbochargers. *SAE International Journal of Engines*. 2008, **1**(1), 218-231.

[10] KÄMMER, N. and M. RAUTENBERG. An Experimental Investigation of Rotating Stall Flow in a Centrifugal Compressor. *ASME 1982 International Gas Turbine Conference and Exhibit: Paper No: 82-GT-82*. 1982, **1**, 1-9.

[11] GREITZER, E. Surge and Rotating Stall in Axial Flow Compressors—Part I: Theoretical Compression System Model. *Journal of Engineering for Power*. 1976, **98**(2), 190-198.

[12] FINK, D., N. CUMPSTY and E. GREITZER. Surge Dynamics in a Free-Spool Centrifugal Compressor System. *Journal of Turbomachinery*. 1992, **114**(2), 321-332.

[13] DEHNER, Rick, Ahmet SELAMET, Philip KELLER and Michael BECKER. Simulation of Deep Surge in a Turbocharger Compression System. *Journal of Turbomachinery*. 2016, **138**(11), 1-12.

ACKNOWLEDGEMENT

The research leading to these results has received funding from the Specific research program at Brno University of Technology, reg. no. FSI-S-20-6267 and has been realised with kind support of project Josef Bozek National Center of Competence for Surface Vehicles, reg. no. TN01000026.

52. MEZINÁRODNÍ VĚDECKÁ KONFERENCE ČESKÝCH A SLOVENSKÝCH UNIVERZIT A INSTITUCÍ ZAMĚŘENÁ NA VÝZKUMNÉ A VÝUKOVÉ METODY SPOJENÉ SE SPALOVACÍMI MOTORY, ALTERNATIVNÍMI POHONY A DOPRAVOU

22.-23. ZÁŘÍ 2021, PRAHA
ČESKÁ ZEMĚDĚLSKÁ UNIVERZITA V PRAZE, TECHNICKÁ FAKULTA,
KATEDRA VOZIDEL A POZEMNÍ DOPRAVY

NÍZKÉ EMISE REAKTIVNÍCH SLOUČENIN DUSÍKU Z LEHKÝCH UŽITKOVÝCH VOZIDEL ZA REÁLNÉHO PROVOZU: LZE JICH DOSÁHNOUT, LZE JE MĚŘIT

Michal Vojtíšek[1], Martin Pechout[2]

Abstrakt
Článek přináší předběžné výsledky měření emisí NO, NO_2, NH_3 a N_2O sériového lehkého užitkového vozidla Toyota ProAce během reálného provozu pomocí přenosného FTIR spektrometru. Slouží jako názorný příklad, že emise NO_x v řádu setin g/km, s průměrnými koncentracemi NH_3 a N_2O v jednotkách ppm, mohou být reálně dosažitelné, a to i při vyšších rychlostech a zatíženích motoru než odpovídá homologační legislativě.

1. ÚVOD

Ve všech typech pístových spalovacích motorů, bez ohledu na palivo a konstrukční parametry, vzniká za vysokých teplot z atmosférického dusíku a kyslíku oxid dusnatý (NO) [1]. NO v atmosféře oxiduje na oxid dusičitý (NO_2), štiplavý, nahnědlý plyn, který poškozuje povrch lidských plic. Další přeměnou NO_2 vznikají částice solí (např. dusičnan amonný), kyseliny dusitá a dusičná, a další sloučeniny dusíku, například dusíkaté deriváty polyaromatických aromatických uhlovodíků (n-PAU, n-PAH), z nichž např. 3-nitro-benz[a]benzantron patří mezi sloučeniny s nejvyšší zatím zjištěnou mutagenitou. Fotolýzou NO_2 ultrafialovou složkou slunečního záření vzniká kyslíkový radikál, který se dále přeměňuje na ozon. Oxidy dusíku (zpravidla suma NO a NO_2; nestabilní oxidy N_2O_3, N_2O_5 a dimery N_2O_2 a N_2O_4 jsou zastoupeny v malé míře; N_2O je stabilní plyn relativně neškodný lidskému zdraví, avšak s velmi vysokým skleníkovým potenciálem) a přízemní (troposférický) ozon mají, spolu s částicemi, majoritní podíl na dopadech znečištění ovzduší na lidské zdraví. Ty lze považovat, například s počtem předčasných úmrtí vyčísleným na přibližně 1 promile populace ročně [2], za enormní. Podrobnější shrnutí lze dohledat v příspěvcích autorů z let 2017 a 2020 této konference [3,4].

[1] Michal Vojtíšek, Centrul vozidel udržitelné mobility, ČVUT v Praze, michal.vojtisek@fs.cvut.cz
[2] Martin Pechout, Katedra vozidel pozemní dopravy, Česká zemědělská univerzita, pechout@tf.czu.cz

Právě zejména z důvodu ochrany zdraví obyvatel v hustě osídlených oblastech byly zavedeny emisní limity, které se postupně snižovaly, v případě NO_x od začátku tisíciletí přibližně o řád. Koncentrace NO_2 v ovzduší se však nesnižovaly úměrně obměně vozového parku i proto, že mnozí evropští výrobci produkovali vozidla, jejichž emise NO_x v každodenním provozu násobně až řádově převyšovaly emise NO_x dosahované během homologačních zkoušek vybraných exemplářů vozidel. Tam, kde jej bylo skutečně dosaženo, bylo snížení primárních emisí NO v mnoha případech doprovázeno emisemi jiných škodlivých látek: přeměna NO na škodlivější NO_2, navýšení emisí částic z důvodu snížení teplot ve spalovacím prostoru, vznik amoniaku (NH_3) v třícestných katalyzátorech motorů pracujících se stechiometrickou směsí, vznik NH_3 a N_2O v redukčních katalyzátorech vznětových motorů, emise nezreagovaného NH_3 z katalyzátorů se selektivní redukcí. Pro sledování emisí reaktivních sloučenin dusíku (NO, NO_2, NH_3, ...), skleníkových plynů (CO_2, CH_4, N_2O) a dalších plynných látek bylo autory vyvinuto a sestaveno několik přenosných zařízení, založených na komerčních infračervených spektrometrech, ve kterých je infračervené spektrum získáváno Fourierovou transformací interferogramu širokopásmového infračerveného záření po průchodu kyvetou s výfukovými plyny (FTIR spektrometry). Validace tří různých FTIR analyzátorů pro měření za provozu byla popsána ve dřívějších publikacích autorů [4-7], ve kterých jsou také detailnější popisy včetně přehledů stavu poznání a zdrojů.

Během dřívějších ročníků této konference byly během oficiálních i neoficiálních diskuzí vzneseny pochybnosti o tom, zda současné či plánované limity EU pro emise NO_x jsou v běžném provozu skutečně dosažitelné. V případě zážehových motorů lze pomocí přes čtyřicet let známé technologie řízených třícestných katalyzátorů [8] dosáhnout emisí v řádově jednotkách miligramů na km, což bylo převedeno na ukázkovém automobilu na přelomu tisíciletí [9] a následně na sériově vyráběném automobilu [10]. V případě vznětových motorů tzv. nové generace, kterými jsou od roku 2010 osazována těžká vozidla v USA, lze pomocí sestavy oxidačního katalyzátoru, filtru částic, selektivně redukčního katalyzátoru (SCR) a katalyzátoru pro oxidaci amoniaku dosáhnout u dálničních tahačů emisí v řádu několika desetin gramu NO_x na kilometr (kamiony vyrobené v letech 2013-2014, [11,12]), což je zhruba poloviční hodnota oproti osobním automobilům se vznětovým motorem Euro 5 v Evropě [13]. Rozšířením homologačních testů o měření za provozu se emise NO_x během jízdy mimo laboratoř snížily, ovšem není zřejmé, zda za všech podmínek – experimentální data poukazují na značné rozdíly v závislosti na provozních podmínkách (např. [14]).

Cílem této práce bylo posoudit emise základních reaktivních sloučenin dusíku – NO, NO_2 a NH_3 – a dalších plynných látek během mezinárodní cesty lehkého užitkového vozidla, zahrnující podmínky málo časté v běžných testech, včetně vysokého zatížení motoru, jízdy nad 130 km/h, a pojezdu v koloně. Výsledky jsou předběžné a orientační.

2. MĚŘENÍ

Víceúčelový lehký automobil Toyota Proace Verso (max. 9 osob, zadní dvě řady sedadel lze demontovat a místo využít jako proctor pro náklad), r.v. 2020, vybavený

vznětovým motorem 2.0 110 kW, oxidačním katalyzátorem, filtrem částic a redukčním katalyzátorem SCR, nájezd 4-6 tis. km v době testování, plně naložený experimentálními aparaturami pro měření v rámci mezinárodních projektů uCARe a CARES (H2020 814966, City Air Remote Sensing, a 815002, You can always reduce emissions), byl osazen přenosným FTIR analyzátorem (Bruker Matrix), v autory upravené verzi se sníženou hmotností a spotřebou elektrické energie (Obr. 1), vzorkujícím z vyhřívané vzorkovací hadice napojené na sondu zasunutou do koncovky výfukového potrubí. Pro vyloučení možnosti ovlivnění řídící jednotky nebyla sbírána data z palubní diagnostiky ani nebyl motor osazen snímači; k dispozici je tak pouze složení výfukových plynů, které lze orientačně přepočítat na emise na kg paliva. Aktuální poloha, rychlost jízdy a zrychlení, a s větší nepřesností i podélný sklon vozovky, byly průběžně měřeny pomocí mobilního telefonu vybaveného GPS. Takto vybavený vůz absolval trasu z Prahy na zkušební okruh v Lelystadu (NL) a zpět. Trasa je znázorněna na mapě na Obr. 2 (vodorovná osa stupně východní délky, svislá osa stupně severní šířky, podkladová mapa www.mapy.cz).

Obr. 1: FTIR analyzátor (vlevo) a jeho instalace ve vozidle Toyota Proace (vpravo)

Obr. 2: Trasa Praha-Lelystad

3. VÝSLEDKY

Záznamy rychlosti jízdy, koncentrací NO ve výfukových plynech (koncentrace NO_2 byly relativně velmi nízké) a měrnými emisemi NO_x vyjádřenými v g na kg paliva jsou vyneseny pro první etapu (349 km) trasy Praha-Lelystad na obr. 3 a pro první etapu trasy Lelystad-Praha (432 km) na obr. 4. Zatímco trasa tam byla projeta dle zásad ekojízdy (klidná, předvídavá jízda), při zpáteční trase se střídala jízda dle zásad ekojízdy s dynamickou jízdou při dodržení silničních pravidel, bezpečnosti provozu a při respektování charakteru nákladu.

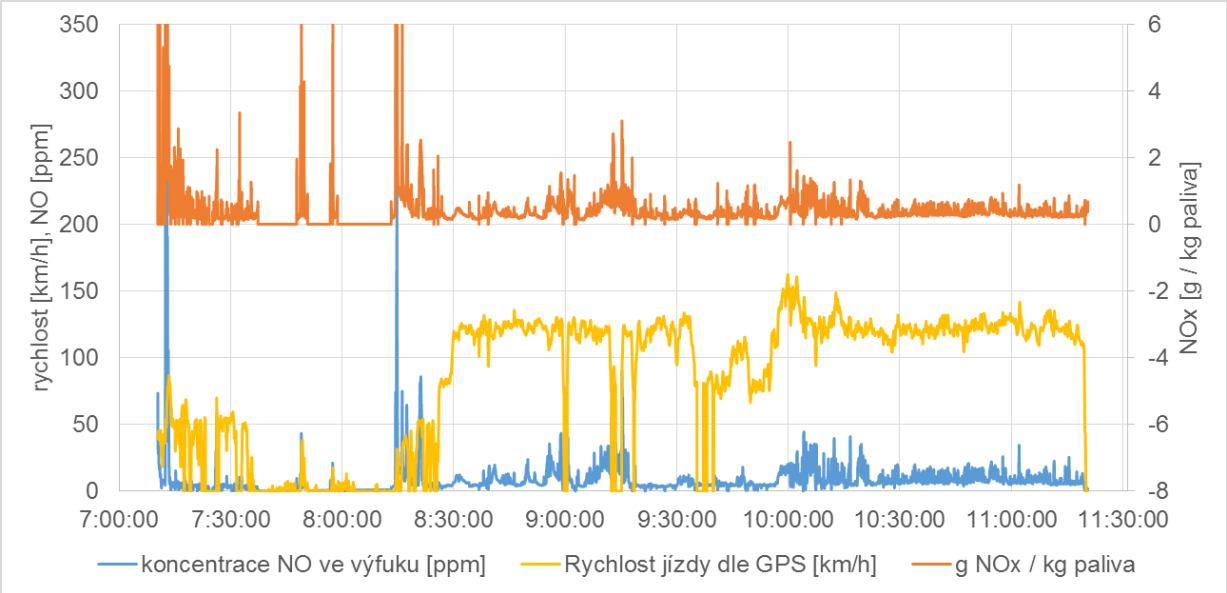

Obr. 3: Emise NO_x během první etapy jízdy Praha-Lelystad (prvních 349 km)

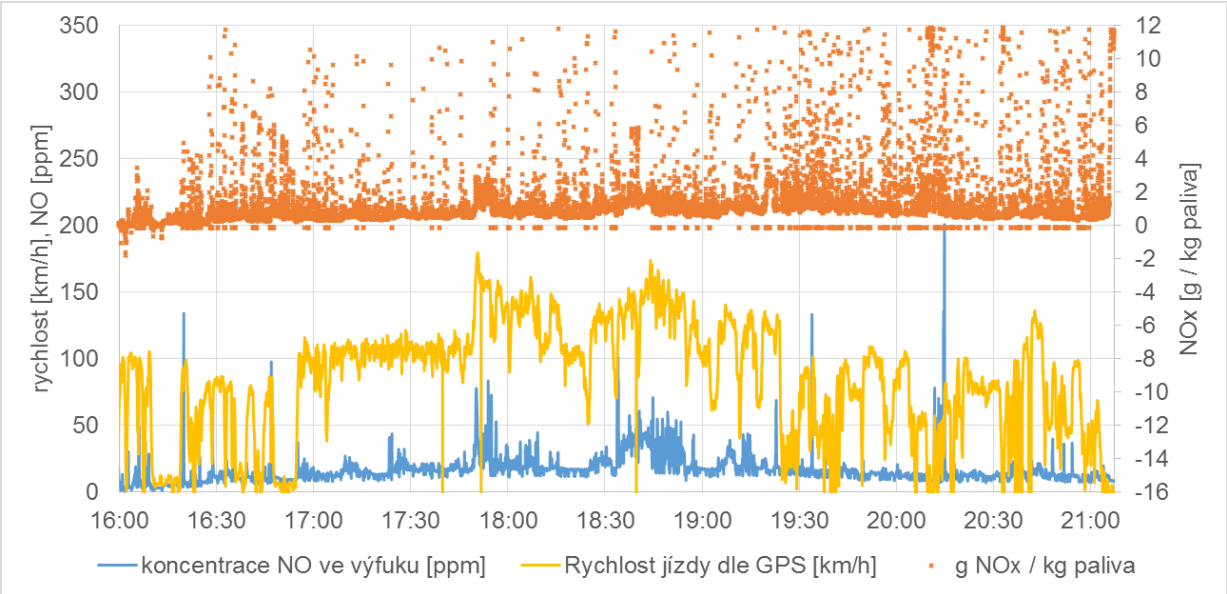

Obr. 4: Emise NO_x během první etapy jízdy Lelystad-Praha (prvních 432 km)

Při trase tam byly průměrné měrné emise (počítané jako běžný průměr měrných emisí, nikoliv jako vážený průměr, přičemž byly zahrnuty pouze úseky, kdy bylo ve výfuku alespoň 1 % CO2) 0,46 g NO_x na kg paliva (první etapa) a při cestě zpět (první a druhá etapa) 1,11 a 1,34 g NO_x na kg paliva. Při průměrné spotřebě motorové nafty 66,5 g/km tyto hodnoty hrubě odpovídají (nejistota vychází z nepříliš reálného předpokladu nezávislosti měrných emisí na okamžité spotřebě paliva) emisím NO_x 31 mg/km při cestě tam a 74 a 89 mg/km při cestě zpět. Koncentrace NO byly po většinu doby jízdy v nízkých desítkách ppm, s krátkými výkyvy do nízkých stovek ppm v souvislosti se studeným startem a akceleracemi ne zcela zahřátého nebo pomalou jízdou prochlazeného motoru.

Průměrné koncentrace nejvýznamnějších látek jsou vyneseny v Tab. 1. Koncentrace legislativou dosud nelimitovaných látek, NH_3 a N_2O, jsou v průměru v nízkých jednotkách ppm, nižší než jeden z možných zvažovaných budoucích limitů 10 ppm. Většina NO_x je emitována jako NO_2. Koncentrace CO jsou řádově 10 ppm, koncentrace formadehydu řádově desetiny ppm, což jsou hodnoty pod mezí kvantifikace přístroje.

Tab. 1: Průměrné koncentrace v surových výfukových plynech v ppm

	NH_3	NO	NO_2	CO_2	N_2O	CO	HCHO
Praha-Lelystad, část 1, 349 km	1.5	9.4	0.5	63396	1.7	10.4	0.3
Lelystad-Praha, část 1, 432 km	3.6	17.1	0.3	50024	4.5	4.9	0.1
Lelystad-Praha, část 2, 355 km	4.9	17.9	2.2	49145	3.5	12.9	0.1

Na celkových emisích NO, NH_3 a skleníkového plynu N_2O má velký podíl provoz s nižšími teplotami katalytických zařízení, ovšem nikoliv setrvalý (viz. obr. 3), ale po delším dálničním provozu. Tři ukázky z druhé etapy cesty z Lelystadu do Prahy jsou vyneseny na obr. 5.

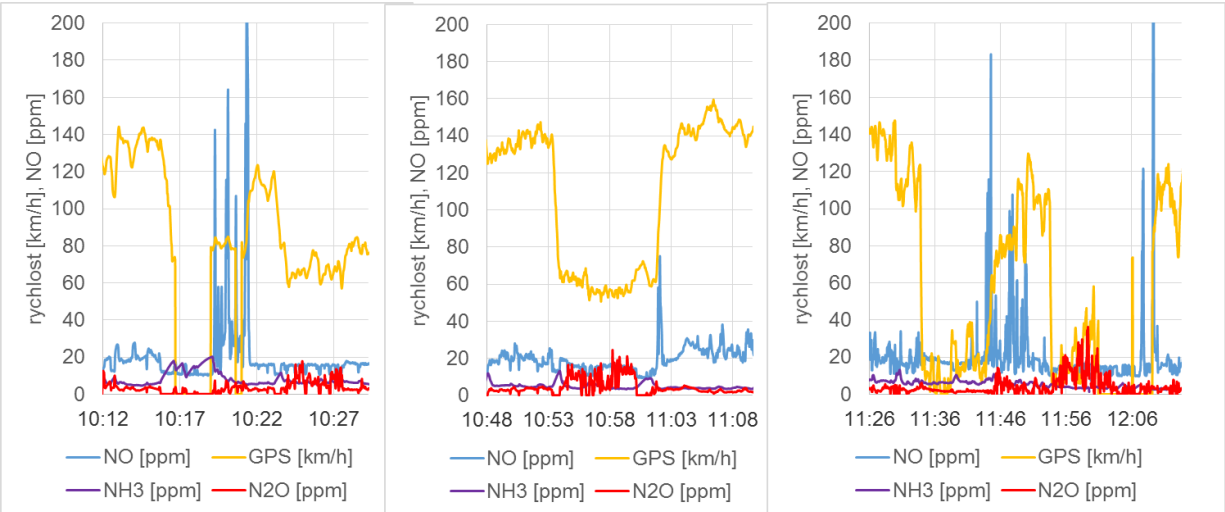

Obr. 5: Koncentrace NO, NH_3 a N_2O ve výfukových plynech při teplotě výfukových plynů snížené pomalou jízdou.

4. DISKUZE A ZÁVĚR

Již na první pohled je zřejmé, že koncentrace NO_x ve výfukových plynech jsou řádově nižší než je běžné u klasických vznětových motorů bez redukčních katalyzátorů. Z obr. 3 je patrné, že po studeném startu koncentrace NO výrazně klesají a po dobu městského provozu jsou v řádu jednotek ppm. Při provozu na dálnici koncentrace NO rostou, ale jen do nízkých desítek ppm (viz. obr. 3), do středních desítek ppm se dostávají pouze při dynamickém provozu při rychlosti nad 150 km/h (viz. obr. 4), kde díky vysokému průtoku výfukových plynů (násobně vyššímu oproti maximu homologačního cyklu WLTC) by bylo možné očekávat sníženou účinnost katalyzátorů. Exkurze nad 100 ppm jsou krátké a velmi řídké, a dle očekávání pravděpodobně souvisí se startem studeného motoru a s přechodovými jevy po ochlazení motoru provozem na nízké zatížení. Ač emise NO_x nelze z důvodu absence měření průtoku výfukových plynů kvantifikovat přesně, je patrné, že tyto jsou v řádu setin g na km, a to i v provozních režimech, ve kterých automobilové motory testované v dřívějších studiích vykazovaly emise v řádu jednoho g/km. Na rozdíl od některých jiných případů není snížení NOx provedeno na úkor navýšení emisí NH3 a/nebo N2O. S ohledem na nájezd 4-6 tis. km lze očekávat spíše příznivější výsledky, nicméně i tak lze konstatovat, že emise je možné označit pro lehké užitkové vozidlo za příkladné. Autoři poukazují na to, že se jedná o sériový vůz bez jakýchkoli dodatečných úprav, nikoliv o vývojový prototyp, a že instalace měřicích přístrojů proběhla tak, že je řídícím systémem motoru prakticky nezjistitelná. Výsledky naznačují, že požadavek na dodržení číselných hodnot limitů Euro 6d, při výrazně širší škále provozních režimů v porovnání s homologačním cyklem WLTC i podmínkami pro měření emisí za provozu pro účely homologace (RDE), může být možné reálně splnit, a to bez zřejmého navýšení emisí jiných, legislativou dosud nelimitovaných látek. Výsledky tím vyvracejí různá tvrzení, že požadavky emisní legislativy na emise v reálném provozu nejsou technicky splnitelné. Výsledky rovněž slouží jako praktická ukázka měření NH3 a N2O za provozu vozidla.

POUŽITÉ ZDROJE

[1] ZELDOVICH, Y.B. The Oxidation of Nitrogen in Combustion Explosions. Acta Physicochim. 1946, 21, 577–628. (Poznámka: Článek lze dohledat v Knihovně Akademie věd ČR, Národní třída, Praha.)

[2] EEA (European Environment Agency). Air Quality in Europe; Report; European Environment Agency: Copen-hagen, Denmark, 2020, doi:10.2800/786656. https://www.eea.europa.eu/publications/air-quality-in-europe-2020-report

[3] VOJTÍŠEK, M.: Addressing the last frontier of clean diesel engines: Measurement of real-world emissions of reactive nitrogen compounds and greenhouse gases using portable on-board systems. In: XLVIII. mezinárodní vědecká konference českých a slovenských univerzit a institucí zabývajících se výzkumem motorových vozidel a spalovacích motorů. TU v Liberci, 2017. ISBN 978-80-7494-354-6. http://koka2017.tul.cz/downloads/KOKA%202017_Sbornik.pdf

[4] VOJTÍŠEK, M.: Assessment of real-world primary emissions of reactive nitrogen species from mobile sources using molecular spectroscopy in mid-infrared region. In: XLVIII. mezinárodní vědecká konference českých a slovenských univerzit a institucí

zabývajících se výzkumem motorových vozidel a spalovacích motorů. ČVUT v Praze, 2020. p. 36-45. ISBN 978-80-01-06744-4.
[5] SUAREZ-BERTOA, R.; MENDOZA-VILLAFUERTE, P.; RICCOBONO, F.; VOJTÍŠEK, M.; PECHOUT, M. et al.: On-road measurement of NH3 emissions from gasoline and diesel passenger cars during real world driving conditions. Atmospheric Environment. 2017, 166 488-497. ISSN 1352-2310.
[6] VOJTÍŠEK, M.; BERÁNEK, V.; KLÍR, V.; JINDRA, P.; PECHOUT, M.; VOŘÍŠEK, T. On-road and laboratory emissions of NO, NO2, NH3, N2O and CH4 from late-model EU light utility vehicles: Comparison of diesel and CNG. Sci. Total Environ. 2018, 616–617, 774–784, doi:10.1016/j.scitotenv.2017.10.248.
[7] SUAREZ-BERTOA, R.; PECHOUT, M.; VOJTÍŠEK, M.; ASTORGA, C.: Regulated and Non-Regulated Emissions from Euro 6 Diesel, Gasoline and CNG Vehicles under Real-World Driving Conditions. Atmosphere. 2020, 11(2), ISSN 2073-4433.
[8] FALK, C. D., & MOONEY, J. J. (1980). Three—Way Conversion Catalysts: Effect of Closed—Loop Feed—Back Control and Other Parameters on Catalyst Efficiency. SAE Transactions, 1822-1832.
[9] JETTER, J., MAESHIRO, S., HATCHO, S., AND KLEBBA, R., "Development of an On-Board Analyzer for Use on Advanced Low Emission Vehicles," SAE Technical Paper 2000-01-1140, 2000, doi:10.4271/2000-01-1140.
[10] CALIFORNIA AIR RESOURCES BOARD: Executive Order no. A-023-0683, 2018,https://www.arb.ca.gov/msprog/onroad/cert/pcldtmdv/2018/honda_pc_a0230683_1d5_s3-30.pdf
[11] QUIROS, D.C.; et al.: Real-world emissions from modern heavy-duty diesel, natural gas, and hybrid diesel trucks operating along ma-jor California freight corridors. Emiss. Control. Sci. Technol. 2016, 2, 156–172, doi:10.1007/s40825-016-0044-0.
[12] JIANG, Y.; et al.: Characterizing emission rates of regulated pollutants from model year 2012 + heavy-duty diesel vehicles equipped with DPF and SCR systems. Sci. Total Environ. 2018, 619–620, 765-771, doi:10.1016/j.scitotenv.2017.11.120.
[13] WEISS, M.; et al. Will Euro 6 reduce the NOx emissions of new diesel cars?—Insights from on-road tests with Portable Emissions Measurement Systems (PEMS). Atmos. Environ. 2012, 62, 657–665, doi:10.1016/j.atmosenv.2012.08.056.
[14] SUAREZ-BERTOA, R.; et al.: On-road emissions of passenger cars beyond the boundary conditions of the real-driving emissions test. Environ. Res. 2019, 176, 108572. doi 10.1016/j.envres.2019.108572.

PODĚKOVÁNÍ

Měření proběhlo v rámci H2020 projektu č. 814966, uCARe – You can always reduce emissions. Samotná cesta vozidla proběhla v rámci H2020 projektů uCARe a 815002, CARES – City Air Remote Sensing.

52. MEZINÁRODNÍ VĚDECKÁ KONFERENCE ČESKÝCH A SLOVENSKÝCH UNIVERZIT A INSTITUCÍ ZAMĚŘENÁ NA VÝZKUMNÉ A VÝUKOVÉ METODY SPOJENÉ SE SPALOVACÍMI MOTORY, ALTERNATIVNÍMI POHONY A DOPRAVOU

22.-23. ZÁŘÍ 2021, PRAHA
ČESKÁ ZEMĚDĚLSKÁ UNIVERZITA V PRAZE, TECHNICKÁ FAKULTA,
KATEDRA VOZIDEL A POZEMNÍ DOPRAVY

SUPERCHARGED TWO-STROKE SPARK IGNITION ENGINE

Marek Žák[1], Jiří Čupera[2]

Abstract
The article presents an invention of a two-stroke internal combustion engine comprised of an engine housing and a crankcase comprising a crankshaft which is connected to a piston moving in a cylinder, an exhaust port leading from the cylinder space wherein the said exhaust port is open when the crankshaft is at its bottom dead centre and the said exhaust port is closed by the piston when the crankshaft is at its top dead centre, wherein the engine further comprises a rotary disk with an opening or recess on a part of its circumference, or with a protrusion on a part of its circumference, wherein the circumference of the said rotary disk extends into the exhaust port so that the exhaust port is completely closable / openable by means of the rotary disk.

1. INTRODUCTION

Although it has recently been decided in Brussels to ban, from 2035, the production of new cars with internal combustion engines, many industries still rely on the source of internal combustion engines. The following presented solution was created on the basis of a demand from a commercial company, and now, based on a patent application, the production of a prototype has started. Although the middle stream of engine developers is now copying stable solutions based on four-stroke supercharged engines, the demanded solution requiring extreme performance parameters at very limited weight necessarily requires the throwback of a two-stroke engine that will be supercharged with a mechanical compressor to achieve high performance. As is known, a two-stroke internal combustion engine is a piston engine in which each two-stroke of the piston is working. Compared to a four-stroke engine, a two-stroke engine has higher power (but the factor is not 2, but only 1.2 to 1.6), a simpler construction, a lower weight, and other advantages [1]. The principle of operation of a two-stroke engine has been known for more than 140 years [2] and,

[1] Ing. Marek Žák, Ph.D., Mendel University in Brno, Faculty od AgriSciences, Department of Technology and Automobile Transport, Zemědělská 1, 613 00 Brno, Czech Republic, marek.zak@mendelu.cz
[2] doc. Ing. Jiří Čupera, Ph.D., Mendel University in Brno, Faculty od AgriSciences, Department of Technology and Automobile Transport, Zemědělská 1, 613 00 Brno, Czech Republic, marek.zak@mendelu.cz, jiri.cupera@mendelu.cz

given the introduction of an innovative design solution, it is further described very briefly. The two-stroke engine is constructed so that the engine housing includes a crankcase in which a crankshaft connected to a piston moving in a cylinder is located. An air supply or a mixture of fuel and air, which can be closed by a reed valve, opens into the crankcase, and the crankcase is connected to the space above the piston by an overflow channel. The overflow channel is open at the bottom dead centre of the crankshaft, closed at the top dead centre of the crankshaft by the piston. From the space above the piston, an exhaust pipe leads away from the cylinder, which is open in the lower dead centre of the crankshaft, and is closed in the upper dead centre of the crankshaft by the piston.

When the piston moves from the top dead centre to the bottom dead centre (expansion), the piston first opens the exhaust duct and then the overflow. Since the mixture is compressed in the crankcase space by moving the piston to the bottom dead centre, at the moment of opening the overflow channel, the pressure in the crankcase is higher than in the cylinder space, forcing the exhaust gas to be forced out. When the piston moves from the bottom dead centre, the piston first closes the overflow channel and then the exhaust channel, which makes it impossible to achieve a higher charging pressure in the cylinder. The movement of the piston to the top dead centre causes negative pressure in the crankcase, into which the fresh mixture or air is sucked in. A common part of the exhaust duct is a rotary disk or a slider, which extends into the upper part of the duct and serves to aerodynamically move the upper edge of the exhaust duct downwards, which results in prolonged expansion and increased torque at lower engine speeds. However, this is not a closure of the exhaust duct. Since the given design does not allow one to increase the charging pressure, there are solutions of diesel engines with an external source of compressed air, which is fed through the intake ducts directly into the cylinder (not through the overflow channel through the crankcase). These intake ducts are opened by a piston as well as overflow ducts, the exhaust duct is replaced by a mechanically operated exhaust valve in the upper part of the combustion chamber. The auxiliary valve reduces the output, because work is required to open it. There are a number of design solutions described in detail in the literature, which rely on, for example, conventional valve distribution and allow the installation of sophisticated injection systems, such as GDI [3], or there are a number of patents that have the same goal [4].

The present technical solution shown in Fig. 1 aims to create such a design of the exhaust pipe closure, which would be structurally simple, efficient and easy to control.

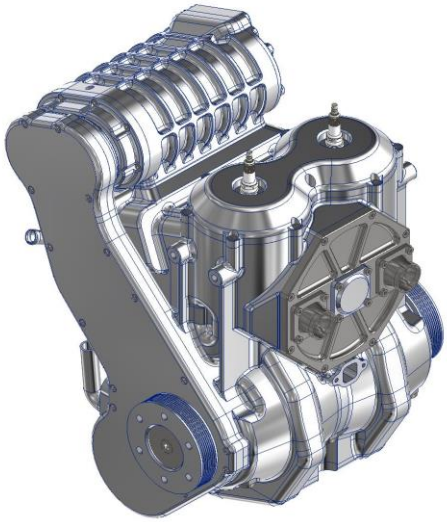

Figure 1: *A look at the concept of the developed supercharged two-stroke two-cylinder engine*

2. CONSTRUCTION SOLUTIONS

The presented technical solution achieves the above-mentioned object by providing a rotating disk with an opening or recess on part of the circumference, or with a protrusion on part of the circumference, this rotating disk extends through its circumference into the exhaust duct so that the exhaust duct is completely closable (see Fig. 2).

The subject of the innovation is, therefore, a two-stroke internal combustion engine comprised of an engine housing comprising a crankcase in which a crankshaft connected to a piston moving in a cylinder is located, the exhaust pipe leads out of the cylinder space, which is open at the bottom dead centre of the crankshaft and closed at the top dead centre of the crankshaft, the essence of which consists in that it further comprises a rotating disk with an opening or recess on part of the circumference, or with a protrusion on part of the circumference, this rotating disk extends into its circumference into the exhaust duct so that the exhaust duct is completely lockable / openable with a rotating disk. The term “close completely” means to close the entire cross-sectional area of the exhaust duct. In detail, the engine contains a crankcase, which is separated from the space above the piston, so the engine uses lossless lubrication. The change of the working charge is ensured by the ducts (intake and exhaust) located in the lower part of the cylinder. The arrangement of the intake and exhaust ducts corresponds to the arrangement of the overflow and exhaust ducts in some two-stroke engine designs. The suction ducts supply the fresh working charge from an external pressure source, such as a mechanical (contemporary design) or an electrified boosting solution (considered for some applications). In order to be able to achieve over boosting, i.e., increase the boost pressure above atmospheric pressure,

even if the exhaust duct is higher than the suction and the pressure would, thus, escape into the exhaust duct, the exhaust duct, according to the presented solution, is supplemented with a rotating disk. The rotating disk in the exhaust duct ensures its closure so that the cylinder charge cannot escape. The closing must take place in good time before the suction channels are closed by the piston, but late enough for the charge from the suction channels to push the exhaust gas residue out of the cylinder space, ideally beyond the position of the rotating disk, so that it is not stressed too much.

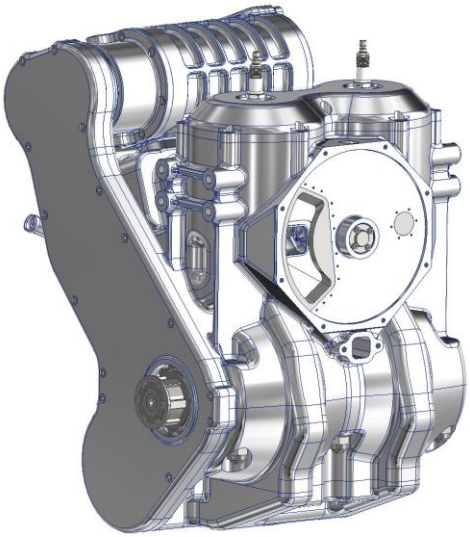

Figure 2: *View of the rotating disk of the developed engine*

The rotating disk is preferably placed as close as possible to the cylinder so that the volume of the exhaust channel between the piston and the disk is as small as possible. In some embodiments, the rotating disk may be substantially mounted perpendicular to the cross section of the exhaust duct. This ensures that the area enclosed by the disk is as small as possible, which makes it possible to minimise the size of the rotating disk. The rotating disk has an axis on which it is mounted and about which it rotates, located outside the exhaust duct. Since the exhaust gases can reach temperatures of around 1000 ° C, it is necessary that the disk storage and the drive are shielded from these temperatures. Possible embodiments of the rotating disk are schematically shown in Fig. 3. Fig. 3a shows a rotating disk with a protrusion on part of the circumference, Fig. 3b shows a rotating disk with a recess on part of the circumference, and Fig. 3c shows a rotating disk with a hole in part of the circumference.

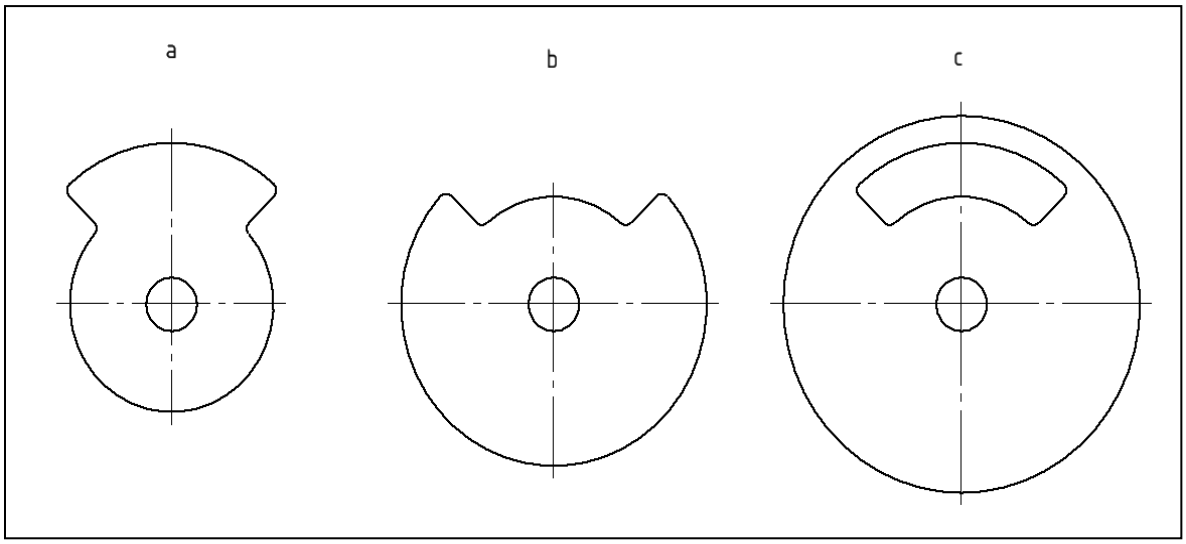

Figure 3: *View of the rotating disks of the developed engine*

The open part of the circumference of the rotating disk, i.e., the hole, the recess or the part of the circumference without the protrusion, corresponds to the opening time of the exhaust duct. The full part of the circumference of the rotating disk corresponds to the closing time of the exhaust duct. The case of the rotating disk in Fig. 3a corresponds to the angular section of the protrusion at the time of closing the exhaust duct. The rotating disk is then arranged so that the exhaust duct is closed by a protrusion from the moment when the piston is in the bottom dead centre area, which means between 20° before the bottom dead centre and 20° after the bottom dead centre (the intake ducts are still open and increase the charging pressure), at least until the exhaust duct is closed by the piston moving to the top dead centre, and at the same time that the exhaust duct is open (i.e., not closed by the rotating disk protrusion) when the piston moving from the top dead centre opens the exhaust duct. In the case of the rotating disks shown in Fig. 3b and 3c, the angular section of the orifice or recess corresponds to the opening time of the exhaust duct, i.e., the time from the opening of the exhaust duct by the piston on the way to the bottom dead centre alignment (which is in the range of 20° before the bottom dead centre to 20° after the bottom dead centre) so that after filling the exhaust duct with the full part of the edge of the disc, an increase in the charging pressure can be achieved. The angular dimension of the section of the hole, recess, resp. part of the circumference of the disc without the protrusion, is directly proportional to the gear ratio between the crankshaft and the rotating disc (the larger the gear, the larger the angle). The angular range also directly limits the gear ratio. If the transmission between the crankshaft and the rotating disk is solved purely mechanically, the meaningful values of the transmission ratio are 1; 2; 3, because a lower gear ratio does not close the exhaust duct fast enough, and a higher gear ratio requires too large of an angle section. The open portion of the circumference of the rotating disk may have a dimension in the range of, for example, 30 to 330 angular degrees, the dimension depending on the particular design as set forth herein. The diameter of the disc depends on the dimensions of the drive used and the bearings supporting its shaft. The rotating disk can be mounted directly on the crankshaft, or on

the shaft itself, which is driven by the drive mechanism from the crankshaft. The drive mechanism can be, for example, gears, a chain or a toothed belt. The purely mechanical coupling of the crankshaft disc complicates the variable timing. Alternatively, the rotating disk may be driven by an electric motor which rotates the disk without any mechanical coupling to the crankshaft. One embodiment may be a constant crankshaft and rotating disk speed. In other embodiments, the variable speed transmission of the crankshaft and the rotating disk may even be the speed of the rotating disk, which may be independent of the speed of the crankshaft (e.g., in the case of a rotating disk driven by an electric motor). This is advantageous because for different engine speeds as the appropriate moment of closing the exhaust duct can be varied to achieve optimal cylinder filling. The variability of the gear ratio, i.e., the variable timing of the exhaust duct closure, can significantly affect the operating parameters of the engine. The drive of the rotating disk can also be provided by a combination of the above options. The purpose of the rotating disk is to create sufficiently large aerodynamic resistance in the exhaust duct so that the charging pressure in the combustion chamber can be increased above atmospheric pressure. This requires the rotating disc to close the exhaust duct when the exhaust gases are already removed and the combustion chamber is purged, but, at the same time, the intake duct is still open (crankshaft bottom dead centre area) and keeping the duct closed until the exhaust duct is closed by the piston moving to the top dead centre. The rotating disk is still rotating during the operation of the engine, i.e., it is more energy efficient, and there is no need to expend the energy needed to compress the valve spring, as is the case with currently designed engines. In order to minimise the mechanical losses, the rotating disk can advantageously be mounted in the space of the exhaust duct with clearance (i.e., it does not touch the walls), the choice of the amount of clearance directly influences the maximum achievable cylinder charging pressure.

3. CONCLUSION

The mentioned design solution of the distribution mechanism for the supercharged two-stroke engine aims to bring simplicity and reliability while, at the same time, good regulation and low energy losses. Applications for high-performance electric generators and some special applications in aviation, including the military, are intended. A prototype is currently being produced, with laboratory testing expected in Q1 2022.

REFERENCES

[1] HEYWOOD J. B., SHER E. The Two-stroke Cycle Engine, Taylor&Francis, 1999, pp. 78. ISBN 978-0-56032-831-5
[2] NUNNEY J. M.. Light and Heavy Vehicle Technology, Butterworth-Heinemann, 2006, pp. 671. ISBN 978-0-7506-8037-0
[3] MACKALINI D. N., THOPSON D. M. L., ZHAO H. Effects of valve timing, valve lift and exhaust backpressure on performance and gas exchanging of a two-

stroke GDI engine with overhead valves, Energy Conversion and Management, 2016, pp. 71-83. ISSN 0196-8904

[4] EICKMANN K. Two-stroke engine with scavenging and charging, 1990, patent DE 3837502